

# **Biotribocorrosion of Hard-on-Hard Bearing Surfaces in Orthopaedic Hip Replacements**

by

**Andrew Robert Beadling**

Submitted in accordance with the requirements for the degree of

**Doctor of Philosophy**

The University of Leeds

School of Mechanical Engineering

July 2017

The candidate confirms that the work submitted is his own, except where work which has formed part of jointly-authored publications has been included. The contribution of the candidate and the other authors to this work has been explicitly indicated below. The candidate confirms that appropriate credit has been given within the thesis where reference has been made to the work of others.

This copy has been supplied on the understanding that it is copyright material and that no quotation from the thesis may be published without proper acknowledgement.

The right of Andrew Robert Beadling to be identified as Author of this work has been asserted by him in accordance with the Copyright, Designs and Patents Act 1988.

© 2017 The University of Leeds and Andrew Robert Beadling.

## Papers Contributing to this Thesis

Beadling, A., Bryant, M., Dowson, D. and Neville, A. The Effect of Microseparation on the Corrosion Rates of Metal-on-Metal Total Hip Replacements. In: *Corrosion 2015, 15-19 March 2015, Dallas (TX, USA)*.

Neville, A., Hesketh, J., Beadling, A. R., Bryant, M. G. and Dowson, D. Incorporating corrosion measurement in hip wear simulators: An added complication or a necessity? *Proc Inst Mech Eng H*. 2016, **230**(5), pp.406-20.

Beadling, A. R., Bryant, M., Dowson, D. and Neville, A. Tribocorrosion of hard-on-hard total hip replacements with metal and ceramic counterfaces under standard and adverse loading conditions. *Tribology International*. 2016, **103**, pp.359-67.

Beadling, A., Bryant, M. G., Dowson, D. and Neville, A. A Link Between the Tribology and Corrosive Degradation of Metal-on-Metal THRs. *Tribology International*. 2017, **113**, pp.354-61.

## Acknowledgements

Firstly I would like to extend my deepest gratitude to my primary academic supervisor, Professor Anne Neville. Without her encouragement, guidance and drive over the four years, and through all challenges, the work would not have been possible.

Secondly it has been a real privilege to work with Professor Duncan Dowson whose insight and advice has been invaluable and made an enormous impact on this work. He is still shaping the forefront of tribology research and no problem seemed insurmountable after a coffee bar discussion with Duncan.

I would also like to thank Dr. Michael Bryant, a true friend and colleague, who was always willing to trade his thoughts and an hour of his time for a cup of tea.

I would like to thank my predecessor, Dr. James Hesketh, whose work and help formed the foundation of this study. Also several past and present members of the iFS research group and support staff who have made my time working on the project a pleasure; in particular Drs. Emily Clark and Louise Austin, Jackie Kidd, Fiona Slade, Ron Cellier, Jordan Thomas and many others.

I would like to thank my partner Rebecca for listening to every complaint and frustration but always cheering me up. I am also indebted to Rebecca's parents, Yvonne and Richard, for their support and Sunday dinners.

Lastly I would like to thank my mum, dad and younger sisters for their support and encouragement. For their every faith in me and for putting up with my constant absence throughout the year, but still having a place at Christmas.

## Abstract

Following higher than acceptable failure rates, the most recent generation of Metal-on-Metal THRs have all but been removed from the market. Many recent studies in the literature attribute their failure to higher wear rates as a result of so-called 'adverse loading' scenarios.

In order to investigate the *in situ* corrosive degradation of 28 mm Metal-on-Metal and Metal-on-Ceramic Total Hip Replacement components under these 'adverse loading' scenarios, two hip simulators were instrumented with three-electrode electrochemical cells. Various DC electrochemical analysis techniques, including Linear Polarisation Resistance and Potentiostatic Polarisation, were used to quantify the corrosion currents released from the bearings during sliding.

Under 0.8 mm of Microseparation the corrosion currents were found to increase by a near order of magnitude compared to Standard Gait; which resulted in an increase of estimated corrosive volume loss from approximately 0.03 - 0.05 mm<sup>3</sup> to as much as 0.24 mm<sup>3</sup>. A similar increase was observed for Metal-on-Ceramic bearings whereby the contribution of corrosion to total material loss from the bearing shifted from approximately 4 - 8 % to as much as 17 %. Under potentiostatic polarisation the resultant anodic current transient was found to increase with increased angle of acetabular inclination. The magnitude of peak current increased from approximately 5 - 10  $\mu$ A at 30° inclination to 80 - 120  $\mu$ A at 50°.

Corrosion at the bearing surface of 28 mm Total Hip Components was found to be a significant source of corrosive material loss and ion release. This was also sensitive to the articulations conditions and did not necessarily scale linearly with total mass loss. Consideration of the mechanisms of degradation is therefore critical to pre-clinical assessment of devices in order to better predict *in vivo* performance.

# Contents

<b>Papers Contributing to this Thesis</b>	<b>iii</b>
<b>Acknowledgements</b>	<b>iv</b>
<b>Abstract</b>	<b>v</b>
<b>Contents</b>	<b>xii</b>
<b>List of Figures</b>	<b>xxiii</b>
<b>List of Tables</b>	<b>xxiv</b>
<b>List of Equations</b>	<b>xxvi</b>
<b>Nomenclature</b>	<b>xxvii</b>
<b>1 Introduction</b>	<b>1</b>
1.1 Motivation . . . . .	1
1.2 Outline . . . . .	3
<b>2 Biotribocorrosion</b>	<b>4</b>
2.1 Principles of Tribology . . . . .	4
2.1.1 Contact of Solids . . . . .	5
2.1.2 Friction . . . . .	7
2.1.3 Wear of Materials . . . . .	8
2.1.3.1 Abrasive Wear . . . . .	9
2.1.3.2 Adhesive Wear . . . . .	10
2.1.3.3 Flow Wear . . . . .	10
2.1.3.4 Fatigue Wear . . . . .	11
2.1.4 Lubrication . . . . .	11
2.1.4.1 Boundary Lubrication . . . . .	13

2.1.4.2	Fluid Film Lubrication . . . . .	13
2.1.4.3	Mixed Lubrication . . . . .	14
2.2	Principles of Corrosion . . . . .	14
2.2.1	Thermodynamics of Corrosion Processes . . . . .	15
2.2.2	Types of Corrosion . . . . .	18
2.2.2.1	Uniform / General Corrosion . . . . .	19
2.2.2.2	Galvanic Corrosion . . . . .	19
2.2.2.3	Crevice Corrosion . . . . .	20
2.2.2.4	Pitting Corrosion . . . . .	20
2.2.2.5	Intergranular Corrosion . . . . .	22
2.2.3	Corrosion Rate . . . . .	22
2.2.4	Three-Electrode Cell . . . . .	24
2.2.5	DC Polarisation . . . . .	25
2.2.5.1	Linear Polarisation Resistance . . . . .	26
2.2.5.2	Tafel Plot . . . . .	28
2.2.5.3	Potentiodynamic & Cyclic Polarisation . . . . .	29
2.3	Tribocorrosion . . . . .	30
<b>3</b>	<b>Literature Review</b>	<b>32</b>
3.1	Biomaterials . . . . .	32
3.1.1	Metals . . . . .	32
3.1.1.1	Iron Based Alloys . . . . .	32
3.1.1.2	Cobalt Based Alloys . . . . .	33
3.1.1.3	Titanium Based Alloys . . . . .	34
3.1.2	Ceramics . . . . .	34
3.1.3	Polymers . . . . .	34
3.2	History of Total Hip Replacements . . . . .	35
3.2.1	Metal-on-Metal (First Generation) . . . . .	37
3.2.2	Metal-on-Polymer . . . . .	38
3.2.3	Metal-on-Metal (Renewed Interest) . . . . .	39

3.3	Modern MoM THRs . . . . .	42
3.3.1	Modular THRs . . . . .	42
3.3.2	Resurfacing . . . . .	43
3.3.3	Adverse Reaction to Metallic Debris . . . . .	44
3.4	Pre-Clinical Assessment of Devices . . . . .	45
3.4.1	Initial Studies . . . . .	46
3.4.2	Adverse Loading . . . . .	50
3.4.2.1	Malpositioning . . . . .	50
3.4.2.2	Microseparation . . . . .	51
3.4.3	Tribocorrosion . . . . .	53
3.4.3.1	Tribometer Studies . . . . .	53
3.4.3.2	Hip Simulator Studies . . . . .	55
3.4.4	Tribochemical Reaction Layers . . . . .	59
3.5	Summary . . . . .	63
3.6	Aims and Objectives . . . . .	63
<b>4</b>	<b>Experimental Methodology and Design</b>	<b>65</b>
4.1	Materials . . . . .	65
4.1.1	Static & Pin-on-Plate Components . . . . .	65
4.1.2	Hip Simulation Components . . . . .	65
4.1.3	Lubricant . . . . .	67
4.1.4	Three-Electrode Cell . . . . .	68
4.2	Electrochemical Test Methods . . . . .	68
4.2.1	Open Circuit Potential . . . . .	68
4.2.2	Linear Polarisation Resistance . . . . .	69
4.2.3	Potentiostatic Polarisation . . . . .	71
4.2.4	Potentiodynamic Scanning & Cyclic Polarisation . . . . .	72
4.2.5	Short-Term Testing . . . . .	72
4.2.6	Long-Term Testing . . . . .	73
4.2.7	Statistical Analysis . . . . .	74

4.3	Tribometer . . . . .	75
4.3.1	Biceri Reciprocating Pin-on-Plate Tribometer . . . . .	75
4.3.2	Integration of Electrochemistry . . . . .	76
4.3.3	Test Methodology . . . . .	77
4.4	Hip Simulation . . . . .	77
4.4.1	ProSim Pneumatic Deep Flexion Hip Simulator . . . . .	78
4.4.2	ProSim Full-ISO Electromechanical Deep Flexion Simulator . . . . .	80
4.4.3	Integration of Electrochemistry . . . . .	82
4.4.4	Test Methodology . . . . .	83
4.4.4.1	Pneumatic Simulator . . . . .	83
4.4.4.2	Full-ISO Electromechanical Simulator . . . . .	84
4.5	Surface Analysis . . . . .	86
4.5.1	Coordinate Measuring Machine (CMM) . . . . .	86
4.5.2	White Light Interferometry (WLI) . . . . .	87
4.5.3	Scanning Electron Microscopy (SEM) and Energy Dispersive X-Ray Spectroscopy (EDX) . . . . .	89
4.5.4	Transmission Electron Microscopy (TEM) . . . . .	89
<b>5</b>	<b>Static &amp; Tribometer Studies</b>	<b>92</b>
5.1	Static Corrosion . . . . .	92
5.2	Tribometer . . . . .	95
5.2.1	Contact Pressures . . . . .	96
5.2.2	Electrochemistry . . . . .	96
5.2.3	White Light Interferometry (WLI) . . . . .	99
5.3	Summary . . . . .	102
<b>6</b>	<b>Hip Simulation (Metal-on-Metal)</b>	<b>104</b>
6.1	Standard Gait . . . . .	104
6.1.1	Open Circuit Potential . . . . .	105
6.1.2	Corrosion Current ( $I_{corr}$ ) . . . . .	106

6.1.3	Estimated Volume Loss . . . . .	107
6.1.4	Anodic Current Transients . . . . .	108
6.2	Microseparation . . . . .	110
6.2.1	Open Circuit Potential . . . . .	110
6.2.2	Corrosion Current ( $I_{corr}$ ) . . . . .	111
6.2.3	Estimated Volume Loss . . . . .	113
6.2.4	Anodic Current Transient . . . . .	114
6.3	Surface Analysis . . . . .	114
6.3.1	Coordinate Measuring Machine (CMM) . . . . .	115
6.3.2	White Light Interferometry (WLI) . . . . .	116
6.3.3	Scanning Electron Microscopy (SEM) and Energy Dispersive X-Ray Spectroscopy (EDX) . . . . .	118
6.3.4	Transmission Electron Microscopy (TEM) . . . . .	120
6.4	Summary . . . . .	123
<b>7</b>	<b>Hip Simulation (Metal-on-Ceramic)</b>	<b>125</b>
7.1	Standard Gait . . . . .	125
7.1.1	Open Circuit Potential . . . . .	126
7.1.2	Corrosion Current ( $I_{corr}$ ) . . . . .	127
7.1.3	Estimated Volume Loss . . . . .	128
7.1.4	Anodic Current Transient . . . . .	129
7.2	Microseparation . . . . .	130
7.2.1	Open Circuit Potential . . . . .	130
7.2.2	Corrosion Current ( $I_{corr}$ ) . . . . .	131
7.2.3	Estimated Volume Loss . . . . .	133
7.2.4	Anodic Current Transient . . . . .	134
7.3	Gravimetric Mass Loss . . . . .	135
7.4	Coordinate Measuring Machine (CMM) . . . . .	136
7.5	Summary . . . . .	138

<b>8</b>	<b>Adverse Loading</b>	<b>140</b>
8.1	Malpositioning . . . . .	140
8.1.1	Inclination (New Bearing) . . . . .	140
8.1.2	Inclination (After 333k Cycles) . . . . .	144
8.1.3	Inclination (Polarisation) . . . . .	147
8.1.4	Retroversion . . . . .	149
8.2	Link Between Corrosion and Tribology . . . . .	150
8.3	Daily Living Activities . . . . .	159
8.4	Summary . . . . .	163
<b>9</b>	<b>Discussion</b>	<b>165</b>
9.1	Adverse Loading . . . . .	169
9.1.1	Microseparation . . . . .	169
9.1.2	Acetabular Malpositioning . . . . .	173
9.2	Metal-on-Metal vs. Metal-on-Ceramic . . . . .	175
9.3	Assessment of Degradation . . . . .	177
9.4	Linking Tribology to Electrochemical Degradation . . . . .	180
9.4.1	Periodicity in Anodic Current Transients . . . . .	183
9.4.2	'Daily Living' Cycles . . . . .	186
9.4.3	Tribocorrosion Modelling . . . . .	188
9.5	Summary . . . . .	192
<b>10</b>	<b>Conclusions and Further Work</b>	<b>193</b>
10.1	Conclusions . . . . .	193
10.2	Limitations . . . . .	196
10.3	Future Work . . . . .	197
	<b>References</b>	<b>200</b>
	<b>Appendix A Oral and Poster Presentations</b>	<b>228</b>
A.1	Oral Presentations . . . . .	228

A.2 Poster Presentations . . . . .	229
<b>Appendix B Image Reproduction Permissions</b>	<b>230</b>

## List of Figures

1.1	Trends in hip replacement bearing couple materials in England and Wales (2003 - 2011). Taken from [6]. . . . .	2
2.1	Contact area between a ball and flat surface under load. . . . .	5
2.2	Illustration of asperity deformation in two contacting surfaces. . .	6
2.3	Illustration of a body in relative motion over a surface, where: $W$ is the Normal Load (N), $R$ is the Reaction Force (N) and $F$ is the Friction Force (N). . . . .	7
2.4	Illustration of the four principal mechanical wear processes: (a) abrasive wear, (b) adhesive wear, (c) flow wear and (d) fatigue wear.	9
2.5	A typical Stribeck curve. . . . .	11
2.6	Simplified schematic of a femoral head articulating within an acetabular cup. . . . .	12
2.7	Illustration of the electrical double layer (EDL) formed by metal ions and electrochemically active species (EAS). . . . .	16
2.8	Pourbaix diagram for chromium in pure water. Data taken from [32].	19
2.9	Illustration of various pit geometries as defined in ASTM-G46 [35].	21
2.10	Evans diagram of the anodic and cathodic half-cell reactions for both iron and hydrogen. . . . .	23
2.11	Illustration of the standard three-electrode cell experiment. . . . .	24
2.12	DC polarisation techniques, where: $E_b$ is the breakdown potential, $E_{pp}$ is the passivation potential and $E_{rp}$ is the repassivation potential.	25
2.13	Example of a linear polarisation curve. . . . .	26
2.14	Example of a typical Tafel plot, where: $\beta_a$ and $\beta_c$ are the anodic and cathodic Tafel constants respectively. . . . .	28
2.15	Illustration of depassivation of a protective oxide film as a result of the sliding action of a counterface. . . . .	30

3.1	Chemical structures of ethylene and polyethylene. . . . .	35
3.2	Estimated joint replacement company market share (2013). Data taken from [64]. . . . .	36
3.3	Examples of various design revisions to the McKee-Farrar hip [68].	37
3.4	Percentage of revisions conducted against time from primary surgery for different THR bearing couples [79]. . . . .	41
3.5	Schematic of a typical modular hip replacement. Adapted from [89].	43
3.6	Image of the McMinn or Birmingham Hip Resurfacing device [97].	44
3.7	Single station on the servo-hydraulic hip simulator (Shore Western Manufacturing Inc, Monrovia, CA) utilised by Anissian <i>et al.</i> [108].	47
3.8	Illustration of Microseparation of the Femoral Head and Acetabular Liner during a gait cycle. . . . .	52
3.9	Wear coefficients for HC and LC CoCrMo alloy and 316L Stainless Steel in different lubricants [141]. Reproduced with permission (see Appendix B). . . . .	54
3.10	Anodic current and friction coefficient for silicon nitride articulating against HC CoCrMo alloy [11]. Adapted and reproduced with permission (see Appendix B). . . . .	55
3.11	Schematic of the pendulum friction simulator used by Yan <i>et al.</i> [153]. Reproduced with permission (see Appendix B). . . . .	56
3.12	Cyclic variation in potentiostatic current during articulation of a 36 mm HC CoCr hip bearing [15]. Reproduced with permission (see Appendix B). . . . .	58
3.13	The acetabular liner (left) and femoral head (right) from an explanted McKee-Farrar prosthesis displaying a visible tribofilm formation on both surfaces [7]. Reproduced with permission (see Appendix B). . . . .	60
3.14	EELS spectra of dried bovine serum, the tribological layer and graphite [9]. Reproduced with permission (see Appendix B). . . . .	61

3.15	TEM image of particles suspended in the tribolayer noted on the surface of 36 mm MoM hip bearings articulated in a hip simulator. Reproduced with permission (see Appendix B). . . . .	62
4.1	Image of unworn 28 mm diameter (left to right) <i>CoCrMo</i> Femoral head, <i>CoCrMo</i> Acetabular Liner and BioloX®delta Ceramic Acetabular Liner. . . . .	66
4.2	3D Models of the acetabular cup fixture (left) and the femoral head fixture and spigot (right) containing 28 mm components. . . . .	66
4.3	Example static (left) and sliding (right) LPR scans with fitting curves.	69
4.4	Illustration of the small volume electrochemical cell utilised for static tests. . . . .	73
4.5	OCP profile of short-term tests highlighting timing of sliding period and DC polarisation techniques. . . . .	74
4.6	Schematic of the three-electrode cell within the Biceri tribometer. .	76
4.7	Flow chart summarising the testing both in static conditions and in tribometer studies completed through the course of this thesis. . .	77
4.8	The ProSim Deep Flexion hip simulator test station. . . . .	79
4.9	Demand vs. output curves for the standard twin-peak profile on the Deep Flexion simulator. . . . .	80
4.10	Pro-Sim Full-ISO Deep Flexion electromechanical adverse loading hip simulator . . . . .	81
4.11	Demand vs. output curves for the ISO 14242-1 [166] cycle on the Full-ISO Deep Flexion electromechanical adverse loading simulator.	82
4.12	Schematic of the three-electrode test cell within the hip simulator station. . . . .	83
4.13	Axial Load and Rotational axes for Daily Living profiles derived from data provided by Bergmann <i>et al.</i> [173, 175]. . . . .	85
4.14	Flow chart summarising the testing completed across the two simulators through the course of this thesis. . . . .	86

4.15	Illustration of ‘point’ CMM profile (left) and resultant RedLux Sphere Profile analysis of a 36 mm femoral head (right). . . . .	87
4.16	Schematic of White-Light Interferometry set-up [178]. Reproduced with permission (see Appendix 2). . . . .	88
4.17	Example 3D WLI scan of a wear scar on a CoCrMo plate following testing in the Biceri tribometer. . . . .	89
4.18	Preparation of TEM slide using FIB SEM [180]: (a) sample surface, (b & c) deposition of protective <i>Pt</i> layer, (d & e) surface milled with <i>Ga</i> ion beam to form slide, (f & g) slide removed and attached to a <i>Cu</i> post and (h) final thinning of slide to approximately 10 nm thickness. . . . .	90
5.1	Average Open Circuit Potential (OCP) plot for HC CoCrMo alloy allowed to stabilise in different physiological electrolytes for one hour. . . . .	93
5.2	Potentiodynamic Scanning curves for HC CoCrMo plates in different physiological electrolytes . . . . .	94
5.3	Mean breakdown potential for HC CoCrMo in different physiological electrolytes. Error bars represent standard deviation, n = 3. . .	95
5.4	Three static (left) and three sliding (right) Linear Polarisation Resistance scans ( $\pm 25$ mV @ 1 mV/s) showing Polarisation Resistance ( $R_p$ ) fit and values. . . . .	97
5.5	Polarisation Resistance ( $R_p$ ) for Metal-on-Metal tribometer contacts under different applied weights for static and sliding conditions. Error bars represent standard deviation between three LPR scans. Three repeats taken at each weight (n = 3). . . . .	98
5.6	Corrosion Current ( $I_{corr}$ ) for Metal-on-Metal tribometer contacts under different applied weights for static and sliding conditions. Error bars represent standard deviation between three LPR scans. Three repeats taken at each weight (n = 3). . . . .	99

5.7	Average Corrosion Current ( $I_{corr}$ ) for Metal-on-Metal tribometer contacts combined from three repeats under different applied weights for static and sliding conditions. Significant difference (ANOVA, Tukey HSD, $p < 0.05$ ) shown and error bars represent standard deviation. . . . .	100
5.8	2D NPFlex White Light Interferometry scans of the plate wear scars after 4,000 cycles of reciprocating tribometer testing under different loads and contact conditions. . . . .	101
5.9	Initial Hertz point contact width, measured wear scar width and average corrosion current during sliding ( $I_{corr}$ ) for metal-on-metal pin-on-plate reciprocating tribometer testing with varying hanging weight. Error bars represent standard deviation. . . . .	101
5.10	WLI determined surface roughness within the wear scar ( $S_a$ ) and estimated wear volume from simple configuration metal-on-metal pin-on-plate reciprocating tribometer testing with varying hanging weights. Error bars represent standard deviation. . . . .	102
6.1	Open Circuit Potential for 28 mm MoM bearings under Standard Gait articulation over 1 million cycles. Vertical dashed lines represent serum changes. . . . .	105
6.2	Corrosion Current ( $I_{corr}$ ) for 28 mm MoM bearings under Standard Gait articulation over 1 million cycles. Vertical dashed lines represent serum changes. . . . .	106
6.3	Estimated Volume Loss as a result of oxidation at the bearing surface for 28 mm MoM bearings under Standard Gait articulation over 1 million cycles. Upper and lower error bars represent possible preferential release of $Co$ and $Cr$ ions respectively. Vertical dashed lines represent serum changes. . . . .	108
6.4	Example Anodic Current Transient (+50 mV vs. OCP) for 28 mm MoM bearings under three cycles of Standard Gait. . . . .	109

6.5	Open Circuit Potential for 28 mm MoM bearings under 0.8 mm Microseparation over 1 million cycles. Vertical dashed lines represent serum changes. . . . .	111
6.6	Corrosion Current ( $I_{corr}$ ) for 28 mm MoM bearings under 0.8 mm Microseparation over 1 million cycles. Vertical dashed lines represent serum changes. . . . .	112
6.7	Estimated Volume Loss as a result of oxidation at the bearing surface for 28 mm MoM bearings under 0.8 mm Microseparation over 1 million cycles. Upper and lower error bars represent possible preferential release of <i>Co</i> and <i>Cr</i> ions respectively. Vertical dashed lines represent serum changes. . . . .	113
6.8	Example Anodic Current Transient (+50 mV vs. OCP) for 28 mm MoM bearings under three cycles of 0.8 mm Microseparation. . . .	114
6.9	Sphere Form Profile Analysis of a 28 mm Metal-on-Metal femoral head after 1 MCycles articulation under Standard Gait. . . . .	115
6.10	(Sphere Form Profile Analysis of a 28 mm Metal-on-Metal femoral head after 1 MCycles articulation under Microseparation.) . . . .	116
6.11	White Light Interferometry scans at the pole of an unworn 28 mm <i>CoCrMo</i> alloy femoral head (a) and after one million cycles of Standard Gait (b) and Microseparation (c). . . . .	117
6.12	SEM image of Carbon rich tribofilm noted on the bearing surface of 28 mm HC CoCrMo Femoral Head after 1 million cycles under Standard Gait. . . . .	119
6.13	EDX Spectra of the surface of 28 mm HC CoCrMo Femoral Head (above) and Carbon rich tribofilm (below) after 1 million cycles under Standard Gait. . . . .	120
6.14	Light Field (a) and Dark Field (b) images of a slide taken from an Unworn section of a 28 mm CoCr Femoral Head. . . . .	121

6.15	Light Field (a) and Dark Field (b) images of a slide taken from the ‘stripe wear’ area of a 28 mm CoCr Femoral Head subjected to 1 Mcycles of 0.8 mm Microseparation. . . . .	122
6.16	Selected Area Electron Diffraction (SAED) patterns taken at the unworn bulk area (a) and at the worn nano-crystalline layer (b). . . . .	122
7.1	Open Circuit Potential for 28 mm MoC bearings under Standard Gait articulation over 1 million cycles. Vertical dashed lines represent serum changes. . . . .	127
7.2	Corrosion Current ( $I_{corr}$ ) for 28 mm MoC bearings under Standard Gait articulation over 1 million cycles. Vertical dashed lines represent serum changes. . . . .	128
7.3	Estimated Volume Loss as a result of oxidation at the bearing surface for 28 mm MoC bearings under Standard Gait articulation over 1 million cycles. Upper and lower error bars represent possible preferential release of $Co$ and $Cr$ ions respectively. Vertical dashed lines represent serum changes. . . . .	129
7.4	Example Anodic Current Transient (+50 mV vs. OCP) for 28 mm MoC bearings under three cycles of Standard Gait. . . . .	130
7.5	Open Circuit Potential for 28 mm MoC bearings under 0.8 mm Microseparation over 1 million cycles. Vertical dashed lines represent serum changes. . . . .	131
7.6	Corrosion Current ( $I_{corr}$ ) for 28 mm MoC bearings under 0.8 mm Microseparation over 1 million cycles. Vertical dashed lines represent serum changes. . . . .	132
7.7	Estimated Volume Loss as a result of oxidation at the bearing surface for 28 mm MoC bearings under 0.8 mm Microseparation over 1 million cycles. Upper and lower error bars represent possible preferential release of $Co$ and $Cr$ ions respectively. Vertical dashed lines represent serum changes. . . . .	133

7.8	Example Anodic Current Transient (+50 mV vs. OCP) for 28 mm MoC bearing under three cycles of 0.8 mm Microseparation. . . . .	134
7.9	Sphere Form Profile Analysis of a new 28 mm <i>CoCrMo</i> alloy femoral head. . . . .	137
7.10	Sphere Form Profile Analysis of a 28 mm <i>CoCrMo</i> alloy femoral head articulated against a ceramic acetabular cup for 1 Mcycle of Standard Gait. . . . .	137
7.11	Sphere Form Profile Analysis of 28 mm <i>CoCrMo</i> alloy femoral head articulated against a ceramic acetabular cup after 1 Mcycle of Microseparation. . . . .	138
7.12	Sphere Form Profile Analysis of a 28 mm Metal-on-Ceramic femoral head after 1 Mcycle articulation under Microseparation showing rear ‘equatorial’ stripe. . . . .	139
8.1	Open circuit potential for a new 28 mm MoM bearing articulating under an ISO 14242-1 profile for 4,000 cycles at varying angles of cup inclination. . . . .	141
8.2	Corrosion current ( $I_{corr}$ ) for a new 28 mm MoM bearing under static and sliding conditions at varying angles of cup inclination. Error bars represent standard deviation, n = 3. . . . .	142
8.3	Anodic current transients (+50 mV vs. OCP) for a new 28 mm MoM bearing articulating under an ISO 14242-1 profile at varying angles of cup inclination. . . . .	143
8.4	Open circuit potential for a 28 mm MoM bearing, after 333 kcycles of sliding, articulating under an ISO 14242-1 profile for 4,000 cycles at varying angles of cup inclination. . . . .	144
8.5	Corrosion current ( $I_{corr}$ ) for a 28 mm MoM bearing, after 333 kcycles of sliding, under static and sliding conditions at varying angles of cup inclination. Error bars represent standard deviation, n = 3. . . . .	145

8.6	Anodic current transients (+50 mV vs. OCP) for a 28 mm MoM bearing, after 333 kcycles of sliding, articulating under an ISO 14242-1 profile at varying angles of cup inclination. . . . .	146
8.7	Anodic current transients (+0 mV vs. Ref.) over the first 600 cycles for a 28 mm MoM bearing, after 333 kcycles of sliding, articulating under an ISO 14242-1 profile at varying angles of cup inclination increased in ‘parallel.’ . . . . .	148
8.8	Anodic current transients (+0 mV vs. Ref.) over the first 600 cycles for a 28 mm MoM bearing, after 333 kcycles of sliding, articulating under an ISO 14242-1 profile at varying angles of cup inclination increased in ‘series.’ . . . . .	149
8.9	Anodic current transients (+0 mV vs. Ref.) over the first 600 cycles for a 28 mm MoM bearing, after 333 kcycles of sliding, articulating under an ISO 14242-1 profile at varying angles of cup retroversion.	150
8.10	Open circuit potential for a 28 mm MoM bearing after 333 kcycles of articulation under an ISO 14242-1 profile at cycle frequencies ranging from 0.4 to 1.4 Hz. . . . .	151
8.11	Anodic current transient (+50 mV vs. OCP) and axial load for a 28 mm MoM bearing under an ISO 14242-1 profile at cycle frequencies ranging from 0.4 to 1.4 Hz. . . . .	153
8.12	Initial OCP cathodic shift and peak anodic current for a 28 mm MoM bearing under an ISO 14242-1 profile at cycle frequencies ranging from 0.4 to 1.4 Hz. . . . .	154
8.13	Time delay between peaks in axial load and anodic current transient for different cycle frequencies. Error bars represent standard deviation, n = 3. . . . .	154
8.14	Three cycles of anodic current transient (+50 mV vs. OCP) for a 28 mm MoM bearing articulating under an ISO 14242-1 profile at cycle frequencies ranging from 0.4 to 1.4 Hz. . . . .	155

8.15	Axial Force and Resultant Entrainment Velocity at the contact for a 28 mm MoM bearing articulating under an ISO 14242-1 profile at cycle frequencies ranging from 0.4 to 1.4 Hz. . . . .	156
8.16	Anodic Current Transient (+50 mV vs. OCP) and Inverted Theoretical Minimum Film Thickness for a 28 mm MoM bearing under an ISO 14242-1 profile at cycle frequencies ranging from 0.4 to 1.4 Hz.	158
8.17	Anodic Current Transient (+50 mV vs. OCP) and Inverted Theoretical Minimum Film Thickness for a 28 mm MoM bearing under a 'Physiological Gait' cycle derived from data provided by Bergmann <i>et al.</i> [173, 175]. . . . .	160
8.18	Anodic Current Transient (+50 mV vs. OCP) and Inverted Theoretical Minimum Film Thickness for a 28 mm MoM bearing under a 'Stair Climb' cycle derived from data provided by Bergmann <i>et al.</i> [173, 175]. . . . .	162
8.19	Anodic Current Transient (+50 mV vs. OCP) and Inverted Theoretical Minimum Film Thickness for a 28 mm MoM bearing under a 'Chair Down - Up' cycle derived from data provided by Bergmann <i>et al.</i> [173, 175]. . . . .	162
9.1	Hip simulator reported volumetric wear rate for MoP devices under walking [108, 214–216] and MoM devices under walking [108, 112, 113, 116, 125, 154, 201, 202, 217–220] and adverse loading conditions [124, 126, 201, 220]. . . . .	167
9.2	Contour plots of the contact pressure (MPa) at the inner surface of acetabular cup with different major radii (mm) under 0.25 mm micro-lateralization [172]. Reproduced with permission (see Appendix 2). . . . .	171

9.3	Sphere form profile analysis of a 28 mm femoral head after 1 MCycles articulation against a metal acetabular liner under 0.8 mm microseparation. The black region represents the deviation from the nominal sphere over the ‘stripe wear’ region. . . . .	172
9.4	Schematic illustration of the hip simulator test cell at different angles of inclination. . . . .	174
9.5	Simulator wear rates for Metal-on-Metal bearings reported across several laboratory studies; the points in red are under some adverse loading scenario. Reproduced with permission. . . . .	178
9.6	Example anodic current transients for 28 mm MoM bearings articulating under an ISO 14242 walking gait cycle. . . . .	181
9.7	Example of how the time delay between the primary and secondary peaks in load and anodic current were determined. . . . .	182
9.8	Severity Factor proposed by Hesketh <i>et al.</i> [15] applied to the parameters used in the Hamrock-Dowson model used in this study. .	185
9.9	Anodic current transients (+50 mV vs. OCP) for a new 28 mm MoM bearing articulating under an ISO 14242-1 profile and upon switching to the physiologic gait daily living cycle. . . . .	187
9.10	Running in wear of Metal-on-Metal bearings versus the predicted film thickness [235]. . . . .	190
9.11	Total, mechanical and chemical mass loss as predicted by the Cao <i>et al.</i> [245, 246] tribocorrosion model for a given articulation cycle [245]. Reproduced with permission (see Appendix 2). . . . .	191

## List of Tables

2.1	Electrochemical series for selected standard electrode potentials at 25°C. . . . .	18
5.1	Initial contact conditions for metal-on-metal pin-on-plate sliding tribometer couples with 100 mm radius domed pin and different hanging weights. . . . .	96
7.1	The Femoral Head and Acetabular Cup radii and calculated radial clearance for 28 mm MoC THR bearings determined by CMM and RedLux Sphere Profile software. ‘SG’ and ‘MS’ refer to Standard Gait and Microseparation respectively. . . . .	126
7.2	Gravimetric Mass Loss for 28 mm MoC Femoral Heads after one million cycles under Standard Gait and Microseparation . . . . .	135

## List of Equations

2.1	Hertzian contact pressure. . . . .	5
2.2	Number of asperity contacts across two surfaces under load. . . . .	6
2.3	Real contact area between two loaded surfaces. . . . .	6
2.4	Amontons' first law of friction. . . . .	7
2.5	Friction force from specific resistance to asperity shearing. . . . .	8
2.6	Archard wear equation. . . . .	8
2.7	Normalised wear coefficient. . . . .	8
2.8	Abrasive wear model for single-asperity contact. . . . .	10
2.9	Lamda ratio for determining lubrication regime. . . . .	12
2.10	Hamrock-Dowson equation. . . . .	13
2.11	Oxidation of metallic elements to metal ions. . . . .	15
2.12	Half-Cell Reaction for the reduction of Oxygen. . . . .	16
2.13	Van't Hoff reaction isotherm. . . . .	16
2.14	Chemical energies in corresponding electrical terms. . . . .	17
2.15	Nernst equation. . . . .	17
2.16	Butler Volmer equation. . . . .	22
2.17	Stern-Geary equation. . . . .	27
2.18	Synergistic effects between wear and corrosion . . . . .	31
3.1	Severity Factor proposed by Hesketh <i>et al.</i> . . . . .	59
4.1	Charge transfer. . . . .	70
4.2	Faraday's Law . . . . .	70
4.3	CMM Length Measurement Tolerance . . . . .	87
8.1	Resultant Entrainment Vector . . . . .	156
9.1	Resolving the Hesketh <i>et al.</i> severity factor. . . . .	184
9.2	The chemical mass loss component of the Cao <i>et al.</i> tribocorrosion model for wear of Metal-on-Metal hip joints. . . . .	188
9.3	Effective normal force for MoM contacts in a hip simulator. . . . .	189

9.4 The resolved chemical mass loss component of the Cao *et al.* tribo-  
corrosion model for wear of Metal-on-Metal hip joints. . . . . 190

# Nomenclature

AA	Abduction / Adduction
AF	Axial Force
ALVAL	Aseptic Lymphocyte-dominated Vasculitis-Associated Lesion
ANOVA	Analysis of variance
ARMD	Adverse Reaction to Metallic Debris
CoC	Ceramic-on-Ceramic
CoCrMo	Cobalt-Chromium-Molybdenum alloy
CoP	Ceramic-on-Polymer
CP-Ti	Commercially Pure Titanium
DMEM	Dulbeccos Modified Eagles Medium
EDX	Energy-Dispersive X-ray Spectroscopy
EELS	Electron Energy Loss Spectroscopy
ELI-Ti	Extra-Low Interstitial Titanium (Ti-6Al-4V)
FBS	Foetal Bovine Serum
FDA	Food and Drug Administration (America)
FE	Flexion / Extension
FIB	Focussed Ion Beam
HC	High-Carbon content ( $> 0.15\%$ )
HipSim	Hip Simulator
HSD	Honest significant difference
HMWPE	High Molecular Weight Polyethylene
IE	Internal / External Rotation
LC	Low-Carbon content ( $< 0.15\%$ )
Mcycle	Mega-cycle (1,000,000 cycles)
MHRA	Medicines and Healthcare Products Regulatory Agency (UK)
MoC	Metal-on-Ceramic
MoM	Metal-on-Metal

MoP	Metal-on-Polymer
MS	Microseparation
NaCl	Sodium Chloride
NBCS	New-born Calf Serum
PBS	Phosphate Buffered Saline
PMMA	Poly(Methyl Methacrylate)
PoB	Pin-on-Ball
PoD	Pin-on-Disc
PoP	Pin-on-Plate
SDS	Stop-Dwell-Start
SEM	Scanning Electron Microscopy
SG	Standard Gait
TEM	Transmission Electron Microscopy
THR	Total Hip Replacement
TJR	Total Joint Replacement
TNF $\alpha$	Tumor Necrosis Factor Alpha
TPC	Total Protein Content
UHMWPE	Ultra-high Molecular Weight Polyethylene
WLI	White Light Interferometry
XPS	X-ray Photoelectron Spectroscopy
ZTA	Zirconia-Toughened Alumina

Tribology:

$\alpha$	Asperity Shape Factor
$\beta$	Degree of wear by abrasive asperity
$\eta$	Viscosity
$\omega$	Rotational Speed (rads <sup>-1</sup> )
$\lambda$	Lambda Ratio
$\mu$	Friction Coefficient

$\phi(z)$	Probability Density Function
$\nu$	Poisson's Ratio
$a$	Contact Half-width (mm)
$A$	Real Contact Area
$A_i$	Single Asperity Contact Area
$d$	Separation of Mean Surface Levels
$E$	Elastic Modulus (Pa)
$E'$	Equivalent Elastic Modulus (Pa)
$F$	Friction Force (N)
$h_{min}$	Theoretical minimum film thickness ( $\mu\text{m}$ )
$H$	Hardness
$k$	Wear Coefficient ( $\frac{\text{m}^3}{\text{Nm}}$ )
$K$	Archard Coefficient
$L$	Sliding Distance (m)
$n$	Number of Asperity Contacts
$N$	Number of Surface Peaks
$r$	Radius (m)
$R$	Reaction Force (N)
$R_a$	Surface Roughness
$R_s$	Characteristic Summit Radius
$R'$	Equivalent Radius (m)
$S_a$	3D Surface Roughness
$u$	Entraining velocity ( $\text{ms}^{-1}$ )
$V$	Volumetric Wear ( $\text{m}^3$ )
$W$	Load (N)
$z$	Peak Heights

Electrochemistry:

$\alpha_a$	Anodic charge transfer coefficient
------------	------------------------------------

$\alpha_c$	Cathodic charge transfer coefficient
$\beta_a$	Anodic Tafel slope (V/decade)
$\beta_c$	Cathodic Tafel slope (V/decade)
$\Delta G$	Gibbs Free Energy
$\Delta G^0$	Standard Free Energy for all Reactants
$\eta$	Applied overpotential (V)
CE	Counter Electrode
CP	Cyclic Polarisation
$e^-$	Electron
$E$	Electrode Potential (V)
$E^0$	Standard Electrode Potential (V)
$E_b$	Breakdown Potential (V)
$E_{OCP}$	Open Circuit Potential (V)
$E_{pp}$	Passivation Potential (V)
$E_{rp}$	Repassivation Potential (V)
$E_{SHE}$	Potential vs. Standard Hydrogen Electrode (V)
EAS	Electrochemically Active Species
EDL	Electrical Double Layer
$F$	Faraday Constant (96,490 Cmol <sup>-1</sup> )
$i$	Current Density (A/cm <sup>2</sup> )
$i_{corr}$	Corrosion Current Density (A/cm <sup>2</sup> )
$I$	Current (A)
$I_{corr}$	Corrosion Current (A)
$J$	Activity Quotient
LPR	Linear Polarisation Resistance
$m$	Corrosive mass loss (g)
$M$	Atomic Mass
$M^{z+}$	Metal Ion
$n$	Number of electrons in half-cell reaction

OCP	Open Circuit Potential
PDS	Potentiodynamic Scanning
$Q$	Charge Transfer (C)
$R$	Ideal Gas Constant ( $8.314 \text{ JK}^{-1}\text{mol}^{-1}$ )
$R_p$	Polarisation Resistance (Ohms)
RE	Reference Electrode
$T$	Temperature (K)
WE	Working Electrode
$z$	Valence Number

Tribocorrosion:

$C_0$	Pure Corrosion
$C_w$	Wear enhanced Corrosion
$S$	Synergistic material loss
$T$	Total material loss
$V_{mech}$	Volume loss as a result of mechanical phenomena
$V_{chem}$	Volume loss as a result of chemical phenomena
$W_0$	Pure Wear
$W_c$	Corrosion enhanced Wear



# Chapter 1 - Introduction

## 1.1 - Motivation

Total Joint Replacement (TJR) involves replacing a natural human joint with an artificial prosthesis in order to restore function and relieve pain caused by degenerative diseases or trauma to the joint. Joint replacements have been common place over the last 150 years with the first known surgery performed in the late 1800's [1]. Much of the early research into Total Hip Replacements (THR) surrounded material selection for the devices.

Little progress was made until Sir John Charnley, a surgeon based at Wrightington Hospital, developed a Stainless-Steel on Teflon® articulating device but moved to High Molecular Weight Polyethylene (HMWPE) following high wear rates [2]. The Charnley Metal-on-Polymer (MoP) hip has remained largely unchanged since and is still widely regarded as the gold standard for hip replacements. Hip replacement surgery has since been regarded as one of the most successful surgical interventions in terms of cost and patient outcome [3, 4]. Charnley advised against implanting his MoP design into patients below the age of 65. He even advocated delaying surgery until this age was reached. This was due to wear of the polymer insert, which releases inert sub-micron sized polymer debris. This debris is known to illicit an immune response and cause aseptic loosening; one of the major causes of prosthesis failure for MoP designs. Much of the research into Hard-on-Hard THRs such as Metal-on-Metal (MoM) has been driven by a need for a low-wear bearing capable of longer term success in younger, more active patients.

The first MoM devices (McKee-Farrar and Ring designs) were introduced around the same time as Charnley's MoP hip. Poor manufacturing technologies and mechanical material properties caused high wear rates, loosening and even stem fractures in these 'first generation' devices [5]. Improvements in manufacturing tech-

nologies and a greater theoretical understanding of lubrication at the bearing interface led to renewed interest in the Metal-on-Metal design philosophy. The new ‘second generation’ MoM devices not only promised to match the performance of the Charnley, but greatly improve the longevity of a hip replacement through vastly reduced wear rates. This promise was not realised in all patients however, with higher than acceptable revision rates across the entire class; across different manufacturers and designs.

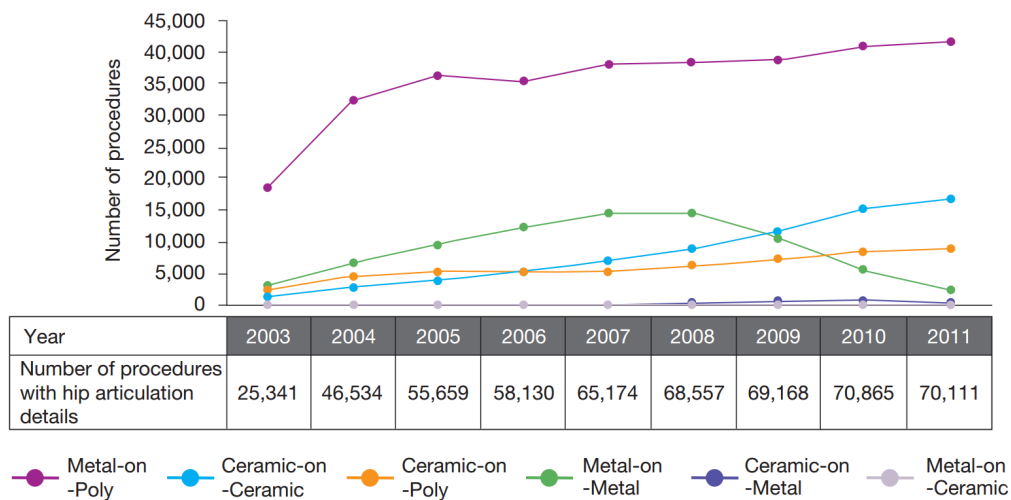


Figure 1.1: Trends in hip replacement bearing couple materials in England and Wales (2003 - 2011). Taken from [6].

The failure mechanisms of these devices are not fully understood but have largely been attributed to soft tissue reactions to metallic debris and ions (Adverse reactions to metal debris (ARMD), pseudotumor). An entire class of devices has been written off within the industry as a result. Figure 1.1 shows National Joint Registry data for the UK [6] and highlights the rise and decline of MoM hips over the previous decade. To date the use of MoM hips has almost entirely halted through a combination of alerts issued by governing bodies, product recalls and implant manufacturers no longer offering a MoM bearing couple.

Recently the significance of electrochemical degradation and tribochemical reaction films to implant performance has been highlighted within the literature [7–15]. Despite their rapid decline, MoM bearings are still being implanted. In the UK

1,096 primary Metal-on-Metal THR operations were performed in 2014 [16] and 783 were performed in 2015 [17]. Further work is required to fully understand the degradation processes and how they lead to failure of the prosthesis.

## 1.2 - Outline

This thesis contains ten chapters including this introductory chapter.

Some basic principles of tribology and corrosion are presented in **Chapter 2** and how their respective mechanisms can interact.

An extensive review of the existing literature in relation to total joint replacement and specifically Metal-on-Metal articulation is presented in **Chapter 3**.

The materials and experimental methodology for the studies described in this thesis are presented in **Chapter 4**.

**Chapter 5** presents experiments performed on a simple reciprocating tribometer for Metal-on-Metal pin-on-plate tribocouples.

Hip simulation testing of 28 mm diameter bearings with a focus on electrochemical assessment is presented in **Chapters 6 and 7** for Metal-on-Metal and Metal-on-Ceramic couples respectively.

A parametric study examining some adverse loading conditions on a 28 mm MoM bearing is presented in **Chapter 8**.

**Chapter 9** contains a discussion of all results presented in this thesis and implications for hip simulation going forward.

**Chapter 10** presents the main conclusions and limitations of this thesis and explores suggested further work.

## **Chapter 2 - Biotribocorrosion**

Tribocorrosion is the interaction and synergies between mechanical and electrochemical phenomena which occur at the interface of two surfaces in relative motion and within a corrosive environment. This combines two separate disciplines, namely Tribology and Corrosion. Biotribocorrosion specifically is concerned with these interactions occurring within a biological environment, i.e. the human body, and is useful for the study of biomedical engineering applications such as orthopaedics.

Tribocorrosion is a relatively new field of study; the significance of interactions between mechanical and electrochemical forces has only recently been highlighted. Material degradation can be drastically altered by tribocorrosion processes when compared to pure tribological or corrosive mechanisms and is therefore a critical consideration for systems interacting under both conditions.

This chapter aims to give an introduction to the principles of tribology and corrosion and how they interact, as well as standard test methods for both disciplines and how they can be related to biomedical applications.

### **2.1 - Principles of Tribology**

The word 'Tribology' is derived from the Greek 'TRIBOS,' meaning to rub. It is defined as the "science and technology of interacting surfaces in relative motion and of related subjects and practices." [18] Parameters such as wear, friction and lubrication of articulating systems, for example bearings, all fall within the scope of Tribology.

### 2.1.1 - Contact of Solids

When two engineering surfaces are brought into contact and loaded there will always be some deformation at the contact. This deformation may be purely elastic although it is also possible that plastic deformation, and thus damage to the surface, occurs. Figure 2.1 demonstrates this deformation for a ball of radius ‘ $R$ ’ on Flat configuration. The radius of the ball at the contact area deforms under load to produce a circular or ellipsoid contact with a half-width of ‘ $a$ ’ [18].

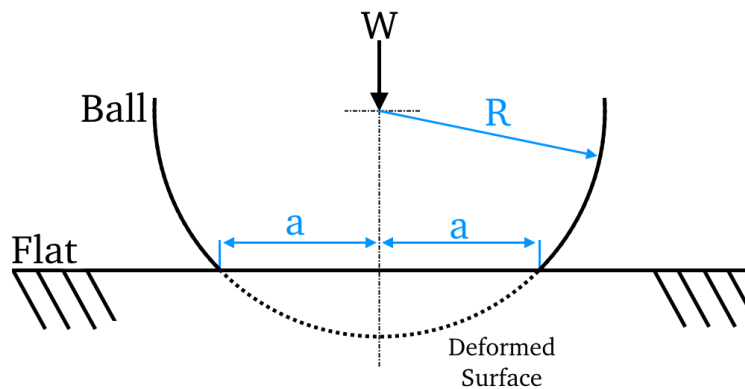


Figure 2.1: Contact area between a ball and flat surface under load.

Equation 2.1 describes the contact pressures associated with such a contact based on the effective modulus and radius of the two surfaces [19].

$$P_{mean} = \frac{2}{3}P_{max} = \frac{1}{2\pi} \left( \frac{3WE'^2}{R'^2} \right) \quad (2.1)$$

- Where:
- $P_{mean}$  = Mean Hertzian Contact Pressure (MPa)
  - $P_{max}$  = Maximum Hertzian Contact Pressure (MPa)
  - $W$  = Load
  - $E'$  = Effective Elastic Modulus
  - $R'$  = Effective Radius

Nominally flat surfaces are not perfectly flat however, but consist of valleys and peaks which are described by the surface roughness. When two surfaces come into contact and a force is applied, as shown in Figure 2.2, the peaks will deform such that the load is carried by these ‘asperities’. The number of asperity contacts for a

given interface is described by Equation 2.2 [18].

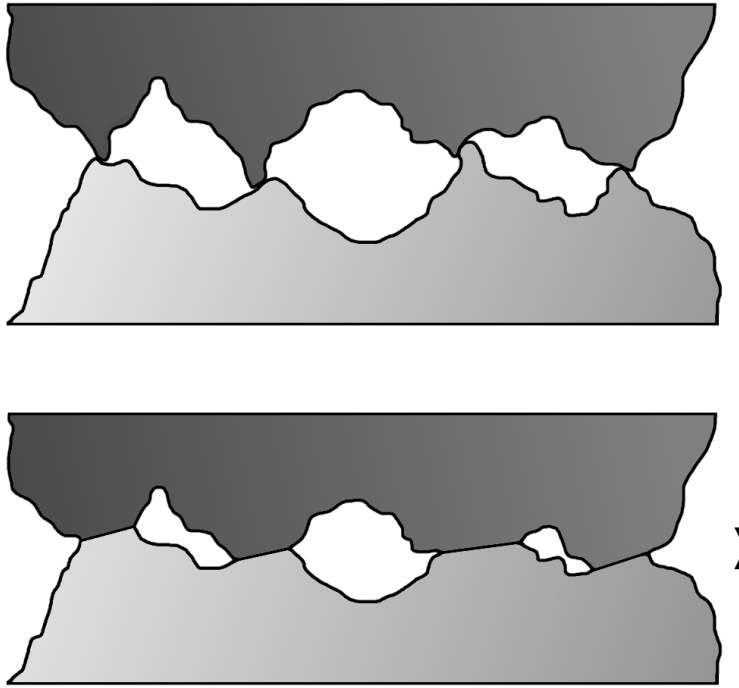


Figure 2.2: Illustration of asperity deformation in two contacting surfaces.

$$n = N \int_d^{\infty} \phi(z) dz \quad (2.2)$$

- Where:
- $n$  = Number of asperity contacts
  - $N$  = Number of peaks
  - $d$  = Separation of mean surface levels
  - $\phi(z)$  = Probability Density Function
  - $z$  = Peak heights

It is possible to treat each asperity contact as a separate Hertzian contact; thus the true contact area between two surfaces is the sum of the ' $n$ ' asperity areas across the interface, given by Equation 2.3 [18]. In reality therefore an engineering contact consists of interlocking and deformed asperities across the two surfaces. This is critical in understanding how the surfaces behave in contact and under relative motion and thus how wear of the material occurs.

$$A = \sum A_i = N\pi R_s \int_f^{\infty} \phi(z)(z - d) dz \quad (2.3)$$

Where:  $A$  = Real Contact Area  
 $A_i$  = Single Asperity Contact Area  
 $R_s$  = Characteristic Summit Radius

### 2.1.2 - Friction

Friction is defined as the resistance one surface or object encounters when moving over another [20]. The cost of overcoming uncontrolled friction has been estimated to have been as high as 1.4 % of UK GDP (2007 rates) in the past [21]. The study and improvement of how materials interact in a sliding contact can therefore have dramatic economic impact.

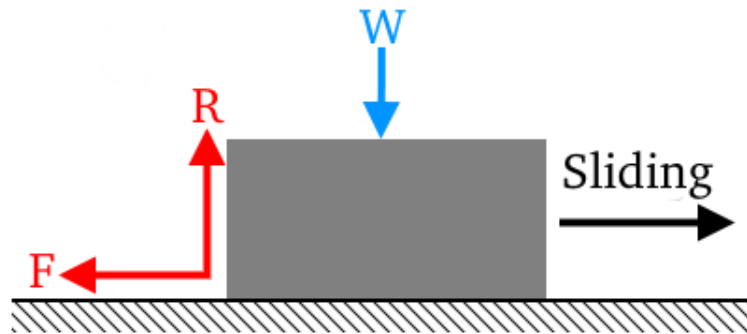


Figure 2.3: Illustration of a body in relative motion over a surface, where:  $W$  is the Normal Load (N),  $R$  is the Reaction Force (N) and  $F$  is the Friction Force (N).

The laws of friction were first stated quantitatively by Guillaume Amontons in 1699 [18]. Amontons' First Law stated that the resultant frictional force ( $F$ ) of two surfaces in relative motion is proportional to the normal load ( $W$ ), shown in Figure 2.3. The constant of proportionality was first termed the *coefficient of friction* ( $\mu$ ) by Leonhard Euler such that;

$$F = \mu W \tag{2.4}$$

Where:  $F$  = Friction Force (N)  
 $\mu$  = Coefficient of Friction  
 $W$  = Normal Load (N)

Amontons' second law states that the friction force experienced at the sliding interface of a body in contact and relative motion is independent of the *apparent* contact area [18]. This is as we know because two surfaces under contact are in reality a series of interlocking and deformed asperities which can be independent of the nominal contact area. The friction force in this case is a function of the true contact area and the specific resistance to shearing of those asperities, shown in Equation 2.5.

$$F = A \times \tau \quad (2.5)$$

Where:  $F$  = Friction Force  
 $A$  = Real Contact Area  
 $\tau$  = Specific Resistance to Asperity Shearing

### 2.1.3 - Wear of Materials

Wear is the gradual removal of material from surfaces as a result of relative motion against each other [18]. Archard proposed the volumetric wear of a sliding tribosystem in an adhesive wear scenario is proportional to the contact area [22]. This is a function of load, surface hardness, and the sliding distance, shown in Equation 2.6. This expression can be reduced to normalise wear volume for both load and sliding distance in order to produce a wear coefficient, shown in Equation 2.7, and is often used to represent the wear severity of a system.

$$K = \frac{KWL}{H} \quad (2.6)$$

$$k = \frac{V}{WL} \quad (2.7)$$

Where:  $V$  = Volumetric Wear ( $\text{m}^3$ )  
 $K$  = Archard Coefficient  
 $H$  = Hardness  
 $L$  = Sliding Distance (m)  
 $W$  = Load (N)  
 $k$  = Wear Coefficient ( $\frac{\text{m}^3}{\text{Nm}}$ )

There are four principal sliding wear mechanisms: abrasive wear, adhesive wear, flow wear and fatigue wear. These mechanisms are shown in Figure 2.4 and discussed below. Other mechanisms such as corrosive, diffusive or melt wear are classified separately as chemical or thermal processes [23] and are discussed elsewhere in Section 2.2.

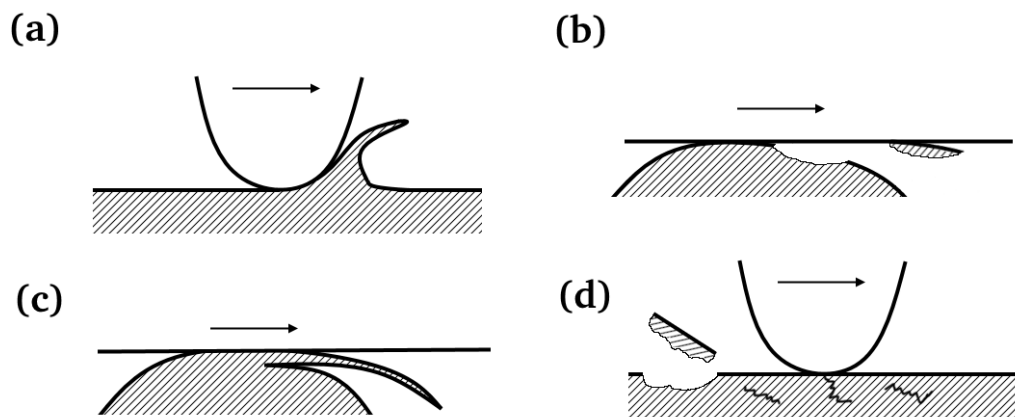


Figure 2.4: Illustration of the four principal mechanical wear processes: (a) abrasive wear, (b) adhesive wear, (c) flow wear and (d) fatigue wear.

### 2.1.3.1 - Abrasive Wear

Abrasive wear, illustrated in Figure 2.4(a), occurs as a result of asperity contact between a hard and a more ductile surface in relative motion [23]. This can also be as a result of a hard third body particulate present within the interface. Several different mechanisms can result in abrasive wear, such as: micro cutting, ploughing or grain pull-out.

Attempts to model abrasive wear in the past have seen good agreement between

the theoretical prediction and experimental results [24, 25]. Equation 2.8 describes the volumetric wear as a result of single-asperity abrasive wear:

$$V = \alpha\beta \frac{WL}{H} \quad (2.8)$$

Where:  $\alpha$  = Asperity shape factor  
 $\beta$  = Degree of wear by abrasive asperity  
 $H$  = Hardness

### 2.1.3.2 - Adhesive Wear

Adhesive wear, illustrated in Figure 2.4(b), occurs during sliding surface contact where asperities adhere together due to high local pressure and are 'plucked' from one surface. The debris either remains adhered to the second surface or forms wear particles [18]. Adhesive wear can also be termed galling, scoring or seizing and can result in an increase in surface roughness which can accelerate wear of the surface.

Attempts to model adhesive wear have met with difficulty and often do not produce good agreement to experimental results. Following on from Archard, adhesive wear volume does increase linearly with load and sliding distance however [23].

### 2.1.3.3 - Flow Wear

Flow wear, illustrated in Figure 2.4(c), occurs as a result of plastic shear flow of material at a surface which is ultimately lost from the bulk [23]. This type of wear is also known as 'ratchetting' and the mechanism of flow wear is similar to that of 'low-cycle' fatigue although, due to the plasticity of the material, crack initiation and propagation is not needed to form wear particles.

### 2.1.3.4 - Fatigue Wear

Fatigue wear, illustrated in Figure 2.4(d), occurs as a result of repeated cyclic sliding and can also be termed ‘spalling’ [23]. The cyclic stresses induced at the surface result in crack initiation and propagation which eventually causes loss of material. Fatigue wear can result in high levels of plastic strain at the surface and cause changes in the material micro-structure. This can change the wear performance of the tribosystem going forward [18].

### 2.1.4 - Lubrication

The lubrication of two surfaces in relative motion occurs when a fluid is present within the articulating interface and can have profound effects on both the friction and wear of the tribological system [18, 20]. Several different lubrication regimes exist which describe how the load is supported at the interface, and ultimately how the lubrication can affect the wear performance and resulting friction coefficient. The transition between regimes can be seen clearly on a Stribeck Curve, an example of which can be seen in Figure 2.5.

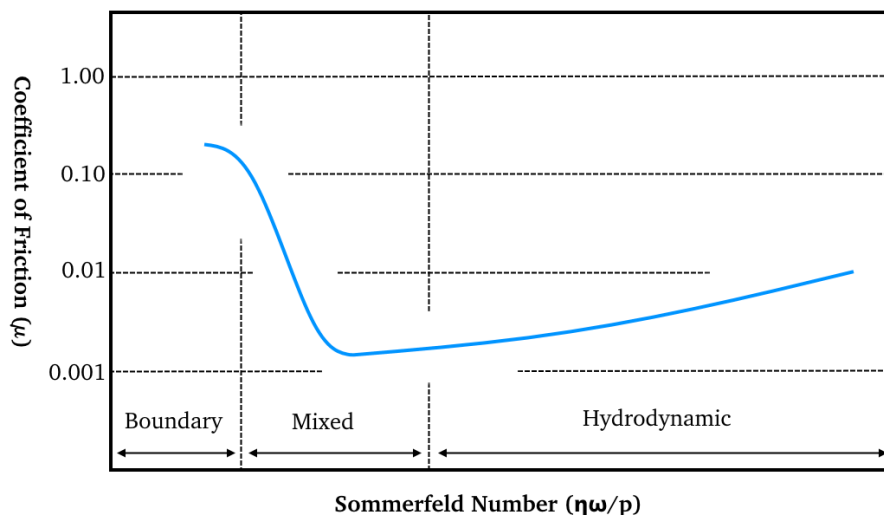


Figure 2.5: A typical Stribeck curve.

The Stribeck Curve relates the coefficient of friction to the Sommerfeld or Hersey number [18]. This dimensionless number is a function of the lubricant viscosity

( $\eta$ ), rotational speed ( $\omega$ ) and load ( $p$ ). The lubrication regime is linked to the roughness of the sliding surfaces. A modified Stribeck Curve, which replaces the Sommerfeld number with the Lambda Ratio, is often used to describe regimes [26]. The Lambda Ratio relates the theoretical minimum film thickness generated during sliding to the composite surface roughness, and can be seen in Equation 2.9.

$$\lambda = \frac{h_{min}}{\sqrt{R_{a1}^2 + R_{a2}^2}} \quad (2.9)$$

- Where:
- $\lambda$  = Lambda ratio
  - $h_{min}$  = Theoretical minimum film thickness ( $\mu\text{m}$ )
  - $R_{a1}$  = Roughness of surface 1
  - $R_{a2}$  = Roughness of surface 2

For the case of a femoral head articulating within an acetabular cup, illustrated in Figure 2.6, the steady-state Hamrock-Dowson equation (Equation 2.10) can be used to calculate the theoretical minimum film thickness for a given bearing couple. This can then be used to calculate the Lambda Ratio for that articulating interface, and thus what lubrication regime the hip is expected to operate in.

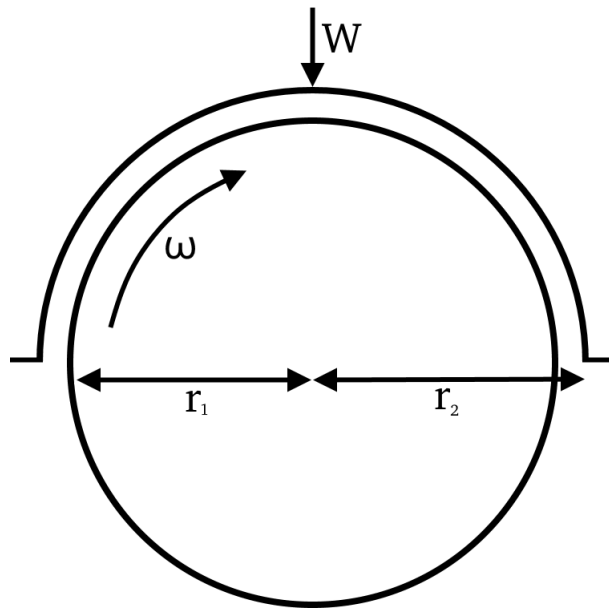


Figure 2.6: Simplified schematic of a femoral head articulating within an acetabular cup.

$$h_{min} = 2.8R' \left( \frac{\eta u}{E' R'} \right)^{0.65} \left( \frac{W}{E' R'^2} \right)^{-0.21} \quad (2.10)$$

- Where:
- $h_{min}$  = Theoretical minimum film thickness ( $\mu\text{m}$ )
  - $R'$  = Equivalent radius (m)
    - =  $\frac{r_1 r_2}{r_2 - r_1}$
  - $r_1$  = Femoral head radius (m)
  - $r_2$  = Acetabular cup radius (m)
  - $\eta$  = Lubricant viscosity (Pas)
  - $u$  = Entraining velocity (m/s)
    - =  $\frac{\omega r_1}{2}$
  - $E'$  = Equivalent Elastic Modulus (Pa)
    - =  $2 \left( \frac{1-\nu_1^2}{E_1} + \frac{1-\nu_2^2}{E_2} \right)$
  - $E_1, \nu_1$  = Femoral head Elastic Modulus and Poisson's Ratio
  - $E_2, \nu_2$  = Acetabular cup Elastic Modulus and Poisson's Ratio

#### 2.1.4.1 - Boundary Lubrication

Boundary lubrication is prevalent when the theoretical minimum film thickness is less than the composite surface roughness of the sliding bodies. The lambda ratio for such a system is less than unity ( $0 < \lambda < 1$ ). Most of the load applied to the interface is supported by asperity contact. The friction force generated during articulation is therefore largely a result of this contact [20]. Natural synovial joints tend to operate within the boundary or mixed regime, where the wear is dominated by surface interactions [27].

#### 2.1.4.2 - Fluid Film Lubrication

Fluid film lubrication occurs when the minimum film thickness is much greater than the composite surface roughness of the articulating surfaces. The lambda ratio is therefore much greater than unity ( $\lambda > 3$ ). The exact value of  $\lambda$  which indicates full fluid film lubrication is system dependant. Under fluid film the two

surfaces are completely separated by the lubricant, which compresses and supports the load applied to the bearing [26]. This type of lubrication is also termed 'hydrodynamic' lubrication and the friction force at the interface is mostly generated by the viscous properties of the lubricant.

#### **2.1.4.3 - Mixed Lubrication**

Mixed lubrication occurs between boundary and fluid film, when the minimum film thickness and composite surface roughness values are comparable. The lambda ratio is only slightly greater than unity ( $1 < \lambda < 3$ ) in this system [26]. The load applied to the bearing is therefore supported both by asperity contact and lubricant pressure. As the lambda ratio approaches unity, the regime is termed 'severely' mixed and a greater proportion of that load relies on asperity interaction. Most hard-on-hard total hip replacements are thought to operate under the mixed regime, with elasto-hydrodynamic-lubrication (EHL) causing elastic deformation of the articulating surfaces as a result of the high pressures generated in the fluid lubricant [28].

## **2.2 - Principles of Corrosion**

Corrosion is defined as the destruction or deterioration of a material because of a chemical reaction with its environment [29]. Principally corrosion is associated with metallic materials, although polymers and ceramics are also known to corrode or oxidise. The environment is also typically aqueous, although it can be gaseous. Electrochemistry is defined as the study of chemical reactions that result in the transfer of electrons, typically between an electrical conductor (metal) and an ionic conductor (electrolyte) [30]. This is the primary mechanism for corrosion of metals in aqueous environments and thus the terms are often used interchangeably. As the focus of this report is metal-on-metal hip replacements, the principles of corrosion will be discussed in relation to common metals used for biomedical devices in aqueous environments.

### 2.2.1 - Thermodynamics of Corrosion Processes

When in equilibrium a corrosive process consists of half-cell reactions, namely oxidation and reduction reactions. The dissolution of a metal into an aqueous solution (electrolyte) for example, shown in Equation 2.11, produces metal ions and free electrons. This loss of electrons is termed oxidation, and the sites at which oxidation reactions occur are known as anodic electrodes (anodes) [31].



Where:  $M$  = Metal  
 $M^{z+}$  = Metal Ion  
 $z$  = Valence state  
 $e^{-}$  = Electron

The freed electrons remain within the bulk metal which creates a potential difference and limits the further release of ions. This can also result in the reverse reaction, i.e. a metal ion can discharge back into the substrate, forming a dynamic equilibrium. This reverse reaction is termed reduction and sites at which it occurs are known as cathodic electrodes (cathodes) [31]. Some metals can form a hydroxide layer in an electrolyte, preventing the ions from discharging and returning to the substrate [30].

The electrons can be consumed in other half-cell reduction reactions as oxidising agents come into contact with the metal surface. A common example of a reduction reaction in aerated solutions is the reduction of oxygen, shown in Equation 2.12. The oxidation reactions can therefore continue and corrosive degradation of the metal proceeds at the interface [31]. This forms a layer at the metal surface termed the Electrical Double Layer (EDL) which has both a resistance and capacitance caused by the separation of charge. An illustration of the EDL can be seen in Figure 2.7.



Oxidising agents are termed Electrochemically Active Species (EAS) which are any species present within the electrolyte carrying a charge. Not all EAS will consume an electron at the metal surface and reduce. Some, such as  $Cl^-$  and  $SO_4^-$ , will form an ionic bond with released metal ions to form metal chlorides and sulphides [31].

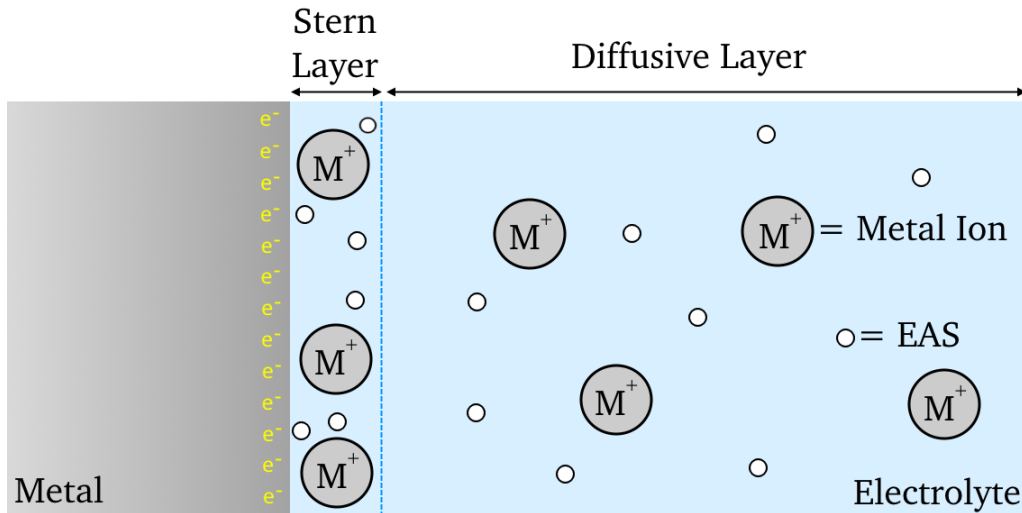


Figure 2.7: Illustration of the electrical double layer (EDL) formed by metal ions and electrochemically active species (EAS).

The conditions of equilibrium at a given temperature can be derived from a variant of the Van't Hoff reaction isotherm (Equation 2.13) [30]:

$$\Delta G = \Delta G^0 + RT \ln J \quad (2.13)$$

- Where:
- $\Delta G$  = Gibbs Free Energy change
  - $\Delta G^0$  = Standard Free Energy for all Reactants
  - $R$  = Ideal Gas Constant
  - $T$  = Temperature
  - $J$  = Activity Quotient
  - =  $\frac{[a_{product1}][a_{product2}][etc]}{[a_{reactant1}][a_{reactant2}][etc]}$

The Gibbs Free Energy ( $\Delta G$ ) is a useful measure of the propensity for a given element to either oxidise or reduce. For elements with a positive Gibbs Free En-

ergy ( $\Delta G > 0$ ) energy is required to oxidise the metal and is therefore considered stable. For elements with a negative Gibbs Free Energy ( $\Delta G < 0$ ) energy is released upon oxidation and therefore may happen spontaneously. In the presence of an electrolyte the ions are able to diffuse away from the bulk, resulting in the degradation of the material.

At equilibrium the chemical energies are balanced by the potential acquired at an electrode and can thus be expressed in corresponding electrical terms, shown in Equation 2.14. This gives rise to the Nernst Equation (Equation 2.15) which mathematically relates the EDL composition to the electrical potential [31].

$$\Delta G = -zFE \text{ and } \Delta G^0 = -zFE^0 \quad (2.14)$$

$$\Delta E = \Delta E^0 - \frac{RT}{zF} \ln J \quad (2.15)$$

Where:  $F$  = Faraday Constant (96,490 Cmol<sup>-1</sup>)  
 $E$  = Electrode Potential (V)  
 $E^0$  = Standard Electrode Potential (V)

The electrochemical series, shown in Table 2.1, ranks some common half-cell reactions according to the standard electrode potential. More stable (noble) metals appear towards the top of the table with positive values, whilst metals likely to corrode appear towards the bottom with negative values.

Whilst a good guide to a metals susceptibility to corrosion, other factors can affect the corrosion of a metal. Some metals for example have a propensity to form a passive oxide layer under given conditions. Chromium for example tends to form an oxide (typically  $Cr_2O_3$ ) spontaneously both in air and aqueous solutions. This can be seen in Pourbaix diagrams, such as that presented for chromium in Figure 2.8 [32]. Given a neutral pH,  $Cr^{3+}$  ions will tend to form an oxide across a wide potential range which is why chromium is often used as an alloying element.

Table 2.1: Electrochemical series for selected standard electrode potentials at 25°C.

Metal	Half Reaction	Standard Electrode Potential $E^0V$ (SHE)
Gold	$Au^{3+} + 3e^- \longrightarrow Au$	+ 1.500
Platinum	$Pt^{2+} + 2e^- \longrightarrow Pt$	+ 1.200
Silver	$Ag^+ + e^- \longrightarrow Ag$	+ 0.799
Iron	$Fe^{2+} + e^- \longrightarrow Fe^{3+}$	+ 0.771
Copper	$Cu^+ + e^- \longrightarrow Cu$	+ 0.520
	$Cu^{2+} + 2e^- \longrightarrow Cu$	+ 0.337
Hydrogen	$2H^+ + 2e^- \longrightarrow H_2$	0.00 (by definition)
Lead	$Pb^{2+} + 2e^- \longrightarrow Pb$	- 0.126
Tin	$Sn^{2+} + 2e^- \longrightarrow Sn$	- 0.136
Nickel	$Ni^{2+} + 2e^- \longrightarrow Ni$	- 0.250
Cobalt	$Co^{2+} + 2e^- \longrightarrow Co$	- 0.280
Iron	$Fe^{2+} + 2e^- \longrightarrow Fe$	- 0.440
Chromium	$Cr^{3+} + 3e^- \longrightarrow Cr$	- 0.740
Aluminium	$Al^{3+} + 3e^- \longrightarrow Al$	- 1.660
Magnesium	$Mg^{2+} + 2e^- \longrightarrow Mg$	- 2.370
Sodium	$Na^+ + e^- \longrightarrow Na$	- 2.714

This is termed ‘passivity’ and the oxide forms a film on the surface of the metal, often only nanometers thick, which can protect the bulk metal from a corrosive environment.

### 2.2.2 - Types of Corrosion

Corrosive attack can take on several forms or have different initiation mechanisms. Fontana [29] described eight main types of corrosion processes; this section aims to describe some of the most common forms relating to biomedical devices.

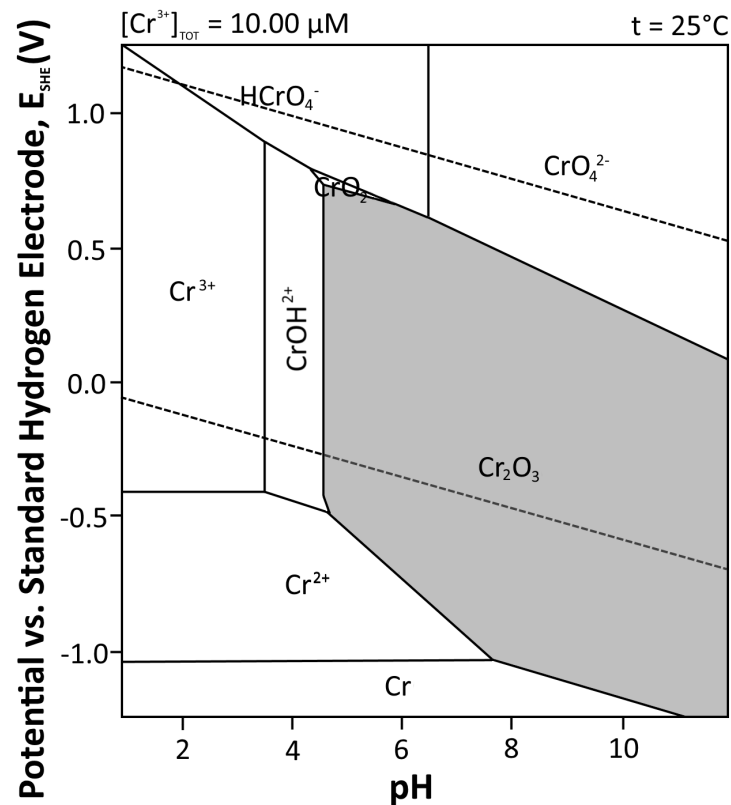


Figure 2.8: Pourbaix diagram for chromium in pure water. Data taken from [32].

### 2.2.2.1 - Uniform / General Corrosion

Uniform or general corrosion involves the chemical or electrochemical degradation of a sample proceeding uniformly over the entire exposed surface. Uniform corrosion is most commonly associated with metals that do not form a protective oxide layer, and is thought to be the most commonly found form of corrosion [29].

### 2.2.2.2 - Galvanic Corrosion

Galvanic corrosion occurs when two dissimilar metals are electrically connected and immersed in or otherwise exposed to the same electrolyte. As mentioned previously the tendency for a given metal to corrode can be predicted and ranked against other metals. In the case of galvanic corrosion when a metal with a higher tendency to corrode is coupled to another, that metal will have a lower potential in a given electrolyte. A potential difference is therefore formed between the metals and electrons flow from the corroding metal to the other.

The second metal therefore becomes a net cathode and is protected from corrosive attack by the corroding metal, which acts as a net anode. This phenomenon can be exploited and metals are often protected from corrosive degradation by attaching a sacrificial anode to the system. The rate of galvanic corrosion can be affected by several factors, such as the ratio of anode to cathode surface area and the properties of the electrolyte. Ranking the potential of metals against each other in a given environment is termed a galvanic series and can be used to predict the preferentially corroding metal for a given couple [29].

### **2.2.2.3 - Crevice Corrosion**

Crevice corrosion is a form of localised corrosion and occurs when a volume of electrolyte close to a metal or alloy surface is stagnant. This stagnant volume becomes starved of oxygen and ionic species migrate into the crevice [33]. Crevice corrosion typically occurs in alloys which form a passive oxide layer on their surface. This layer usually acts as a barrier to charge transfer and thus protects the bulk alloy from electrochemical degradation.

Once crevice corrosion is initiated the passive layer is disturbed within the crevice, but remains in place outside. Several different models for the initiation of crevice corrosion have been proposed but once initiated the reaction can become self-sustaining and rapidly corrode the bulk alloy within the crevice [29].

### **2.2.2.4 - Pitting Corrosion**

Pitting corrosion is another form of localised corrosive attack and like crevice corrosion is usually associated with alloys which owe their corrosion resistance to a protective oxide film. Interruption of the film creates an anodic site which is electrically coupled with the remaining passive film outside the pit. The passive film acts as a cathode, creating a local galvanic circuit [29].

Local passivity can be lost by the actions of aggressive anions; the most common of

which associated with metallic corrosion is chloride ( $Cl^-$ ). Pits initially go through a metastable phase, where passivity can be temporarily restored, before the pit geometry and chemistry lead the pit to become stable. This only occurs once the local potential passes the pitting potential of the metal and causes rapid material loss within the pit [34]. The film can also be interrupted by physical damage to the surface, or in the case of metals deliberately coated to prevent corrosion, by a defect in the coating film.

Pits can take on many shapes, as shown in Figure 2.9, and are thought to be one of the most difficult forms of corrosion to combat due to the nature of the process. For a relatively small amount of material loss through corrosive attack, pitting can cause extreme structural weakness within a metal, resulting in the failure of a component.

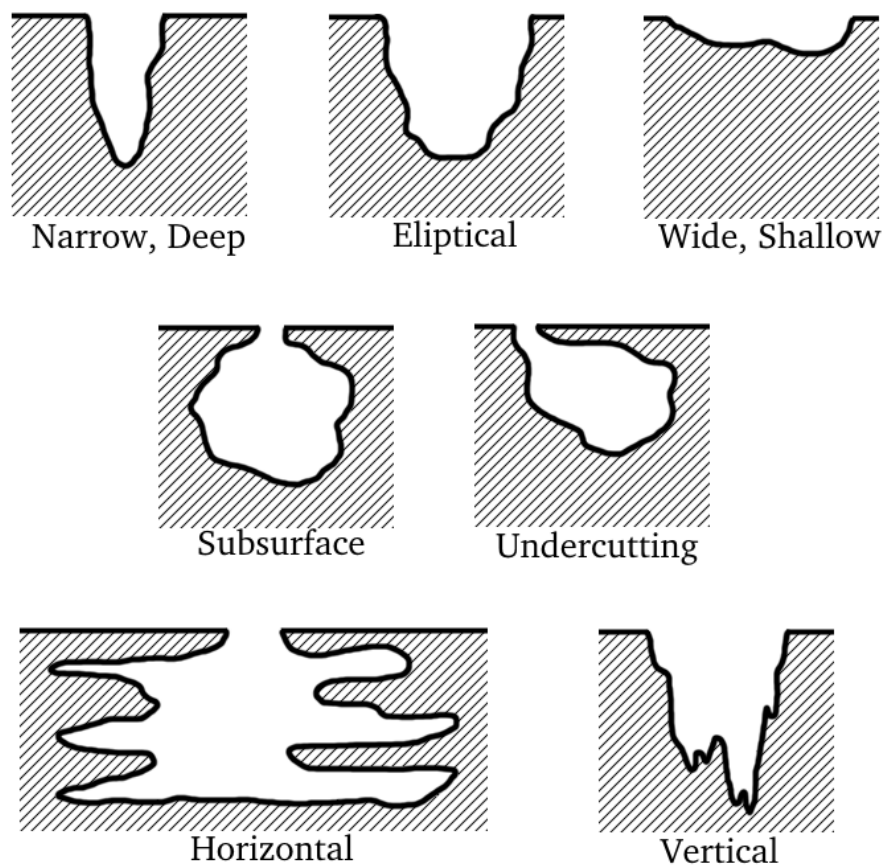


Figure 2.9: Illustration of various pit geometries as defined in ASTM-G46 [35].

### 2.2.2.5 - Intergranular Corrosion

Intergranular corrosion is the preferential corrosive attack of material at, or adjacent to, the metallic grain boundaries of an alloy. In biomedical alloys chromium is often added to aid in the formation of a passive oxide film. Chromium carbides ( $Cr_{23}C_6$ ) can be precipitated along these grain boundaries, through a process known as sensitisation, which leads to chromium depleted zones along the grain boundary. The depleted regions have a different potential to the bulk alloy, resulting in a galvanic circuit with the depleted zones acting as an anode and thus electrochemical degradation at the grain boundary [29].

### 2.2.3 - Corrosion Rate

The Nernst equation only gives a relationship between the EDL composition and the electrical potential of the metal. A measure of net electrical current would be more useful to corrosion engineers as it can give an indication of the rate of degradation of the material and a subsequent mass loss. The Butler Volmer (BV) equation (Equation 2.16) relates changes in the potential of a metal and the resulting electrical current [31]. These changes can either be the result of an external power source or between mixed metals. The potential of the metal in the absence of the applied potential is referred to as open circuit potential (OCP). The BV equation can be used to produce simplified Current vs. Potential plots, known as Evans diagrams. Figure 2.10 for example shows the Evans diagram of the half-cell reactions for both Iron and Hydrogen, the anodic and cathodic branches extrapolated from the linear portions of measured values.

$$i = i_{corr} \left\{ \exp \left( \frac{\alpha_a n F \eta}{RT} \right) - \exp \left( -\frac{\alpha_c n F \eta}{RT} \right) \right\} \quad (2.16)$$

- Where:
- $i$  = Current density as a result of applied potential (amps/cm<sup>2</sup>)
  - $i_{corr}$  = Corrosion current density at OCP (amps/cm<sup>2</sup>)
  - $\alpha_a$  = Anodic charge transfer coefficient
  - $\alpha_c$  = Cathodic charge transfer coefficient
  - $n$  = Number of electrons in the half-cell reaction
  - $\eta$  = Applied overpotential (V)
  - $= E - E_{OCP}$
  - $E$  = Electrode potential (V)
  - $E_{OCP}$  = Open Circuit Potential (V)

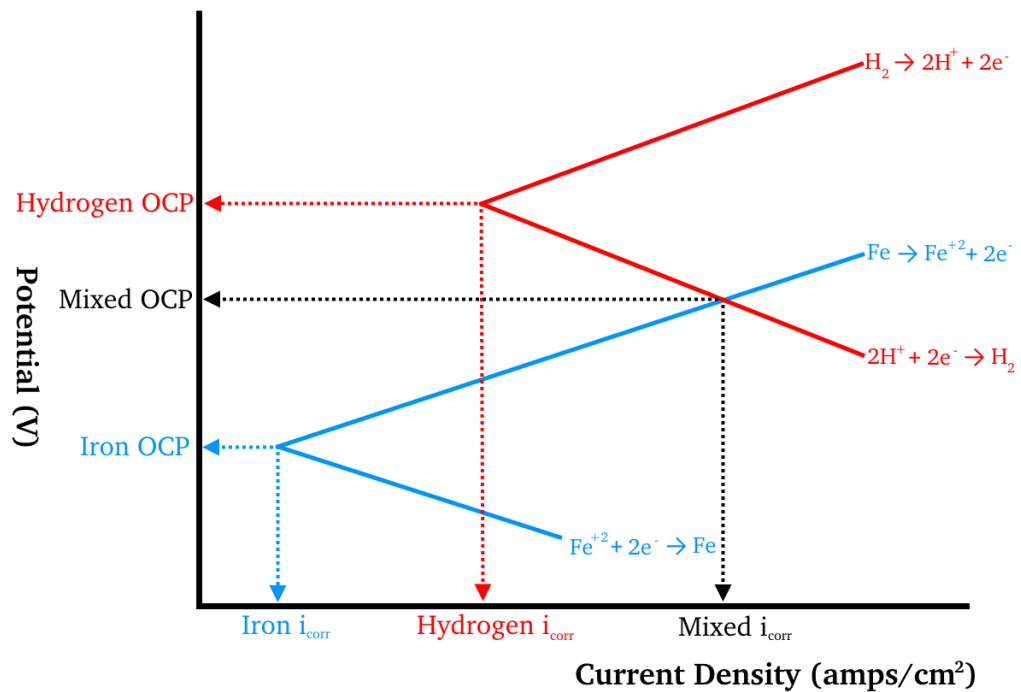


Figure 2.10: Evans diagram of the anodic and cathodic half-cell reactions for both iron and hydrogen.

For a system where both reactions are occurring at the surface, the measured OCP and  $i_{corr}$  values will be a mix of both reactions, shown where the Iron anodic branch intersects the Hydrogen cathodic branch. This is termed mixed potential theory, and most real world applications will be operating under a mixed potential as multiple different reactions occur on the electrode surface [31].

In an aqueous environment a metal is therefore generally unlikely to reach the

potential required for the reduction and deposition of released metal ions in the electrolyte. This is because the reduction and evolution of Hydrogen at the surface increases the mixed potential of the sample well above that required for the reduction of the metal ions.

#### 2.2.4 - Three-Electrode Cell

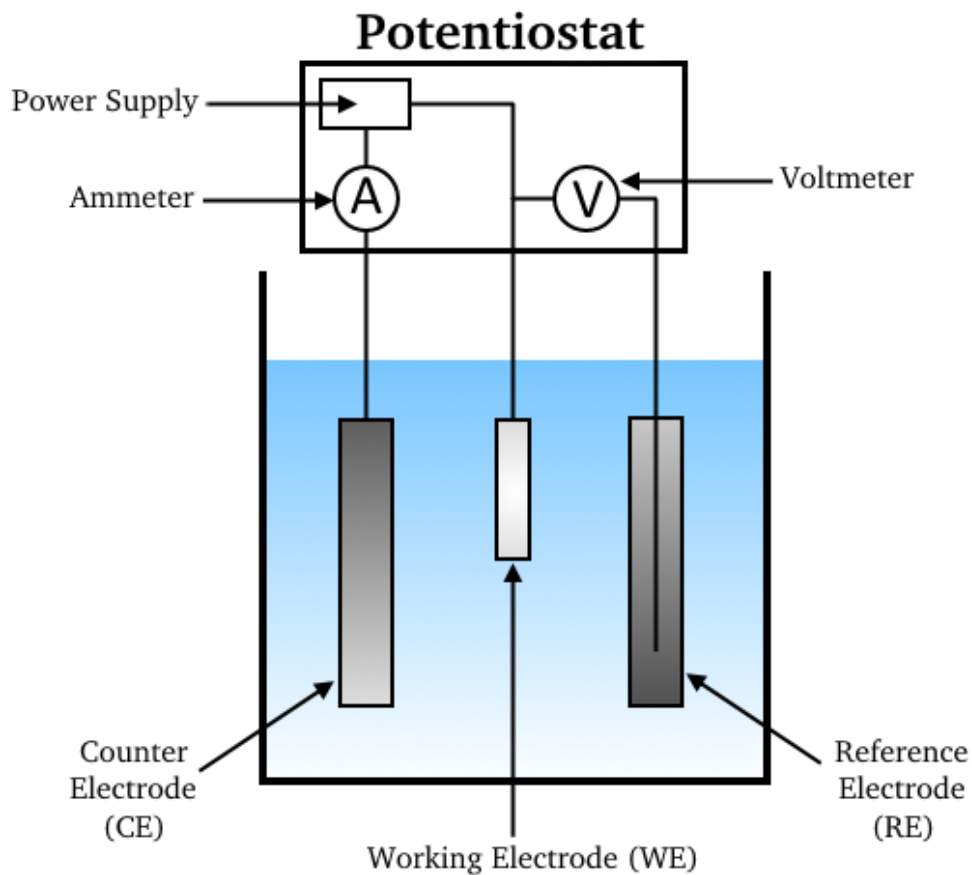


Figure 2.11: Illustration of the standard three-electrode cell experiment.

A standard three-electrode cell consists of the test sample (Working Electrode, WE), a Counter Electrode (CE) and a Reference Electrode (RE) submerged in an electrolyte, as shown in Figure 2.11. The reference electrode is typically an individual cell with a metal submerged in a specific electrolyte which provides a stable known potential to measure the WE against [31]. A potentiostat is used to simultaneously measure this potential difference and apply an overpotential to

the working electrode for the purposes of electrochemical testing.

This is done by means of enforcing a current between the working and counter electrode by supplying or removing electrons. This changes the potential of the WE, known as polarisation, and the direction of the current determines whether the sample is anodically or cathodically polarised [30]. The circuit is completed by an ionic current through the electrolyte as anions and cations flow between the WE and CE. The sample is at its OCP when no net current is flowing between the WE and the CE.

### 2.2.5 - DC Polarisation

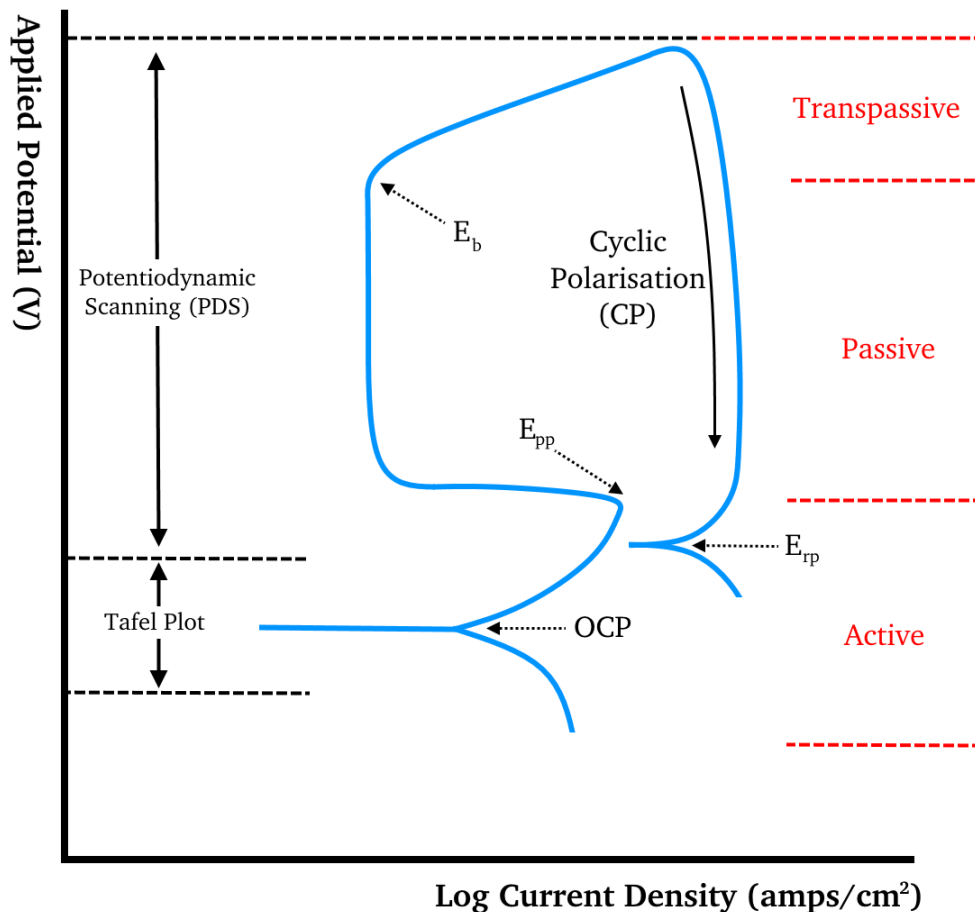


Figure 2.12: DC polarisation techniques, where:  $E_b$  is the breakdown potential,  $E_{pp}$  is the passivation potential and  $E_{rp}$  is the repassivation potential.

Through the use of a three-electrode cell experiment, the corrosion characteristics

or performance of a material / test sample can be investigated using several DC polarisation techniques. Figure 2.12 shows a typical polarisation plot for a passive metal. The figure highlights the potential ranges of different DC techniques and the different states (active, passive etc.) the material passes through as a result of the applied potential.

### 2.2.5.1 - Linear Polarisation Resistance

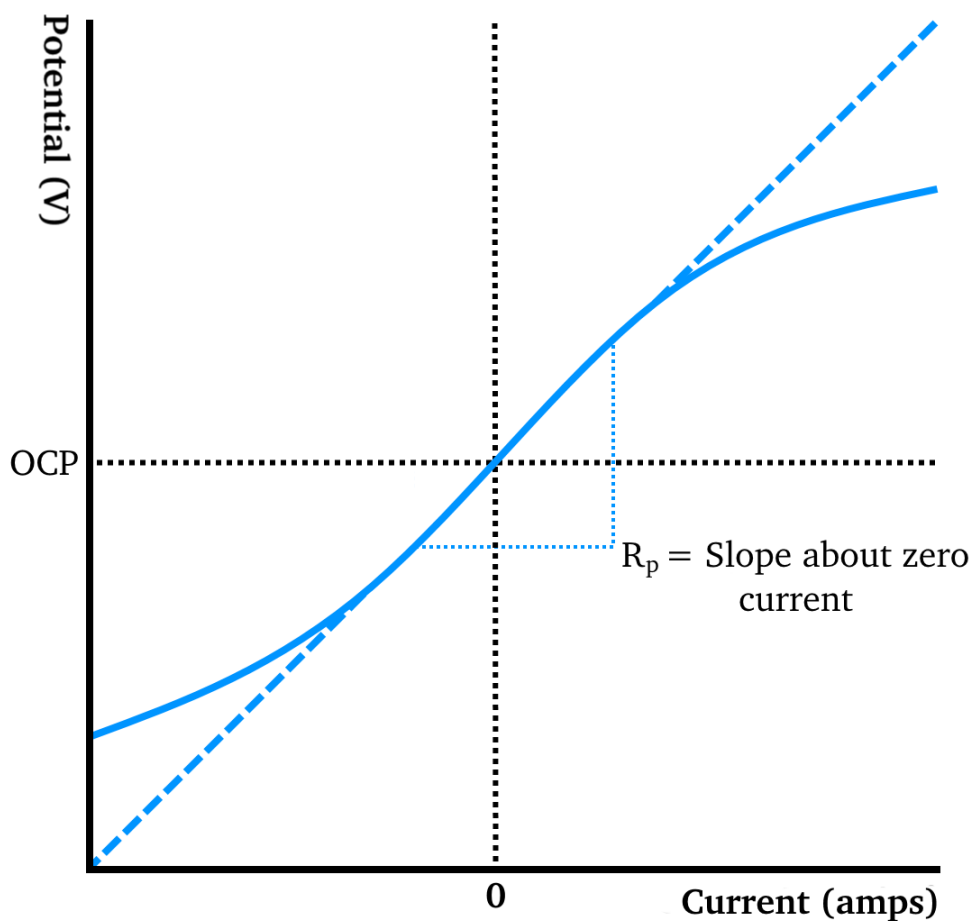


Figure 2.13: Example of a linear polarisation curve.

A linear polarisation resistance (LPR) scan is conducted around OCP, by cathodically polarising the working electrode (typically - 25 mV) then sweeping anodically past OCP to a positive potential (typically + 25 mV). The sweep rate (typically  $0.25 \text{ mVs}^{-1}$ ) must be carefully considered as the EDL must be allowed to adjust at each potential step. Too fast a sweep may discharge the surface giving

non-representative corrosion data [31].

LPR scans are considered to be non-destructive due to the small polarisation range and are thus useful for long-term corrosion monitoring as they can be assumed not to disturb the sample. The resultant current between the working and counter electrodes can then be plotted against the applied potential, an example of which is shown in Figure 2.13. The slope of the curve, as it approaches linearity about zero current, is known as the polarisation resistance ( $R_p$ ) and can be used to calculate the corrosion current ( $i_{corr}$ ) using the Stern-Geary equation, shown below (Equation 2.17).

$$i_{corr} = \left[ \frac{1}{2.303R_p} \right] \left[ \frac{\beta_a\beta_c}{\beta_a + \beta_c} \right] \quad (2.17)$$

Where:

- $i_{corr}$  = Corrosion current density at OCP (amps/cm<sup>2</sup>)
- $R_p$  = Polarisation Resistance (Ohms)
- =  $\frac{\Delta E}{\Delta i}$
- $\left[ \frac{\beta_a\beta_c}{\beta_a + \beta_c} \right]$  = Tafel Constant
- $\beta_a$  = Anodic Tafel slope (Vdec<sup>-1</sup>)
- $\beta_c$  = Cathodic Tafel slope (Vdec<sup>-1</sup>)

Whilst useful for long-term monitoring of a corroding system, an LPR scan cannot distinguish between localised or general corrosion [31]. The anodic and cathodic Tafel slopes of the system must also be determined in order to use the Stern-Geary equation to obtain  $i_{corr}$  values. Some standards simply use a set value (e.g.  $\beta_a = \beta_c = 120 \text{ mVdec}^{-1}$ ), but the calculated corrosion rate can be relatively sensitive to the Tafel constant used. Some discrepancies between other degradation methods (e.g. weight loss) may possibly be explained by using the wrong Tafel constant [31].

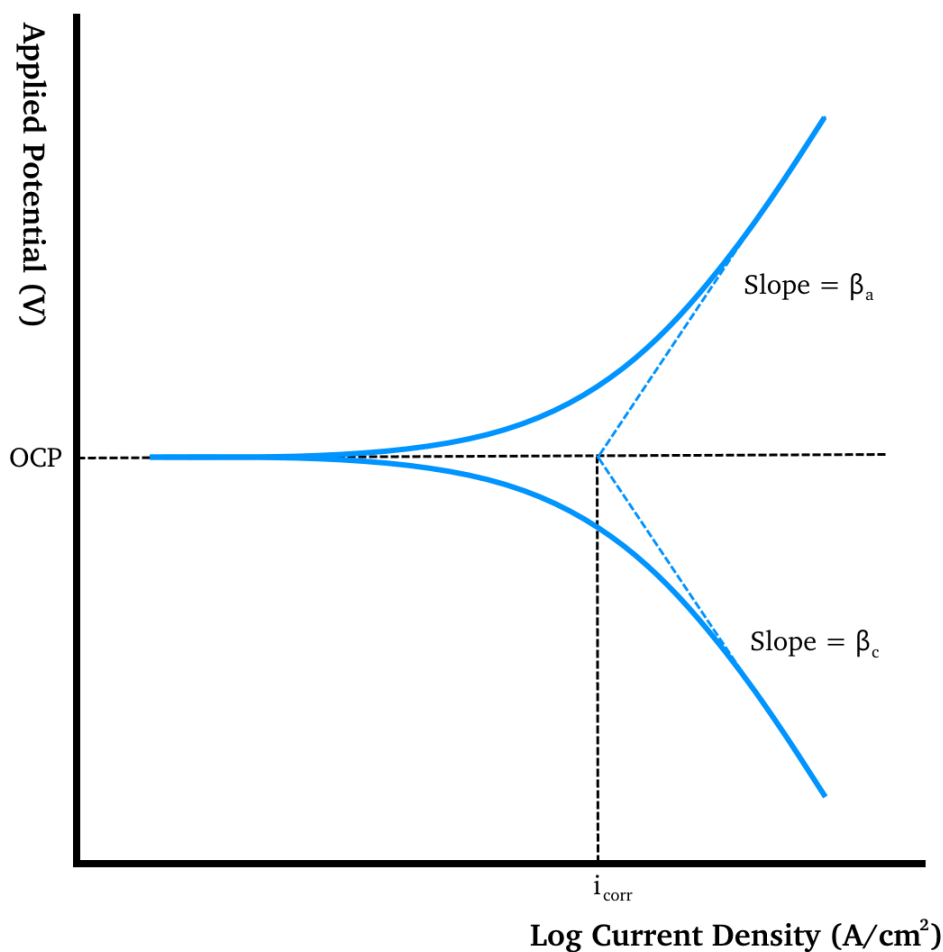


Figure 2.14: Example of a typical Tafel plot, where:  $\beta_a$  and  $\beta_c$  are the anodic and cathodic Tafel constants respectively.

### 2.2.5.2 - Tafel Plot

A Tafel scan is similar to an LPR scan in that the working electrode is cathodically polarised, and then swept back through OCP to an anodic polarisation potential. The voltage range for a Tafel scan is much greater than that of an LPR scan however, typically  $\pm 250$  mV from OCP. A second method for acquiring Tafel data involves using two separate test electrodes to generate separate data for the anodic and cathodic branches. One test sample is swept from OCP into the anodic half of the polarisation range and a second sample is swept from OCP into the cathodic half. A typical Tafel plot can be seen below in Figure 2.14, showing both the anodic and cathodic branches which typically become linear on a log scale at

around 50 mV from OCP [31].

A Tafel plot can be used to describe some aspects of a corroding system, such as whether the corrosion rate is activation or diffusion controlled. Activation control means the corrosion rate is determined by how fast the metal substrate can transfer electrons to EAS in the electrolyte and is typically represented by increasing current density magnitudes for both branches, as in Figure 2.14. A diffusion controlled system's corrosion rate is determined by how fast EAS within the electrolyte can migrate to the metal surface and is represented by a much smaller increase in current density magnitude for the cathodic branch [31].

The corrosion current of a system can be read directly from a Tafel plot, and thus gives a more accurate measure for corrosion rate as opposed to the estimated values derived from LPR scans. A sample can only undergo a limited number of Tafel plots as some degree of surface roughening occurs due to the larger polarisation range which can affect the system [31].

### **2.2.5.3 - Potentiodynamic & Cyclic Polarisation**

Similar to LPR and Tafel plots, a potentiodynamic scan (PDS) imposes a cathodic potential, then sweeps to an anodic potential. The anodic sweep is continued well past the limit reached by a Tafel scan however, resulting in a much more complex curve. A cyclic polarisation scan (CP) is an extension of a PDS scan in that the polarisation sweep is reversed back through OCP and into the cathodic branch when a given limit is reached (e.g. a set potential or current density).

Figure 2.12 shows an example of a PDS and CP curve, and highlights several points of interest over the course of the scan. The passivation potential ( $E_{pp}$ ) for example occurs when the current density either decreases or becomes constant for a finite period. The breakdown potential ( $E_b$ ) occurs at a rapid onset of current and the region between  $E_{pp}$  and  $E_b$  is known as the passive region. These values and the width of the separate regions can be used to describe the behaviour of the

corroding system and how effective a passive film is at protecting the bulk material from corrosive attack.

The results of the CP curve can also be used to describe a material's tendency to undergo localised corrosion and how readily a passive film can repair itself. Once the sweep reaches the transpassive region the passive film becomes damaged and pitting occurs. It is thought that pits will continue to grow until the OCP falls below the repassivation potential ( $E_{rp}$ ), as shown in Figure 2.12 [31].

### 2.3 - Tribocorrosion

As mentioned previously, several metals and alloys owe their corrosion resistance to a passive oxide film which forms spontaneously on the metal surface. When two surfaces under relative motion come into contact the passive film can become damaged, exposing the bulk metal to the electrolyte. The dissolution of metal ions can therefore proceed in the wear track which becomes an anodic site, illustrated below in Figure 2.15. Some authors hypothesise this forms a local galvanic link with the undisturbed film outside the wear scar, which acts as a cathode [36, 37].

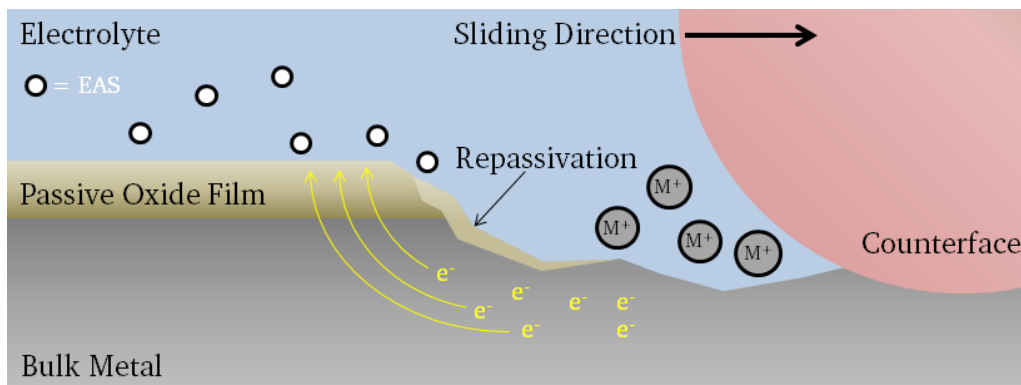


Figure 2.15: Illustration of depassivation of a protective oxide film as a result of the sliding action of a counterface.

Some of the released ions will react with oxygen from the electrolyte to repair the passive film, once again protecting the bulk metal. This process is not instantaneous however, and the material is free to degrade in the meantime.

Some tribological systems, such as the bearing of a MoM hip replacement, undergo

sliding in the presence of an electrolyte where the passive film is continuously disturbed and reformed as a result of mechanical wear and corrosive phenomena respectively. First proposed by Watson *et al.* [38] a method for calculating the synergistic effect between these processes is shown in Equation 2.18. Watson also reviewed several previous studies which highlighted that such systems display an accelerated rate of material degradation.

$$T = W_0 + C_0 + S \quad (2.18)$$

- Where:
- $T$  = Total material loss
  - $W_0$  = Pure Wear (absence of corrosion)
  - $C_0$  = Pure Corrosion (absence of wear)
  - $S$  = Synergistic material loss
  - $= W_c + C_w$
  - $W_c$  = Corrosion accelerated Wear
  - $C_w$  = Wear accelerated Corrosion

For passive materials the depassivation of the oxide film through wear can result in accelerated corrosion ( $C_w$ ). The electrochemical degradation of the surface can also result in an increase of surface roughness or weakened grain boundaries, which may accelerate the material lost through wear ( $W_c$ ). Some recent studies have suggested that the synergistic component in tribocorrosion systems can account for 12 - 42% of material loss depending on the tribological system [12, 14, 15, 39, 40].

## Chapter 3 - Literature Review

The aims of this literature review are to first define common engineering materials used in replacement joints, then go on to provide a brief summary of the history of Total Hip Replacements (THR) to establish the state of the art in tribocorrosion of hip joints. The resurgence of Metal-on-Metal hip replacements and the current knowledge based on their performance and failure mechanisms is explored.

### 3.1 - Biomaterials

A biomaterial is defined as “a nonviable material used in a medical device, intended to interact with biological systems” [41]. The scope of biomaterials is therefore wide and varied, ranging from materials used in joint replacements to stents, drug delivery methods and artificial scaffolds. This section will be limited to materials relevant to total hip replacement devices.

#### 3.1.1 - Metals

One of the critical concerns for a total joint replacement, and a measure of the success of the device, is the restoration of natural function. Due to the load-bearing nature of human joints, metals and their alloys have long been used for joint reconstruction due to their ductility, high elastic modulus and yield strength when compared to other materials [42].

##### 3.1.1.1 - Iron Based Alloys

Stainless steels were some of the first metals to be used in total joint replacements with the initial McKee-Farrar attempts and the Charnley prosthesis using a stainless steel femoral head and stem [1, 2]. The most common types of SS used today are termed 316 and 316L, the latter of which is defined by ASTM F138 for surgical applications [43]. 316 stainless steel is an iron (*Fe*) based alloy with chromium

(*Cr*), nickel (*Ni*) and molybdenum (*Mo*) constituents. The 'L' is used to describe lower carbon content.

The key function of the *Cr* constituent is to form a dense surface oxide film ( $Cr_2O_3$ ,  $\approx 5$  nm thick) that enhances the corrosion resistance of the material by acting as a barrier to charge transfer. Stainless steels are known to be susceptible to localised forms of corrosion such as pitting and crevice corrosion, where a breakdown in the film can cause high levels of material loss [29, 33].

### 3.1.1.2 - Cobalt Based Alloys

Cobalt based alloys have long been used in orthopaedics, with the most common being alloyed with chromium and molybdenum constituents (*CoCrMo*). Early trade names for such alloys were Vitallium® [1] and Haynes-Stellite 21 [42]. The compositions of these materials are defined by the standards ASTM F75 and F1537 which describe cast and wrought *CoCrMo* respectively [44, 45].

CoCrMo alloys are typically used for the bearing surface components due to a high Young's Modulus ( $\approx 220$  GPa) and Hardness (40-50 HRC) [46] which enables a high degree of polishing, critical for lubrication, and performs well as a self-mating sliding material. *CoCr* alloys are not often used in load bearing applications such as the femoral stem as the high modulus can lead to complications such as Stress-Shielding [47].

CoCrMo is commonly used in both low-carbon ( $< 0.15$  %) and high-carbon ( $> 0.15$  %) variants. High-carbon *CoCrMo* is a harder alloy, and thus typically used for sliding bearing surfaces. Like stainless steels, *CoCrMo* owes its corrosion resistance to a passive oxide layer comprised of chromium oxides [48].

### 3.1.1.3 - Titanium Based Alloys

Commercially pure (CP) titanium and extra-low interstitial (ELI)  $Ti - 6Al - 4V$  alloy are the two most common titanium based biomaterials [49]. These alloys are typically used for femoral stems and acetabular shells in modular components and are not used as bearing surfaces due to their poor self-mating tribological properties [50].

### 3.1.2 - Ceramics

A Ceramic-on-Ceramic (CoC) TJR was first developed in 1972 by P. Boutin [51] using an alumina ( $Al_2O_3$ ) ceramic femoral head, articulating against an alumina ceramic acetabular cup. As with other ceramics it can be brittle and thus susceptible to fractures in the femoral head and catastrophic breakage of the cup. Improvements to both the initial design and the quality of the alumina ceramic have reduced the risk of such complications considerably [52]. Modern ceramics used in Total Hip Replacements include Zirconia-toughened alumina (ZTA) which have 'yttria-stabilized' zirconia particles dispersed through a stable alumina matrix [53, 54]. Some ZTA ceramics, such as BioloX®delta (CeramTec, Germany), also use platelet-like alumina crystals to prevent crack propagation [55, 56]. Other manufacturers are also exploring the use of Silicon Nitride ( $Si_3N_4$ ) ceramic components (Amedica, USA) [57, 58].

### 3.1.3 - Polymers

A polymer is defined as "a molecule consisting of many (poly-) repeating units (-mer)" [59]. They represent the largest category of biomaterials with applications in orthopaedic, dental, soft tissue and cardiovascular implants and can be derived from natural sources or synthetic organic processes [60].

Polyethylene is a polymer formed from ethylene gas ( $C_2H_4$ ) with a chemical struc-

ture which can be seen in Figure 3.1. There are several types of polyethylene with different chain structures but the commonly used variety in total joint replacements is ultra-high molecular weight polyethylene (UHMWPE) which can have a chain length (n) of up to 200,000 monomer units of ethylene [59]. As mentioned previously HMWPE was first used in THR operations by John Charnley as the acetabular cup counterface which was articulated against by the metallic femoral head. UHMWPE is now a standard material for many types of joint arthroplasty following Charnley's successful designs in the 1960's.

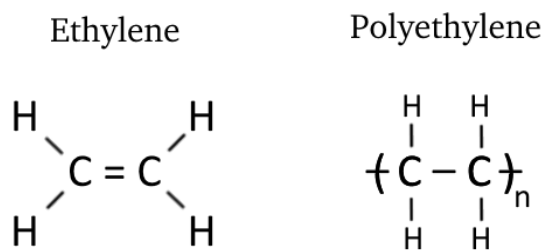


Figure 3.1: Chemical structures of ethylene and polyethylene.

UHMWPE has a composite structure with two distinct regions. In one region, the chains exist in highly ordered crystalline lamellae due to the high molecular weight (2-6 million g/mol) of the material. Secondly, the chains exist in an amorphous region which consists of many chains randomly overlapping. Modern UHMWPE is often subjected to irradiation in order to form cross-links between these chains in the amorphous region [61]. This process improves the wear resistance of the material in multi-direction sliding as it prevents the chains from aligning as a result of plastic deformation and becoming weak to cross-shear [62].

### 3.2 - History of Total Hip Replacements

Total Joint Replacement is a surgical procedure in which the joint is replaced by a prosthetic implant. TJR is considered a very effective treatment for degenerative diseases such as rheumatoid or osteoarthritis and joint reconstruction following trauma.

According to the National Joint Registry 94,228 hip replacement operations were conducted in 2014 in United Kingdom [16]. World-wide these figures approach 1 million total operations per year. The global market for hip replacement implants was estimated to have been worth \$6.2 billion in 2012 and is forecast to grow to \$7.1 billion by 2019 [63]. The market itself is dominated by 4-5 main manufacturers and several smaller companies providing a smaller range of services, shown in Figure 3.2.

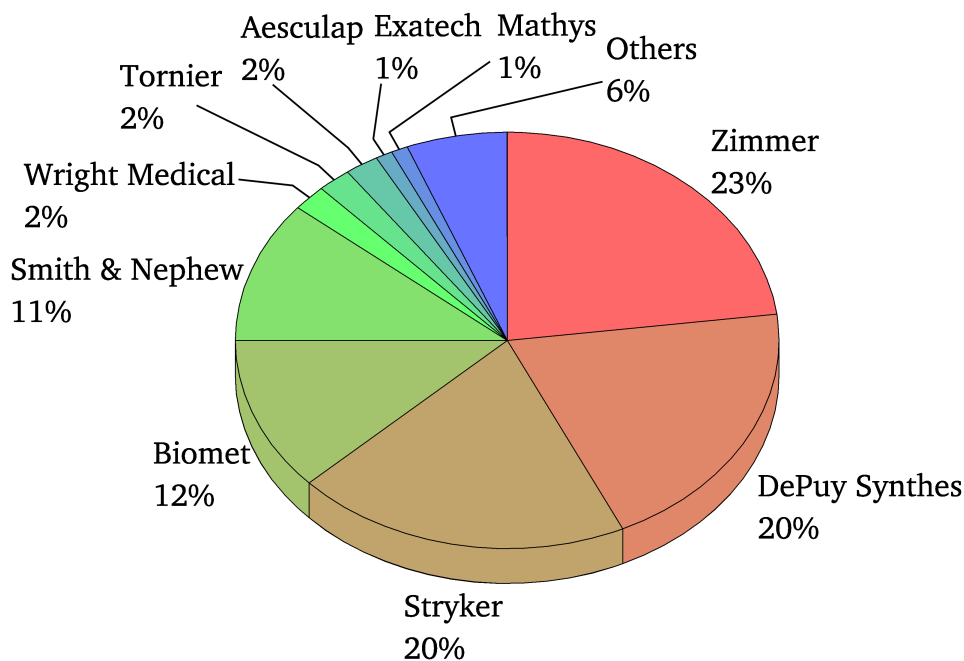


Figure 3.2: Estimated joint replacement company market share (2013). Data taken from [64].

The first documented hip replacement was conducted by Glück in 1891 which consisted of a carved ivory ball and socket joint secured in place with nickel-plated screws. Other surgeons experimented with other materials including rubbers and acrylics. Some early success was seen with a CoCrMo alloy, trade name Vitalium®, in the Thompson prosthesis. This device replaced the femoral head and neck with the alloy and demonstrated much more promising results [1].

### 3.2.1 - Metal-on-Metal (First Generation)

George Kenneth McKee [65] was a surgeon at Norfolk and Norwich University Hospital who began work on a full THR based on the Thompson prosthesis in the 1950s. McKee's design included an acetabular component for a MoM articulating bearing and dental cement for fixation. The design was a MoM bearing hip replacement consisting of stainless steels or cobalt chromium alloys (CoCr) for bearing surfaces. These 'first generation' MoM devices, shown in Figure 3.3, were cemented in place and underwent several design revisions. The bearings were initially machined and lapped in bearing pairs due to the limitations in the manufacturing processes of the time. The McKee-Farrar joint performed poorly in the body with the first series obtaining a 90 % success rate at only 4 years follow-up [65]. The main cause of failure was cited as loosening of the components which some believed was a direct result of the Metal-on-Metal articulation. The device ultimately did not gain favour due to concerns over the toxicity of released wear debris and higher friction in the MoM bearing [66, 67].

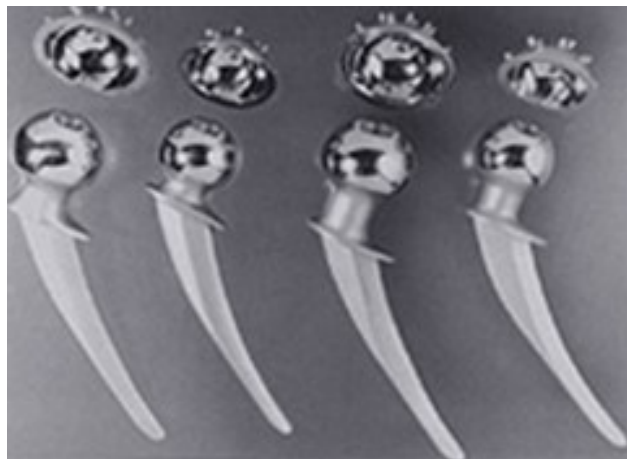


Figure 3.3: Examples of various design revisions to the McKee-Farrar hip [68].

Peter Ring, a surgeon based at the Redhill and Nethern Group of Hospitals, was also developing a MoM device based on an earlier femoral replacement known as the Austin Moore prosthesis [69]. Ring matched the Moore prosthesis to an acetabular component, but unlike the McKee-Farrar, did not use bone cement for

fixation. The acetabular component was held in place by means of a screw and the stem relied on 'natural weight transmission' for stability [70].

Early results for the Ring prosthesis also displayed high failure rates. Patterson [70] demonstrated a 20.6 % revision rate at five years follow-up (21 of 102 hips). Ring also offered a MoP design, the Uncemented Polymer-on-Metal (UPM) device, which displayed comparably poor performance. Harper *et al.* [71] demonstrated a 22 % revision rate at five years follow-up, citing granulomatous loosening as the main indication for revision.

### **3.2.2 - Metal-on-Polymer**

Sir John Charnley was a surgeon who was also developing a THR device in the late 1950s and early 1960s [72]. The Charnley Low-Friction THR had a metal-on-polymer (MoP) bearing, consisting of a forged stainless-steel femoral component with a polished spherical head and a high molecular weight polyethylene (HMWPE) acetabular component. With a Charnley device, patients could expect a 95 % survivorship rate or greater at ten years follow-up [2]. The design has remained largely unchanged and is considered the "gold standard" for THRs, still in use today. The prosthesis was so effective that hip replacement surgery is considered the most successful surgical procedure in terms of relieving pain and restoring joint function.

The wear of the HMWPE acetabular cup remains a limiting factor to the longevity of a Charnley hip however, and much research has gone into improving the wear performance of the polyethylene material. This is due to the size and volume of polymer debris produced by wear at the articulating interface. The wear debris generated by UHMWPE ranges in size greatly for both hip and knee joint replacements. Particles retrieved from hip replacements ranged from 250  $\mu\text{m}$  length platelets to globular shaped spheres, the vast majority of which were sub-micron in size (0.1 - 0.5  $\mu\text{m}$ ) [73]. This sub-micron debris can elicit an immune response

from the human body [52, 62]. Macrophages within the body attempt to surround and digest the debris in order to neutralise a perceived threat, however the bulk material polymer is bioinert and the immune system cannot remove them. Macrophages then release chemical signals known as cytokines to alert other cells to the foreign material, which stimulates inflammation around the joint. The cytokines, the most significant of which to the process is Tumour Necrosis Factor Alpha (TNF- $\alpha$ ), also activate osteoclasts, which go on to resorb bone around the prosthesis [52, 73]. This bone resorption can weaken the fixation of the prosthesis within the femur, resulting in aseptic loosening which is one of the major causes of implant failure.

Over the last 20 - 30 years the age of patients undergoing orthopaedic surgery has dropped as younger and more active patients require joint replacements. The significant driving factor in improving these devices has been the reduction of the volume of wear produced by the bearing. Less wear debris released into the joint should improve the longevity of a joint replacement as they are required to perform and last for longer in younger patients. Significant research has been conducted into improving the polyethylene used for the acetabular component, moving to Ultra-high molecular weight (UHMWPE) and processing techniques such as chain cross-linking through gamma irradiation and doping with antioxidants [61, 62].

### **3.2.3 - Metal-on-Metal (Renewed Interest)**

Hard-on-hard bearings have therefore also been of great interest over the last three decades, with Ceramic-on-Ceramic (CoC) and Metal-on-Metal (MoM) bearing couples. Several case studies demonstrated favourable long-term survivorship rates for the McKee-Farrar design. Schmalzried *et al.* [74] studied 15 surviving McKee-Farrar hips with a follow-up of 21 - 26 years. The average Harris hip score for these hips was '86' with all patients satisfied with their replacement. Jacobsson *et al.* [75] directly compared 107 McKee-Farrar hips to 70 Charnley hips and

demonstrated 77 and 73 % survivorship at an average 20 year follow-up respectively. Brown *et al.* [49] reported a series of 153 hips with survivorship rates of 84 and 74 % at 20 and 28 year follow-up respectively. All authors commented that the MoM design philosophy should be seriously considered for longer-term survivorship, which was becoming critical for younger patients.

Analysis of the wear debris from these devices also appeared favourable. Tipper *et al.* [76] compared the wear debris generated from MoP, MoM and CoC hip replacements after articulation in a hip simulator. The MoM couples produced much lower wear rates compared to the MoP bearings with  $1.23 \pm 0.5 \text{ mm}^3/\text{Mcycle}$  and  $31 \pm 4 \text{ mm}^3/\text{Mcycle}$  respectively. The particle morphology and size distribution were also vastly different, with metal and polymer particles found to be  $30 \pm 2.25 \text{ nm}$  and  $300 \pm 200 \text{ nm}$  respectively. The polymer particles presented in several shapes such as platelets and large flakes whereas the metal particles were predominantly round or oval. Catelas *et al.* [77, 78] also examined metal particle debris from hip simulators and tissues surrounding *in vivo* devices. From the hip simulator generated particles were isolated during the 'run-in' phase at 0.25 Mcycles and in 'steady-state' between 1.75 - 2 Mcycles. During 'run in' the average particle size presented at  $52 \pm 4 \text{ nm}$  and the majority were oval in shape, with approximately 21 % needle-like particles [77]. During 'steady-state' the average particle size was found to be slightly lower at  $46 \pm 3 \text{ nm}$  with less needle-like particles (7 - 13 %) [77]. The particles isolated from tissues surrounding *in vivo* implants varied from  $48 \pm 12 \text{ nm}$  to  $58 \pm 1 \text{ nm}$  depending on the design [78].

The osteolytic potential of the metal particles was thought to be far lower than polymer wear debris [76]. This was due to the smaller size range falling outside the 'bioactive'  $0.1 - 1.0 \mu\text{m}$  range discussed above [52] although the long term systemic effects from metal debris were still unknown.

This renewed interest in the metal-on-metal design philosophy resulted in several manufacturers bringing different designs to the market. The idea of a de-

vice, which produced minimal wear volume, held great promise for longevity in younger, more active patients. This promise was not fulfilled however, with higher than acceptable revision rates across the entire MoM class, across different manufacturers and designs. Figure 3.4 below from the NJR 2012 Annual Report demonstrates much higher failure rates for MoM bearings when compared to other bearing combinations [79]. This data has also been corrected to remove a particularly poor performing device (DePuy ASR), which inflated the failure rates even further, termed the ASR effect.

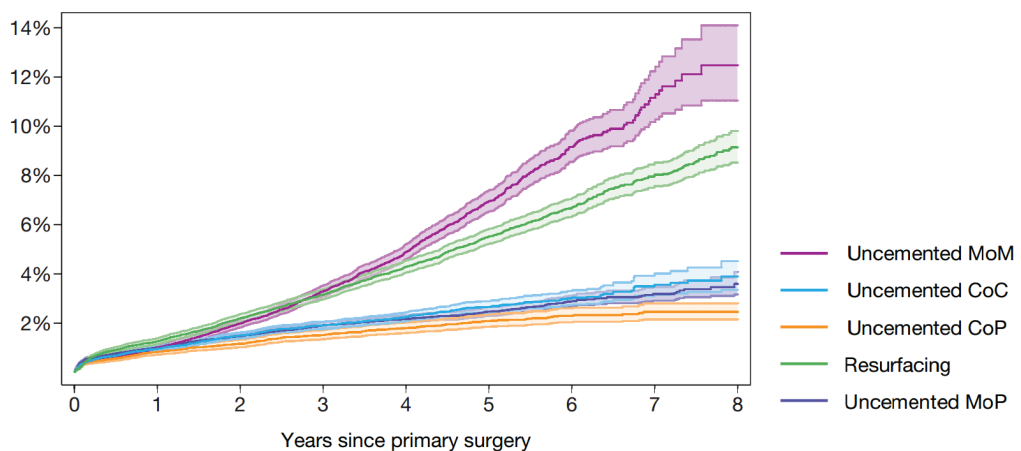


Figure 3.4: Percentage of revisions conducted against time from primary surgery for different THR bearing couples [79].

The Medicines and Healthcare Products Regulatory Agency (MHRA) in the UK issued clinical advice and several medical device alerts in 2010 - 2012, warning surgeons of particular devices and advising yearly monitoring of blood ion levels in all patients with any MoM prosthesis [80–82]. The Food and Drug Administration (FDA) in the US has also issued a Safety Communication for MoM devices, advising surgeons only use a MoM bearing if the benefits outweigh the risks compared to other bearing couples. They also advised the monitoring of blood ion levels [83]. To date the use of MoM hips has almost entirely halted through the combination of alerts, product recalls and both national and international press coverage.

More recent studies have suggested the ‘bioactive’ range of polymer particles extends down to approximately 50 nm [84]; which brings this close to the size

distribution of metal debris. A review of metal debris generation and toxicology noted larger (up to 1  $\mu\text{m}$ ) metal particles generated under adverse loading scenarios, such as malpositioning [85]. These particles both persisted longer in the joint space and resulted in an inflammatory response which was not produced by the nano-particles [85]. There is also evidence that the morphology of particles produced at the taper interfaces can be vastly different from those at the bearing surface and similarly may have negative effects [86].

### **3.3 - Modern MoM THRs**

Modern MoM total hip replacements, introduced over the last two decades, were typically presented in two broad categories: a conventional total hip replacement with modular interfaces and a hip resurfacing device. The next sections aim to highlight the differences in design philosophy between the two categories and discuss the failure mechanisms for these devices.

#### **3.3.1 - Modular THRs**

Modular total hip replacements (THRs) consist of a femoral stem, fixed either using cementless osseointegration or conventional bone cement, and a femoral head often attached to the stem by an interference fit Morse taper. The acetabular component is often comprised of two components also assembled using an interference fit taper. An acetabular shell is fixed to the bone and holds an acetabular liner that acts as the counterface for the femoral head to articulate against. The total modular assembly, an illustration of which is shown in Figure 3.5, allows surgeons to interchange components to obtain better fit and alignment for a given patient. The modularity also enables a surgical practice to carry reduced stock levels as given components, such as the stem and shell, are compatible across several bearing sizes and other acetabular liner bearing materials [87, 88].

The possible locations of corrosion taking place are also highlighted in Figure 3.5.

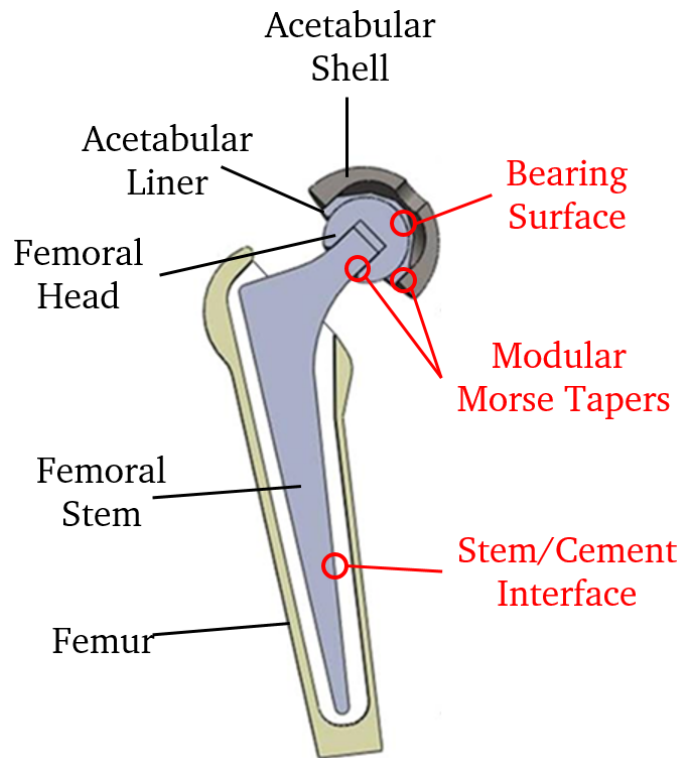


Figure 3.5: Schematic of a typical modular hip replacement. Adapted from [89].

Removal of the passive oxide layer at the bearing surface as a result of articulation will expose the bulk metal and enable corrosion. The stem-cement interface has also been shown to be susceptible to fretting and crevice corrosion processes [90–94].

The modular tapers can also be susceptible to degradation through fretting and corrosive phenomena and thus provide another source for the release of metallic ions and debris [90, 95]. The corrosion processes occurring at a given interface can have an effect on the others, thus it is important to understand each interface both in isolation and as a total construct.

### 3.3.2 - Resurfacing

Hip resurfacing devices forgo the use of a traditional stem, instead preserving bone stock by using a component designed to simply replace the articulating surface of the head. Resurfacing was first pioneered by Derek McMinn in the 1990's [96] with the McMinn prosthesis, later called the Birmingham Hip Resurfacing device

(BHR) shown in Figure 3.6. The McMinn/BHR showed highly promising initial success rates in the hands of the designing surgeon [97]. Several manufacturers released competing devices in the wake of the BHR, such as the DePuy ASR and Stryker/Corin Cormet system.



Figure 3.6: Image of the McMinn or Birmingham Hip Resurfacing device [97].

These devices were marketed as longer lasting bearings ideally suited for young and active patients with the advantage of an easy conversion to a traditional THR should the device require revision [98]. As shown in Figure 3.4 however MoM resurfacing devices displayed higher revision rates than other bearing combinations; although not as high as MoM with a traditional THR design. These figures have been adjusted to remove a particular device however, the DePuy ASR that had both traditional THR and resurfacing variants, which displayed failure rates as high as 24.2 % at seven years [79].

### **3.3.3 - Adverse Reaction to Metallic Debris**

Adverse Reaction to Metal Debris (ARMD) is a general term to cover soft tissue conditions that are thought to be related to the release of metallic ions and debris into the joint from the device [99]. The exact definitions of the different conditions are unclear and are sometimes used interchangeably. They include Aseptic Lymphocyte-dominated Vasculitis-Associated Lesion (ALVAL) [100], metallosis

[101], pseudotumors [102] and others.

ARMD is generally diagnosed by pain reported by the patient and has also been linked to other failure mechanisms such as osteolysis and aseptic loosening [99, 103]. Aspirated synovial fluid is often dark in colour and cloudy and upon revision surgery soft tissue can be stained grey and / or be necrotic [104]. ARMD can also be diagnosed in otherwise asymptomatic patients by elevated metal ion levels within the blood. The UK MHRA recently recommended annual monitoring of all patients with MoM devices for cobalt and chromium blood ion levels levels greater than 7 ppb possibly indicating an issue [80].

Previously the National Joint Registry of England and Wales only split the causes of failure into broad categories, the highest of which for MoM devices are pain, aseptic loosening and “other reason” in the 2012 Annual Report [79]. Only recently the presence of ARMD and other soft tissue reactions described above have been clearly distinguished within the registry.

### **3.4 - Pre-Clinical Assessment of Devices**

Mechanical hip simulators have a long history of being used to test the wear rates of hip replacement devices. Initial simulator designs by O’Kelly *et al.* [105–107] in the late 1970’s aimed at investigating the lubrication and friction of implant bearings. Several commercial manufacturers today produce hip simulators for research institutes and medical device manufacturers. During the development of the modern generation of MoM devices, simulators were used to benchmark them against the existing MoP gold standard. This was done using simple gravimetric assessment of components to determine material loss over the course of a test to determine a ‘wear rate.’ For MoM tribocouples however the material degradation is often a complicated synergy between wear and corrosion, as discussed in Chapter 2, and has other implications within the body when compared to MoP devices. This was often not considered within the initial studies, which simply

reported promisingly low wear rates and thus presented advantages over polymer bearings.

### 3.4.1 - Initial Studies

Anissian *et al.* (1999, [108]) reported that wear rates for 28 mm MoM bearings were two orders of magnitude lower than those shown for 28 mm MoP couples to 10 Mcycles (1,000,000 cycles = 1 Mcycle). The simulator used was an anatomically inverted Shore Western with a Paul loading cycle [109] and lubricated using 100 % bovine serum (70 g/L protein content). During steady-state conditions the MoP devices lost an average of 10.96 mg/Mcycle compared to 0.70 and 0.29 mg/Mc for the MoM liners and heads respectively. The results of this study were extremely promising for the wear rates of MoM devices. The simulator and lubricant, shown in Figure 3.7 were not representative of *in vivo* conditions. The orientation of the components were inverted from an anatomical positioning. As a result entrainment of lubricant into the bearing interface would have been assisted by gravity. Also the total protein content (TPC) of the FBS was much higher than in human synovial fluid which may have caused more favourable lubrication conditions.

A further study by Anissian *et al.* (2001, [110]) examined the difference in wear rates for 28 mm MoM bearings during bedding-in and steady-state wear rate. The lubricant used was 50 % bovine serum (20 g/L TPC) in the same simulator reported previously. Steady-state was found to generally occur around 1 Mcycles, although was sometimes difficult to determine. Wear rates were assessed gravimetrically and presented in terms of volumetric loss. The liners averaged a loss of 0.72 and 0.28 mm<sup>3</sup>/Mcycle during bedding-in and steady-state respectively. The heads also showed a similar trend with bedding-in and steady-state losses of 1.50 and 0.69 mm<sup>3</sup>/Mcycle respectively. It was interesting to note that decreasing the concentration of the lubricant, down to 50 % (v/v), resulted in an eight-fold increase in the wear rate of MoM couples when compared to their previous study



Figure 3.7: Single station on the servo-hydraulic hip simulator (Shore Western Manufacturing Inc, Monrovia, CA) utilised by Anissian *et al.* [108].

[108]. This hinted at the importance of protein interaction in the lubrication of the joints.

Dowson *et al.* (2000, [111]) employed a resistivity technique on a ProSim (Simulation Solutions, Stockport, UK) hip simulator to examine the separation of the femoral head and acetabular cup during a cycle for lubricants. Experimental evidence of surface separation, demonstrated by cyclic variation in the resistance between the head and liner, supported lubrication models at the time. The lubrication regime was operating towards fluid film occurring as a result of load and entrainment during articulation. Proteinaceous lubricants examined, 100 and 25 % new-born calf serum, demonstrated a greater propensity to cause this surface separation than water and other viscous fluids. While not the focus of this study, utilising this technique during wear tests would need careful consideration of its effects on possible corrosion processes taking place as a voltage drop of 100 mV

was applied to the sample in order to measure the variance of resistance across the cycle.

Goldsmith *et al.* (2000, [112]) presented a direct comparison between an existing 28 mm MoM bearing and a new larger diameter 36 mm MoM design. The components were articulated to 5 Mcycles in an anatomically correct ProSim hip simulator. The lubricant used was new-born calf serum diluted to 25 % with deionised water and enhanced with 0.1 % (v/w) sodium azide to retard bacterial growth. The average steady-state wear rates were calculated at 0.45 and 0.36 mm<sup>3</sup>/Mcycle for the 28 and 36 mm bearings respectively, demonstrating lower wear for the larger device. Interestingly the point at which the bearings reach steady state varied widely across both bearing diameters. Some of the components did reach steady state before 1 Mcycle, although some took up to 2 Mcycles to hit steady-state, later than reported by Anissian *et al.*

Smith *et al.* (2001, [113, 114]) further expanded on both Dowson and Goldsmith's work by employing the resistivity technique and conducting wear tests for a variety of bearing diameters (16, 22.25 and 28 mm). The 16 and 22.25 mm bearings showed no surface separation at any point of the cycle and no bedding-in phase was noted with linear wear up 2 Mcycles. Mean wear rates of 4.85 and 6.30 mm<sup>3</sup>/Mcycle were reported for 16 and 22.25 mm diameters respectively. The author noted that the ratio of wear rate between the two was similar to that between the bearing diameters, suggesting a linear relationship. The 28 mm devices did appear to hit steady-state after 2 Mcycles with an initial wear rate of 1.60 mm<sup>3</sup>/Mcycle that dropped to 0.54 mm<sup>3</sup>/Mcycle. Some degree of surface separation was also noted in the 28 mm bearings and these experimental results supported the theory that larger diameters resulted in some degree of mixed/fluid-film lubrication, and thus were lower wearing, whereas smaller bearings operated in boundary.

Firkins *et al.* (2001, [115]) investigated the effect of different articulation pro-

files for 28 mm bearings in different hip simulators. The lubricant used was FBS diluted to 25 % with deionised water and the bearings were tested to 5 Mcycles. Both simulators used a standard twin-peak Paul loading cycle [109] however the first simulator articulated on three independent axes of motion (PA3), flexion/extension, internal/external rotation and abduction/adduction. The second simulator only replicated the flexion/extension and internal/external rotation axes (PA2). The PA2 simulator demonstrated much higher wear rates of 3.09 and 1.23 mm<sup>3</sup>/Mcycle during bedding-in and steady-state respectively, compared to 0.31 and 0.04 mm<sup>3</sup>/Mcycle for PA3. The authors believed this to have been a result of a more eccentric elliptical motion on the two-axis simulator. This would have translated to a longer wear-path and thus increased sliding distance. The loading profile can therefore have a significant effect on the wear rate of the device.

While around an order of magnitude higher, these wear rates were still much lower than those observed for MoP bearings reported in the same simulator of 53 and 32 mm<sup>3</sup>/Mcycle. The simulators also appeared to produce different wear debris, with an average particle length of 10 - 15 nm for PA2 compared to 30 - 35 nm for PA3 during steady state. This highlighted that the simulation technique utilised can have a dramatic effect on the contact conditions within the bearing and the wear rate of these devices.

Scholes *et al.* (2001, [116]) compared the average wear rates of 28 mm MoM bearings with different radial clearances (22 and 40 μm) over 5 Mcycles. While both bearings displayed similar average volumetric losses during the bedding-in phase (approximately 0.9 mm<sup>3</sup>/Mcycle), the bearings with clearances of 22 microns displayed lower wear rates during steady-state wear (approximately 0.1 vs. 0.25 mm<sup>3</sup>/Mcycle). While highlighting the importance of radial clearance on the lubrication and wear of the device, there was no observable difference in the measured friction factor between the bearings. Again these results were compared to a traditional MoP bearing which displayed much higher wear rates of 102

mm<sup>3</sup>/Mcycle during both bedding-in and steady-state phases.

Initial simulator studies and promising clinical results for the McMinn prosthesis [97] showed that second generation MoM bearings were much lower wearing than MoP designs. The wear debris produced at the articulation interface was also found to be approximately an order of magnitude smaller than polymer debris, which was thought to reduce the likelihood of eliciting an immune response and thus aseptic loosening. However the observed high early failure rates for these devices suggest that the prediction for success of MoM contacts is much more complicated than simple wear rates. Other compounding factors and the simulation technique utilised must therefore be carefully considered.

### **3.4.2 - Adverse Loading**

Following the high failure rate and subsequent withdrawal of several devices from the market there has been a need within the community to understand the reasons *in vivo* performance has not matched the promising *in vitro* results from pre-clinical testing. So called 'Adverse Loading' scenarios are fast becoming the main focus of research groups looking to investigate the failure mechanisms of Hard-on-Hard THRs.

This section aims to explain some of the types of adverse loading that have been examined to date and highlight where the literature is still lacking in the explanation for failure of these devices.

#### **3.4.2.1 - Malpositioning**

As part of the design of a hip replacement device, consideration of the orientation of the implant is critical. The values and how the positioning is determined and measured to ensure successful implantation varies between manufacturer and design. Critical parameters such as inclination angle and version of the acetabular cup are typically 45° inclination and 20-30° anteversion respectively [117–119].

When the orientation of components exceed these values this can have adverse effects on the performance on the device.

The study of malpositioning of the acetabular component has largely been focused on Hard-on-Hard bearings. This is because such devices rely on the fluid pressure generated by elasto-hydrodynamic lubrication to support a degree of the load and reduce asperity contact during sliding. Myant *et al.* demonstrated the load supporting properties of the fluid pressure [120]. With high inclination the contact area may be impaired [118], and thus provide an avenue for this fluid pressure to escape the bearing. For large diameter MoM devices loss of lubricant may be particularly devastating [121–123]

Another explanation is a high angle of inclination results edge-loading effects, as has been demonstrated by Williams *et al.* [124] and Al-Hajjar *et al.* [125, 126]. High inclination in these devices have been shown in to increase levels of cobalt and chromium ions in synovial fluid [127, 128] and as much as a 17x fold increase in hip simulator wear rates [129]. A high inclination angle can lead to a large increase in the contact stress experienced in a Metal-on-Polymer bearing [130]. As MoP devices largely operate under boundary lubrication conditions, an increase in contact stress may also increase the wear rate and plastic deformation of the soft polymer cup.

### **3.4.2.2 - Microseparation**

Microseparation is the term used to describe the phenomena where the femoral head and acetabular cup separate relative to each other during a gait cycle. Whilst under normal articulation the centre of rotation for both the femoral head and acetabular cup are essentially the same. Microseparation causes a shift in these centres, resulting in the femoral head pulling out of the cup. This may be caused by joint laxity, component migration, an abnormal gait profile (for example due to leg-length discrepancy) or impingement of the femoral stem causing the head to

lever out of the socket [131–134].

Figure 3.8 shows how microseparation may occur during a normal walking profile. After normal articulation through the step the centres of rotation shift during the swing phase of the cycle. Upon reapplication of the load at "heel-strike" the head and cup are brought back together and impact. The severity and location of this impaction will depend on the patient activity and the degree of separation of the components. Potentially this impaction occurs at the rim of the cup, resulting in rim loading and the associated negative effects discussed previously.

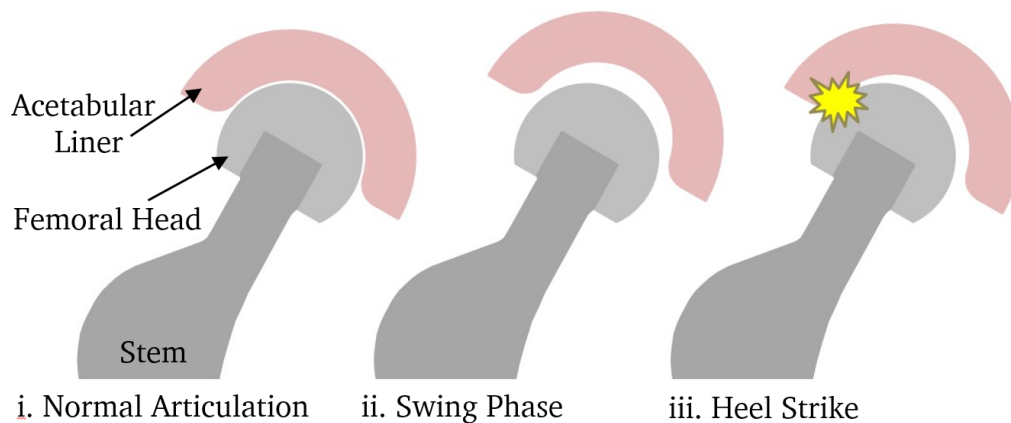


Figure 3.8: Illustration of Microseparation of the Femoral Head and Acetabular Liner during a gait cycle.

Microseparation was first noted in patients with Metal-on-Polymer replacements by Lombardi *et al.* and termed 'pistoning' or 'separation' [135]. Fluoroscopy was used to image the replacements of 10 patients and pistoning was determined to occur if the separation exceeded 0.75 mm (the calculated linear error of the technique). All 10 patients exhibited a degree of separation, with a maximum value of 2.8 mm found in one patient.

Dennis *et al.* continued the work with a larger cohort of 20 patients, 5 of which were natural hip joints and 5 were a constrained THR design which should display minimum separation [131]. The natural joints were found to not microseparate, and the constrained devices demonstrated 0.3 - 0.5 mm separation. The patients with the traditional replacements however displayed separation of between 1.9

and 5.2 mm during gait.

Komistek *et al.* then also compared this cohort to patients with Metal-on-Metal devices and determined that separation of the components did not occur for MoM bearings [132]. Smaller separation values of 0.3 - 0.51 mm were measured for the MoM bearings, but were not considered as separation due to the cut-off value of 0.75 mm selected in this study. Clarke *et al.* noted that separation was possible through gravity for MoM devices with the smaller measured values explained by the "suction-fit" of the bearings and the limited time point during swing phase [136]. More recent work has demonstrated that large separation values can in fact occur for both Metal-on-Metal and Ceramic-on-Ceramic devices [137].

### **3.4.3 - Tribocorrosion**

Tribocorrosion is the interaction and synergies between mechanical and electrochemical phenomena which occur at the interface of two surfaces in relative motion and within a corrosive environment. Matthew *et al.* [138] pointed out that as tribocorrosion is still a relatively young field there is relatively little standardisation in experimental test methods. This section aims to explore the existing test methods in the literature, with a particular focus on those applied to the study of biomedical materials.

#### **3.4.3.1 - Tribometer Studies**

Simple configuration tribometers have long been used to assess the performance of tribological couples. The tribometer configuration can vary significantly although most consist of a pin or ball articulating against a plate. The motion can be unidirectional sliding, often termed Pin-on-Disk (PoD), or reciprocating sliding, often termed Pin-on-Plate (PoP). For assessment of the tribocorrosion of biomedical materials reciprocating Pin-on-Plate or Pin-on-Ball tribometers are the most used configuration in an attempt to recreate the motion of the hip or knee joint.

Research groups working in this area include Yan *et al.* [11, 12, 139–142], Wimmer and Fischer [7, 143, 144] and Mischler, Landolt, Papageorgiou and Viera [37, 145–149].

Yan *et al.* (2006, [139, 140]) utilised an electrochemically-instrumented, reciprocating tribometer to study the effect of lubricant on the corrosion of passive alloys under sliding. A silicon nitride ball was articulated against high-carbon (HC) and low-carbon (LC) CoCrMo alloy, as well as 316L stainless steel. The lubricants used were 0.3 % NaCl solution, Dulbecco’s Modified Eagle’s Medium (DMEM) and 50 % calf bovine serum. Under static conditions anodic polarisation scans found lubricants containing proteins reduced the potential required for breakdown of the passive film of cobalt alloys; indicating an increased susceptibility for corrosive damage. Sliding tests were conducted under free corroding conditions and under cathodic protection, to assess the role of corrosion in the degradation of the materials.

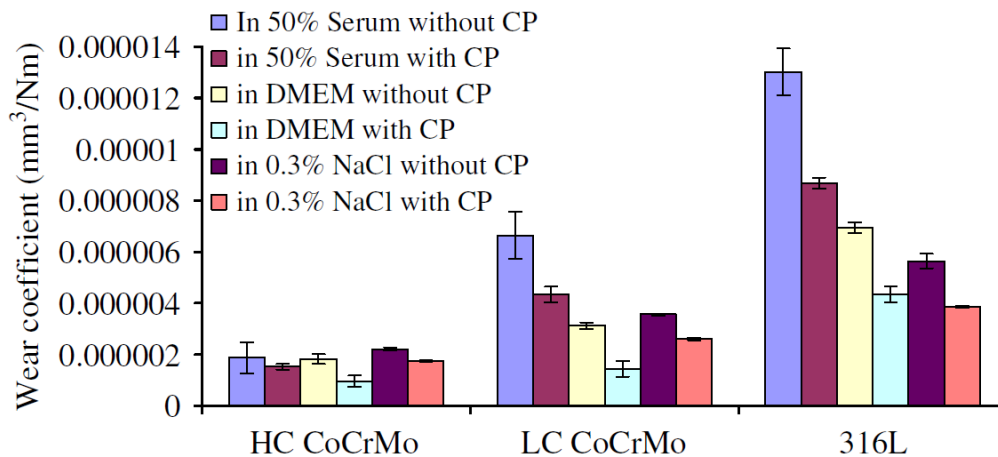


Figure 3.9: Wear coefficients for HC and LC CoCrMo alloy and 316L Stainless Steel in different lubricants [141]. Reproduced with permission (see Appendix B).

The results are shown in Figure 3.9 and corrosion-related damage in the boundary lubricated contact within the tribometer was found to be responsible for between 22 and 50 % of total material loss, depending on lubricant and material. Lubricants containing proteins appeared to increase the material degradation rate for LC CoCr and 316L, although no significant difference was noted in HC CoCr. The

contact conditions replicated were much more severe than those seen in actual prostheses. The CoM contact had an initial Hertzian contact pressure of approximately 2 GPa, compared to typical pressures of 30 - 50 MPa [150].

Yan *et al.* [11, 142] went on to perform potentiostatic polarisation tests during sliding in serum, DMEM and 0.3 % NaCl. For the DMEM, under certain conditions the resulting anodic current dropped to near zero, shown in Figure 3.10. This was attributed to the formation of a protective organometallic tribofilm during sliding, which was assessed post-test via XPS analysis. This behaviour was not noted in 0.3 % NaCl solution, suggesting the proteins contained in physiological lubricants may act to protect the material [11].

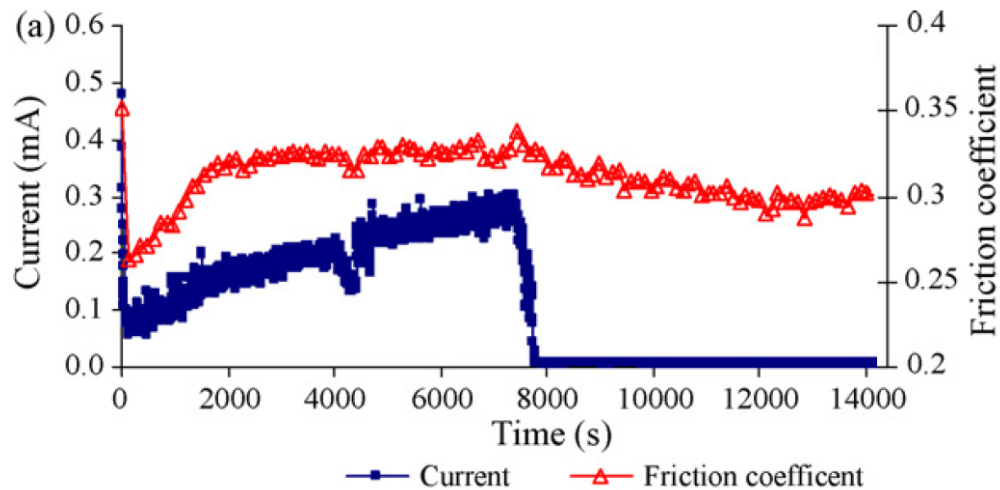


Figure 3.10: Anodic current and friction coefficient for silicon nitride articulating against HC CoCrMo alloy [11]. Adapted and reproduced with permission (see Appendix B).

### 3.4.3.2 - Hip Simulator Studies

The use of full hip simulators to study the electrochemistry is a relatively new analytical technique with only two known research centres having instrumented full hip simulators with electrochemical cells [13–15, 151, 152]. This section aims to explore the current knowledge in the literature for electrochemistry in hip simulators.

The first known hip simulator instrumented with a three-electrode cell was pub-

lished in 2009 by Yan *et al.* [153], following on from the author's tribometer work. The simulator was an inverted pendulum friction simulator, shown schematically in Figure 3.11. The simulator allowed simultaneous measurement of electrochemical processes and friction coefficients in the articulating bearing. However the design of the simulator meant that only the flexion / extension axis of articulation was reproduced. Also, the lubrication was not an accurate replication of the hip *in vivo* as the cup is inverted; allowing gravity to ensure lubricant is pulled into the bearing.

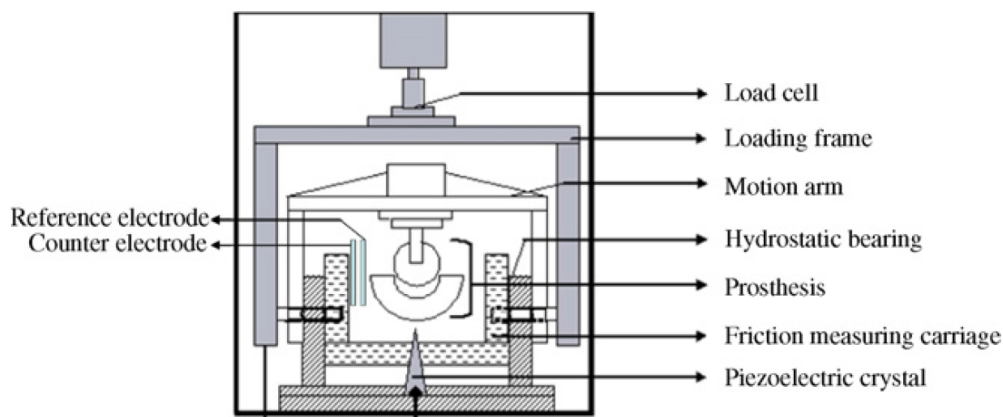


Figure 3.11: Schematic of the pendulum friction simulator used by Yan *et al.* [153]. Reproduced with permission (see Appendix B).

Yan *et al.* [153] investigated the effect of metallic nanoparticles (28 nm diameter), which are produced as a result of wear during articulation, on the tribology and corrosion of 36 mm MoM bearings. Yan noted that upon the initiation of sliding the OCP of the system dropped and stabilised, but the subsequent addition of nanoparticles resulted in a further drop in OCP. This indicated further removal of the protective oxide film and formed tribochemical reaction layers. The friction of the bearing was also investigated, showing a higher friction factor under higher loads and a lower friction factor in a physiological lubricant (FBS). The lower friction in FBS was coupled with a higher release of metallic ions in the solution however, as measured by ICP-MS.

The effects of load and lubricant were further explored by Yan *et al.* [151] using

the same instrumented pendulum simulator and 36 mm MoM bearings. Higher metallic ion release was noted for a higher swing phase loads, and also in FBS over NaCl solution. This was not coupled with a significant change in OCP however.

In 2010 Yan *et al.* [13] published initial results from a new instrumented hip simulator, the ProSim deep flexion simulator used in the present study. The simulator included an internal/external rotation articulation axis and the anatomical orientation of the components allowed for a more realistic approximation of lubrication conditions *in vivo*. However the new simulator was not fitted with any type of friction measurement. Initial OCP results for 36 mm MoM bearings to 500,000 cycles, thought to operate towards fluid film, were compared to tribometer studies, operating in boundary lubrication. Both scenarios displayed a clear drop in OCP at the initiation of sliding, indicative that in both conditions depassivation of the surface does occur.

Bellefontaine, 2010 [152] also instrumented a pendulum friction simulator and monitored the OCP potential of 50 mm diameter components as well as conducting anodic potentiostatic tests. As cast components were compared against heat treated and double heat treated parts. The only significant difference noted was during anodic polarisation tests, the double heat treated parts showed higher corrosion currents than as cast components, indicating an increased susceptibility to corrosion. A change in the carbide structure of the alloy was also noted through SEM analysis, with heat treated components displaying fewer and reduced carbide size as they dissolve into the matrix. The OCP shifts noted by Bellefontaine were much smaller than those noted in other studies discussed here, often only involving a negative shift of less than 200 mV as compared to approximately 400 mV.

Hesketh *et al.* [14] continued the work at Leeds on the deep flexion hip simulator and published initial results for 36 mm MoM bearings to 1 Mcycles. Up to approximately 450,000 cycles the OCP shift on the initiation of sliding was similar to

that observed previously by Yan *et al.* [13], but gradually ennobled and remained relatively stable up to 1 Mcycles. This wear induced passivation had not been reported previously in hip simulator studies, and was thought to have been as a result of the formation of a proteinaceous tribofilm on the surface. TEM analysis on the femoral head revealed a nano-crystalline layer of the metal in the uppermost region of the surface. Within the observed wear scar this layer displayed finer crystals; approximately 40 nm vs 20 nm. The depth of the layer was also larger at the contacting region. This differs from a previous study conducted by Pourzal *et al.* [10], which showed a coarser crystal structure within the wear scar.

Hesketh *et al.* [15], also studied the effect of surface degradation on 36 mm MoM bearings to 1 Mcycles. Open circuit potential, corrosion current (LPR) and ionic mass loss (Faradaic and ICP-MS) all appeared to support the hypothesis that depassivation of the passive oxide layer occurred as a result of sliding.  $I_{corr}$  and ionic mass loss rates also fell in conjunction with the previously reported wear-induced passivation. This study also made an early attempt in linking the tribology of the bearing to the electrochemistry by performing anodic potentiostatic tests in order to monitor the depassivation/repassivation of the surface over the course of a cycle. A clear periodicity was shown at given points during the test, as shown in Figure 3.12. This periodicity was not always observed however, and the exact conditions which result in depassivation are still unknown.

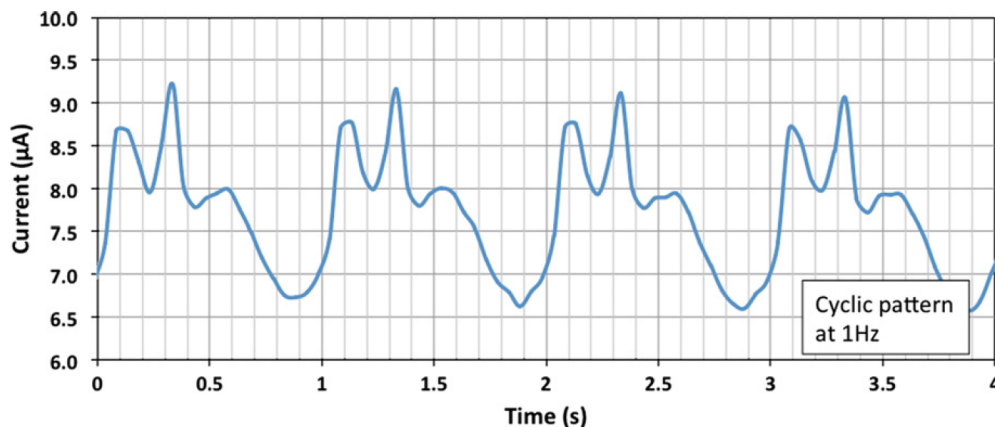


Figure 3.12: Cyclic variation in potentiostatic current during articulation of a 36 mm HC CoCr hip bearing [15]. Reproduced with permission (see Appendix B).

Hesketh *et al.* [15, 150] made an initial attempt to correlate the repeating patterns noted in anodic currents measured from Metal-on-Metal bearings with a so called ‘severity factor:’

$$I \propto \frac{W\omega}{h_{min}} \quad (3.1)$$

Where:    I        =    Current generated by sliding (Amps)  
              W        =    Axial Load (N)  
               $\omega$         =    Angular Velocity (rad/s)  
               $h_{min}$     =    Theoretical Minimum Film Thickness (nm)

As conditions become more severe at the interface, i.e. load increases or the lubricating film thickness reduces, this should cause an increase in depassivation of the surface and correspond to an increase in the measured anodic current transient. The ‘severity factor’ demonstrated a similar shaped profile to anodic current transients. The peaks did not appear to align however, and the onset of current was often in advance of high severity portions of the cycle. This noted phase difference was not well understood as current should align with or follow surface damage.

To date the author knows of no studies which have taken a MoM bearing beyond 1 Mcycles in an electrochemically-instrumented hip simulator. Most traditional studies have demonstrated bi-phasic wear behaviour in hip bearings, with higher initial wear rates during a ‘bedding in’ period before hitting a ‘steady state’ phase after 1 - 2 Mcycles [110, 116, 154].

### 3.4.4 - Tribochemical Reaction Layers

Wimmer *et al.* [7, 143] first observed the formation of tribochemical reaction layers or tribofilms *in vivo*. These films were observed both on pins and plates used for tribometer studies [7] and on a series of 42 retrieved McKee-Farrar MoM devices [7], shown in Figure 3.13. EDS analysis revealed these layers to be carbon-rich and also containing oxygen. Other trace constituents such as calcium, nitrogen,

sulphur, sodium and others were also noted at different locations. The formation of these layers are thought to be as a result of denaturing of proteinaceous material in bovine serum *in vitro* and synovial fluid *in vivo* [7–9, 14, 15, 150, 155]. Maskiewicz *et al.* suggested the primary cause of denatured proteins in Metal-on-Metal bearings was high mechanical shear at the sliding interface, possibly coupled with interactions with metal ions [156].

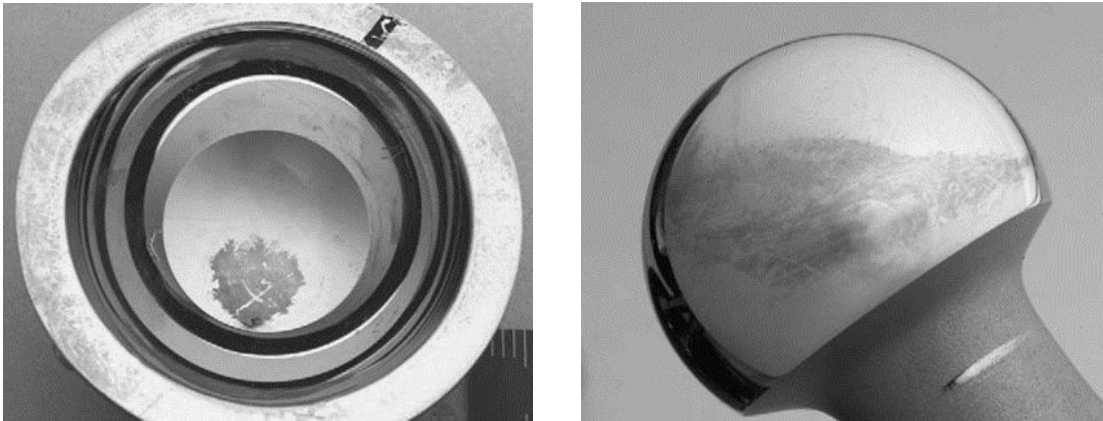


Figure 3.13: The acetabular liner (left) and femoral head (right) from an explanted McKee-Farrar prosthesis displaying a visible tribofilm formation on both surfaces [7]. Reproduced with permission (see Appendix B).

XPS analysis revealed these layers to be around 100 nm thick, although this varied, and mostly homogenous. A protein assay comparison between bovine serum albumin and samples of the layers confirmed the layers to be of organic nature. The author hypothesised the films are comprised of proteins from human synovial lubricant which have denatured during articulation. Once formed these layers may act as a solid lubricant, reducing adhesive and abrasive wear [7].

Milosev *et al.* (2008, [157]) also identified a carbon-rich deposited layer on the surface of a single MoM retrieval. The composition of the observed film varied with the film thickness, which was measured at up to 1  $\mu\text{m}$  thick. XPS analysis revealed the thicker areas were carbon, nitrogen and oxygen rich and organic in nature. In areas with thinner deposits the organic layer was mixed with metal oxides and hydroxides, suggesting complex interaction with debris produced at the interface.

Liao *et al.* (2011, [9]) noted areas within tribofilms found on retrievals, from the same series presented in [7], which were highly ordered. Electron energy loss spectroscopy (EELS) of these ordered layers displayed a  $\pi^*$  pre-peak, shown in Figure 3.14, which in amorphous carbon compounds is indicative of the presence of  $sp^2$  carbon bonds [158, 159].

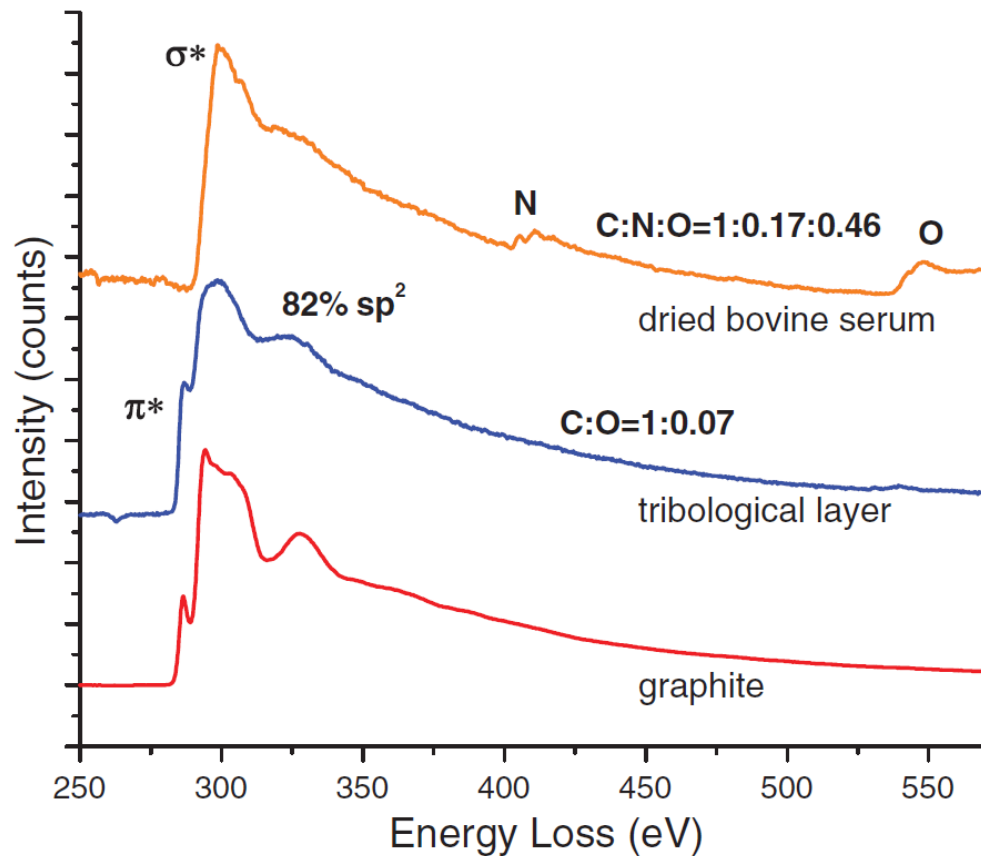


Figure 3.14: EELS spectra of dried bovine serum, the tribological layer and graphite [9]. Reproduced with permission (see Appendix B).

Analysis of spectra from unknown carbon films can reveal the percentage of planar  $sp^2$  bonds within the film by comparing to a spectrum of graphitised carbon. The film present on the retrievals was determined to be 82 %  $sp^2$  carbon bonds and the author hypothesised the formation of graphitic carbon layers during articulation.

Other evidence such as Raman spectroscopy and high resolution electron microscopy techniques appeared to support the presence of graphitised carbon. The formation of graphite however typically requires temperatures and pressures greatly in excess of those observed within the hip during articulation [160, 161].

Recent work by Hesketh *et al.* [162] supported the findings of Milosev [157] with thicker films observed on the surface of components tested within a hip simulator. The thickness of the tribofilm was found to range from  $\approx 200 - 800$  nm and in cross-section homogenous carbon-rich layers were seen as well as agglomerated metal oxide particles, shown in Figure 3.15.

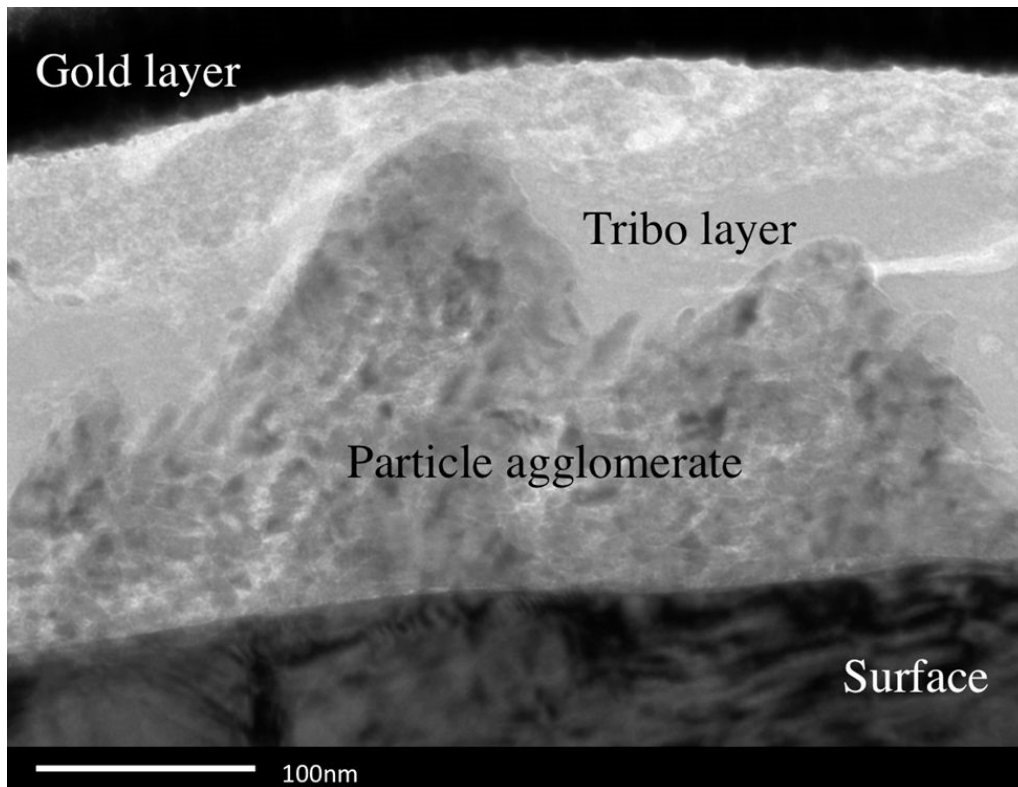


Figure 3.15: TEM image of particles suspended in the tribolayer noted on the surface of 36 mm MoM hip bearings articulated in a hip simulator. Reproduced with permission (see Appendix B).

EELS analysis of the tribofilm also revealed a  $\pi^*$  pre-peak, although the spectrum bore a much closer resemblance to amorphous carbon. The ratio of planar  $sp^2$  bonded carbon was determined to be  $\approx 65\%$ , much lower than that observed by Liao *et al.* [9]. The discrepancy was attributed to different fitting procedures used during analysis. Hesketh noted an asymmetrical  $\pi^*$  pre-peak, which may have been comprised of two separate peaks, one of which is more commonly associated with non-planar  $sp^2$  bonds or carbon singly bonded to hydrogen or nitrogen [162]. The exact composition of these films and their formation mechanism is therefore still very much in question.

### 3.5 - Summary

Tribocorrosion is still a relatively young field, and the importance of tribocorrosion processes in biomedical applications has only really been highlighted over the last decade, particularly with MoM hip replacements. The knowledge base within the literature is still lacking information on what goes on at the articulation interface due to the complex synergies taking place.

Instrumentation of full hip simulators with a three-electrode cell appears to be a viable analytical tool for assessing the tribocorrosion processes occurring during articulation of MoM bearings and further work is needed to make better predictions on how these devices will perform *in vivo*. This study aims to investigate the corrosion of MoM hip bearings with a particular focus on adverse loading scenarios. Lubrication aspects such as regime and protein interaction in the formation of tribofilms will also be explored, with an attempt to understand their effects on the degradation of the device.

The ultimate goal is a better prediction for the performance of MoM devices *in vivo* in order to inform future product development and patient care.

### 3.6 - Aims and Objectives

The aim of this thesis is therefore to expand the working knowledge of Hard-on-Hard Total Hip Replacements with a metallic surface in the bearing sliding interface. Specifically in terms of biotribocorrosive phenomena under standard and adverse articulation conditions through *in vitro* testing and analysis of materials and devices.

- Exploit instrumentation of three-electrode electrochemical cell across new simulation techniques to assess corrosive degradation of Metal-on-Metal total hip replacements.

- Assess the effect of adverse loading scenarios, such as microseparation and malpositioning, on the contribution of corrosion to total material loss.
- Attempt to link the *in situ* corrosion current to the tribological conditions of an articulation cycle.
- Investigate the use of metal and ceramic counterfaces in hard-on-hard hip articulation.

## Chapter 4 - Experimental Methodology and Design

### 4.1 - Materials

#### 4.1.1 - Static & Pin-on-Plate Components

25 mm diameter High-Carbon (HC) CoCrMo alloy plates were polished to a mirror finish using progressively finer Silicon Carbide (*SiC*) grit paper (320 - 1200). Finally the plates were polished using 9 and 3  $\mu\text{m}$  diamond paste and polishing mops. Pins were domed with a 100 mm radius and polished as well as possible without compromising the radius. All samples were also passivated according to standard ASTM F86-09 [163] for 30 minutes in 32.5% Nitric Acid ( $\text{HNO}_3$ ) in order to create a uniform passive oxide film between samples.

#### 4.1.2 - Hip Simulation Components

Two different bearing couples were assessed in this thesis. Clinical THR components of 28 mm diameter were used throughout. The first bearing couple was a Metal-on-Metal combination which comprised of a *CoCrMo* alloy femoral head articulating against a *CoCrMo* alloy acetabular cup. Both components were manufactured from a High Carbon (HC) grade of *CoCrMo*. The second combination was a Metal-on-Ceramic bearing, sourced from a different manufacturer. This combination comprised of a Low Carbon (LC) *CoCrMo* femoral head and a Bi-olox® ceramic acetabular liner. Examples of a femoral head and the different acetabular liners can be seen in Figure 4.1.

Figure 4.2 shows example 3D models of test fixtures, which were used to hold the hip components in the simulators. In order to isolate the metallic hip replacement samples from the simulator as much of the fixturing as possible was manufactured from non-conductive materials such as polyetheretherketone (PEEK) plastic and

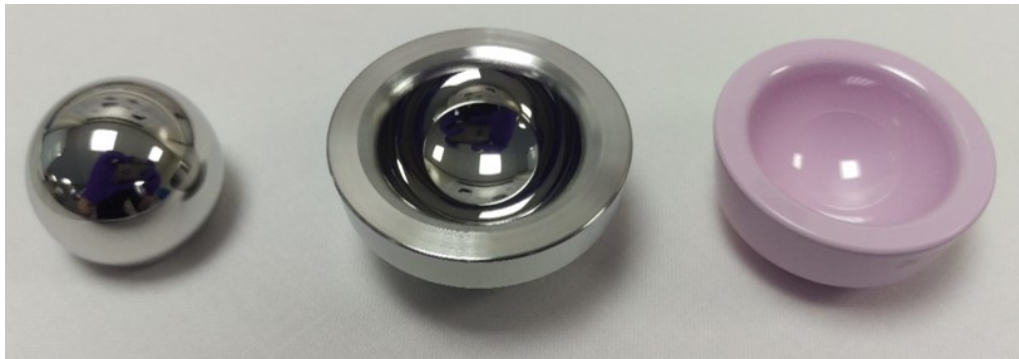


Figure 4.1: Image of unworn 28 mm diameter (left to right) *CoCrMo* Femoral head, *CoCrMo* Acetabular Liner and Biolox®delta Ceramic Acetabular Liner.

Torlon 4203 high-strength compressive resin. This also prevents contamination of the serum from other metallic ions which may be released through passive degradation of metallic fixtures.

Custom designed ‘spigots’ were utilised to hold the femoral heads in place using the modular morse tapers already present in the heads. These spigots were either made from Torlon 4203 high-strength compressive resin or 316L Stainless Steel, depending on the simulator. Care was taken to seal any other possible sources of metallic tribocorrosion with silicone sealant, such as the femoral head modular taper, to ensure the only active interface monitored by the cell was the bearing surface.

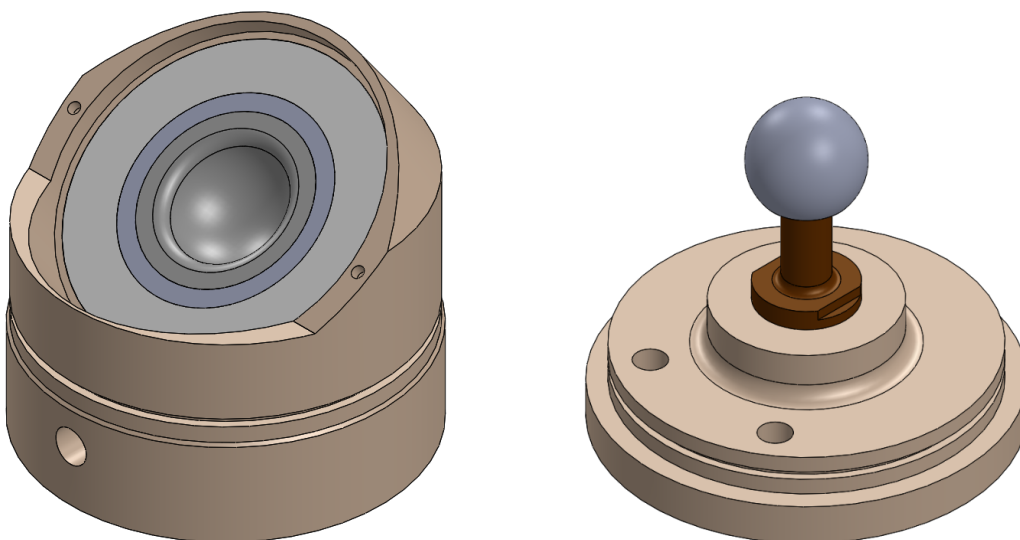


Figure 4.2: 3D Models of the acetabular cup fixture (left) and the femoral head fixture and spigot (right) containing 28 mm components.

Titanium alloy acetabular shells were used to hold the cups in place within the simulators. The acetabular shells were cemented within the fixtures using laboratory grade Poly(methyl methacrylate) (PMMA) resin. Different support fixtures were therefore needed to hold the liner in place during the cementing process. These fixtures varied depending on the experimental requirements, such as different component design (e.g. modular components) or simulator fixturing. Once in place the components are surrounded with a silicone gaiter in order to hold the lubricant within the test cell and prevent the station running dry.

### 4.1.3 - Lubricant

Typically simulator studies use foetal bovine or new-born calf serum as the lubricant in order to mimic the proteins present in human synovial fluid and their approximate concentrations [108, 110, 112–114]. The first version of the ISO 14242-1 standard for hip simulation was released in 2002 and stipulated a 25% (v/v) lubricant concentration of serum, or to a minimum protein content of 17 g/L, diluted with deionised water [164]. Upon revision in 2012 and 2014 the standard called for an increased concentration of 30 g/L and made no more reference to percentage volume dilution [165, 166]. Despite this many modern studies still use and quote the 25 % (v/v) dilution and make no reference to their measured protein content. The standards also still call for deionised water to dilute the serum which does not mimic the conductivity of synovial fluid [167]. In order to facilitate electrochemical measurement a salt solution such as sodium chloride (*NaCl*, 0.35 or 0.9% (w/v)) or phosphate buffered saline (PBS) must be used. This is also representative of the anions and cations present in synovial fluid.

Unless otherwise stated the lubricant selected for all tests throughout this thesis was Foetal Bovine Serum (FBS). The serum was diluted to 17 g/L total protein content (TPC) as per the qualification previously set by Hesketh *et al.* [14, 15, 150]. The serum was diluted using Phosphate Buffered Saline (PBS) in order to better replicate the conductivity and conditions found *in vivo*. This also facilitated

the electrochemical testing. Sodium Azide was also added to the lubricant (0.03% w/v) in order to retard bacterial growth.

#### **4.1.4 - Three-Electrode Cell**

In each test configuration a connection was made to the sample, as described below. The sample therefore formed the working electrode (WE). A combination Silver/Silver Chloride (*Ag/AgCl*) reference electrode (RE) and Platinum (Pt) counter electrode (CE) was used to complete the cell. All measurements were performed using a PGSTAT101 Potentiostat (Metrohm Autolab, Netherlands).

### **4.2 - Electrochemical Test Methods**

A three-electrode electrochemical cell has been integrated into all experiments outlined in this report in order to employ electrochemical test methods to investigate the degradation of biomedical alloys under sliding conditions. The test cell is typically comprised of a working electrode (WE) which is the test sample, and a combination reference / counter electrode which consisted of a silver-silver chloride (*Ag/AgCl*) reference electrode (RE) and platinum disc counter electrode (CE). The working electrode and combination reference / counter were then submerged in the lubricant and electrochemically monitored during the course of the test using the following DC electrochemical techniques.

#### **4.2.1 - Open Circuit Potential**

As discussed in Chapter 2 the Open Circuit Potential (OCP) of a test sample occurs when the anodic and cathodic half-cell reactions are in equilibrium and thus no current flows between the WE and CE. The test sample is therefore neither a net anode nor net cathode. During DC test methods the OCP of the system is often termed the free-corroding potential and referred to as  $E_{corr}$ . The OCP is monitored by measuring the potential difference between the WE and the stable and known potential of the RE. The progression of OCP over the course of a test can give a

semi-quantitative assessment of the corrosion of the system.

## 4.2.2 - Linear Polarisation Resistance

Linear Polarisation Resistance (LPR) scans were conducted by monitoring OCP for 120 seconds and taking the final value as a stable OCP point. The working electrode was then cathodically polarised to -25 mV from OCP and swept anodically to +25 mV from OCP at a sweep rate of 1 mV/s. This sweep rate was chosen in order to minimise the length of time each scan takes to reduce possible errors introduced through system changes. The working electrode was then allowed to stabilise without polarisation for 600 seconds before OCP was monitored again.

LPR scans are considered to be non-destructive as they operate close to the OCP of the sample. In reality however the OCP of a sample is a mixed measure of different local anodic and cathodic sites at the surface, which may be polarised further beyond OCP during the course of a scan. The time between scans was therefore spread out as much as possible in order to minimise disturbance to the system.

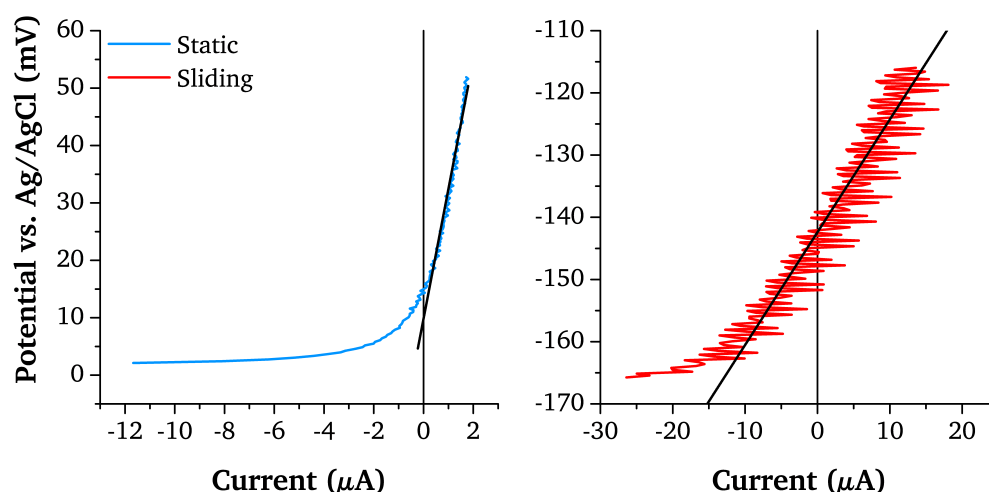


Figure 4.3: Example static (left) and sliding (right) LPR scans with fitting curves.

Some example LPR scans taken during pre-sliding static conditions and during sliding can be seen in Figure 4.3. Both static and sliding conditions typically presented with a cathodic tail due to the sudden application of a -25 mV overpotential

at the start of the scan. The LPR scans taken during sliding also typically displayed more noisy data when compared to static conditions. How the LPR data is fitted is critical to the calculation of the polarisation resistance ( $R_p$ ) of the system at that point in time. Therefore effort was taken to ensure LPR data was interpreted uniformly across all tests.

Figure 4.3 also shows example fitting curves for both conditions. As much of the cathodic tail as possible was omitted from the fit. The slope of the scan, which represents the polarisation resistance, was therefore taken within linear regions of the data. Any noise and spread of data during sliding conditions was also accounted for when fitting the slope.

The values obtained for  $R_p$  were then converted into a corrosion current ( $I_{corr}$ ) using the Stern-Geary equation (Equation 2.17) and standard Tafel constants of 120 mV/decade. The corrosion current is a direct measure of the loss of metallic ions as a result of corrosion.  $I_{corr}$  was then integrated with respect to time over the course of the test to find the Charge transfer of ions lost, shown in Equation 4.1.

$$Q = \int_0^t I_{corr} dt \quad (4.1)$$

Where:  $Q$  = Charge Transfer (C)  
 $I_{corr}$  = Corrosion Current (A)  
 $t$  = Time (s)

Thus an estimated mass loss of material through corrosion was calculated using Faraday's Law:

$$m = \frac{MQ}{nF} \quad (4.2)$$

Where:  $m$  = Corrosive mass loss from the working electrode surface  
 $M$  = Atomic Mass  
 $n$  = Valence Number  
 $F$  = Faraday Constant (96,490 C/mol)

Due to the assumptions commonly made for pure metals there is some uncertainty in applying Faraday's Law to an alloy. As CoCrMo has three main constituent elements, each with different molar masses and half-cell valence numbers, interpretation of the data can be critical. A weighted average molar mass (59.20) and valence number (2.35) were used based on the approximate percentage alloy composition (Co  $\approx$  62.5%, Cr  $\approx$  28%, Mo  $\approx$  6%). This assumes a stoichiometric release of ions from the working electrode surface, which may not be the case. Upper and lower error bars therefore represent the values for Cobalt (58.9, 2) and Chromium (51.99, 3) respectively, to account for possible preferential release of those elements. A density of 8.29 g/cm<sup>3</sup> was used to convert mass to volume loss.

### 4.2.3 - Potentiostatic Polarisation

Potentiostatic polarisation involves imposing a fixed potential on the working electrode. The sample therefore becomes a net anode or cathode, depending on the direction of polarisation. This allows the potentiostat to monitor the resultant current between the working electrode and counter electrode within the three-electrode cell. The sampled current will not be the corrosion current ( $I_{corr}$ ) of the system, but rather an anodic or cathodic current ( $I_a / I_c$ ) transient which is a measure of the kinetics taking place at the sample surface.

Potentiostatic tests have long been used to assess tribocorrosion systems and the depassivation mechanisms of the materials in question [145, 146, 168–170]. The anodic current measured by the potentiostat only accounts for oxidation at the metal surface. The total ionic release into the electrolyte may therefore be greater, for example from oxidation of metallic wear debris particles.

For the present studies OCP was monitored for 120 seconds, similar to LPR scans, and a final value taken. The working electrode was then polarised to +50 mV vs. OCP and the resultant anodic current transient sampled at 100 Hz. During hip simulation an analogue voltage signal was taken from the load cell and sampled by the potentiostat along with the current in order to examine the current over a cycle.

#### **4.2.4 - Potentiodynamic Scanning & Cyclic Polarisation**

Static DC electrochemical tests were performed on 25 mm diameter HC CoCrMo alloy plates utilising a small volume electrochemical cell illustrated in Figure 4.4. The plates were polished under the same regime as the tribometer samples. The cell was filled with 5 mL of electrolyte and the working electrode connection was taken from the rear of the plate. The area of the plate exposed to the electrolyte was 1 cm<sup>2</sup>. The cell was completed with a combination Ag/AgCl reference / Pt disc counter electrode probe. The plates were allowed to stabilise in the electrolyte for one hour and OCP was recorded every second. An average of the three OCP curves was taken. A cathodic potential of -50 mV was applied and the potential was swept anodically at 1 mV/s until the current density exceeded 500  $\mu\text{A}/\text{cm}^2$ . At this point the sweep direction was reversed and swept back cathodically until OCP was reached again.

The electrochemical behaviour of the CoCr alloy was examined in six different electrolytes: Phosphate Buffered Saline (1x PBS), 17 and 30 g/L Foetal Bovine Serum (FBS) with and without 0.03% w/v Sodium Azide and finally unfiltered Bovine Synovial Fluid. Three repeats were taken of each electrolyte.

#### **4.2.5 - Short-Term Testing**

Short term tests performed both on the tribometer and Full-ISO hip simulator followed a test profile highlighted in Figure 4.5. Samples were allowed to stabilise

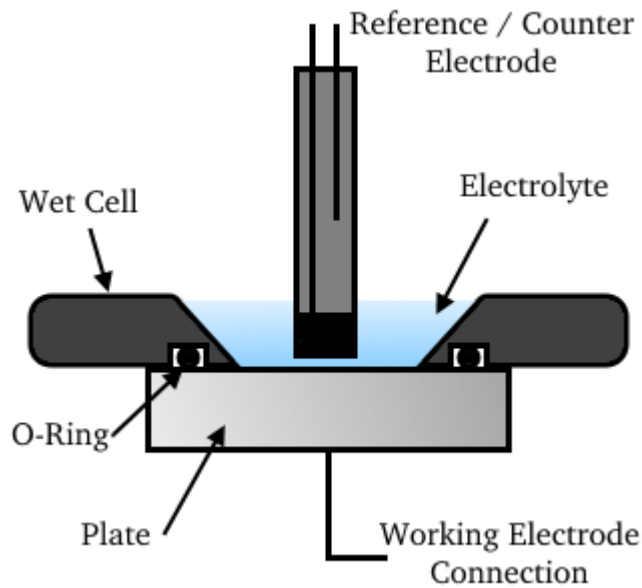


Figure 4.4: Illustration of the small volume electrochemical cell utilised for static tests.

*in situ* for one hour and OCP was sampled at 1 Hz throughout the test. During this phase three ‘Static’ LPR sweeps were conducted every 15 minutes. Articulation was then initiated for 4,000 cycles during which time three more ‘Sliding’ LPR sweeps were taken and an additional anodic polarisation performed. The OCP was also then monitored during the final static period.

Additional polarisation tests were performed on the Full-ISO simulator whereby the components were polarised at 0 mV versus the reference electrode before the initiation of sliding. This was done to investigate the anodic current transient over the first 600 cycles.

#### 4.2.6 - Long-Term Testing

Under long term testing on the pneumatic simulator OCP was monitored continuously throughout the test and sampled every 60 seconds. After a DC polarisation test the OCP was allowed to settle for 10 minutes before sampling again to prevent artificial spikes in the data. The results were then plotted against the experiment time or number of sliding cycles performed by the tribocouple.

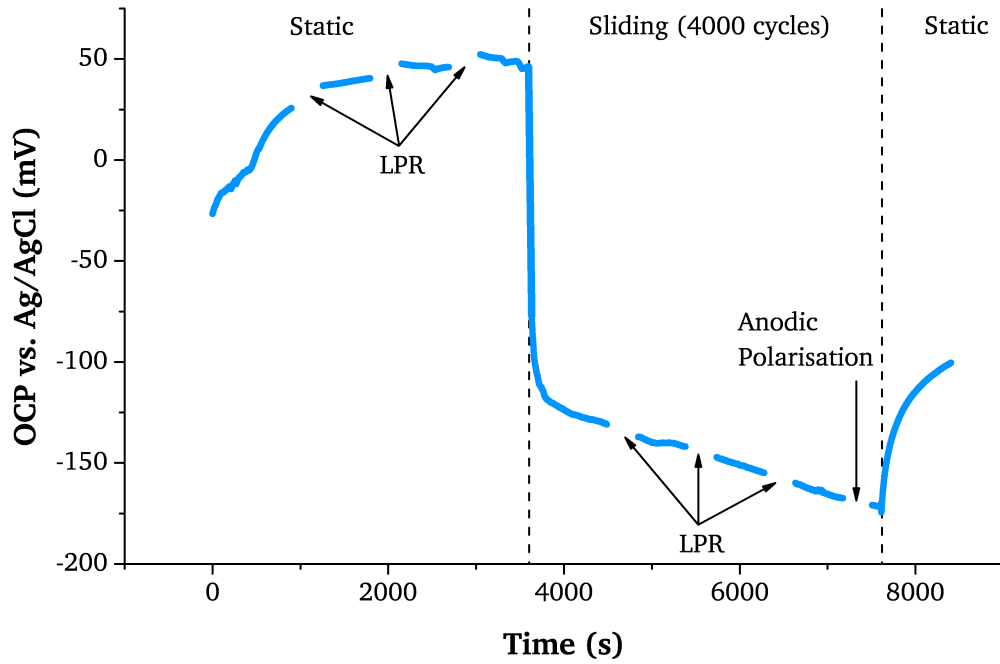


Figure 4.5: OCP profile of short-term tests highlighting timing of sliding period and DC polarisation techniques.

For DC techniques the OCP was monitored for 120 seconds before hand to ensure stability and the final value was taken. Polarisation was then performed versus this OCP value. LPRs were performed as described in Section 4.3.2 from -25 to +25 mV at a scan rate of 1 mV/s every 10,000 cycles. Anodic Polarisations were performed in-between LPR scans as described in Section 4.3.3 with potential held at +50 mV and the resultant anodic current sampled at 100 Hz. By monitoring the corrosion current ( $I_{corr}$ ) via LPR sweeps the corrosive degradation of the bearings can be monitored as a function of time/cycles completed over the bedding-in period.

#### 4.2.7 - Statistical Analysis

Where statistical analysis was appropriate, unless otherwise stated, data was analysed via a one-way analysis of variance (ANOVA,  $p < 0.05$ ). When no significant difference was found between group means, this was reported. If a statistical difference was noted a post hoc Tukey's honest significant difference (HSD) test was carried out to determine which group means presented with a statistically signif-

icant difference. Tukey's HSD test was used in order to correct for family-wise errors.

### **4.3 - Tribometer**

A tribometer is a piece of machinery designed to articulate one surface against a counter surface in order to simulate a tribological system. Tribometers have long been used to assess the tribological properties and performance of given materials, bearing couples or lubricants for specific situations. The aim of this section is to expand on the use of a given tribometer for the purposes of testing biomedical materials in relative motion and in the presence of a relevant lubricant / electrolyte.

#### **4.3.1 - Biceri Reciprocating Pin-on-Plate Tribometer**

A schematic of the test set-up within the Biceri tribometer is shown in Figure 4.6. The tribometer is a reciprocating pin-on-plate wear test machine. The rotational action of an electric motor is translated to lateral reciprocation via a scotch yoke mechanism. The mechanism drives a platform on a low-friction track which holds a heating element and a test bath. The stroke length of the platform is variable between 5 - 20 mm through adjustment of the mechanism and the machine is capable of sliding at a frequency of up to 2 Hz.

The test bath fixture holds a plate, with or without lubricant, and the loading arm fixture holds a pin against the plate. When engaged, the reciprocating bath causes the plate to articulate against the pin. The normal load is applied by hanging weights on the loading arm, which acts as a pivot beam. The beam arm is supported laterally against a load cell which enables the resultant force from articulation to be monitored in order to gain a measure of friction between the samples. The test samples are isolated from the rest of the machine by using plastic fixtures in order to facilitate electrochemical testing. A standard hot plate and peristaltic pump was therefore used to drive hot water around a heating coil placed within

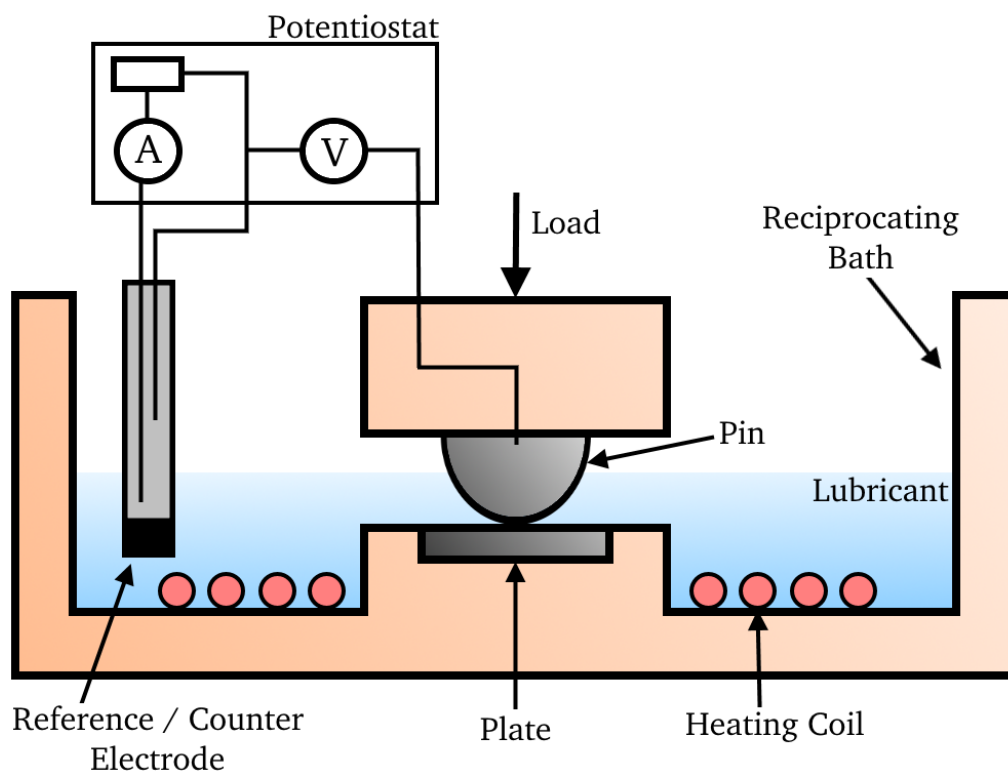


Figure 4.6: Schematic of the three-electrode cell within the Biceri tribometer.

the lubricant bath. A thermocouple within the bath controls the hot-plate in order to create a closed circuit control on the lubricant temperature.

### 4.3.2 - Integration of Electrochemistry

The tribometer was instrumented with a three-electrode electrochemical test cell as illustrated in Figure 4.6. The working electrode connection was taken from the pin, which is assumed to remain in contact with the plate under load, hence giving a working electrode comprised of the entire submerged surface area of both the pin and plate. The fixtures also allow a connection to be made to the plate, should a non-conductive pin be used (e.g. ceramic) or separate monitoring is required for future testing.

Warm water was driven through flexible plastic piping via a peristaltic pump in order to form a 'heating coil'. The temperature of the water was controlled by a thermocouple present in the lubricant in order to keep the lubricant temperature at 37°C during a test.

### 4.3.3 - Test Methodology

Electrochemical testing was performed according to the profile described in Section 4.2.5. The load applied by the loading arm was progressively increased by hanging increasing weights from 5 to 12.5 kg in 2.5 kg increments. A 5.0 kg starting weight was used according to a previous method set by Hesketh [150]. This translated to approximately 122.6 N load on the pin and a 210 MPa Mean Hertzian Contact Pressure according to Equation 2.1. This rapidly decreased as the test progressed as wear occurs and the contact pressures drops to the order of MoM THR contacts, as demonstrated by Hesketh *et al.* [150, 171] The load was increased in an attempt to simulate the higher contact pressures under edge loading. Contact pressures of as high as 927 MPa have been estimated for a 28 mm MoM bearing operating under 0.25 mm of microseparation [172]. Due to the limits of the machine and contact configuration a Maximum Hertzian Contact Pressure of 429.0 MPa was achievable. Figure 4.7 describes the testing conducted throughout the course of this thesis under static and tribometer scenarios.



Figure 4.7: Flow chart summarising the testing both in static conditions and in tribometer studies completed through the course of this thesis.

### 4.4 - Hip Simulation

As discussed in Chapter 3, custom designed machinery has long been used in an attempt to fully simulate the motion of the human hip, knee and spinal joints. These simulators can provide useful information on the tribological performance

of different prostheses and *in vitro* data can be used to benchmark one device against another to gain an idea on how it might perform *in vivo*.

Traditionally simulator studies articulate devices to several million cycles. One million cycles used to be thought to equate to one year of service *in vivo* [15]. This is no longer the case with some suggesting 10 million cycles could represent only 3.9 years service for active patients [173]. The mass loss of the components after articulation is measured to gain a measure of wear at the bearing surface. Different simulator designs can allow investigation of factors beyond prosthesis design, such as the effect of acetabular cup placement (inclination or version) or third body particulates present in the interface. Limited studies have investigated the tribocorrosion performance of devices within hip simulators to date [13, 14, 151, 153].

Two separate commercially available hip simulators, both supplied by Simulation Solutions (Stockport, UK), were utilised for different aspects of this thesis. A single-station ProSim Deep Flexion simulator was used for standard long-term testing. A more advanced ProSim Full-ISO Deep Flexion simulator was used for shorter term testing of adverse loading cycles.

Both simulators were instrumented with a three-electrode electrochemical cell to facilitate *in situ* monitoring of electrochemical degradation.

#### **4.4.1 - ProSim Pneumatic Deep Flexion Hip Simulator**

The ProSim Deep Flexion hip simulator (S/N: DFHS-003) is a pneumatically operated single-station biomechanical simulator, specifically designed for the purpose of long term wear testing of Total Hip Replacement components. The simulator approximates the motion of a human hip joint by controlling three axes of motion:

- Axial Load (6 kN)
- Flexion / Extension ( $\pm 60^\circ$ )

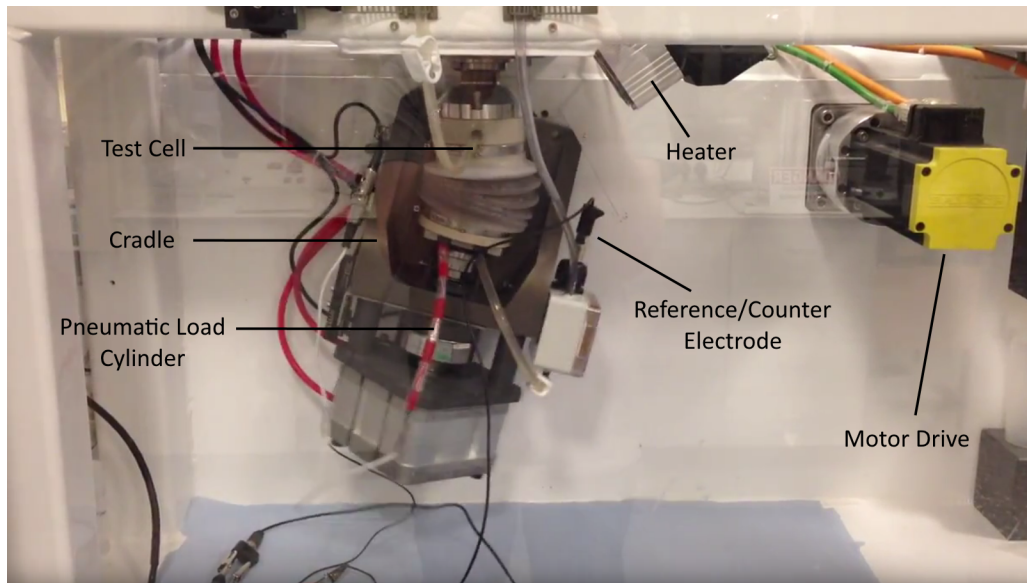


Figure 4.8: The ProSim Deep Flexion hip simulator test station.

- Internal / External Rotation ( $\pm 30^\circ$ )

The axial load is applied by means of a pneumatic load cylinder and the acetabular rotation and flexion / extension axes are electromechanically controlled by programmable motor drives. The drives are capable of replicating  $\pm 30^\circ$  acetabular rotation and  $\pm 60^\circ$  flexion / extension from the mid-position. The maximum possible load from the pneumatic cylinder is 6 kN with a resolution of 0.1 N.

Due to the nature of the pneumatics which applies the load during sliding, the actual load applied differed from the input demand profile. Load peaks measured through the simulator load cell typically lagged behind the demand profile, shown in Figure 4.9, and were of lower magnitudes.

The test station is shown in Figure 4.8 during a test which shows both the test cell and outer cradle. A heater above the station is used to heat the lubricant within the cell, and the temperature of the lubricant is monitored by means of a thermocouple running through the femoral head fixture.

The design of the test cell necessitates that the centre of rotation of the hip replacement bearing must match that of the simulator during sliding. If the bearing was

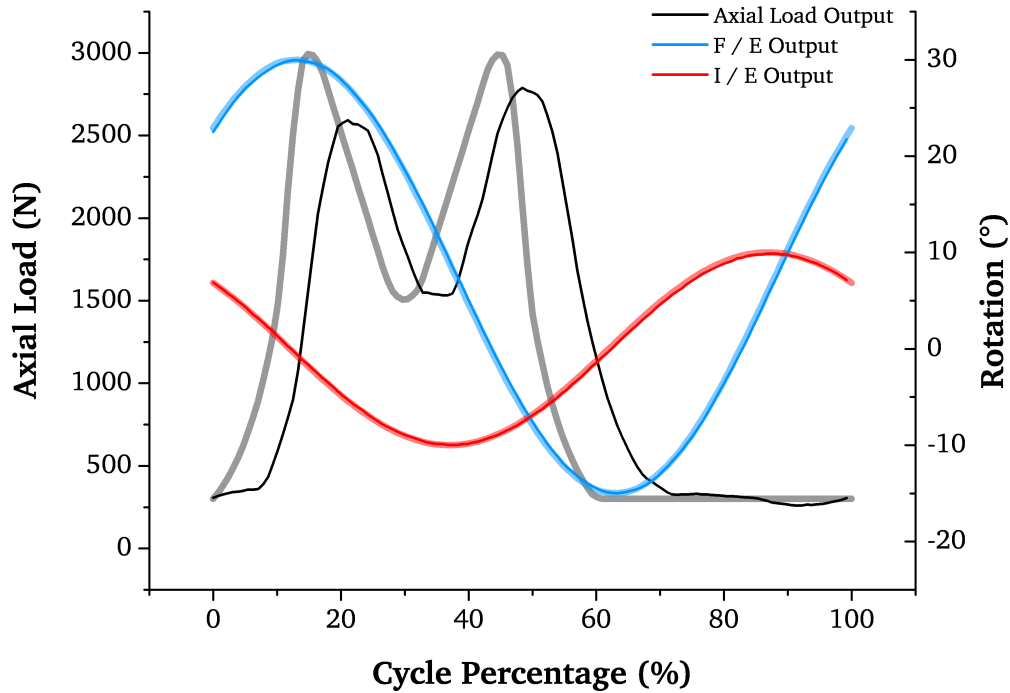


Figure 4.9: Demand vs. output curves for the standard twin-peak profile on the Deep Flexion simulator.

out of alignment the simulator may have applied irregular forces and articulation conditions to the components, meaning any test results may be non-representative of hip motion. The centre of rotation of the bearing was controlled by adjusting the position of the components relative to the fixtures. The femoral head and acetabular liner centres of rotation were required to be  $70 \pm 0.1$  mm and  $55 \pm 0.1$  mm respectively from the base of their respective fixtures. The height of the femoral head was controlled using different length spigots depending on how the head engaged on the modular taper.

#### 4.4.2 - ProSim Full-ISO Electromechanical Deep Flexion Simulator

The second simulator used was the ProSim Full-ISO Deep Flexion (HipSim, S/N: LLEH03-02) electromechanical simulator. An image of one of the stations of this simulator can be seen in Figure 4.10. The nature of full electromechanical control mitigated any delay or lag in applying axial load through pneumatics and gave

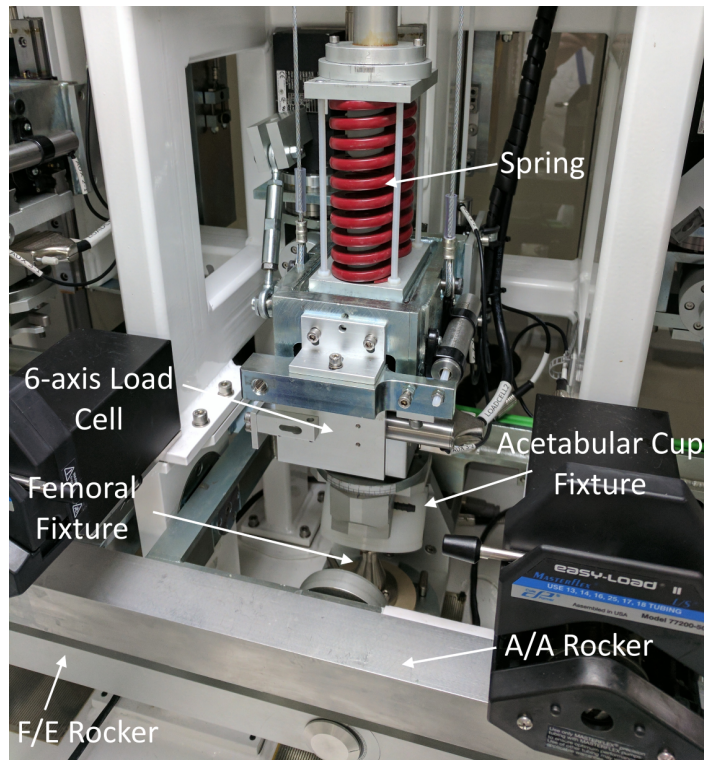


Figure 4.10: Pro-Sim Full-ISO Deep Flexion electromechanical adverse loading hip simulator

a much better agreement between the input of a given cycle to the actual forces measured, shown in Figure 4.11.

The Full-ISO simulator was capable of greater ranges of motion and also recreated the motion of the hip joint by controlling more axes than the pneumatic single-station. This allowed much more freedom in investigating adverse loading scenarios. Inclination and ante/retroversion of the acetabular cup could be easily varied and set. Coupled with the increased number of controlled axes, and the precision of that control, it was possible to investigate severe articulation conditions as well as loading cycles beyond the typical twin-peak ISO profile.

- Axial Load (8 kN)
- Flexion / Extension ( $\pm 61^\circ$ )
- Abduction / Adduction (+25, -10 $^\circ$ )

- Internal / External Rotation ( $\pm 40^\circ$ )
- Medial / Lateral Displacement ( $\pm 5$  mm, 1.5 kN)

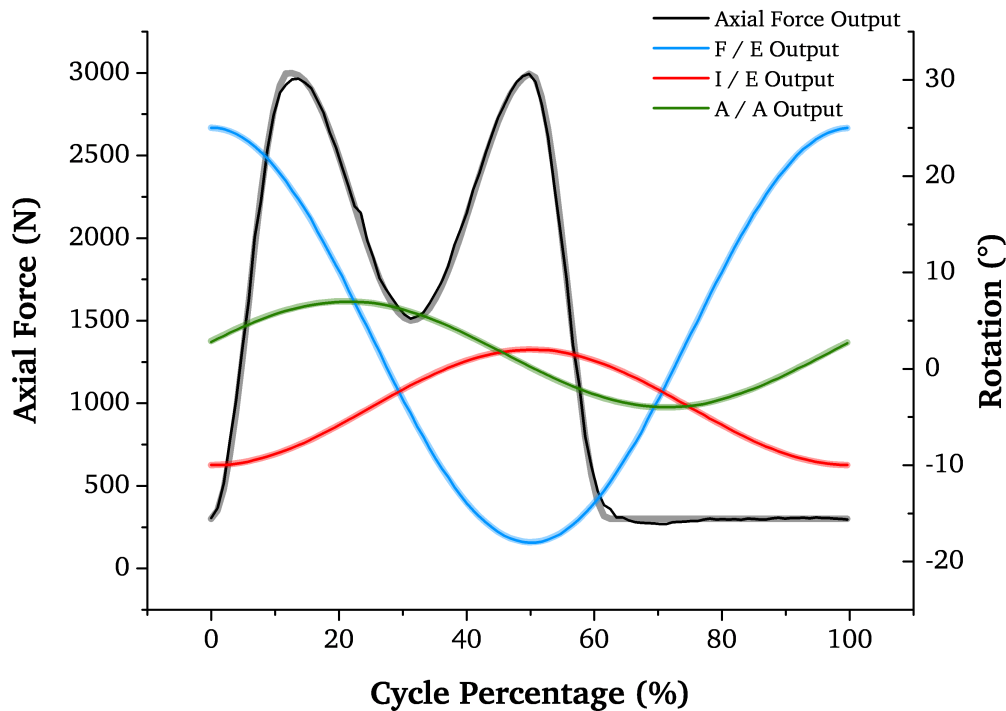


Figure 4.11: Demand vs. output curves for the ISO 14242-1 [166] cycle on the Full-ISO Deep Flexion electromechanical adverse loading simulator.

Fitted with a six-axis load cell it was also possible to investigate the frictional forces experienced during articulation as the torques produced around each axis of motion. All forces and positional displacements were sampled at 1,024 Hz and recorded along with the profile inputs by the simulator software.

Only the first station (Station 1) was instrumented for electrochemistry and all experiments performed on this simulator were conducted on this station, the results of which are presented in Chapter 8. An example of the simulator station can be seen in Figure 4.10.

#### 4.4.3 - Integration of Electrochemistry

The working electrode connection was made both through the acetabular cup fixture to the back of the liner or shell, and via the 316L Spigot to the femoral head.

During articulation it is assumed that the femoral head remains in contact with the acetabular liner, meaning the working electrode consists of the acetabular shell / liner and the femoral head, shown in Figure 4.12.

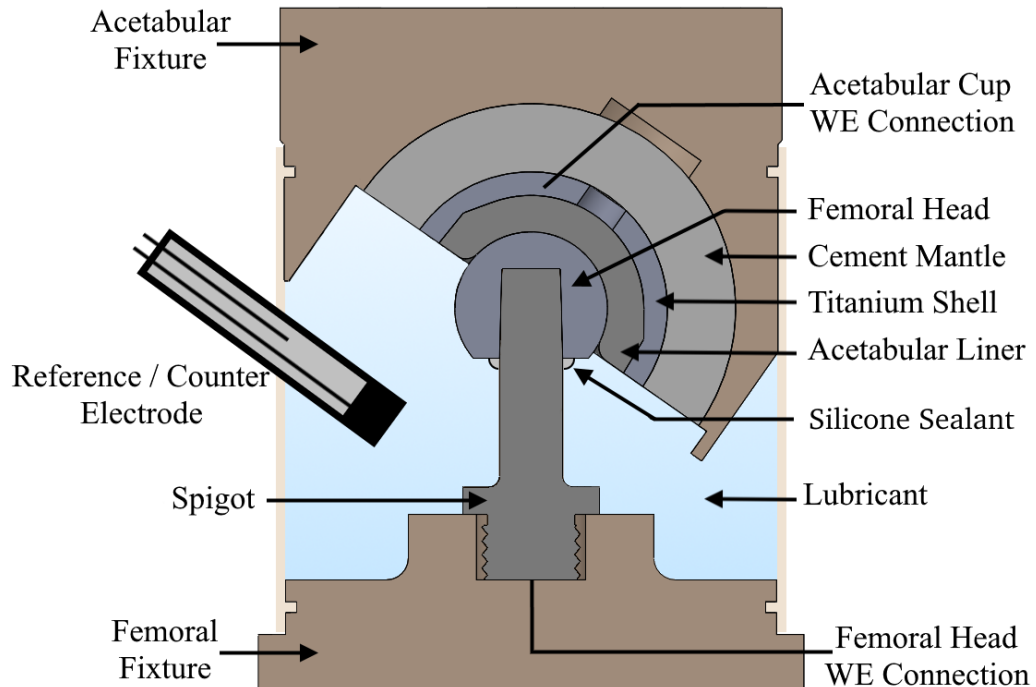


Figure 4.12: Schematic of the three-electrode test cell within the hip simulator station.

In the Pneumatic simulator the spigot was manufactured from Torlon 4203 high-strength compressive resin. For the Full-ISO simulator the spigot had to be manufactured from 316L medical grade stainless steel. Attempts to use the Torlon on this simulator resulted in rapid fracture of the spigot.

#### 4.4.4 - Test Methodology

##### 4.4.4.1 - Pneumatic Simulator

On the single-station ‘long-term’ tests were performed with a standard twin-peak loading profile which was derived in part reference to ISO 14242-1 [166]. The standard describes a twin-peak load input and sinusoidal inputs for the flexion / extension and rotation axes, similar to a Paul curve [174]. Figure 4.9 demonstrates the profile used. A peak load of 3,000 N with a swing-phase load of 300 N was

selected. The flexion / extension axis was set to +30° and -15° from the vertical mid-point and rotation was  $\pm 10^\circ$  from the mid-point.

The components were placed in the simulator and allowed to settle for at least two hours before the test was commenced. The bearings were tested under ‘Standard Gait’ and ‘Microseparation’ conditions. The microseparation was affected by applying a negative load during the swing phase, limited to 0.8 mm separation of the centres of rotation of each component. Every 333,000 cycles the test serum was changed and the station was flushed three times with deionised water. OCP was monitored throughout the course of the test and LPR scans were used to assess the corrosion rate of the system. Following testing the samples were removed from the apparatus and rinsed with deionised water before air drying.

#### **4.4.4.2 - Full-ISO Electromechanical Simulator**

The Full-ISO electromechanical simulator was used to perform ‘short-term’ tests to investigate electrochemical degradation across different malpositioning scenarios and loading profiles. The design of the simulator enabled the angle of acetabular inclination and version to be set independently of the loading cycle. Also having more axes of control and a greater degree of precision in that control enables the use of adverse loading profiles and daily living activities.

A 28 mm diameter MoM hip replacement was placed in the simulator and ‘short term’ electrochemical tests were performed over 4,000 cycles as described in Section 4.2.5 - Electrochemical Test Methods. A standard ISO 14242-1 profile [166] was used and the angle of acetabular inclination was increased from 30 - 50° in 5° increments. Retroversion was also increased from 0 - 20° in 5° increments during a separate series of tests.

Some daily living profiles were also investigated including a physiological loading profile, stair climbing and sitting in and getting out of a chair. These profiles are henceforth referred to as ‘Physiological Gait’, ‘Stair Climb’ and ‘Chair Up & Down’

and shown in Figure 4.13. These profiles were derived from data supplied by Bergmann *et al.* [173, 175, 176].

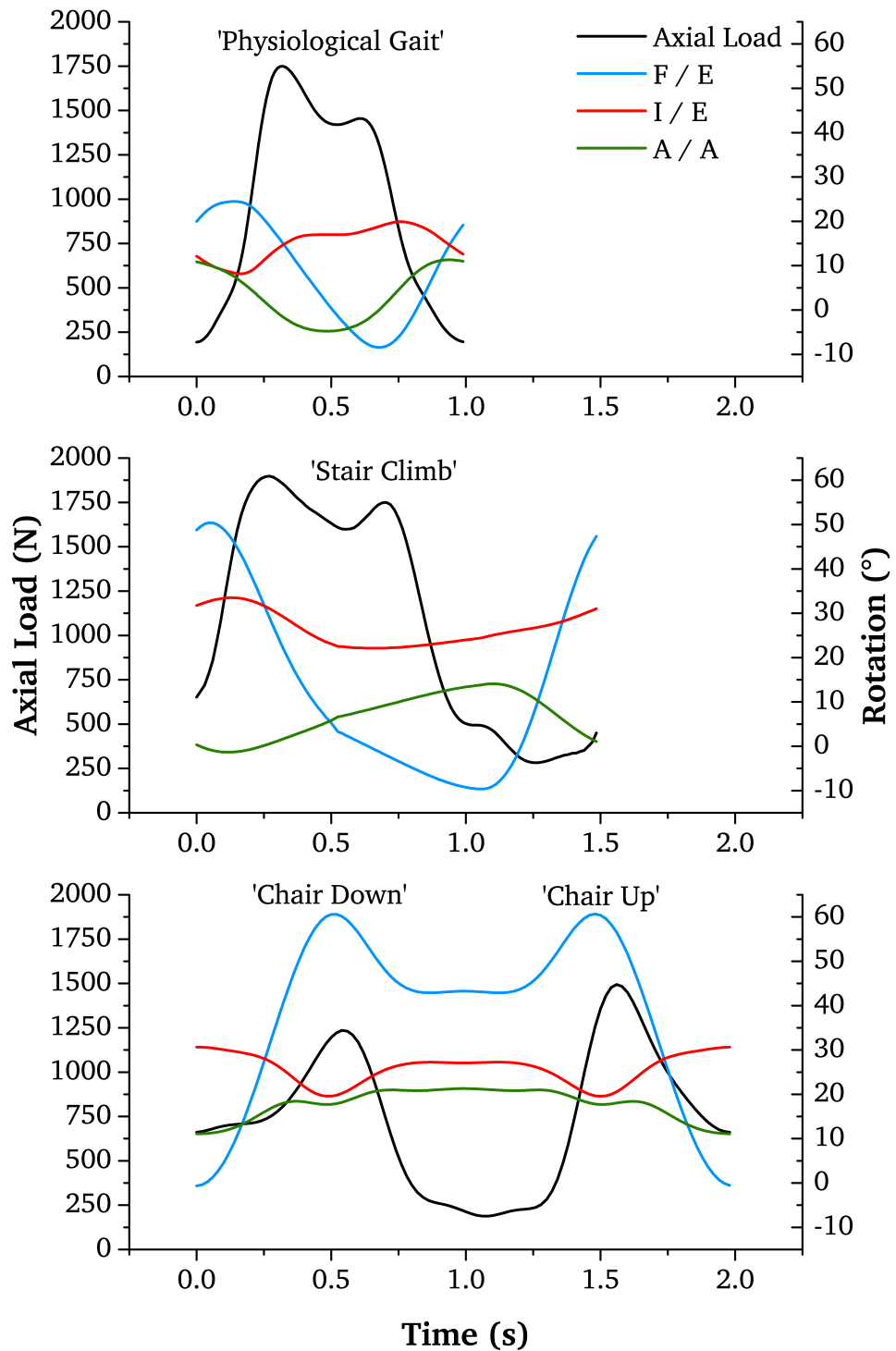


Figure 4.13: Axial Load and Rotational axes for Daily Living profiles derived from data provided by Bergmann *et al.* [173, 175].

Figure 4.14 describes the testing conducted throughout the course of this thesis under hip simulation.

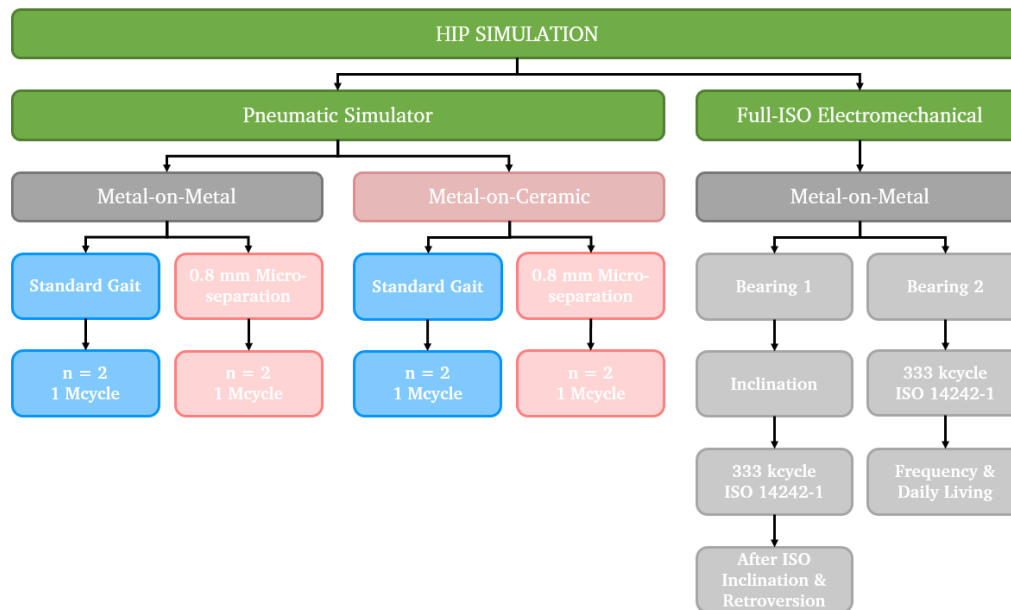


Figure 4.14: Flow chart summarising the testing completed across the two simulators through the course of this thesis.

## 4.5 - Surface Analysis

This section describes the various surface analysis techniques utilised to study test samples post-articulation.

### 4.5.1 - Coordinate Measuring Machine (CMM)

A Mitutoyo (Kanagawa, Japan) Legex 322 sub-micron Coordinate Measuring Machine (CMM) was used to map the surface of the bearings before and after experiments for analysis of the surface form profile. Features were added to the fixtures in order to zero the CMM and ensure the components were in the same orientation and rotation post-test. A ‘point’ mapping technique, illustrated in Figure 4.15, was used in order to minimise distance travelled by the probe.

The guaranteed accuracy of a trace on a CMM is dependant on the total distance travelled by the probe. Specifically for the Legex 322 this accuracy is governed by Equation 4.3. The greater distance travelled by the probe, the less accurate the data is towards the end of the scan with reference to the beginning. The spacing between points was therefore set to be no more than 0.5 mm on the horizontal

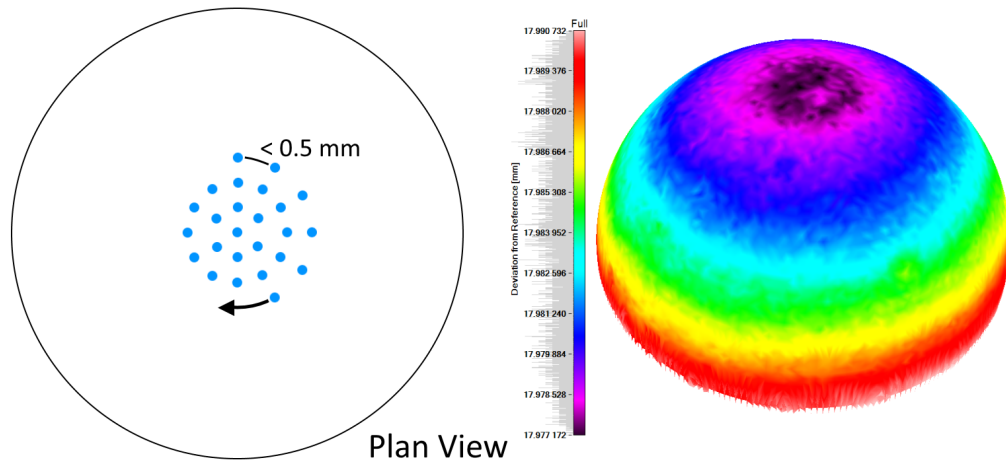


Figure 4.15: Illustration of 'point' CMM profile (left) and resultant RedLux Sphere Profile analysis of a 36 mm femoral head (right).

plane or any given arc. This was higher than the 1 mm resolution called for by ISO 14242-2 [177].

$$T = \left( \frac{0.8 + 0.2L}{100} \right) \quad (4.3)$$

Where:  $T$  = Length measurement tolerance ( $\mu\text{m}$ )

$L$  = Measuring length (mm)

The points on the surface were used to generate an XYZ coordinate cloud and this was imported into commercially available RedLux Sphere Profiler software (Southampton, UK). The surface map is then compared to a reference sphere of the same radius as the surface. Over specific areas of damage the deviation between the measured surface and the reference sphere was taken as an estimate of volume loss over that area.

#### 4.5.2 - White Light Interferometry (WLI)

A Bruker (Massachusetts, USA) NPflex White Light Interferometer was used to obtain three dimensional profile data from a surface. White Light Interferometry (WLI) uses the wave superposition principle; a schematic of the process is shown in Figure 4.16. White light from a source is passed through a beam splitter and reflects on both a reference mirror and the sample surface. The two beams are

then recombined and imaged using a camera. The phase difference between the two waves results in interference in the final signal, termed fringes. By varying the vertical height of the sample with a piezoelectric actuator these fringes can be used to map the surface [178].

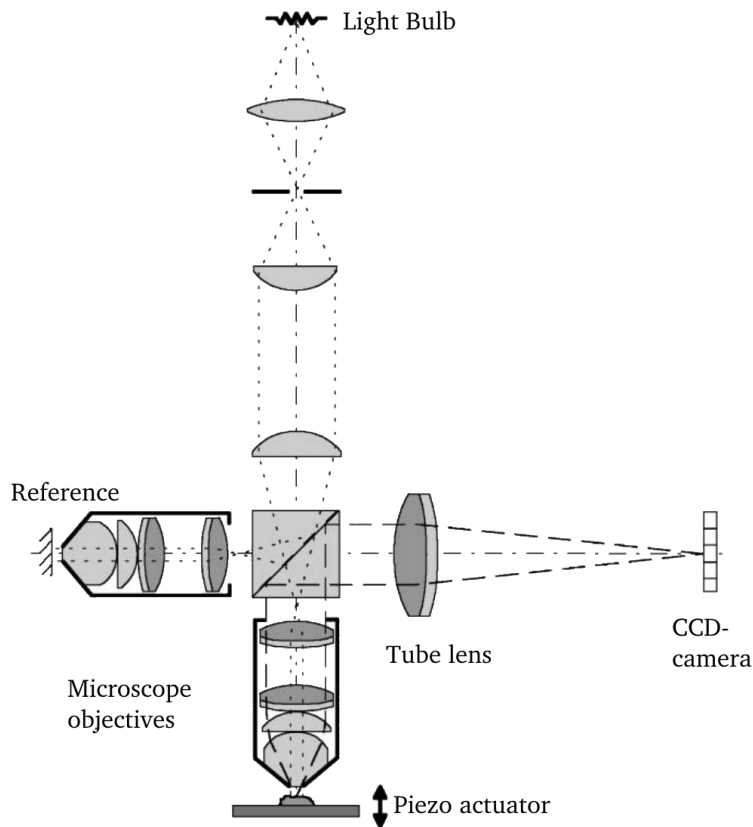


Figure 4.16: Schematic of White-Light Interferometry set-up [178]. Reproduced with permission (see Appendix 2).

Figure 4.17 shows an example scan of a wear scar on a CoCrMo plate following testing on the Biceri Reciprocating Tribometer. Software analysis techniques present in the NPflex operating software allowed the estimation of the volume of the wear scar and thus an estimation of the wear produced as a result of sliding. The WLI was also used to investigate the level of damage present on the bearing surfaces of components tested within the hip simulator.

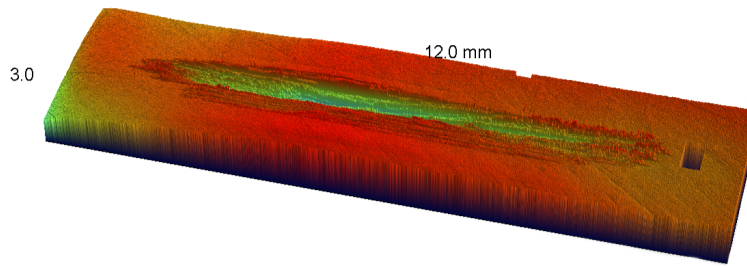


Figure 4.17: Example 3D WLI scan of a wear scar on a CoCrMo plate following testing in the Biceri tribometer.

### 4.5.3 - Scanning Electron Microscopy (SEM) and Energy Dispersive X-Ray Spectroscopy (EDX)

A Zeiss (Oberkochen, Germany) EVO MA15 Scanning Electron Microscope (SEM) was utilised in order to take extremely high magnification images of the sample surfaces. The SEM is equipped with both secondary electron and back-scatter electron detectors as well as an Oxford Instruments (Abingdon, UK) XMAX Energy Dispersive X-Ray (EDX) spectrometer to enable quantification of the elemental composition of the sample.

The EDX spectrometer fires a high-energy electron beam at the sample that excites inner shell electrons causing transition to a higher energy state and a move to the outer shell. This forms an ‘electron hole’ and results in a higher energy electron transitioning to a lower energy state and moving to the inner shell. This change in energy level causes the emission of a corresponding x-ray which can be used to describe the atomic structure of the element in question. As the structure of each element is unique the EDX can produce a spectrum highlighting the elemental composition of the area in question.

### 4.5.4 - Transmission Electron Microscopy (TEM)

An FEI (Oregon, USA) Tecnai F20 Field Emission Gun Transmission Electron Microscope (FEGTEM), fitted with an Oxford Instruments (Abingdon, UK) XMAX EDX, was used to examine changes in the sub-surface micro structure of CoCr al-

loys as a result of sliding. A TEM works via passing a beam of electrons through an extremely thin sample. This electron beam interacts with the atoms present in the ‘slide’ specimen and an image is formed and magnified. As a result a TEM is capable of much higher resolutions than an optical microscope.

TEMs are also capable of a technique known as Selective Area Electron Diffraction (SAED). As electrons pass through the crystal lattice of atoms present in the ‘slide’ they are diffracted due to the ‘de Broglie’ wavelength of electrons ( $\approx 2.5$  pm at 200 kV) being much smaller than the lattice structure [179]. A particular crystal structure will result in particular angles of diffraction for some electrons. This enables investigation of the atomic structure at a particular site on the sample ‘slide’.

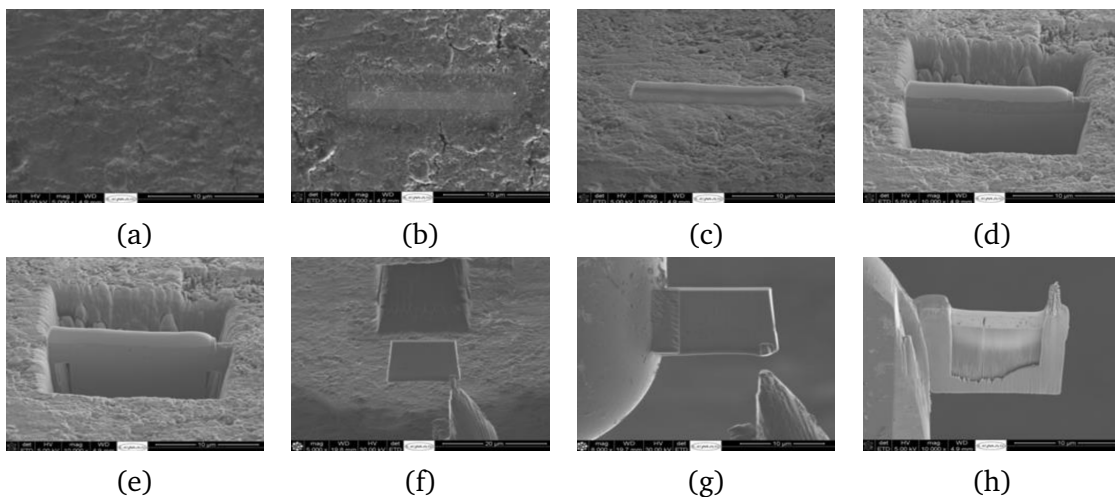


Figure 4.18: Preparation of TEM slide using FIB SEM [180]: (a) sample surface, (b & c) deposition of protective *Pt* layer, (d & e) surface milled with *Ga* ion beam to form slide, (f & g) slide removed and attached to a *Cu* post and (h) final thinning of slide to approximately 10 nm thickness.

An FEI Nova 200 Nanolab dual beam SEM/Focused Ion Beam (FIB) microscope was used to prepare the ‘slide’ samples. The process is shown in Figure 4.18 [180]. First two platinum layers were deposited on the surface (b & c) in order to protect the immediate subsurface from damage. A gallium ion beam ( $Ga^+$ ) at 30 kV was then used to mill away sections on either side of the deposited Pt layer (d & e) to an approximate depth of  $10 \mu\text{m}$ . The formed ‘slide’ was then removed from the

sample using a Kleindiek Nanotechnik (Reutlingen, Germany) Micromanipulator (f) and attached to a copper post (g). The centre of the sample was then further thinned using the ( $Ga^+$ ) beam at 5 kV to approximately 10 nm thick (h).

Images produced by the TEM were then analysed using DigitalMicrograph® software (Gatan, USA). This enabled measurement of features visible on the slides. Depth of the nano-crystalline layer was assessed using a simple line tool. The approximate size of crystallites within the nano-crystalline layers was assessed by taking the dimensions of bright spots within the dark field images [150]. These corresponded to crystals orientated to give 'Bragg' diffraction, and the width and height of these spots gave crystal size.

## Chapter 5 - Static & Tribometer Studies

One of the key features of Adverse Loading scenarios in Hard-on-Hard hip replacements is an increased contact pressure at the interface when compared to normal sliding. Several studies have modelled the contact under increased inclination and microseparation conditions [172, 181–185]. As early as 2002 Mak *et al.* [181] modelled an increase in maximum contact pressures from approximately 80 to over 800 MPa as a result of adding a 250  $\mu\text{m}$  microseparation to a 28 mm diameter Ceramic-on-Ceramic bearing. Soriali *et al.* [183] modelled a smaller increase for a 32 mm Ceramic-on-Ceramic bearing to over 200 MPa under 500  $\mu\text{m}$  microseparation. Wang *et al.* [172, 184] modelled Metal-on-Metal bearings and also noted increases in maximum contact pressure from approximately 200 to over 900 MPa as a result of microseparation on a 28 mm bearing.

This chapter primarily details the results of varying the applied load, and thus maximum contact pressure, in a simple configuration reciprocating pin-on-plate tribometer in order to investigate the effect on the tribocorrosion of a metal-on-metal contact. Different lubricant compositions were also investigated by means of a static electrochemical test cell.

### 5.1 - Static Corrosion

The initial studies by Hesketh *et al.* [14, 15, 162] investigating the tribocorrosion of THRs used 17 g/L FBS and PBS. This was still the standard at the time and enabled comparison to the majority of the literature. Few studies have examined the effect of change in protein concentration on the electrochemistry of *CoCrMo* alloy, although some suggest it can have a dramatic effect on the corrosive degradation [186, 187]. The test cell and methodology described in Section 4.2.4 was used to assess the static corrosive behaviour of *CoCrMo* alloy. FBS was diluted to 17 and 30 g/L total protein concentrations with PBS. The addition of 0.03%

(w/v) sodium azide to retard bacterial growth was also investigated. The results were compared to pure PBS and actual bovine synovial fluid. All serum and synovial fluid samples were provided by Sera Laboratories International (UK). Three repeats in each electrolyte were performed and the open circuit potential over the first hour of stabilisation can be seen in Figure 5.1.

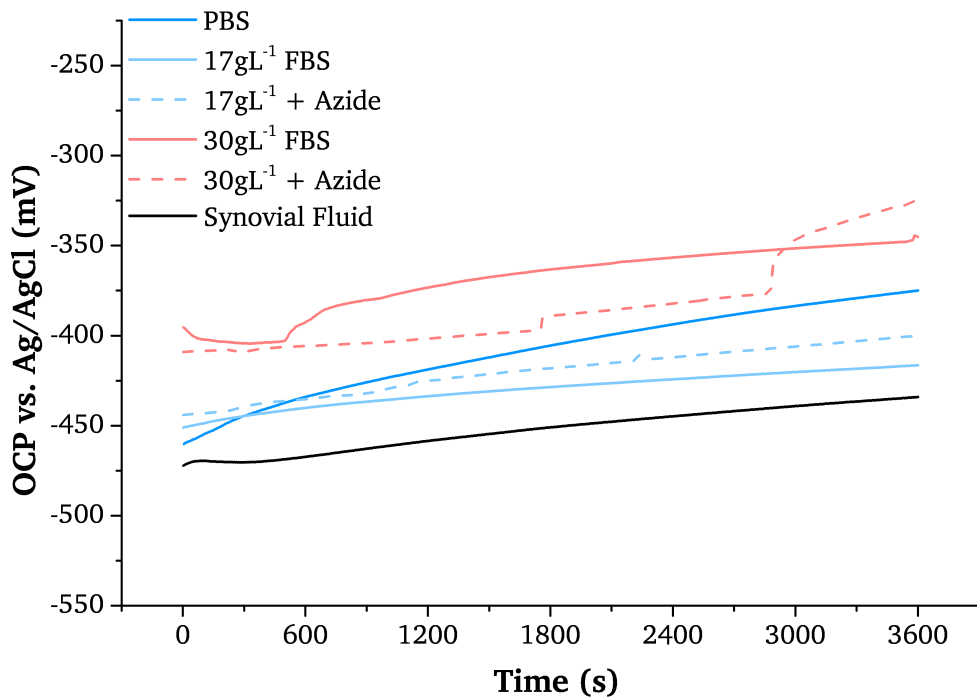


Figure 5.1: Average Open Circuit Potential (OCP) plot for HC CoCrMo alloy allowed to stabilise in different physiological electrolytes for one hour.

All samples started at an initial OCP of between approximately -400 and -475 mV and gradually ennobled to a similar extent over the hour of stabilisation. This was typical behaviour for passive samples in the presence of an electrolyte. Generally values for OCP were noted to be lower at 17 g/L when compared to 30 g/L. Despite this the PBS samples, without any protein content, were similar to both protein concentrations. The bovine synovial fluid displayed the lowest values of OCP amongst the lubricants. The addition of sodium azide appeared to have minimal effect on the OCP at both concentrations, displaying similar values to the non-azide samples during stabilisation. The OCP is only a qualitative assessment however, and whilst different trends can be observed, further electrochemical methods are needed to quantify any differences.

Typical examples of the potentiodynamic (PDS) and cyclic polarisation (CP) scans can be seen in Figure 5.2. All lubricants containing protein, including the synovial fluid, displayed similar results. An extended passive phase was noted up until the breakdown potential was reached at approximately +500 mV vs. *Ag/AgCl* with a rapid onset of current. The pure PBS electrolytes displayed a shoulder in the transpassive region at approximately +740 mV vs. *Ag/AgCl* that was not present for the other samples. This behaviour has been noted previously for *CoCrMo* alloys and may be related to the oxidation of  $Cr^{3+}$  to  $Cr^{6+}$  [188, 189]. This resulted in a higher potential required to generate a current density of 500 mA/cm<sup>2</sup>. Upon the return scan, Cyclic Polarisation (CP) portion of the curve, all samples displayed negative hysteresis, meaning the alloy had no propensity to form pits or localised corrosion in that electrolyte and immediately re-passivated [31].

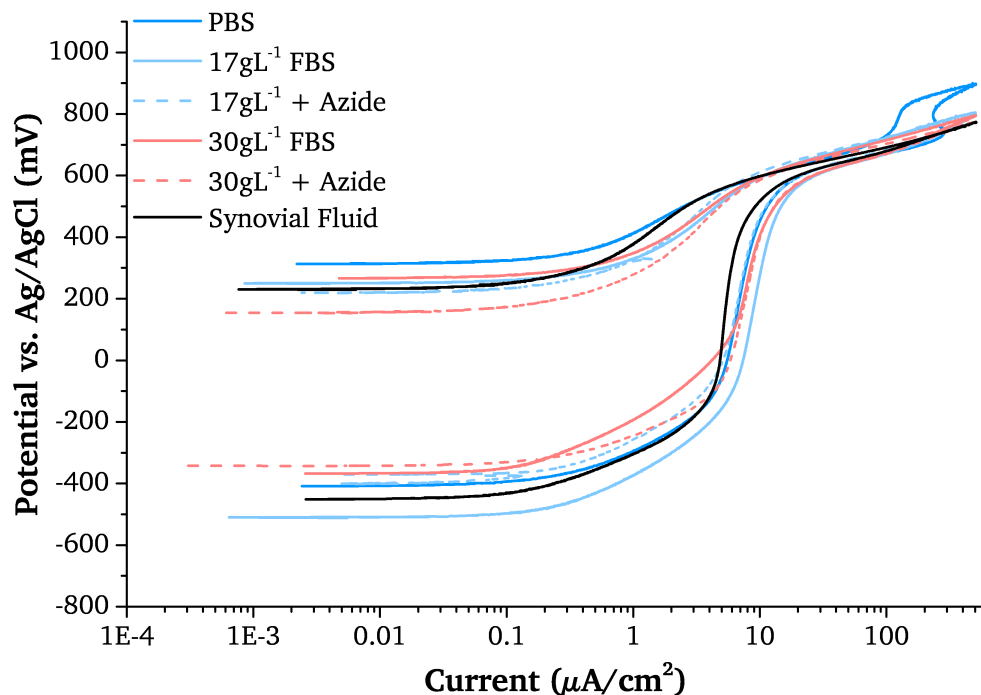


Figure 5.2: Potentiodynamic Scanning curves for HC CoCrMo plates in different physiological electrolytes

From the PDS scans the breakdown potential was determined at the point of rapid onset of current for each electrolyte, and can be seen in Figure 5.3. This point was taken as when the gradient of the curve, i.e. the rate of change in current, was greater than 1  $\mu\text{A}/\text{mV}$ .

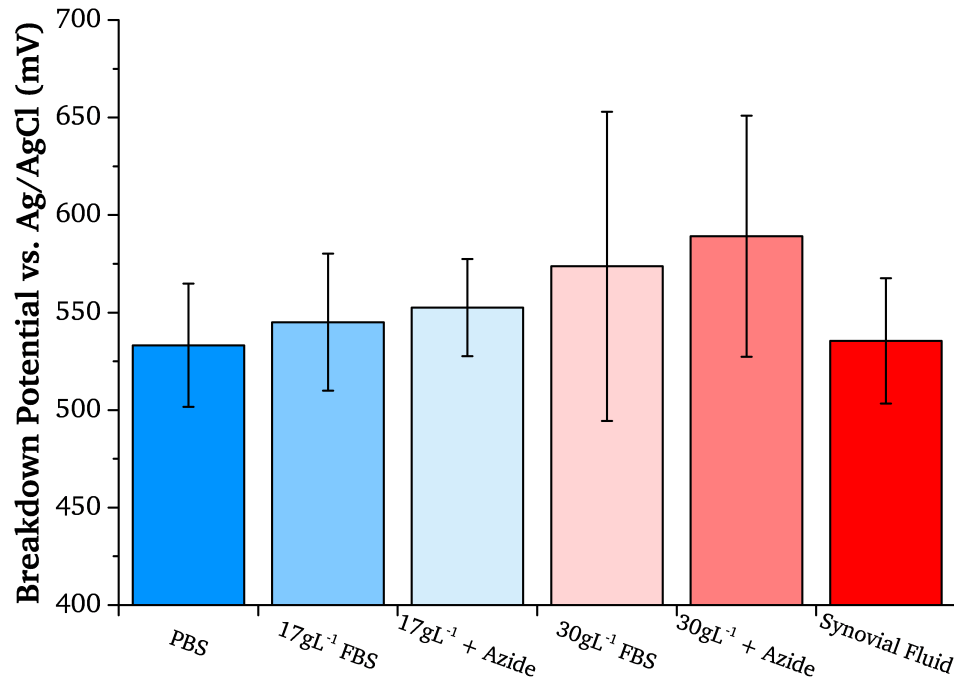


Figure 5.3: Mean breakdown potential for HC CoCrMo in different physiological electrolytes. Error bars represent standard deviation,  $n = 3$ .

No significant differences were noted between any electrolyte (ANOVA,  $p < 0.05$ ) although the average breakdown potential increased with the addition of azide and moving from 17 to 30 g/L. The synovial fluid samples displayed the lowest breakdown potential of all electrolytes. No significant difference in the static corrosion behaviour of *CoCrMo* alloy was noted across the different protein concentrations or with the addition of sodium azide. Therefore in order to enable easy comparison to previous work and the literature a lubricant concentration of 17 g/L with 0.03% (w/v) sodium azide was selected.

## 5.2 - Tribometer

This section details the results and analysis for all tests performed in a simple configuration pin-on-plate reciprocating tribometer couple in order to examine the role of increased contact pressure on corrosive material loss.

## 5.2.1 - Contact Pressures

The Biceri Reciprocating tribometer discussed in Chapter 4 was used for all sliding tests performed in this chapter. A loading arm applied the normal load through the pin and thus the contact pressure was varied by applying more weight to the arm. As per the qualification previously set by Hesketh [150] an initial mean Contact Pressure ( $P_{mean}$ ) of approximately 210 MPa was used by hanging 5.0 kg from the arm. The contact pressure was calculated using Hertzian point contact theory (Equation 2.1) described in Chapter 2. This hanging weight was then increased in 2.5 kg increments up to 12.5 kg which represented the limit of the machine. Thus the initial Maximum Contact Pressure was increased to a maximum of 429.0 MPa as shown in Table 5.1. The pins and plates were subjected to sliding under the short-term testing profile described in Section 4.2.5. The couples were placed in the tribometer and three static linear polarisation resistance scans (LPR,  $\pm 25$  mV @ 1 mV/s) were taken over an hour of settle time and during 4,000 cycles of sliding.

Hanging Weight (kg)	Contact Load $W$ (N)	Contact Half-width $a$ (mm)	Contact Area (mm <sup>2</sup> )	Maximum Contact Pressure $P_{max}$ (MPa)	Mean Contact Pressure $P_{mean}$ (MPa)
5.0	122.6	0.43	0.58	316.1	210.7
7.5	183.9	0.49	0.75	361.9	241.3
10.0	245.3	0.54	0.92	398.3	265.5
12.5	306.6	0.58	1.06	429.0	286.0

Table 5.1: Initial contact conditions for metal-on-metal pin-on-plate sliding tribometer couples with 100 mm radius domed pin and different hanging weights.

## 5.2.2 - Electrochemistry

Example LPR scans taken over a single experiment can be seen in Figure 5.4. The scans were taken both under static and sliding conditions. The static scans demonstrated a typically seen cathodic tail due to the rapid application of -25 mV (vs. OCP) overpotential at the start of the scan.

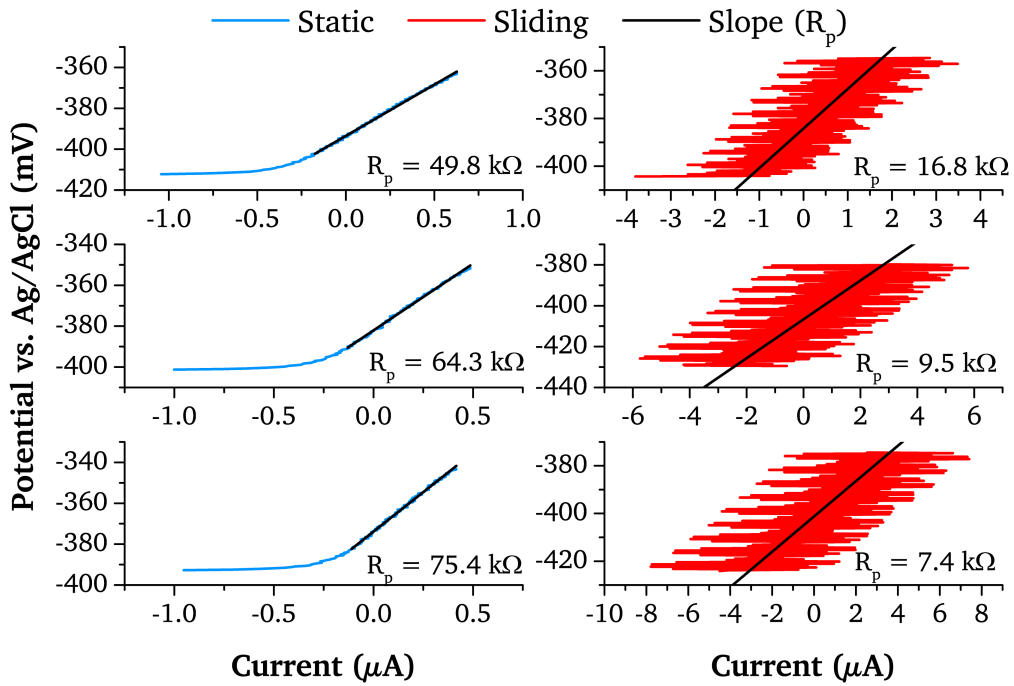


Figure 5.4: Three static (left) and three sliding (right) Linear Polarisation Resistance scans ( $\pm 25$  mV @ 1 mV/s) showing Polarisation Resistance ( $R_p$ ) fit and values.

Under sliding, LPR traces were typically noisier than under static conditions due to the transient depassivation processes within the contact. Figure 5.4 also demonstrates how the LPR curves were fitted throughout this thesis in order to determine the Polarisation Resistance ( $R_p$ ). The values obtained for  $R_p$  were then converted into a corrosion current ( $I_{corr}$ ) using the Stern-Geary equation (Equation 2.17) and standard Tafel constants of 120 mV/decade; as described in Section 4.2.2.

Figure 5.5 shows the average Polarisation Resistance determined across static and sliding conditions for increased hanging weight and contact pressure. Data from one experiment performed at 7.5 kg hanging weight was discarded as the LPR scans were not linear and was thought to have been caused by a problem with the combination electrode used. As expected the resistance to polarisation was much higher under static conditions with mean  $R_p$  values ranging from approximately 60 - 95 k $\Omega$ . Despite the wide spread in  $R_p$  values no significant difference was found between static conditions. Although efforts were taken to ensure the plates were polished and passivated to generate uniform samples, this variable in static

$R_p$  was attributed to slight differences in the passive oxide films.

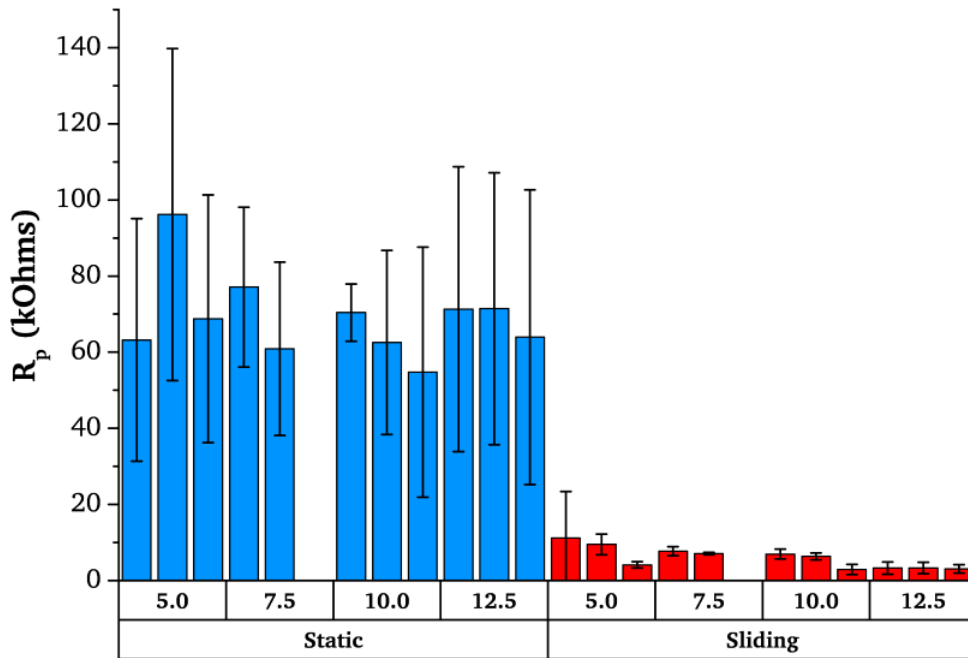


Figure 5.5: Polarisation Resistance ( $R_p$ ) for Metal-on-Metal tribometer contacts under different applied weights for static and sliding conditions. Error bars represent standard deviation between three LPR scans. Three repeats taken at each weight ( $n = 3$ ).

Upon sliding much lower values for  $R_p$  were recorded, varying between approximately 7 to 11 k $\Omega$  at 5.0 and 7.5 kg and as low as 3 k $\Omega$  at 12.5 kg. This was probably due to exposure of the bulk alloy to the electrolyte after disruption of the passive oxide through sliding, accelerating corrosion. A trend of decreased  $R_p$  was noted with increased hanging weight, which suggested higher levels of corrosive material loss with increased contact pressure.

Figure 5.6 shows the average calculated corrosion current  $I_{corr}$  for increased hanging weight and contact pressure, determined from the  $R_p$  values and the Stern-Geary equation. Under static conditions the high values for  $R_p$  converted to lower average corrosion currents across all hanging weights. The current values ranged between approximately 0.3 - 0.5  $\mu A$ . Upon sliding the determined corrosion current was much higher, ranging from approximately 2.6 to 3.7  $\mu A$  at 5.0 and 7.5 kg. At higher weights the determined current increased to between approximately

8.0 and 9.1  $\mu\text{A}$ .

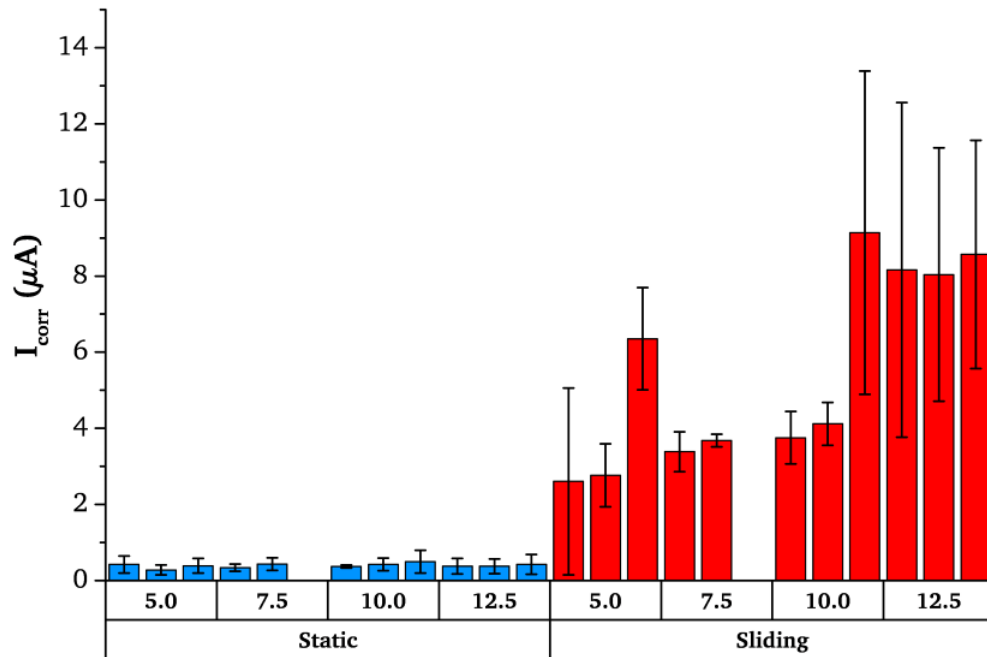


Figure 5.6: Corrosion Current ( $I_{corr}$ ) for Metal-on-Metal tribometer contacts under different applied weights for static and sliding conditions. Error bars represent standard deviation between three LPR scans. Three repeats taken at each weight ( $n = 3$ ).

A further average of  $I_{corr}$  was then taken for all experiments performed at given hanging weights which can be seen in Figure 5.7. The static corrosion currents averaged for each hanging weight condition ranged from approximately 0.36 - 0.43  $\mu\text{A}$ . Under sliding for 5.0 and 7.5 kg hanging weights respectively the average  $I_{corr}$  was approximately 3.9 and 3.5  $\mu\text{A}$ . At 10.0 and 12.5 kg this increased to approximately 5.7 and 8.3  $\mu\text{A}$  respectively. The increase at 12.5 kg was found to be significantly different (ANOVA, Tukey HSD,  $p < 0.05$ ) from 5.0 and 7.5 kg. This reinforced the trend noted in the  $R_p$  data of increased corrosive degradation at higher contact pressures.

### 5.2.3 - White Light Interferometry (WLI)

After testing, the plates were analysed using WLI in order to examine the surface wear scars. Figure 5.8 shows typical images for wear scars for each hanging

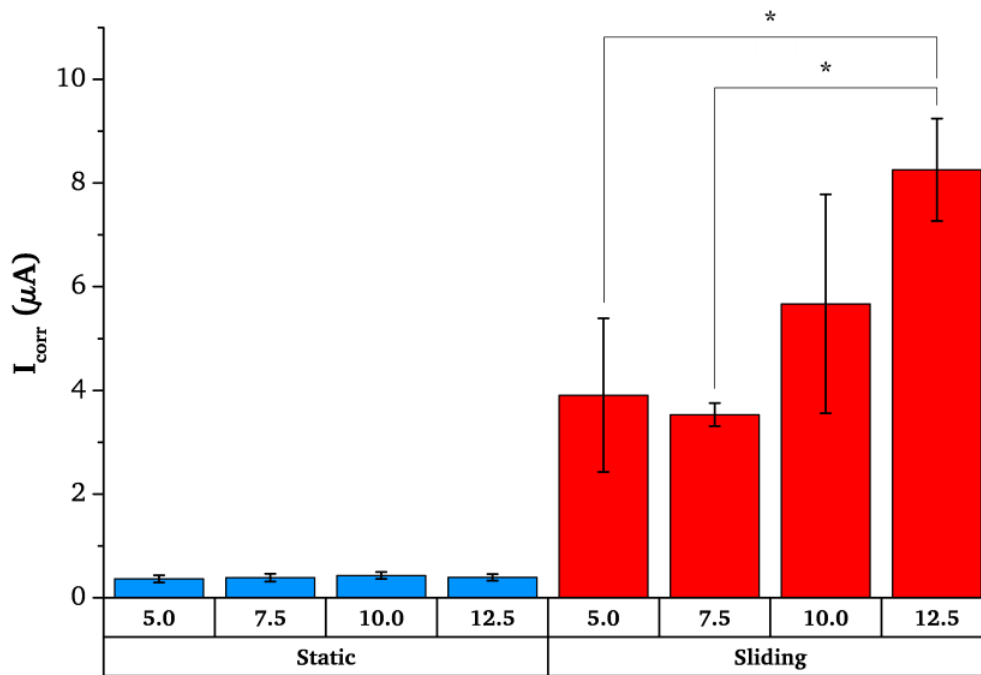


Figure 5.7: Average Corrosion Current ( $I_{corr}$ ) for Metal-on-Metal tribometer contacts combined from three repeats under different applied weights for static and sliding conditions. Significant difference (ANOVA, Tukey HSD,  $p < 0.05$ ) shown and error bars represent standard deviation.

weight condition. As can be seen with increased hanging weight, and thus increased contact area and pressure, the area of wear scars as a result of sliding increased. Moving from 5.0 to 12.5 kg the average wear scar width increased from approximately 1.0 to 2.8 mm. This was a greater increase than the initial predicted contact half-width, derived from Hertz point contact theory, which increased from 0.43 to 0.58 mm. With a greater contact area more asperities are likely to come into contact and equally are more likely to shear and depassivate, resulting in higher corrosion currents. Over time during sliding this results in a wider wear scar.

When compared to the average measured corrosion current ( $I_{corr}$ ) over the course of sliding, the increase in measured wear scar width appeared to increase proportionally along with  $I_{corr}$ . Figure 5.9 shows this relationship although this did not appear to hold at 7.5 kg. The measured wear scar width at this hanging weight appeared disproportionately higher with a lower  $I_{corr}$ . This may have been due to

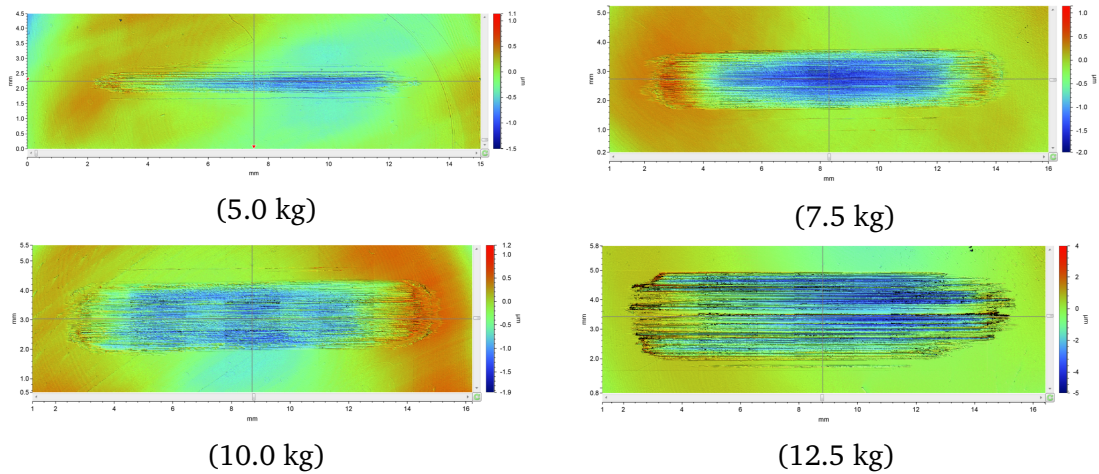


Figure 5.8: 2D NPFlex White Light Interferometry scans of the plate wear scars after 4,000 cycles of reciprocating tribometer testing under different loads and contact conditions.

only two repeats performed at 7.5 kg due to discarded electrochemical data.

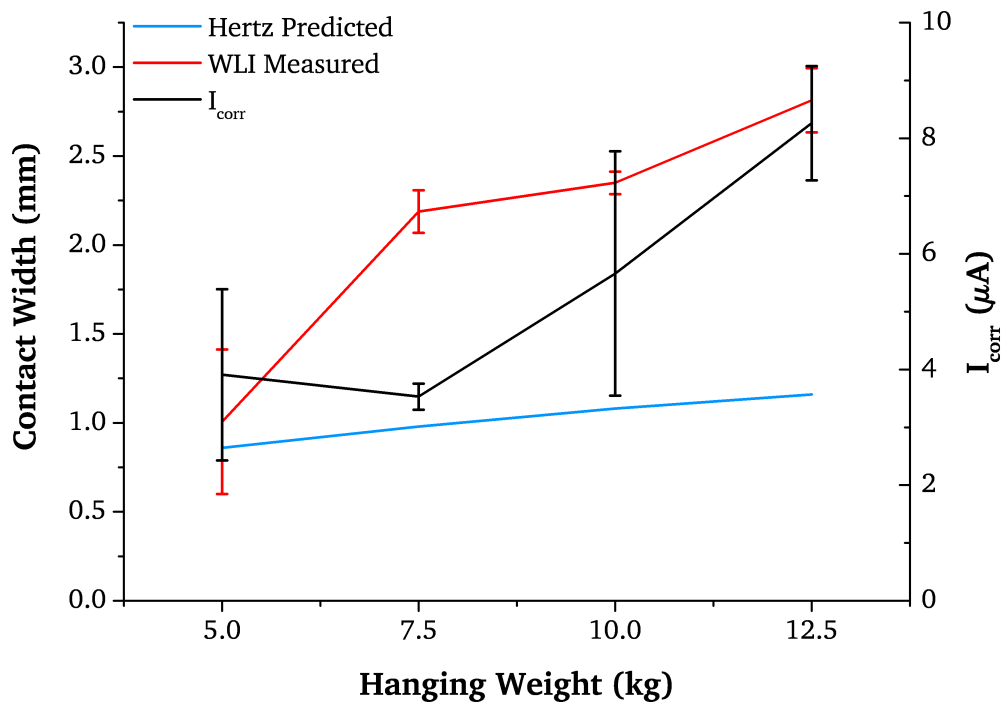


Figure 5.9: Initial Hertz point contact width, measured wear scar width and average corrosion current during sliding ( $I_{corr}$ ) for metal-on-metal pin-on-plate reciprocating tribometer testing with varying hanging weight. Error bars represent standard deviation.

A measurement of the surface roughness ( $S_a$ ) within the wear scar and an estimate of the volumetric material loss as a result of sliding was also found through WLI analysis. Figure 5.10 shows a trend of increased roughness and wear with

increased hanging weight. Moving from 5.0 to 12.5 kg the ( $S_a$ ) increased from an approximate average of 315 to 657 nm. The WLI estimated wear volume also increased from 0.015 to 0.044 mm<sup>3</sup>. Both values were noted to increase linearly with the measure wear scar width and average corrosion current demonstrated in Figure 5.9. No significant difference was found between the means of all groups for surface roughness ( $S_a$ , ANOVA,  $p < 0.05$ ). For wear volume however, wear at 12.5 kg was found to be significantly higher than at 5.0 and 10.0 kg (ANOVA, Tukey HSD,  $p < 0.05$ ).

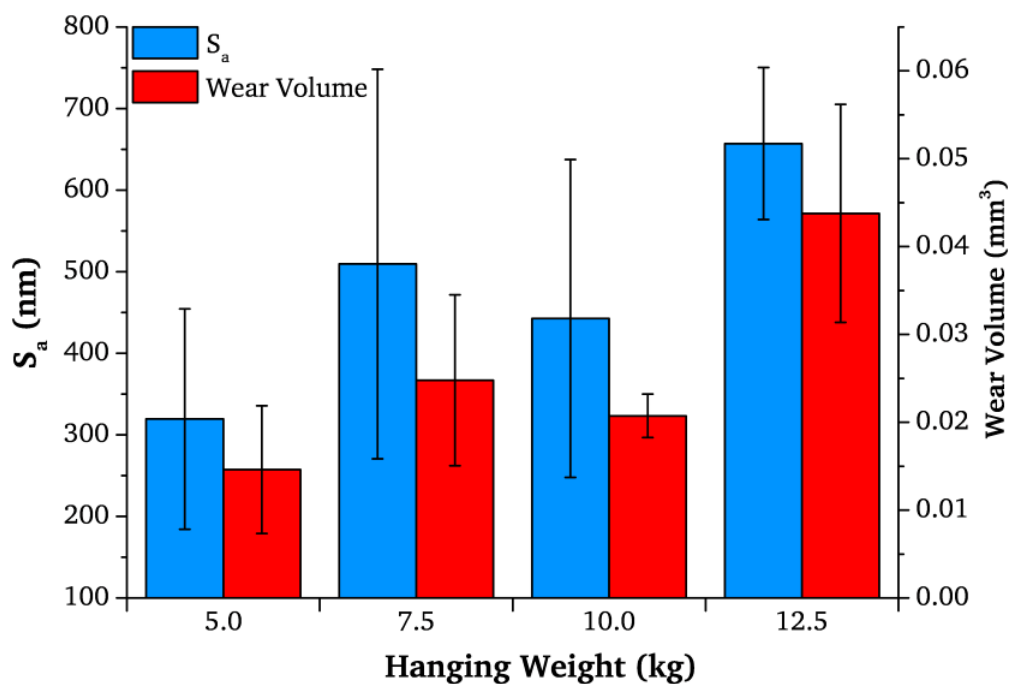


Figure 5.10: WLI determined surface roughness within the wear scar ( $S_a$ ) and estimated wear volume from simple configuration metal-on-metal pin-on-plate reciprocating tribometer testing with varying hanging weights. Error bars represent standard deviation.

### 5.3 - Summary

- Increasing contact pressure in a simple configuration metal-on-metal pin-on-plate reciprocating tribometer was coupled with an increase in measured corrosion current during sliding.
- In this configuration the contact pressures achieved were limited by the pin's

dome radius and capability of the tribometer.

- Due to the domed radius and relatively low contact pressures the surfaces tended to roughen rather than present a clear wear depth.
- A trend of increasing surface roughness and estimated wear volume was noted with increasing contact pressure.

The results of the tribometer testing demonstrated that increasing the contact pressure of a sliding contact can effect the corrosion. In the tribometer this increase was likely due to an increase in the contact half width, as described by Hertz point contact theory. The area of surface depassivated therefore increased due to more asperity-asperity contact and thus more wear over the larger contact area during sliding. The sliding contact for the metal-on-metal hip replacements is very different however and adverse loading conditions can effect this in different ways. Also multi-direction motion is required to accurately replicate clinically wear rates, typically for MoP couples [62]. This was not possible to on the tribometer used in this study.

## Chapter 6 - Hip Simulation (Metal-on-Metal)

Although the use of Total Hip Replacements with Metal-on-Metal bearings has taken a rapid decline over the last decade, there are thousands of patients with implanted devices and their degradation mechanisms are still not well understood. In the UK 1,096 MoM primary hip replacement operations were performed in 2014 [16] and 783 were performed in 2015 [17]. Whilst this only accounts for approximately 1 % of the total operations performed each year, MoM devices are still being implanted in patients. The majority of devices implanted were large diameter (46-54+ mm) resurfacing implants. The most popular size in the low diameter traditional THR range was 28 mm, accounting for around 11 % of MoM prostheses that year [16].

This chapter presents the results of 28 mm High Carbon (HC) Cobalt Chromium Molybdenum (CoCrMo) THRs. The devices were tested under different articulation conditions in the Deep Flexion Hip Simulator and a three-electrode electrochemical cell was used to assess the corrosive degradation during sliding.

### 6.1 - Standard Gait

As described in Chapters 3 & 4, hip simulator studies use a twin-peak profile to mimic the articulation of a bearing during a normal walking cycle. MoM bearings of 28 mm diameter were tested under a walking cycle, henceforth referred to as 'Standard Gait'. The profile consisted of +30° -15° Flexion / Extension,  $\pm 10^\circ$  Internal / External Rotation, and peak and swing phase loads of 3 kN and 300 N respectively (Figure 4.9). The bearings were tested to one million cycles during which time the Open Circuit Potential (OCP) was monitored and the Resistance to Polarisation ( $R_p$ ) was determined every 10,000 cycles, as described in Chapter 4. Periodically the samples were also potentiostatically polarised to +50 mV vs. OCP and the resultant anodic current sampled at 100 Hz.

### 6.1.1 - Open Circuit Potential

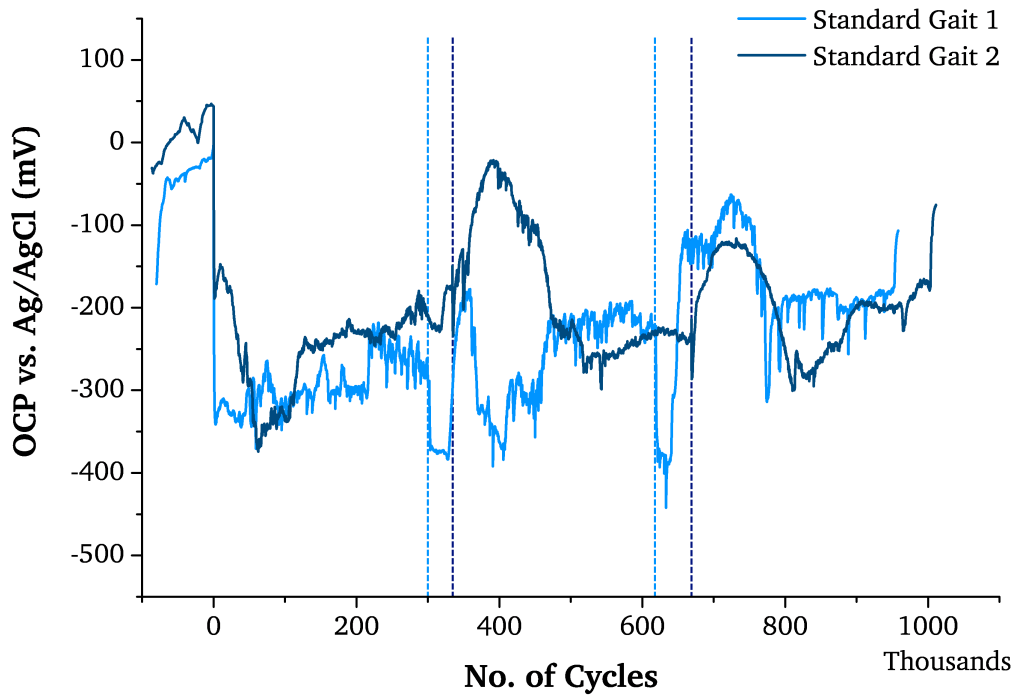


Figure 6.1: Open Circuit Potential for 28 mm MoM bearings under Standard Gait articulation over 1 million cycles. Vertical dashed lines represent serum changes.

The OCP gives a qualitative assessment of the reactions taking place on the exposed surface of the Working Electrode. Figure 6.1 presents the OCP data for the bearings articulated under standard gait. Over an initial static settle period, the OCP for the MoM devices gradually became more noble with one bearing reaching an OCP of approximately -20 mV and the second +50 mV. Upon the initiation of sliding both bearings displayed a cathodic shift to between -340 and -370 mV. In one case this was a near instant drop, whilst the second bearing initially dropped to around -200 mV before recovering slightly and then continuing to shift cathodically over the first 100,000 cycles. Cathodic shifts are typical upon sliding of metallic materials and have been observed both in tribometer and hip simulator studies [11, 14, 15, 139, 190]. These shifts are indicative of an increase in corrosive material loss as a result of depassivation of an area of the surface. This depassivated area becomes a net anode, and the remaining surface which is of a much larger area becomes a net cathode.

During sliding the OCP for both bearings was observed to shift in the noble direction. Upon serum changes at around 333k and 666k cycles a brief interruption to this trend was noted for both bearings. Upon initiating sliding again the OCP shifted cathodically, then rapidly moved noble for a period before re-establishing values observed before the serum change. One bearing displayed much more substantial and longer cathodic shifts than the second, although the noble periods were approximately the same. Both bearings reached OCP values of between -160 and -200 mV towards the final 100,000 cycles. This ennoblement has been noted before with 36 mm bearings operating under a standard gait profile [14]. The shift in that case was observed to be a much more rapid shift after approximately 400k cycles. The authors attributed this sudden shift to a ‘wear-induced’ passivation as a result of the formation of protective proteinaceous tribofilms on the surface of the bearings.

### 6.1.2 - Corrosion Current ( $I_{corr}$ )

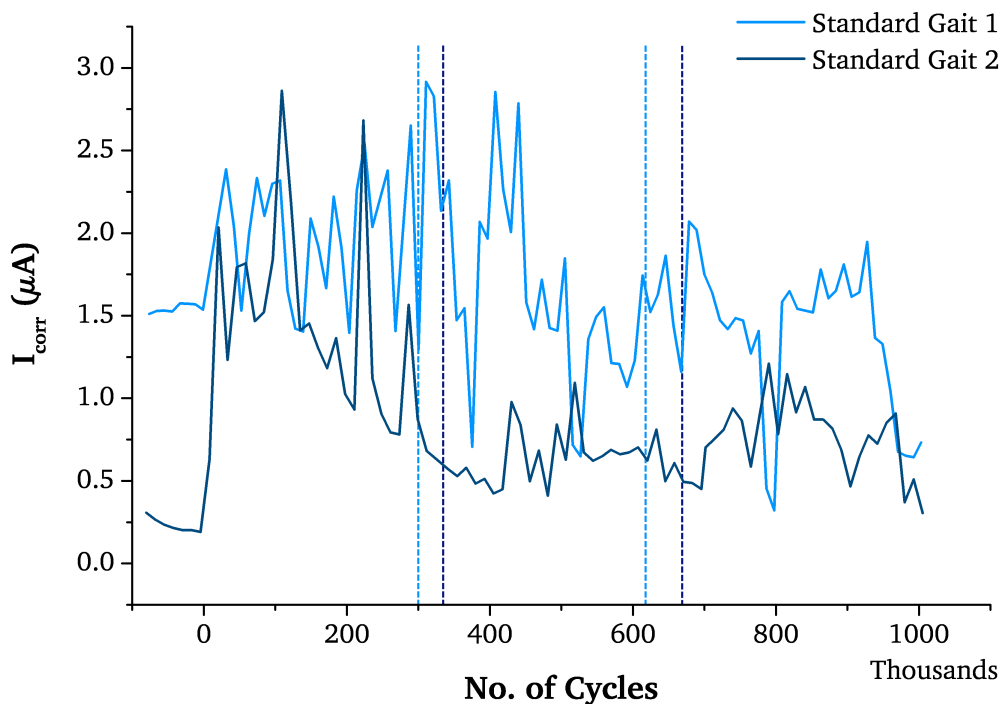


Figure 6.2: Corrosion Current ( $I_{corr}$ ) for 28 mm MoM bearings under Standard Gait articulation over 1 million cycles. Vertical dashed lines represent serum changes.

The corrosion current over the course of a test was calculated using the Resistance to Polarisation ( $R_p$ ), determined from LPR sweeps every 10,000 cycles, and the Stern-Geary Equation (Equation 2.17). As laid out in Chapter 4, standard parameters of 120 mV/decade were assumed for both the anodic and cathodic Tafel constants ( $\beta_a, \beta_c$ ). The corrosion current over one million cycles of standard gait can be seen in Figure 6.2.

The first bearing displayed a value of approximately  $1.5 \mu\text{A}$  for  $I_{corr}$  pre-sliding; the current during this time is associated with passive dissolution of the alloy. The second bearing had a lower static corrosion current of approximately  $0.2 \mu\text{A}$ . A passive current of  $1.5 \mu\text{A}$  is not atypical and was observed in later tests. Upon the initiation of sliding both bearings displayed higher corrosion currents of approximately  $2.4$  and  $2.0 \mu\text{A}$  respectively. Over the full course of the test peak values of approximately  $2.7 \mu\text{A}$  were recorded for both bearings. During sliding, both bearings showed a general trend of decreased  $I_{corr}$  as the test progressed. The first bearing fell back to pre-sliding values averaging approximately  $1.5 \mu\text{A}$ , although dropped to approximately  $0.5 \mu\text{A}$  over the last 100,000 cycles. The second bearing  $I_{corr}$  dropped to approximately  $0.5 \mu\text{A}$  over the first 400,000 cycles and remained relatively stable over the remainder of the test. This decreased corrosion current over the course of sliding has been observed before by Hesketh *et al.* [14, 15] on 36 mm bearings. In this case the current drop appeared to happen around the same time and dropped to similar values of approximately  $0.5 \mu\text{A}$ .

### 6.1.3 - Estimated Volume Loss

As discussed in Chapter 4 the corrosion current ( $I_{corr}$ ) was integrated with respect to time to give an overall charge transfer (Equation 4.1) and used to estimate the volumetric loss as a result of corrosion through Faraday's Law (Equation 4.2). The cumulative volume loss due to corrosion for both bearings under standard gait can be seen in Figure 6.3.

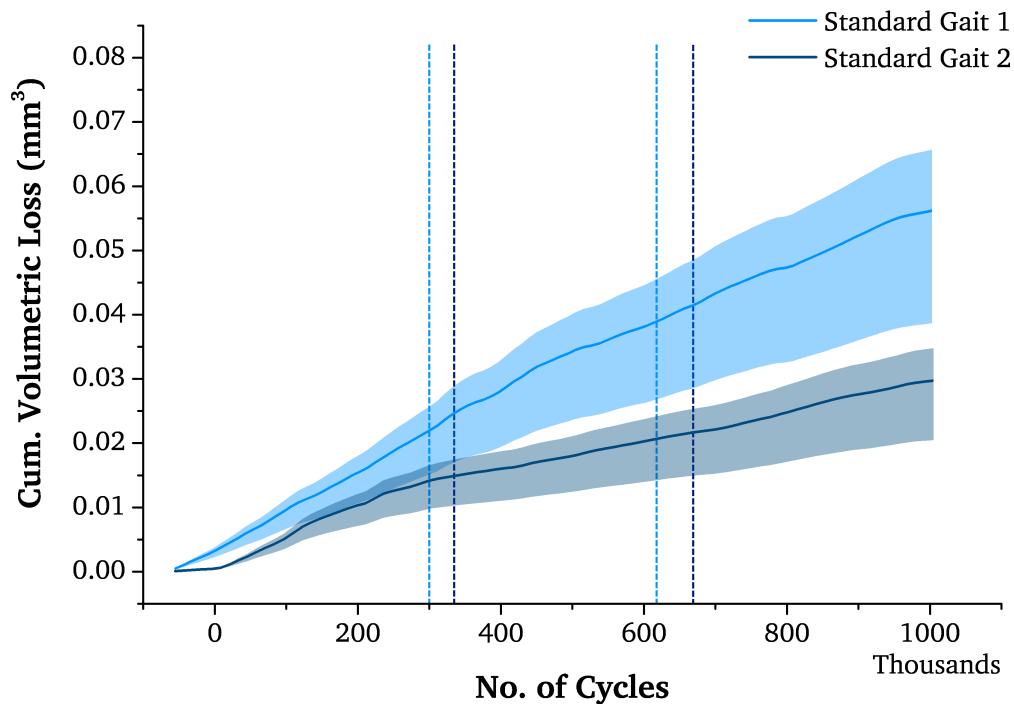


Figure 6.3: Estimated Volume Loss as a result of oxidation at the bearing surface for 28 mm MoM bearings under Standard Gait articulation over 1 million cycles. Upper and lower error bars represent possible preferential release of  $Co$  and  $Cr$  ions respectively. Vertical dashed lines represent serum changes.

Over one million cycles estimated volume loss due to corrosion of approximately  $0.056$  and  $0.029 \text{ mm}^3$  were determined for standard gait. The shaded areas in Figure 6.3 represent non-stoichiometric release of the different metal ions composing the alloy. Overall the second bearing displayed lower volume loss as a direct result of oxidation at the bearing surface, due to lower corrosion currents throughout the test.

#### 6.1.4 - Anodic Current Transients

Periodically the working electrode was polarised anodically ( $+50 \text{ mV vs. OCP}$ ) and the resultant current was sampled at  $100 \text{ Hz}$  along with an analogue voltage signal from the simulator load cell. The resultant net anodic current flow between the working and reference electrodes is a measure of the depassivation and repassivation of the exposed surface. During sliding therefore, depassivation and accelerated corrosive degradation is observed as increased anodic current.

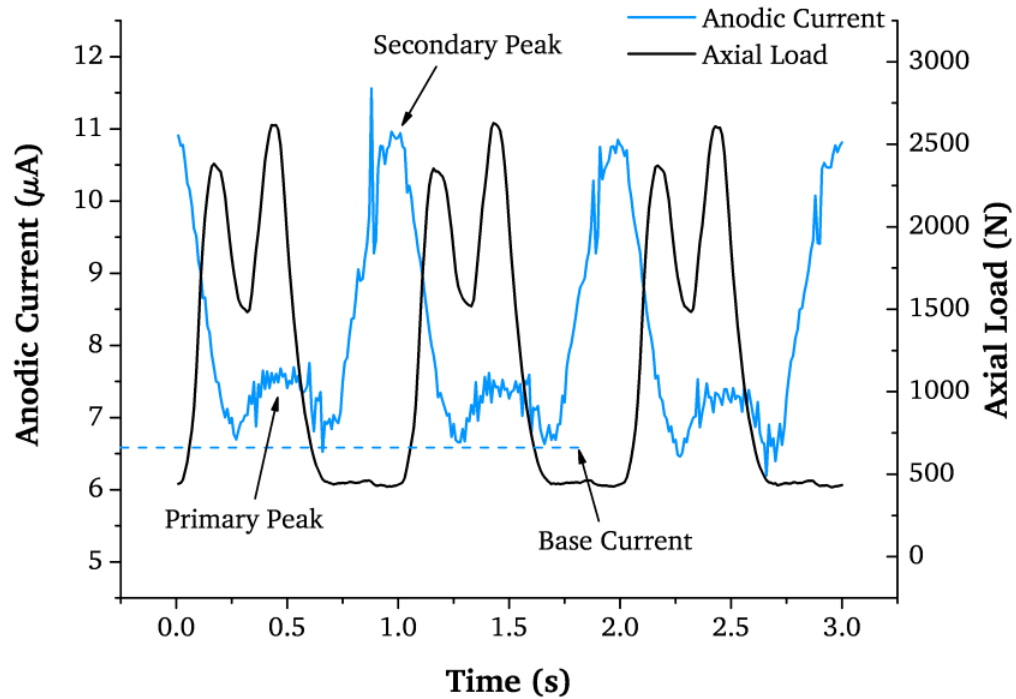


Figure 6.4: Example Anodic Current Transient (+50 mV vs. OCP) for 28 mm MoM bearings under three cycles of Standard Gait.

A typical anodic current transient for three cycles under standard gait can be seen in Figure 6.4. Clear ‘periodicity’, i.e. a repeating pattern in the anodic transient, was noted throughout both tests at the same 1 Hz frequency of sliding. The anodic currents established a twin-peak shape similar to the loading curve with base-line levels of current. Different magnitudes were typically observed for the primary and secondary current peaks. This periodicity suggests a close link between the tribology over a cycle and the resultant tribocorrosive degradation. Typical values for the currents measured are shown in Figure 6.4, with primary and secondary peaks of approximately 7.5 and 11  $\mu\text{A}$  respectively. Base values were noted for anodic current of approximately 6.5  $\mu\text{A}$ . Frequently the secondary current peak was observed to be higher than the primary peak, although this varied over the test with some curves showing similar magnitudes.

The peaks in anodic current were noted to occur after unloading events. The ‘primary’ peaks appeared to begin after the ‘heel-strike’ portion of the cycle, whereas the secondary peaks appeared to begin upon unloading after ‘toe-off’ and continue

to rise through the cycle swing phase. This appeared to agree with previous work by Sun *et al.* [191] which showed in indentation tests, attempting to mimic plastic deformation in single-asperity contacts, current peaks occurred during loading but also larger peaks occurred after unloading.

The potentiostat was only capable of sampling one external voltage signal. Previous studies by Hesketh *et al.* [15] had suggested the axial load was the most critical component affecting the corrosive degradation during sliding, represented by a so called 'severity factor.' Axial load was therefore chosen as the output signal to synchronise with the anodic current. Due to the pneumatic application of load however, it proved unreliable to synchronise the current to the cycle rotational axes. As shown in Figure 4.9, the axial load output is significantly different from the demanded curve and would vary from cycle-to-cycle. This prevented gaining a more in-depth link to the tribology such as the predicted lubrication regime ( $\lambda$ ) and film thickness ( $h_{min}$ ).

## 6.2 - Microseparation

A second series of 28 mm diameter HC CoCrMo bearings were tested under microseparation conditions; an adverse loading scenario of much interest in the literature. As described in Chapter 4 the loading cycle was the same as under standard gait however 0.8 mm microseparation was affected by applying a negative load to the femoral head during the swing phase of the cycle.

### 6.2.1 - Open Circuit Potential

Under microseparation a similar value for OCP was observed under static conditions to that seen for standard gait. Upon the initiation of sliding one bearing displayed a much greater initial cathodic shift to approximately -500 mV. Over the first 333k cycles this value continued to shift cathodically to approximately -625 mV. The OCP remained on average lower than standard gait throughout the

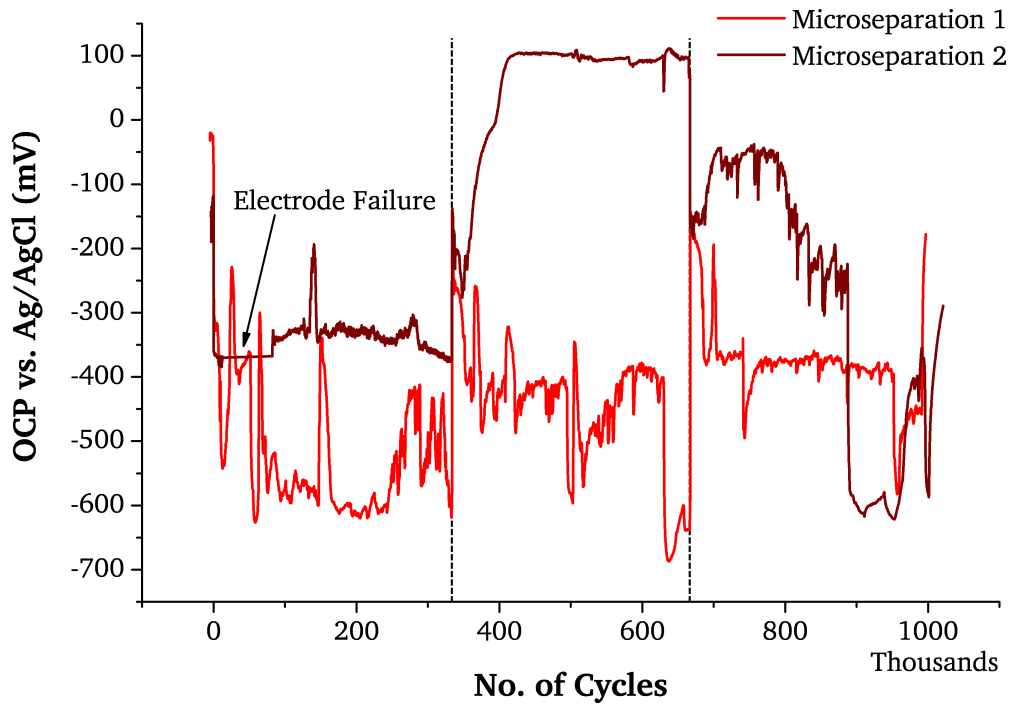


Figure 6.5: Open Circuit Potential for 28 mm MoM bearings under 0.8 mm Microseparation over 1 million cycles. Vertical dashed lines represent serum changes.

test and this bearing also displayed large spikes and transient behaviour when compared to standard gait, varying between -400 and -650 mV.

The second bearing subjected to microseparation also displayed this transient behaviour although appeared more stable at a given time. After the initiation of sliding this device shifted to approximately -350 mV and remained relatively stable there over the first 333k cycles. After the serum change, the observed OCP was more noble at between approximately -500 and -250 mV. The OCP then began to shift more noble to approximately +100 mV and remained stable there. Upon the second serum change at 666k cycles lower OCP values of between -50 and -300 mV were reported and also shifted to as low as -600 mV before the end of the test.

### 6.2.2 - Corrosion Current ( $I_{corr}$ )

The corrosion current for both bearings under microseparation can be seen in Figure 6.6. During the static settle phase both bearings subjected to microseparation initially displayed low values of  $I_{corr}$ . For test one and two respectively values of

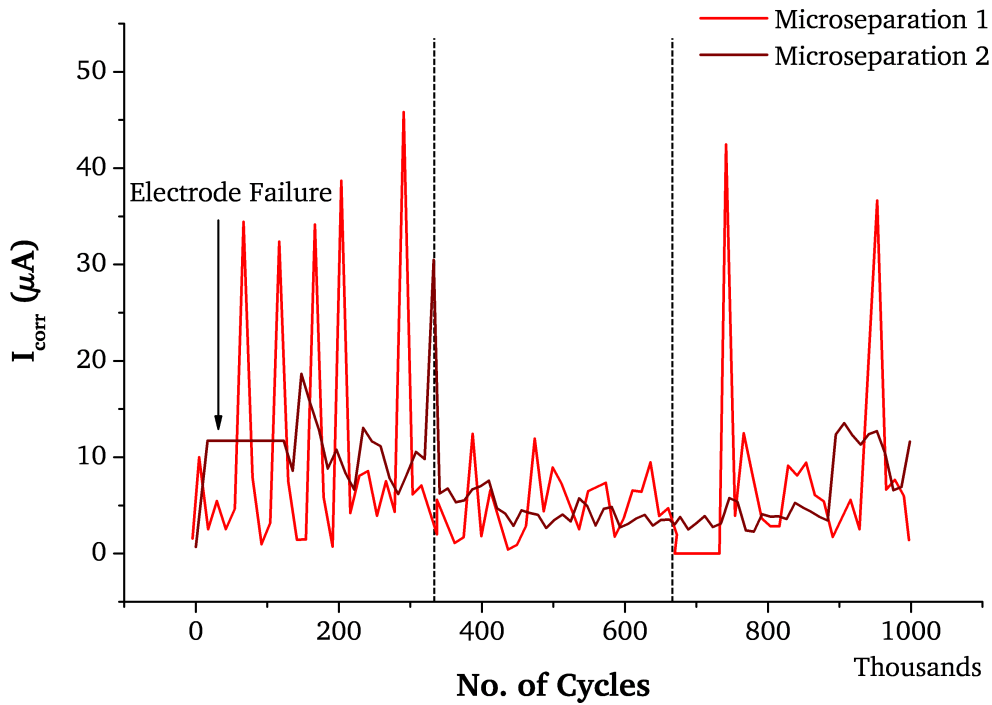


Figure 6.6: Corrosion Current ( $I_{corr}$ ) for 28 mm MoM bearings under 0.8 mm Microseparation over 1 million cycles. Vertical dashed lines represent serum changes.

1.5 and 0.7  $\mu\text{A}$  were measured. This was comparable to the same devices' pre-sliding currents measured during the standard gait tests. After the initiation of sliding however much higher corrosion currents were recorded throughout the test.

The first bearing displayed very transient corrosion current values over the first 333k cycles. Several peaks as high as 32.4 to 45.8  $\mu\text{A}$  were observed. Following the first serum change the current values were more stable but still varied between 3.0 and 12.0  $\mu\text{A}$ . After the second serum change the currents were slightly higher again with large peaks. The second bearing also displayed transient behaviour in current although was less severe. Over the first 333k cycles the measured  $I_{corr}$  varied between approximately 6.2 and 13.0  $\mu\text{A}$  with two peaks of 18.7 and 30.5  $\mu\text{A}$ . Again after a serum change the currents were more stable, more so than the first bearing, varying between 2.7 and 5.7  $\mu\text{A}$ . These current values continued after the second serum change although a slight resurgence was noted at approximately 900k cycles where  $I_{corr}$  increased to 11.5 to 13.5  $\mu\text{A}$ .

Inducing microseparation resulted in an increase in corrosion current from an average of 0.5 - 2.5  $\mu\text{A}$  under standard gait to values of 3.0 - 12.0  $\mu\text{A}$  over the test. Several periods of much higher currents were also observed; suggesting a transient behaviour in the degradation with much higher corrosive degradation.

### 6.2.3 - Estimated Volume Loss

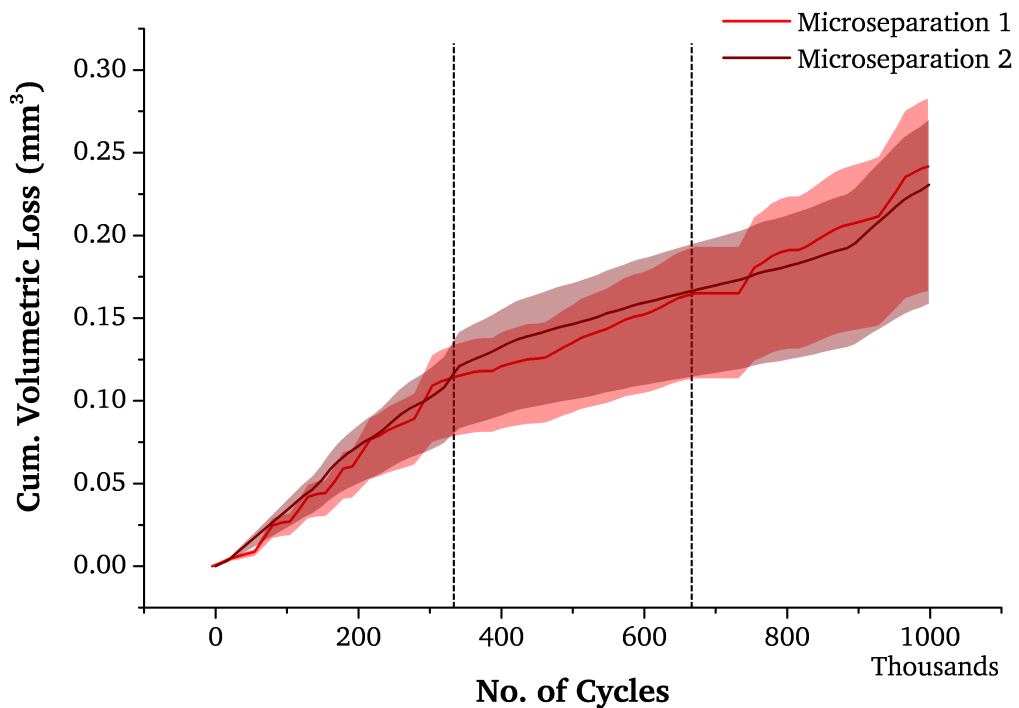


Figure 6.7: Estimated Volume Loss as a result of oxidation at the bearing surface for 28 mm MoM bearings under 0.8 mm Microseparation over 1 million cycles. Upper and lower error bars represent possible preferential release of  $Co$  and  $Cr$  ions respectively. Vertical dashed lines represent serum changes.

The same technique as was applied to standard gait was used to estimate the volume loss from the bearing surface as a result of corrosive degradation, shown in Figure 6.7. Under microseparation the final value for corrosive material loss was found to be much higher than standard gait (0.056 and 0.029  $\text{mm}^3$ ) at 0.24 and 0.23  $\text{mm}^3$ . This represented a near order of magnitude increase in corrosive degradation at the bearing surface compared to Standard Gait 2.

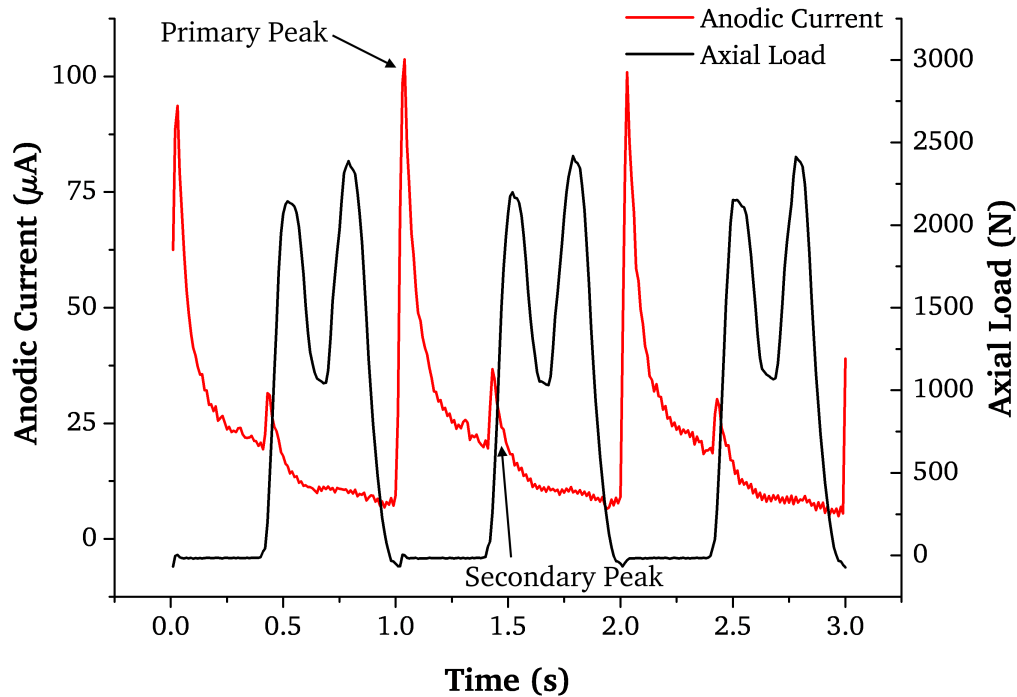


Figure 6.8: Example Anodic Current Transient (+50 mV vs. OCP) for 28 mm MoM bearings under three cycles of 0.8 mm Microseparation.

#### 6.2.4 - Anodic Current Transient

Figure 6.8 shows a typical anodic current transient (+50 mV vs. OCP) recorded from the bearings subjected to microseparation. Compared to standard gait a completely different pattern was observed. A primary peak was noted upon unloading after ‘toe-off’ and the magnitude of this peak was over an order of magnitude greater than standard gait. In the example shown peaks of 100  $\mu\text{A}$  were common although throughout the test peaks as high as 200  $\mu\text{A}$  were observed. After this peak the current decayed until a smaller secondary peak of approximately 30 - 36  $\mu\text{A}$  was observed just before the application of ‘heel-strike.’ The current then continued to decay through the cycle despite the twin-peak loading profile.

### 6.3 - Surface Analysis

Following testing a series of Surface Analysis techniques were used to characterise the damage done to the surfaces of the Metal-on-Metal bearings during articulation.

### 6.3.1 - Coordinate Measuring Machine (CMM)

As described in Section 4.5.1 a map of the bearing surfaces was taken post-test using a Legex 322 (Mitotuyo, Japan) Coordinate Measuring Machine and the surface data was imported into RedLux Sphere Profiler software (Southampton, UK). This generated a 3D view of the bearing surfaces. Example scans for femoral heads articulated under Standard Gait and Microseparation can be seen in Figures 6.9 and 6.10.

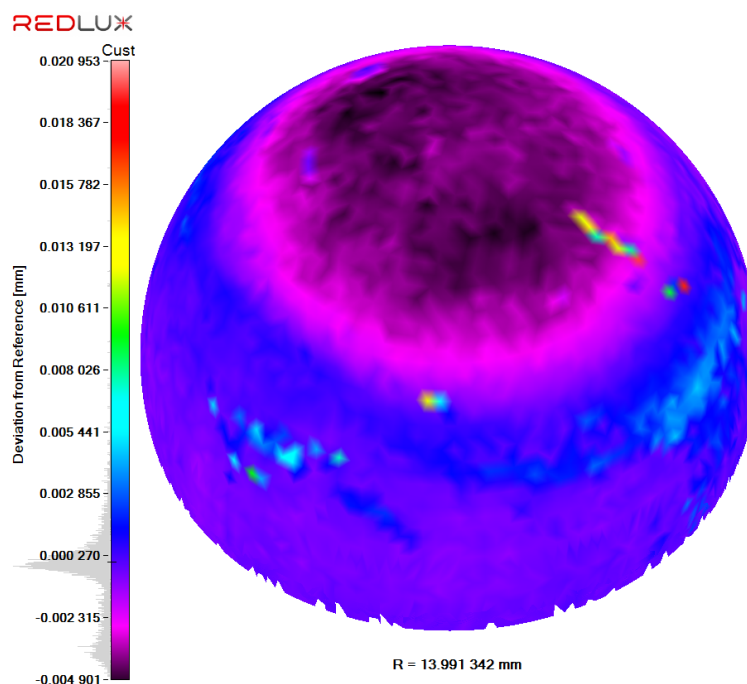


Figure 6.9: Sphere Form Profile Analysis of a 28 mm Metal-on-Metal femoral head after 1 MCycles articulation under Standard Gait.

A flattened area was observed at the pole of the femoral heads articulated under standard gait which at its worst deviated from the nominal sphere by 4.5 - 4.9  $\mu\text{m}$ . The estimated volume of this deviation for the femoral head shown in Figure 6.9 was 0.362  $\text{mm}^3$ . These components typically have flattened poles after manufacturing however. This is accounted for in the manufacturing standard BS ISO 7251-4 [192], which allows a deviation up to 2.5  $\mu\text{m}$  in form. This area likely included a possible deviation as well as material removed as a result of wear during sliding.

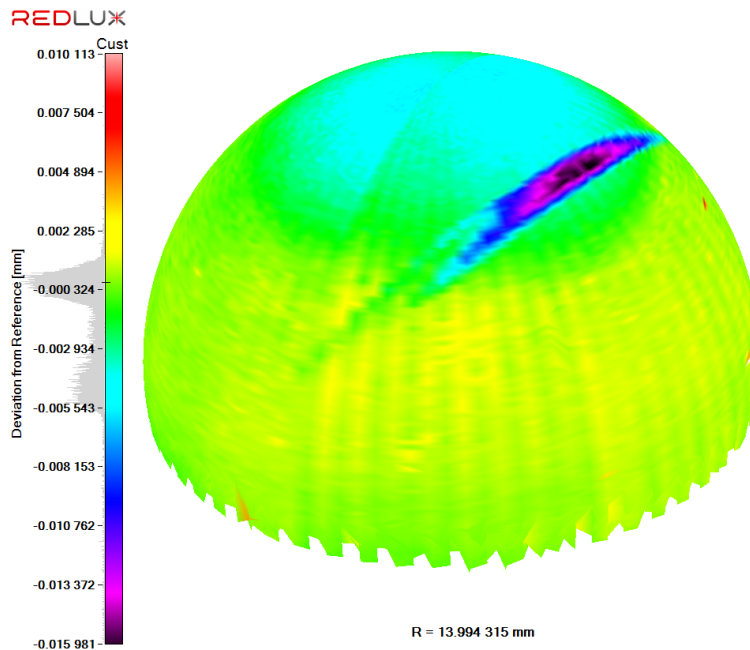


Figure 6.10: (Sphere Form Profile Analysis of a 28 mm Metal-on-Metal femoral head after 1 MCycles articulation under Microseparation.)

For the microseparated head, shown in Figure 6.10, a clear ‘stripe wear’ pattern was observed crossing the femoral head. This pattern is typically associated with hard-on-hard bearings operating under microseparation or under edge-loading conditions such as high acetabular inclination [56, 125, 193]. The depth of this stripe was approximately 16  $\mu\text{m}$  from the nominal sphere. The estimated volume loss within the ‘stripe wear’ scar on the femoral head was approximately 0.167  $\text{mm}^3$ . This was less than the estimated volume of corrosive material loss from the whole bearing (0.242  $\text{mm}^3$ , Figure 6.7). This suggested despite severe material loss within the ‘stripe wear’ region, overall corrosive loss from the entire bearing was more significant.

### 6.3.2 - White Light Interferometry (WLI)

As well as demonstrating increased electrochemical mass loss, the bearings subjected to microseparation were also visibly more damaged than those under standard gait. As discussed in Chapter 4 no attempt was made to determine a gravimetric wear rate for the Metal-on-Metal series as the formation of proteinaceous

tribofilms was of great interest. To get an accurate gravimetric mass loss the bearings would have required cleaning which may have compromised these films.

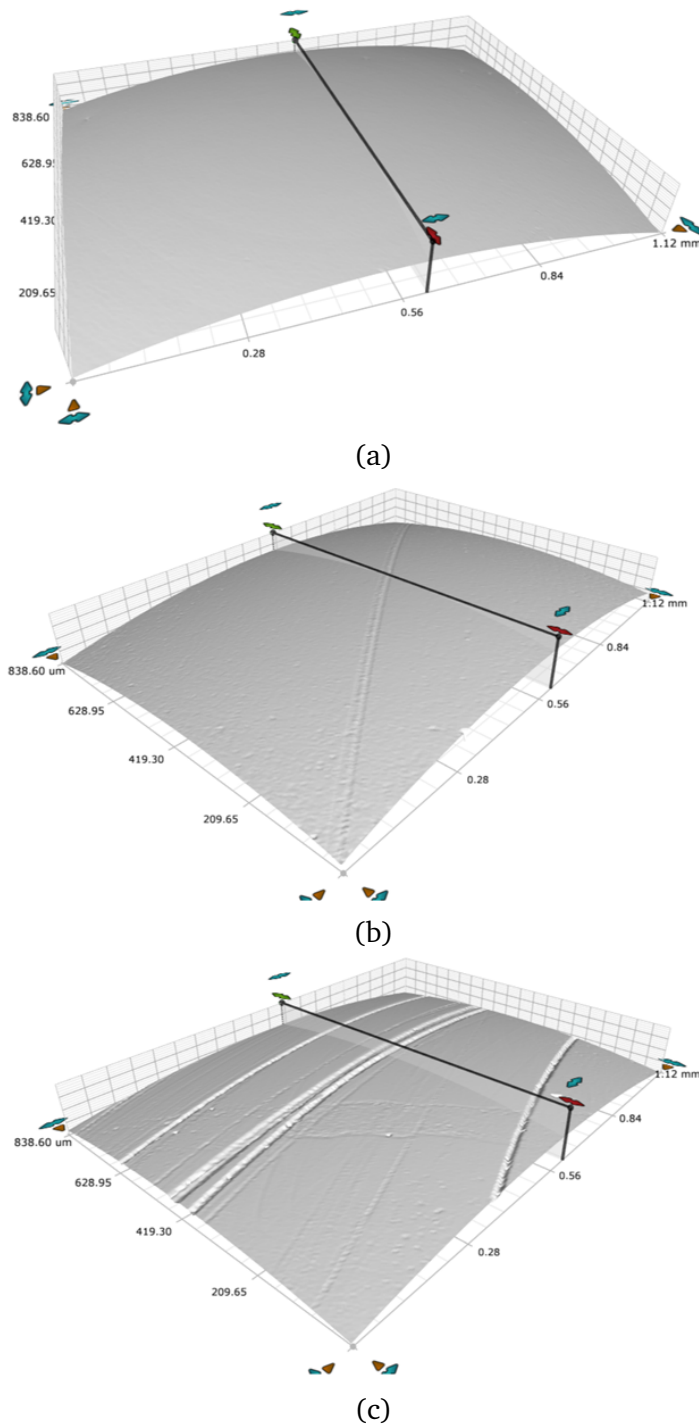


Figure 6.11: White Light Interferometry scans at the pole of an unworn 28 mm *CoCrMo* alloy femoral head (a) and after one million cycles of Standard Gait (b) and Microseparation (c).

The bearings were examined post-test and Figure 6.11 displays WLI scans taken at the pole of a new bearing, one subjected to standard gait and one subjected

to microseparation. Moving from the new, undamaged bearings to the scan taken after one million cycles of standard gait the device became visibly rougher with an increase in 3D surface roughness ( $S_a$ ) from 14.5 to 40.0 nm. Light scratching was also observed across the contacting areas of the surface.

The bearing subjected to one million cycles of microseparation displayed a significantly rougher wear scar, with an average  $S_a$  of 148 nm. Coupled with that the bearing surface also had an increased number of deeper scratches, as shown in Figure 6.11. The scratches captured in the scan at the pole were of an average depth of approximately 1.5 - 2.0  $\mu\text{m}$ . These may have been caused by increased third body wear particles present at or within the contact.

### **6.3.3 - Scanning Electron Microscopy (SEM) and Energy Dispersive X-Ray Spectroscopy (EDX)**

Hesketh *et al.* [14, 15, 150, 162] noted the formation of tribofilms on 36 mm Metal-on-Metal bearings. As discussed in Chapter 3 the formation of these tribofilms, or so-called ‘tribochemical reaction layers,’ and their composition is of great interest in the literature [7–9, 194, 195]. Despite operating in a different lubrication regime the presence of these films was also noted on the 28 mm bearings subjected to standard gait articulation in the present study. Figure 6.12 shows an image of one of these films taken in the SEM.

The location of the tribofilms was similar to those noted previously by Hesketh *et al.* [150] in that they appeared to predominately form around or at the edge of the contact area/wear scar. They also appeared to be present mostly along the main axis of Flexion / Extension entrainment. Figure 6.13 shows two EDX spectra taken from the surface of the implant and over an area of the tribofilm. As expected the surface displayed peaks in the spectra associated with  $Co$ ,  $Cr$  and  $Mo$ , being the main constituents of the alloy. The spectra for the tribofilm displayed a much stronger Carbon peak. The spectra also indicated the presence of phosphorus

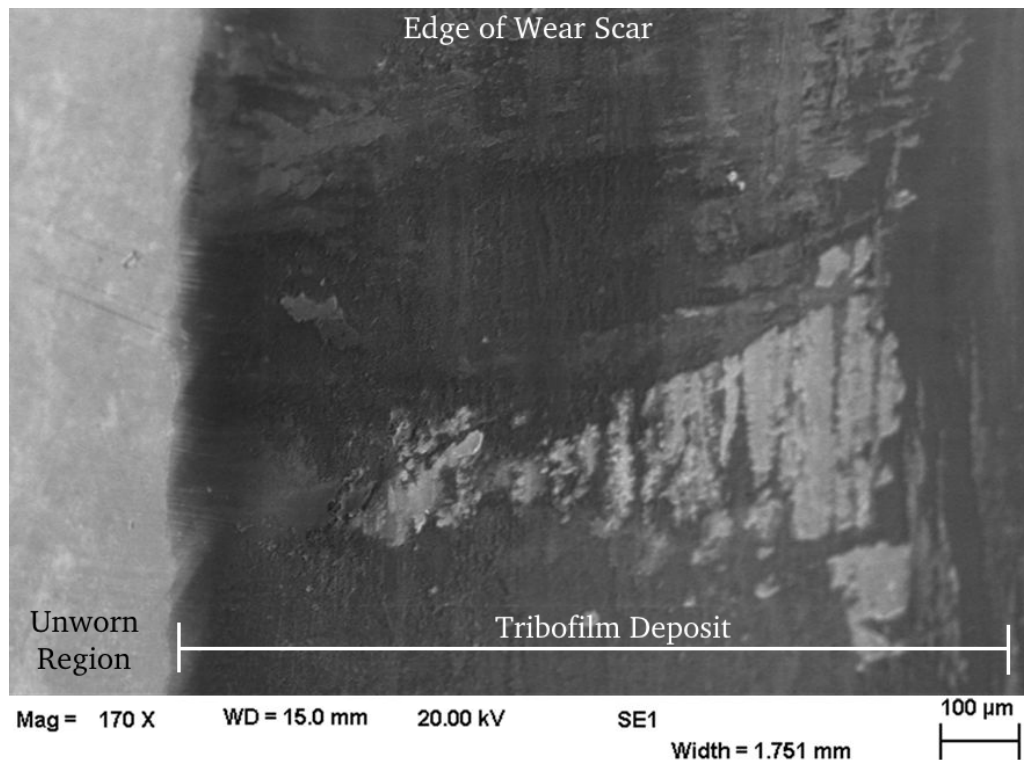


Figure 6.12: SEM image of Carbon rich tribofilm noted on the bearing surface of 28 mm HC CoCrMo Femoral Head after 1 million cycles under Standard Gait.

(*P*), likely originating from the PBS, and sulphur (*S*) and calcium (*Ca*) both of which likely originating from the proteins. This supported the previous findings that these films are carbon-rich and likely originate from proteins present in the lubricant, denatured during articulation and deposited on the surface.

As with Hesketh *et al.* [150, 162] the presence of these films were coupled with evidence of changing electrochemistry. Over the course of the test the OCP gradually shifted more noble and this was also generally associated with lower determined corrosion currents ( $I_{corr}$ , Figure 6.2). This ‘wear induced passivation’ observed by Hesketh *et al.* occurred very rapidly over a period of 100,000 cycles in their testing as opposed to the gradual shift observed for 28 mm bearings in this study. This may be due to differences in the operating lubrication regime for both diameters. For the bearings subjected to microseparation there was no visible evidence of the formation of tribofilms around the normal wear scar or the ‘stripe wear’ pattern noted during CMM analysis.

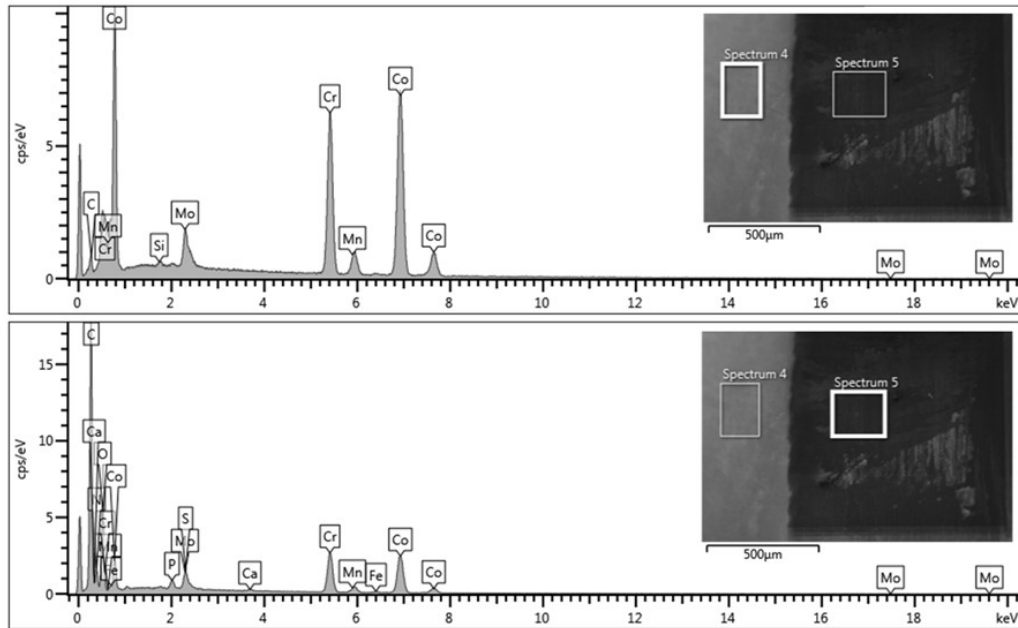


Figure 6.13: EDX Spectra of the surface of 28 mm HC CoCrMo Femoral Head (above) and Carbon rich tribofilm (below) after 1 million cycles under Standard Gait.

### 6.3.4 - Transmission Electron Microscopy (TEM)

Pourzal *et al.* [10] and Hesketh *et al.* [14] have both demonstrated changes to the subsurface micro-structure of *CoCrMo* alloy Metal-on-Metal bearings, specifically the nano-crystalline layer. This layer is typically already present on the surface due to manufacturing processes and surface finishing and polishing. Both studies noted growth of this nano-crystalline layer within the ‘primary wear zones’ from approximately 150  $\mu\text{m}$  at the non-contacting regions. They differ in their estimation of average crystal size however, with Pourzal *et al.* [10] noting an increase in average crystal size from  $< 15$  nm in the non-contacting region to 35 - 40 nm in the primary wear zone. Hesketh *et al.* [14] noted the crystals became finer from approximately 40 nm in the non-contacting region to 20 nm in the wear scar.

Pourzal *et al.* also examined a ‘stripe wear’ region from a microseparated bearing and found a reduction in the thickness of the nano-crystalline layer to 50 nm and still slightly coarser crystals of between 15 - 20 nm [10]. In the present study TEM slides were prepared as described in Section 4.5.4 from an ‘unworn’ or non-

contacting region of a microseparated femoral head and from within the ‘stripe wear’ pattern. Figures 6.14 and 6.15 show the TEM slides from these sections respectively.

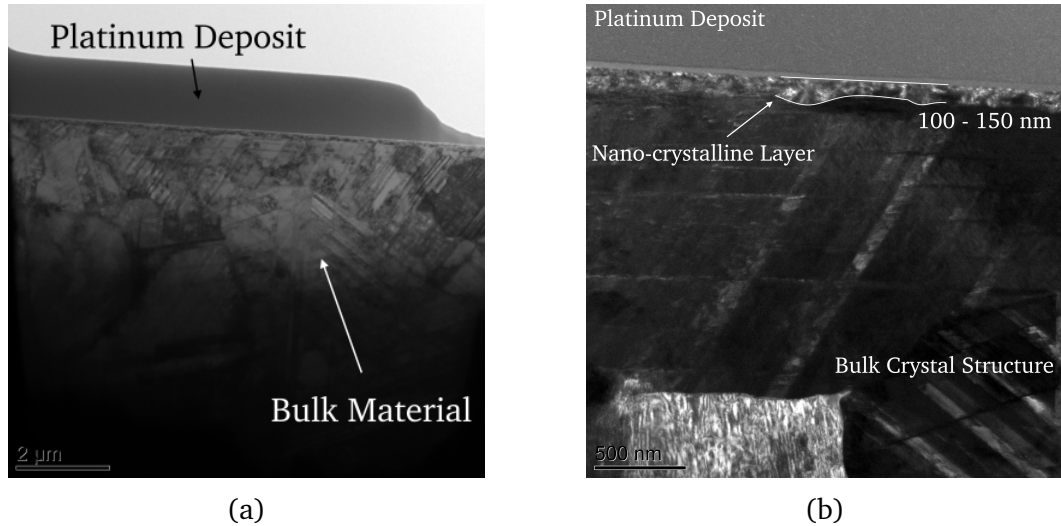


Figure 6.14: Light Field (a) and Dark Field (b) images of a slide taken from an Unworn section of a 28 mm CoCr Femoral Head.

As shown in Figure 6.14(b) the dark field image highlights crystals orientated to give ‘Bragg’ diffraction and are characterised by brighter spots. This enables a clearer view of the nano-crystalline layer underneath the surface at the ‘unworn’ region. The much larger crystal grains within the bulk of the alloy are also clearly distinguished. The thickness of the nano-crystalline layer was measured to be on average approximately 100 - 120 nm. This was similar to the values measured previously both by Pourzal *et al.* [10] and Hesketh *et al.* [14]. The average crystal size in the subsurface layer was also estimated to be approximately 15-20 nm.

For the slide taken at the ‘stripe wear’ region of the femoral head, shown in Figure 6.15, the nano-crystalline layer appeared thicker than at the ‘unworn’ region or had been observed by Pourzal *et al.* [10]. The thickness of the layer varied between approximately 250 - 700 nm across the surface of the slide. The average crystal size also differed depending on the distance from the surface. Close to the top fine crystallites of approximately 15 - 20 nm were observed, similar to the unworn region, whereas closer to the bulk alloy crystal size ranged from approx-

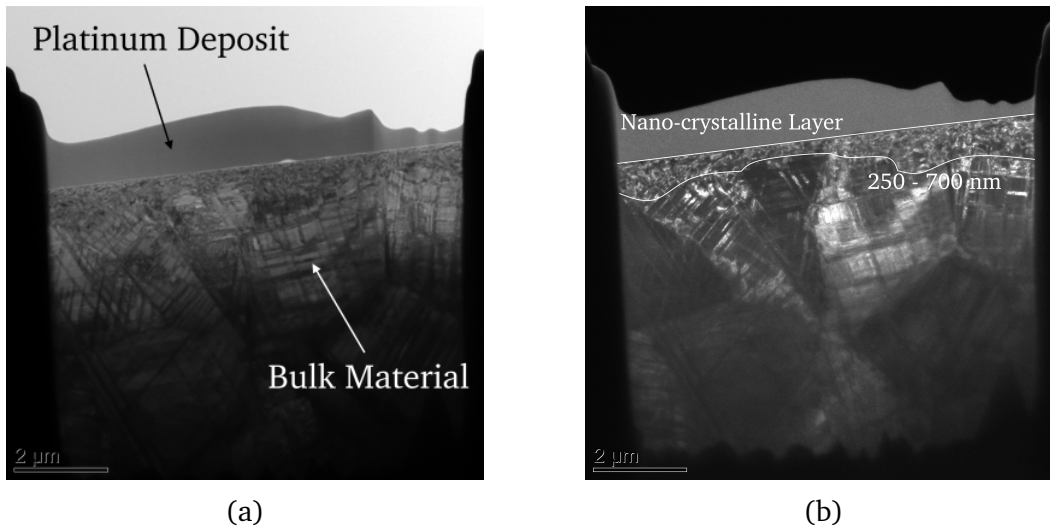


Figure 6.15: Light Field (a) and Dark Field (b) images of a slide taken from the ‘stripe wear’ area of a 28 mm CoCr Femoral Head subjected to 1 Mcycles of 0.8 mm Microseparation.

imately 40 - 60 nm. There was also clear evidence of increasing surface damage with possible areas of twinning and  $\epsilon$ -martensite formation much deeper into the subsurface than was observed for the ‘unworn’ region.

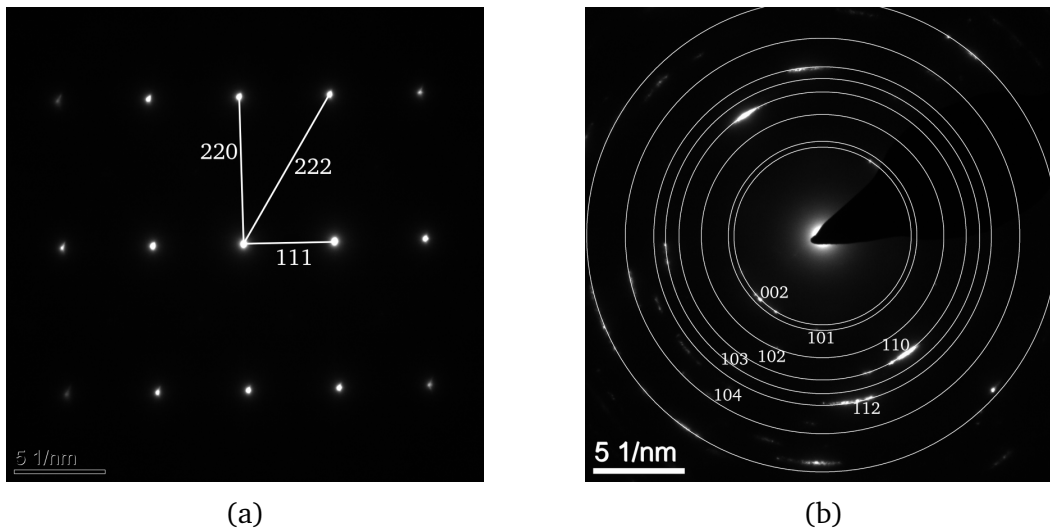


Figure 6.16: Selected Area Electron Diffraction (SAED) patterns taken at the unworn bulk area (a) and at the worn nano-crystalline layer (b).

Figure 6.16 shows Selected Area Electron Diffraction (SAED) patterns, taken from the unworn bulk area and the worn nano-crystalline layer. These patterns give an indication of the alloys atomic arrangement. Figure 6.16(a) demonstrated a typical diffraction for a single large crystal and was indexed against a cubic structure,

suggesting a face-centred cubic (FCC) arrangement. The ringed diffraction pattern shown in 6.16(b) suggested a finer crystal structure in the nano-crystalline layer than the bulk alloy, with a hexagonal close-packed (HCP) arrangement. There was also some symmetry in this diffraction pattern with bright spots occurring exactly opposite each other on the same rings. This suggested some form of preferential arrangement of the crystals within the subsurface layer.

## 6.4 - Summary

- Moving from a standard gait articulation to 0.8 mm of microseparation on 28 mm Metal-on-Metal bearings increased the estimated material loss as a result of corrosion by a near order of magnitude.
- Anodic current transients displayed periodicity, previously observed in 36 mm bearings, suggesting a link between the tribology of a cycle and corrosive degradation. The transient shape and magnitude was also very different between standard gait and microseparation articulation further reinforcing this link.
- The formation of carbon-rich proteinaceous tribofilms on the surface was coupled with changing trends noted in the electrochemistry under standard gait; as had been reported previously for 36 mm bearings. The changes occurred gradually over a million cycles for the 28 mm bearings, as compared to suddenly after approximately 100 kcycles as observed by Hesketh *et al.* [14].
- Similar to what had been seen previously a growth in the subsurface nano-crystalline layer was noted underneath the 'stripe-wear' region of a microseparated 28 mm metal-on-metal femoral head.

Studies in the literature have at most demonstrated a non-significant increase in gravimetric wear rate for 28 mm Metal-on-Metal bearings over the first million

cycles [124], or a three fold increase over the first two million cycles [125], articulating under microseparation. The near order of magnitude increase in corrosive material loss observed through electrochemical techniques poses a significant insight into how the degradation of these bearings can vary depending on contact condition and how that can possibly influence the success of the device *in vivo*.

## Chapter 7 - Hip Simulation (Metal-on-Ceramic)

The use of mixed materials for the bearing in a Hard-on-Hard scenario has never been prevalent for TJR procedures. The Ceramic-on-Metal bearing combination was first conceived by Firkins *et al.* [196] in 2001 before the rise of Metal-on-Metal popularity. Despite good *in vitro* simulator results for 28 mm diameter bearings there was not much follow up research. Later *in vitro* and *in vivo* clinical assessment maintained lower wear rates and blood ion levels when compared to MoM [197–199]. Despite this the uptake of a metal and ceramic bearing combination has been slow and they are not used extensively. Only 45 Ceramic-on-Metal (metal cup) and 11 Metal-on-Ceramic (metal head) prostheses were implanted during primary hip replacement surgeries in the UK during 2014 [16]. This only represented 0.35 % of Hard-on-Hard devices and 0.06 % of overall procedures.

Although very few of these devices make it into patients they may still be useful when considering metal bearing surfaces for THRs. A common practice in tribocorrosion studies with simple pin-on-plate tribometers is to slide a ceramic pin against a metal plate. Thus when instrumented with a three-electrode cell the working electrode comprises only the plate and not a combination of pin and plate surfaces exposed to the electrolyte. Having a single active surface in a tribocouple simplifies the electrochemistry and allows easier study of corrosive degradation and depassivation of that single surface.

This chapter presents the results of a series of Metal-on-Ceramic bearings which were tested according to the same protocol as the Metal-on-Metal devices examined in Chapter 6.

### 7.1 - Standard Gait

28 mm diameter Low Carbon (LC) *CoCrMo* alloy femoral heads were supplied by Peter Brehm (Germany) and were articulated against matched Biolox®delta

ceramic acetabular liners (Ceramtec, Germany). As discussed in Chapter 4 the Metal-on-Ceramic series components were mounted in the pneumatic simulator in the same way as the Metal-on-Metal devices. A connection was taken from inside the modular taper of the femoral head and care was taken to seal this taper with silicone sealant. Thus the working electrode comprised only the bearing surface of the femoral head. Two devices were articulated to one million cycles at 1 Hz in the pneumatic simulator under the same walking cycle used previously and shown in Figure 4.9.

Bearing	Femoral Head Radius (mm)	Acetabular Cup Radius (mm)	Radial Clearance ( $\mu\text{m}$ )
SG 1	13.990	14.023	33
SG 2	13.991	14.025	34
MS 1	13.993	14.028	35
MS 2	13.994	14.036	43

Table 7.1: The Femoral Head and Acetabular Cup radii and calculated radial clearance for 28 mm MoC THR bearings determined by CMM and RedLux Sphere Profile software. ‘SG’ and ‘MS’ refer to Standard Gait and Microseparation respectively.

The MoC bearings were also matched for radial clearance through the developed use of the Legex 322 Coordinate Measuring Machine (Mitutoyo, Japan). A low resolution 2 mm arc scan was taken of each femoral head and acetabular cup before testing. These scans were then imported into the RedLux Sphere Profile software in order to determine their radius, shown in Table 7.1, and the components were matched in order to give similar radial clearance values between tests.

### 7.1.1 - Open Circuit Potential

The OCP for Metal-on-Ceramic bearings over one million cycles of standard gait can be seen in Figure 7.1. Both femoral heads in these bearings displayed different trends in OCP when compared to the complete bearing in the MoM devices. Both heads displayed a much more negative initial static potential when compared to the MoM devices, of approximately -400 to -450 mV. Upon initiation of sliding

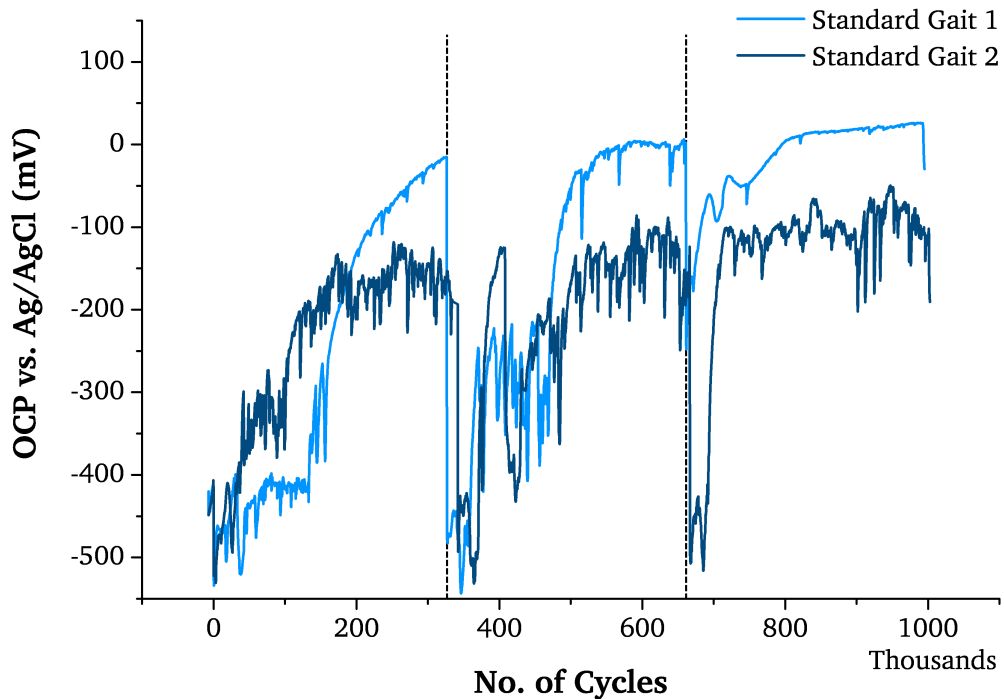


Figure 7.1: Open Circuit Potential for 28 mm MoC bearings under Standard Gait articulation over 1 million cycles. Vertical dashed lines represent serum changes.

there was a small cathodic shift but the gradual ennoblement was much more rapid, reaching relatively noble OCP values of 0 mV for the first bearing and approximately -150 to -200 mV for the second. This occurred over 333,000 cycles and at serum changes the initial low OCP was restored during a brief static period before sliding. Once sliding was initiated again, the OCP immediately began to shift back towards relatively noble values.

### 7.1.2 - Corrosion Current ( $I_{corr}$ )

The corrosion current for Metal-on-Ceramic bearings, determined by LPR, over one million cycles of standard gait can be seen in Figure 7.2. The femoral heads displayed initial static corrosion currents of 1.30 and 0.88  $\mu\text{A}$  for the first and second repeat respectively. Over the first 100,000 cycles of sliding the corrosion current reached maximum values of 2.23 and 1.73  $\mu\text{A}$  before continuously falling to average values of approximately 0.25 and 0.37  $\mu\text{A}$  respectively. After the first serum change and commencement of sliding for both bearings they displayed an

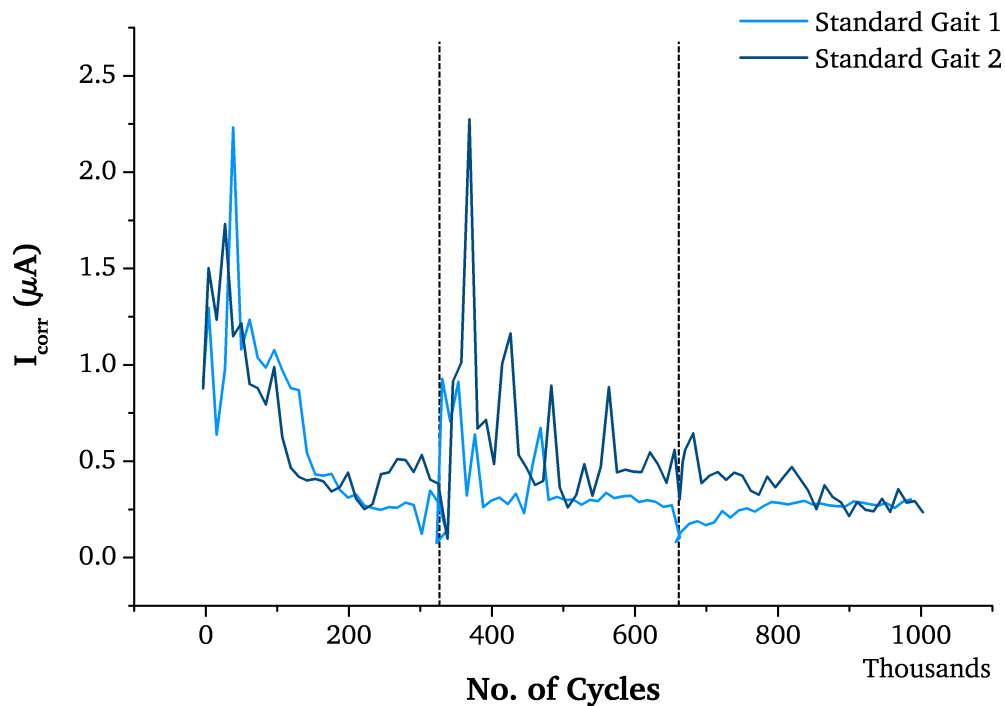


Figure 7.2: Corrosion Current ( $I_{corr}$ ) for 28 mm MoC bearings under Standard Gait articulation over 1 million cycles. Vertical dashed lines represent serum changes.

increase in corrosion current. The first bearing reached a maximum value of 0.93  $\mu\text{A}$ , whereas the second bearing reached a maximum of 2.27  $\mu\text{A}$ . This increase was not seen again after the second serum change at 666,000 cycles and corrosion currents remained relatively low over the remainder of the test.

### 7.1.3 - Estimated Volume Loss

The estimated volumetric loss as a result of corrosion from the femoral head in the Metal-on-Ceramic bearing couples under standard gait can be seen in Figure 7.3. The total volume loss after one million cycles was estimated to have been 0.013 and 0.017  $\text{mm}^3$  for the first and second bearing respectively. As used previously the shaded areas represent possible non-stoichiometric release of  $Co$  and  $Cr$  ions from the alloy.

The estimated volume loss mirrored the trends observed previously in the corrosion current ( $I_{corr}$ ) for these femoral heads (Figure 7.2). Higher rates of corrosive material loss were noted during the first 100,000 cycles and after the first serum

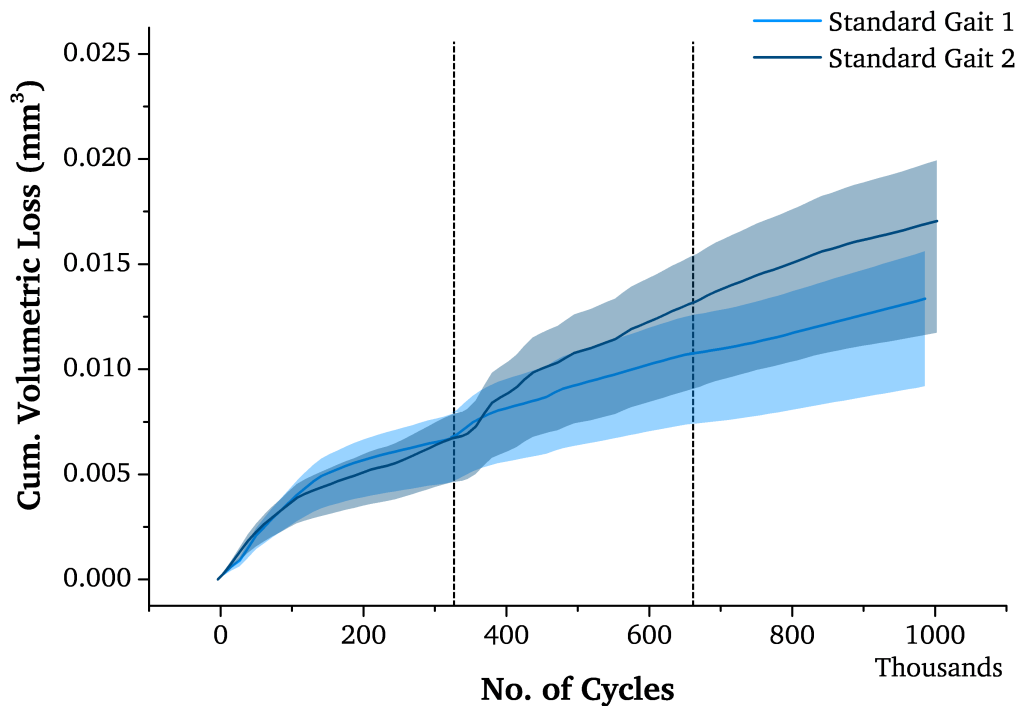


Figure 7.3: Estimated Volume Loss as a result of oxidation at the bearing surface for 28 mm MoC bearings under Standard Gait articulation over 1 million cycles. Upper and lower error bars represent possible preferential release of  $Co$  and  $Cr$  ions respectively. Vertical dashed lines represent serum changes.

change. This aligned with the periods of higher corrosion current. This was followed by lower rates of corrosive material loss during periods of minimum current and more noble OCP.

#### 7.1.4 - Anodic Current Transient

Figure 7.4 shows a typical anodic current transient (+50 mV vs. OCP) versus the loading curve over three cycles. The clear ‘periodicity’ observed previously for MoM bearings was again noted here for the metal femoral heads against ceramic liners. The shape of the current transient was also very similar to the MoM transients under standard gait with a twin-peak repeating pattern. The position of the peaks were also similar with current beginning to rise after unloading of ‘heel-strike’ and ‘toe-off.’ Similar to the corrosion current the magnitude of anodic current transient was lower than typically observed for MoM bearings. Initial primary peaks of approximately 1.6-1.9  $\mu A$  followed by a larger secondary peak of

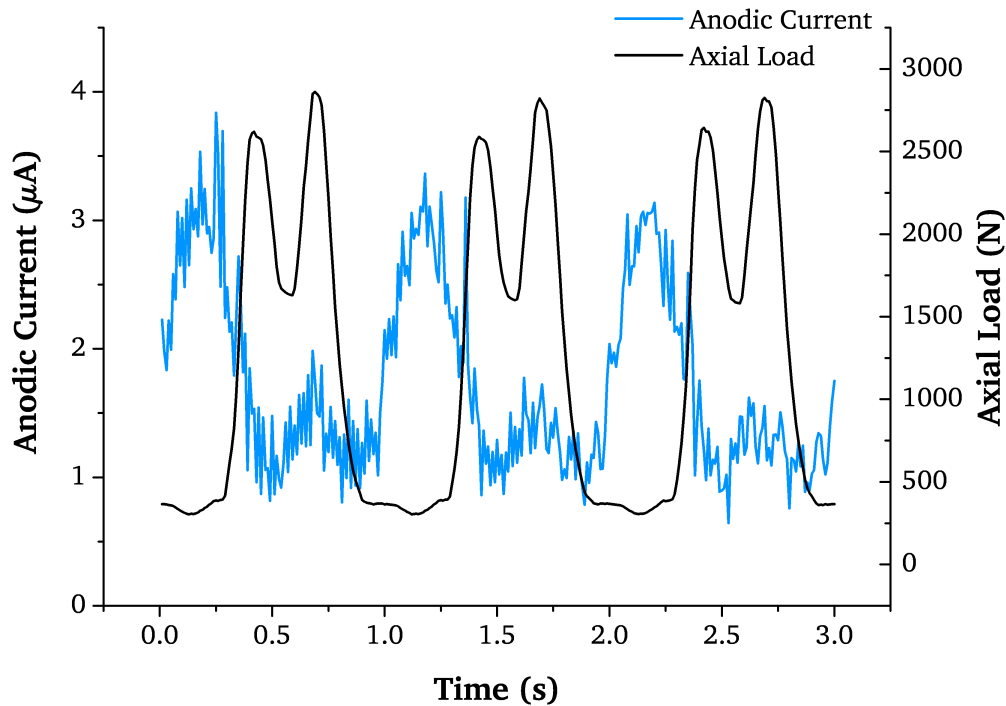


Figure 7.4: Example Anodic Current Transient (+50 mV vs. OCP) for 28 mm MoC bearings under three cycles of Standard Gait.

approximately 3.1-3.8  $\mu\text{A}$ .

## 7.2 - Microseparation

An additional two Metal-on-Ceramic bearings were subjected to one million cycles of walking with the application of 0.8 mm microseparation. These tests were performed in exactly the same way as the microseparated Metal-on-Metal bearings although the working electrode connection was taken solely from the femoral head, through the Torlon resin spigot.

### 7.2.1 - Open Circuit Potential

Under microseparation the initial static conditions displayed similarly lower values of OCP for both bearings, shown in Figure 7.5, than was observed for the Metal-on-Metal devices. Initial static values of approximately -360 and -440 mV displayed very small cathodic shifts upon the initiation of sliding. A brief ennoblement occurred over the first 3,600 cycles of sliding followed by a second more

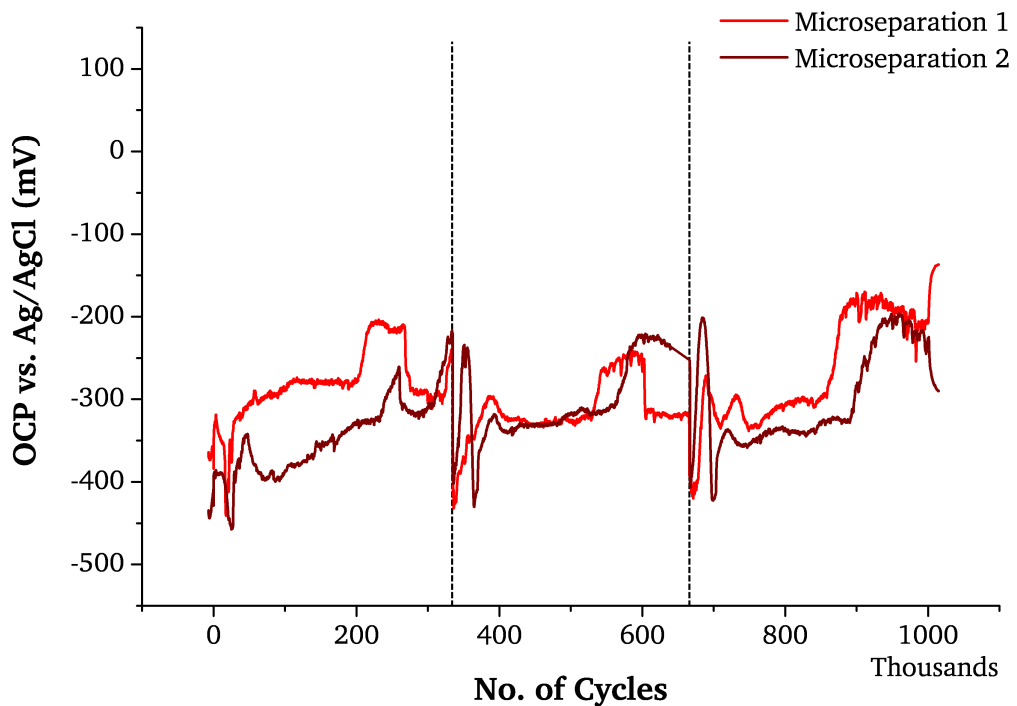


Figure 7.5: Open Circuit Potential for 28 mm MoC bearings under 0.8 mm Microseparation over 1 million cycles. Vertical dashed lines represent serum changes.

severe cathodic shift for both bearings to approximately -450 mV OCP. After this the OCP for both femoral heads continued to ennoble. Overall the OCP remained consistently lower than standard gait with both tests displaying values of OCP between approximately -300 and -400 mV for the majority of the test.

Some brief periods of instability were noted where OCP rapidly shifted more noble for a period of time before reverting back to average values. Particularly after a serum change, large cathodic and anodic shifts of up to 200 mV were observed before becoming stable again. Finally over the last 100,000 cycles both bearings displayed noble shifts in OCP to approximately -200 mV; where they remained for the remainder of the test. Overall the OCP for the MoC bearings remained much more stable for the duration of testing when compared to the MoM series.

### 7.2.2 - Corrosion Current ( $I_{corr}$ )

The corrosion currents from the femoral heads in the MoC series, determined by LPR, can be seen in Figure 7.6. For the first repeat the calculated corrosion currents

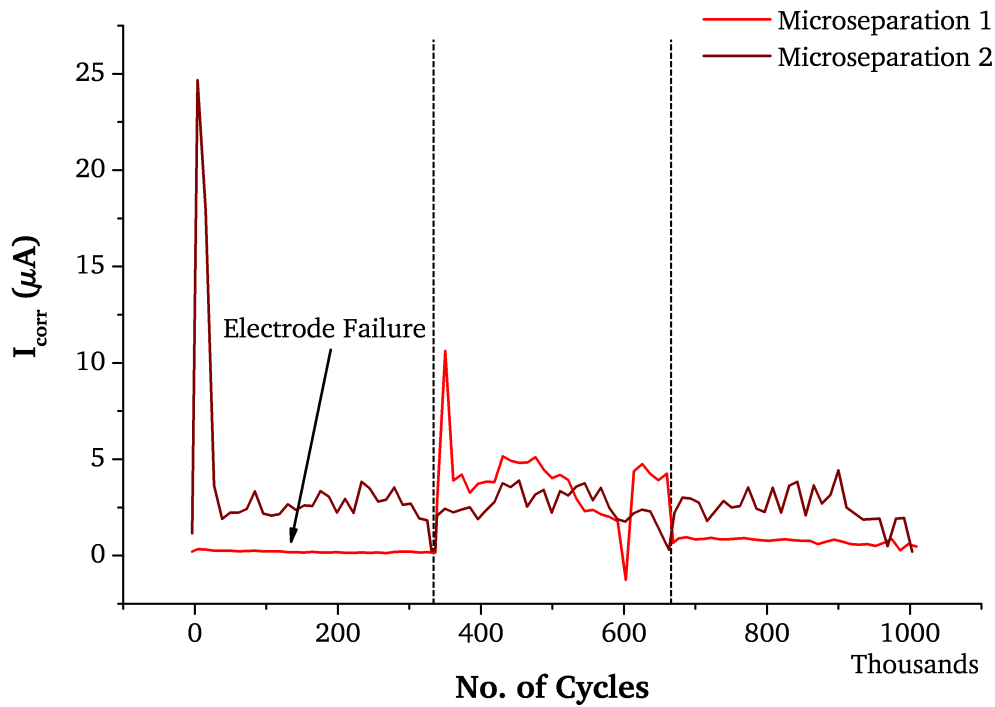


Figure 7.6: Corrosion Current ( $I_{corr}$ ) for 28 mm MoC bearings under 0.8 mm Microseparation over 1 million cycles. Vertical dashed lines represent serum changes.

were lower than values observed under standard gait at between approximately 0.15 and 0.20  $\mu\text{A}$ . This was thought to have been an issue with the reference / counter electrode used in the cell, and after the serum change at 333,000 cycles the electrode was changed. Up to 666,000 cycles, with a new electrode, this device displayed much larger corrosion currents. A peak of 10.6  $\mu\text{A}$  immediately followed the serum change and then the corrosion current remained between 3.3 - 5.1  $\mu\text{A}$ . The current dropped for a brief period between 550,000 and 600,000 cycles before returning to previous values. After the second serum change the corrosion current dropped to values observed during standard gait. They were larger than had been observed over the first 333,000 cycles although it was possible the same electrode had been used.

The second femoral head displayed higher corrosion currents over the entire one million cycles. Following an initial high peak of 24.7  $\mu\text{A}$  after the initiation of sliding, the  $I_{corr}$  remained between 2.0 and 3.5  $\mu\text{A}$  for the majority of articulation. Again the corrosion current for the MoC femoral heads was observed to be much

more stable than the MoM series.

### 7.2.3 - Estimated Volume Loss

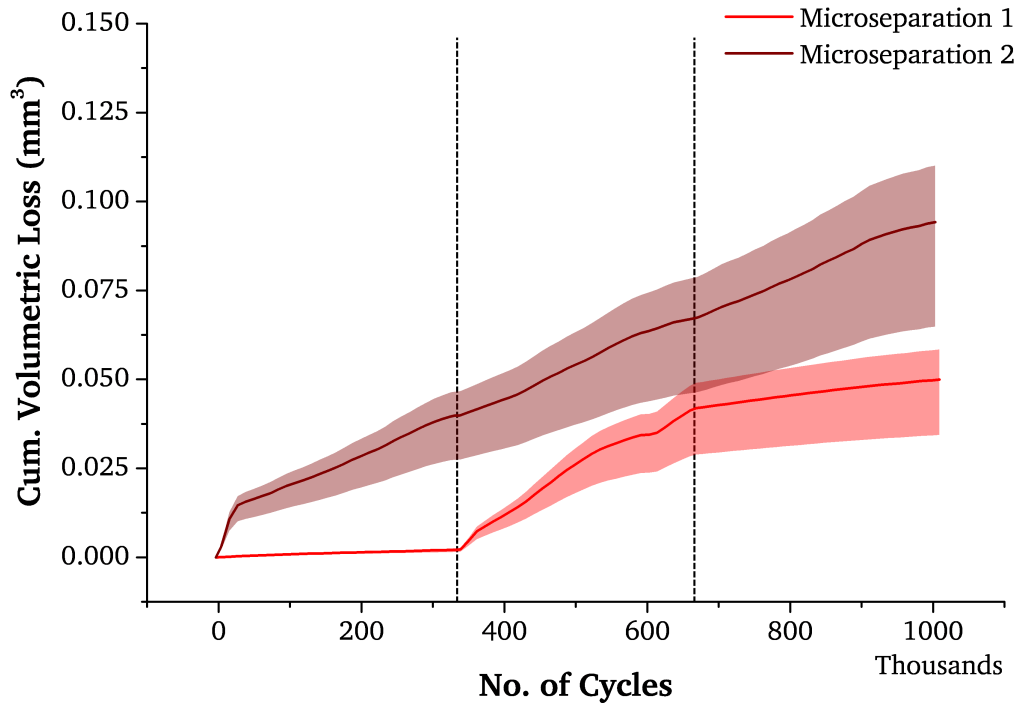


Figure 7.7: Estimated Volume Loss as a result of oxidation at the bearing surface for 28 mm MoC bearings under 0.8 mm Microseparation over 1 million cycles. Upper and lower error bars represent possible preferential release of *Co* and *Cr* ions respectively. Vertical dashed lines represent serum changes.

The estimated volume loss as a result of corrosion from the femoral heads in the MoC series can be seen in Figure 7.7. The final values for corrosive volume loss were 0.05 and 0.09 mm<sup>3</sup> for the first and second bearings respectively. The final value for the first device was considered suspect due to the possible electrode failure. If the first bearing was assumed to have had an equal amount of corrosion take place over the first 333 kcycles, then an equivalent value of 0.09 mm<sup>3</sup> would have also been observed. For the second bearing the final value represented a seven-fold increase in overall estimated corrosive degradation as a result of applying microseparation to the gait cycle. Had the corrosion currents and thus rate of mass loss been consistent over the entire test, and similar to values noted for the second bearing, the final estimated mass loss may have been higher.

## 7.2.4 - Anodic Current Transient

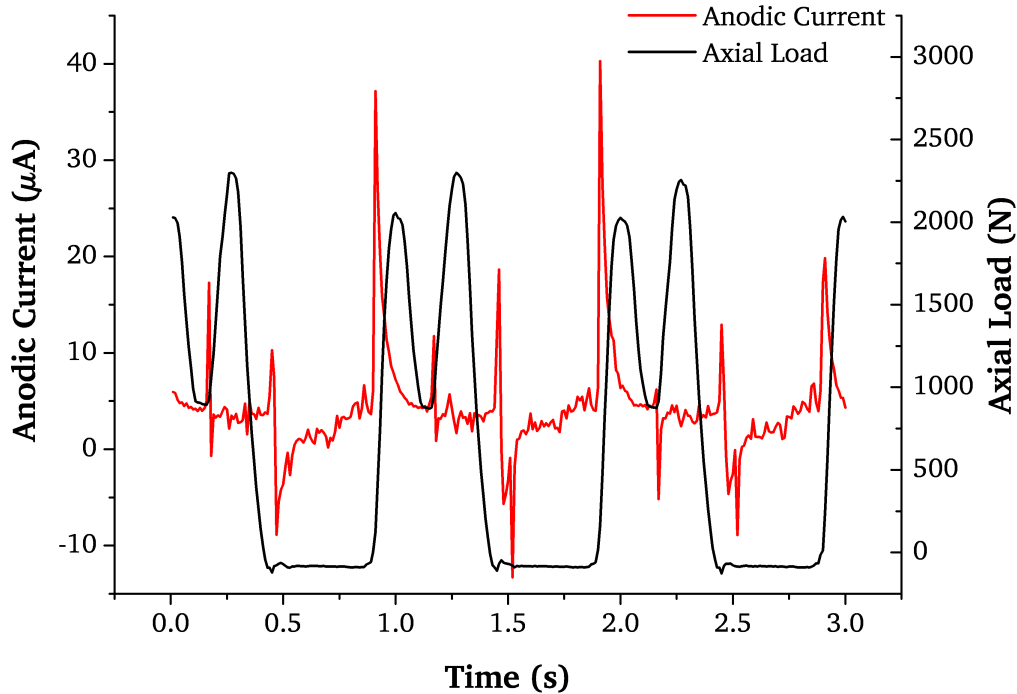


Figure 7.8: Example Anodic Current Transient (+50 mV vs. OCP) for 28 mm MoC bearing under three cycles of 0.8 mm Microseparation.

Figure 7.8 shows a typical anodic current transient (+50 mV vs. OCP) recorded from the MoC series of bearings subjected to microseparation. Again the transient shape was different than those observed during standard gait. The shape was also radically different than for the MoM series under microseparation. Peaks in anodic current of up to 40  $\mu\text{A}$  were frequently noted upon the initiation of ‘heel-strike’ of each cycle. Average values of  $<5.0 \mu\text{A}$  were noted for the majority of the cycle, similar to under standard gait.

The anodic current transients also frequently displayed negative values at the beginning of the swing phase portion of each cycle. Negative currents of between -10 and -20  $\mu\text{A}$  were routinely recorded across both tests (Microsep 1: 333,000-666,000 cycles) before quickly returning to positive values.

### 7.3 - Gravimetric Mass Loss

For the Metal-on-Ceramic series an attempt was made to determine the overall volume loss from the components, in order to estimate the proportion of material loss from the bearing surface as a result of corrosion. This was not undertaken for the Metal-on-Metal series in order to study the formation of tribofilms on the implant surfaces, which may have been affected by the cleaning procedure necessary for gravimetric assessment. The components were cleaned and weighed before the test according to the procedure set out in ISO-14242-2:2000 [177]. The components were weighed on an analytical balance with  $\pm 0.01$  mg precision (XP205, Mettler Toledo, Switzerland) in a controlled atmosphere. Each component was weighed in rotation until five readings within 0.1 mg were obtained.

At serum changes the components were left *in situ* and the cell was flushed three times with deionised water. After one million cycles was reached the components were removed, cleaned and weighed again. The difference between the two gravimetric points was then taken as the total material loss as a result of articulation during the test. The mass loss from the femoral heads can be seen in Table 7.2. After one million cycles under Standard Gait gravimetric material loss of the femoral heads was recorded at 1.27 and 2.96 mg for the first and second bearing respectively. For Microseparation gravimetric mass losses of 6.09 and 4.40 mg were noted. A density of  $8.29 \text{ g/cm}^3$  was taken for *CoCrMo* alloy to convert values to volume losses [46].

	Mass Loss (mg)	Volume Loss ( $\text{mm}^3$ )	Est. Corrosive Loss ( $\text{mm}^3$ )	Percentage Corrosion (%)
SG 1	1.27	0.15	0.013	8.4
SG 2	2.96	0.36	0.017	4.8
MS 1	6.09	0.74	0.090	12.2
MS 2	4.40	0.53	0.094	17.7

Table 7.2: Gravimetric Mass Loss for 28 mm MoC Femoral Heads after one million cycles under Standard Gait and Microseparation

Comparing the gravimetric volume loss to the estimated corrosive loss it is possible to obtain values of 4.8 and 8.4 percentage corrosive loss under Standard Gait and as high as 17.7 percent under Microseparation. Due to the apparent electrode issues during 'Microseparation 1' the final percentage value was calculated assuming a similar rate of corrosion over the first 333 kcycles. Corrosive rates did appear similar between 333,000 and 666,000 cycles. On the acetabular cup side, no significant material loss was noted from the ceramic cups. In two cases, under both standard gait and microseparation, the ceramic inserts displayed a mass gain after one million cycles.

#### **7.4 - Coordinate Measuring Machine (CMM)**

Figures 7.10 and 7.10 shows example pre- and post-test scans respectively for a metal femoral head tested under standard gait Metal-on-Ceramic articulation. The initial scans taken before testing for both Standard Gait bearings displayed a slightly flattened area just off the pole of the femoral head. This was coupled with a slightly raised area on the opposite side of the pole. This pattern was thought to have been a result of the manufacturing process and polishing techniques. For the head shown in Figures 7.9 and 7.10, this difference was very pronounced over the pole, moving from  $-5.5 \mu\text{m}$  from the nominal sphere to  $+7.3 \mu\text{m}$ .

After one million cycles of standard gait articulation the head still displayed this pattern although it covered a wider portion of the bearing surface. The range of deviation from the nominal sphere over the pole of the head also shifted from approximately  $-6.9$  to  $+6.3 \mu\text{m}$ . This suggested wear over the pole had increased the flattened area and worn down the raised portion slightly.

Figure 7.11 shows an example post-test scan for a metal femoral head tested under microseparation Metal-on-Ceramic articulation. After 1 Mcycle of microseparation 'stripe wear' patterns, as had been seen previously in the Metal-on-Metal bearings, were noted on the surface. The deviation of these wear scars from the nominal

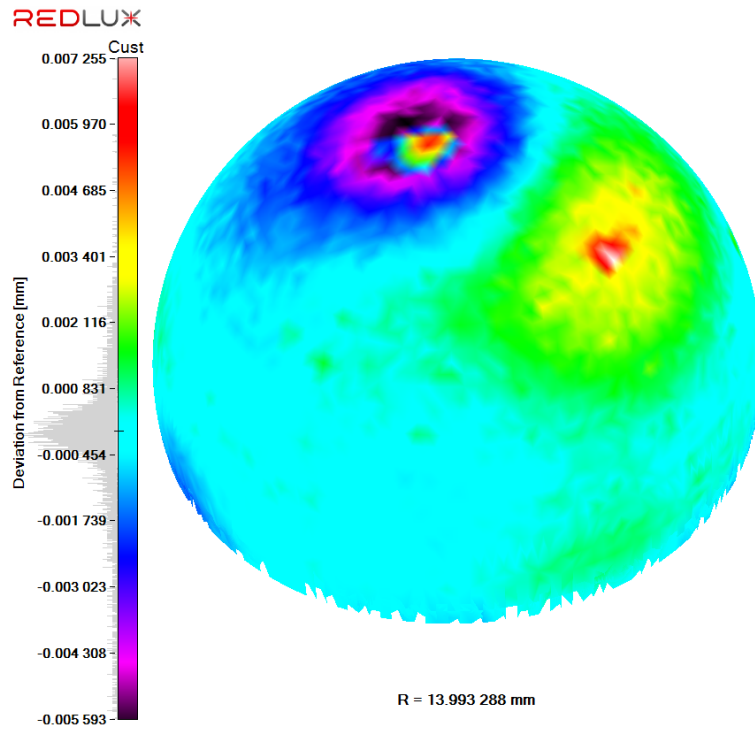


Figure 7.9: Sphere Form Profile Analysis of a new 28 mm *CoCrMo* alloy femoral head.

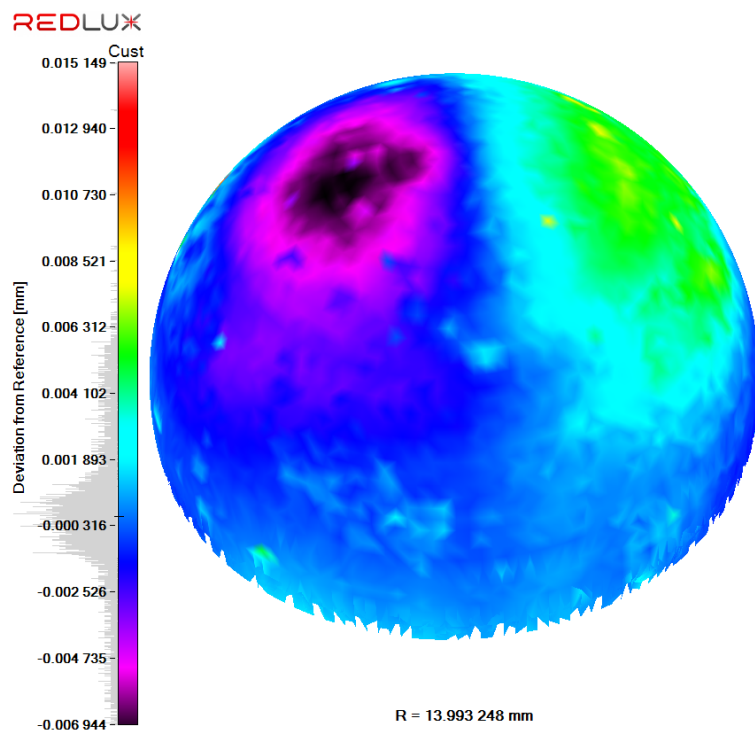


Figure 7.10: Sphere Form Profile Analysis of a 28 mm *CoCrMo* alloy femoral head articulated against a ceramic acetabular cup for 1 Mcycle of Standard Gait.

spheres was approximately  $-25.2$  and  $-18.8 \mu\text{m}$  for MS-1 and MS-2 respectively. The estimated volume loss within the 'stripe wear' scars was 0.247 and 0.188

mm<sup>3</sup> respectively.

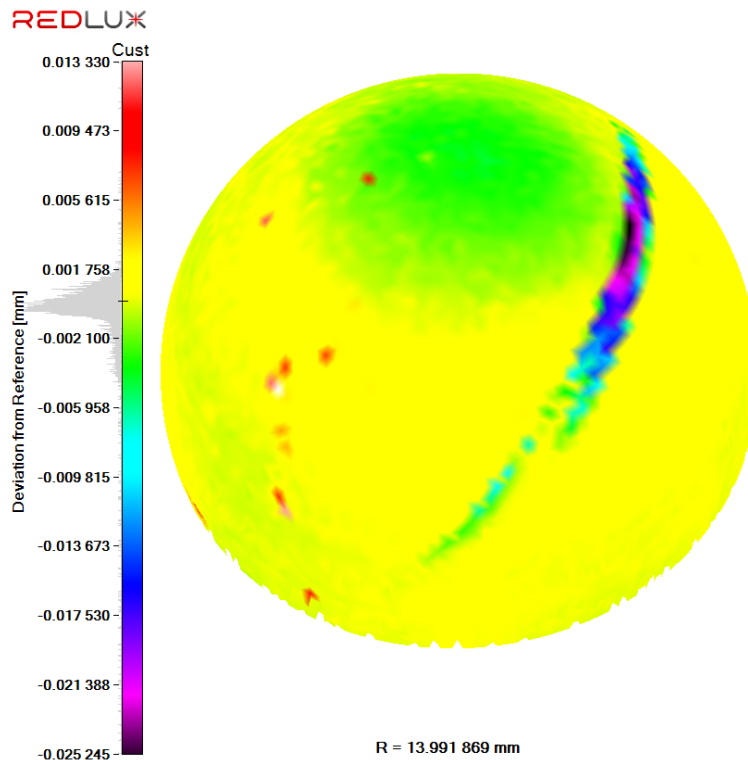


Figure 7.11: Sphere Form Profile Analysis of 28 mm *CoCrMo* alloy femoral head articulated against a ceramic acetabular cup after 1 Mcycle of Microseparation.

Figure 7.12 also highlights noted areas to the rear of the femoral head showing a secondary stripe region. Such regions of damage had been observed previously by Clarke *et al.* [200] in 28 mm Metal-on-Metal retrievals and were termed ‘equatorial’ or ‘basal’ stripes depending on their position on the head and if they continued over the edge of the articulating surface. These stripes were observed to be approximately 2-4  $\mu\text{m}$  deeper from the nominal sphere than the immediately surrounding areas of the head and could represent another area of significant wear and material loss.

## 7.5 - Summary

- For Metal-on-Ceramic bearings moving from a standard gait articulation to a microseparation increased the estimated material corrosive mass loss from the femoral head from 0.013 and 0.017 mm<sup>3</sup> to 0.094 mm<sup>3</sup>.

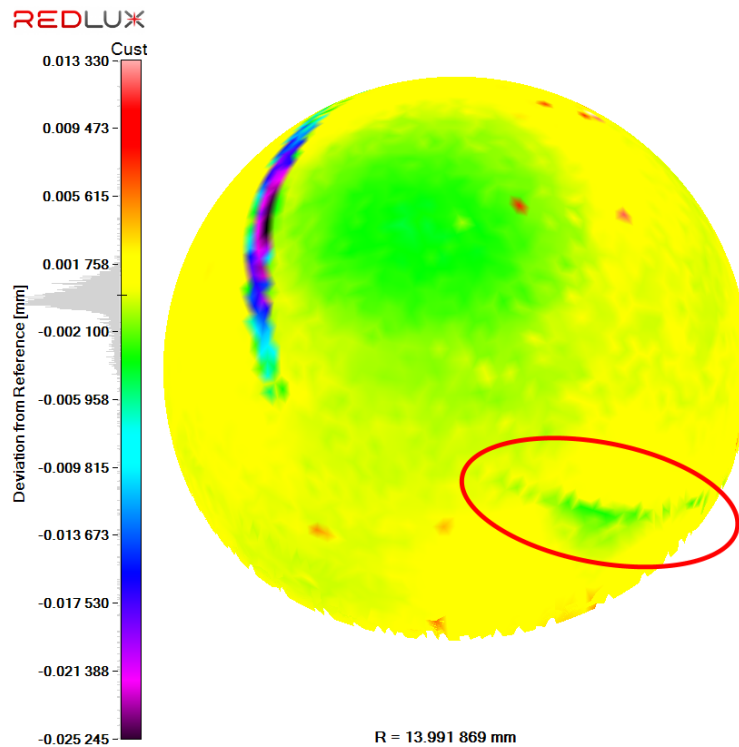


Figure 7.12: Sphere Form Profile Analysis of a 28 mm Metal-on-Ceramic femoral head after 1 Mcycle articulation under Microseparation showing rear 'equatorial' stripe.

- Comparing this increase to the gravimetrically determined mass loss the percentage contribution of corrosion from the femoral head to total degradation increased from approximately 4-8% to as much as 17.7%.
- Peaks in the anodic current transients also increased by a near order of magnitude, similar to the Metal-on-Metal bearings, although a different typical transient shape was noted under microseparation.
- CMM and RedLux sphere profile analysis showed minimal wear under standard gait but clear 'stripe wear' and 'basal stripe' patterns under microseparation. After only 1 Mcycle however the wear scars did not deviate sufficiently from the nominal sphere to attain accurate volume loss measurements.

## Chapter 8 - Adverse Loading

This chapter presents the results of short-term tests performed on the Full-ISO Electromechanical Simulator. The more advanced simulator, with more accurate following of input profiles as shown in Chapter 4, was used to investigate the electrochemical effects of various adverse loading scenarios of increasing interest in the literature. As discussed in Chapter 3, many studies equate the poor performance of the MoM class of total hip replacements to adverse loading. Much of the current research reported in the literature is therefore concerned with improvement of simulation techniques in order to capture these failure modes [124–126, 136, 200–202].

This chapter therefore utilizes the sensitive and real-time nature to *in situ* electrochemical measurement to observe the role of tribology and contact conditions as a function of malpositioning and daily living cycle profiles.

### 8.1 - Malpositioning

Malpositioning of hip replacement components has been discussed in Chapter 3 of this thesis. Several studies have demonstrated the effects of malpositioning on simulator wear rates and ion release [127–129]. Other studies suggested that certain MoM devices may have been particularly susceptible to various types of malpositioning [203, 204]. In this section two types of acetabular cup malpositioning; inclination and retroversion are discussed.

#### 8.1.1 - Inclination (New Bearing)

The Full-ISO Electromechanical Simulator was used to investigate the effect of acetabular cup inclination on corrosive material loss. To begin, a new 28 mm MoM bearing was taken and subjected to the short-term testing profile described in Section 4.2.5. OCP was monitored continuously throughout the test and after

an initial rest period of 3,600 seconds, an ISO 14242-1 profile [166] was run for 4,000 cycles. After sliding the components were allowed to stabilise again. During the static and sliding periods three LPR sweeps were performed ( $\pm 25$  mV, 1 mV/s) in order to determine the corrosion current ( $I_{corr}$ ) as described previously. A potentiostatic anodic polarisation (+50 mV vs. OCP) was also performed during sliding and the resultant anodic current sampled at 5 Hz.

The angle of inclination was varied from 30 to 50° in 5° increments. The maximum angle was limited to 50° for 28 mm bearings by the design of the simulator. As the head was held in place on a vertical spigot (shown in Figure 4.12) a higher angle would have resulted in the bottom of the cup impinging on the 316L stainless steel spigot. The bearing was then allowed to stabilise for an hour before the inclination was adjusted for the next test. The OCP data for this series can be seen in Figure 8.1.

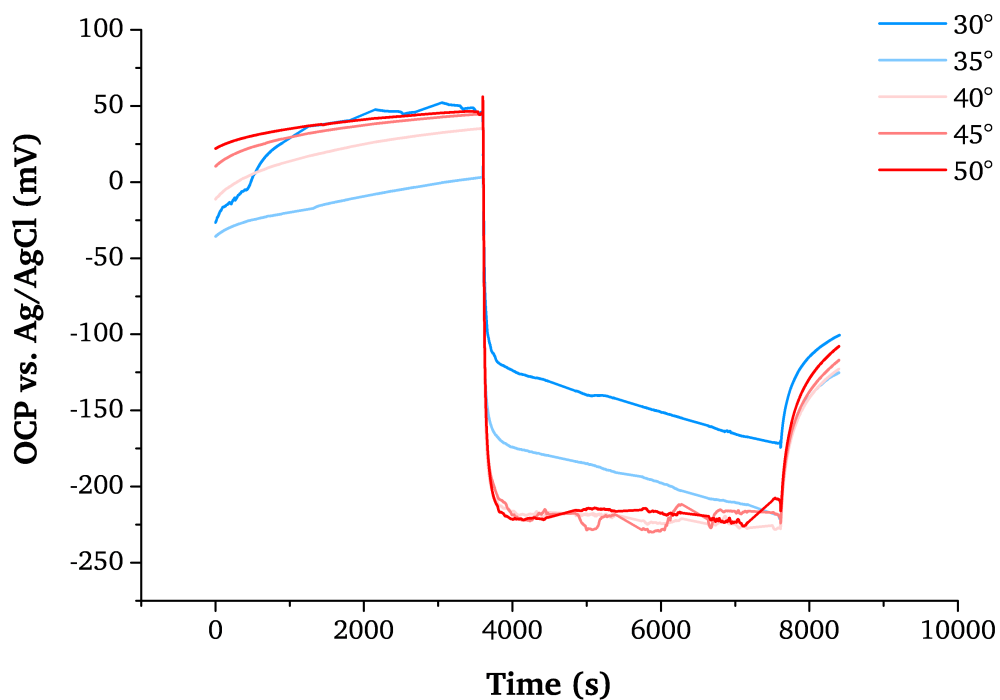


Figure 8.1: Open circuit potential for a new 28 mm MoM bearing articulating under an ISO 14242-1 profile for 4,000 cycles at varying angles of cup inclination.

During the initial static period the bearing displayed a gradual ennoblement for all angles, resulting in potentials of between 0 and +50 mV. Upon the initiation

of sliding a cathodic shift in OCP was noted for all angles of inclination as had been seen previously on the pneumatic simulator. Both 30 and 35° inclinations displayed a shift of approximately -150 mV. The OCP for these angles continued to shift cathodically during sliding with final potential values of -171 and -220 mV respectively.

The higher angles of inclination displayed larger cathodic shifts upon sliding of approximately -250 to -260 mV, reaching a final value of approximately -225 mV. The larger shifts qualitatively suggested more corrosion was taking place. The bearing at these angles of inclination remained stable at an OCP of -225 mV over the 4,000 cycles of articulation. When sliding was halted all angles then displayed a typical ennoblement in OCP.

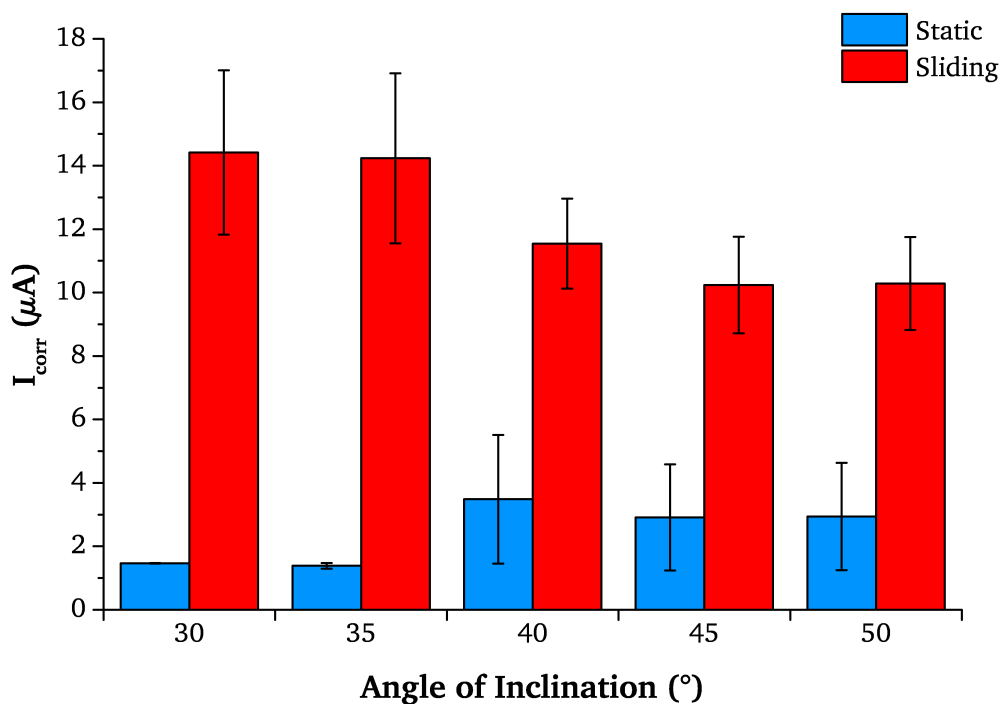


Figure 8.2: Corrosion current ( $I_{corr}$ ) for a new 28 mm MoM bearing under static and sliding conditions at varying angles of cup inclination. Error bars represent standard deviation,  $n = 3$ .

Figure 8.2 displays the average corrosion currents calculated from the Polarisation Resistance ( $R_p$ ) during static and sliding conditions. As expected the current was found to be higher during sliding. However increasing the angle of inclination did not appear to result in increased corrosion. In fact the calculated corrosion current

during sliding fell from approximately  $14.5 \mu\text{A}$  at  $30^\circ$  and  $35^\circ$  to approximately  $10 \mu\text{A}$  at  $45^\circ$  and  $50^\circ$ . No significant difference was noted in static or sliding  $I_{corr}$  at different angles of inclination (ANOVA,  $p < 0.05$ ).

This was thought to be caused by the nature of the sample. On a fresh bearing initial corrosion currents may have been dominated by initial contact conditions; when mechanical wear (asperity shearing) was greatest. The initial high corrosion current seems to support this as an  $I_{corr}$  of  $14.5 \mu\text{A}$  was much larger than steady-state values observed for these devices under standard gait in Chapter 6. This trend was also noted in the anodic currents, shown in Figure 8.3.

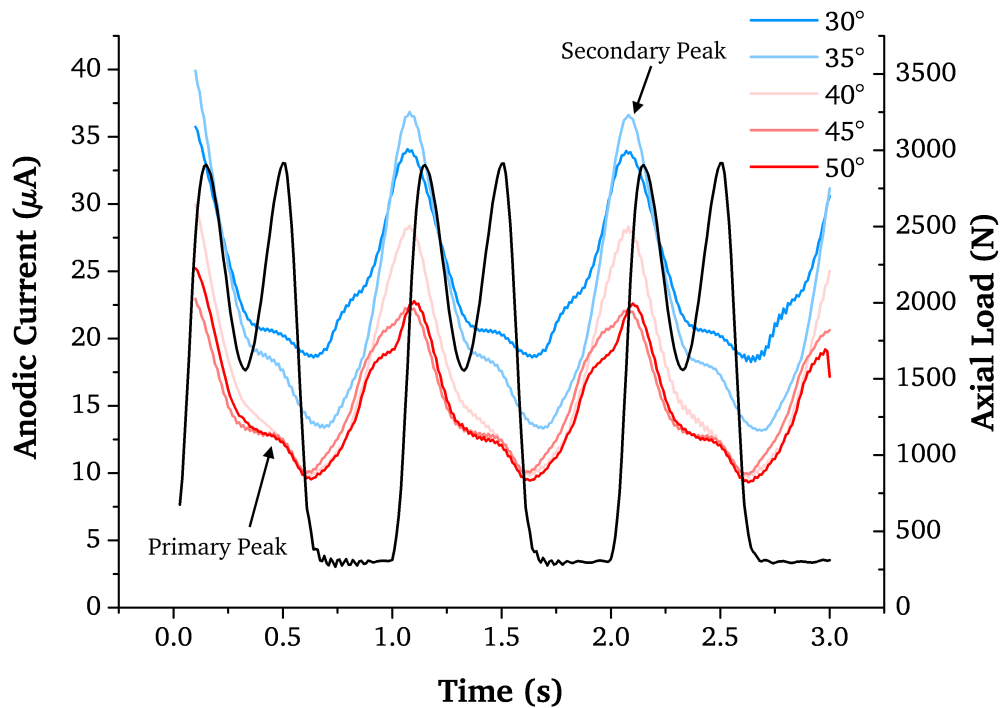


Figure 8.3: Anodic current transients (+50 mV vs. OCP) for a new 28 mm MoM bearing articulating under an ISO 14242-1 profile at varying angles of cup inclination.

The anodic current transients reduced in magnitude with increasing angle of acetabular inclination. At  $30^\circ$  a base-line current of approximately  $20 \mu\text{A}$  was established with peak values of  $37 \mu\text{A}$ . Moving to  $45^\circ$  and  $50^\circ$  the base-line current fell to approximately  $10 \mu\text{A}$  with peaks of approximately  $22 \mu\text{A}$ . This was again thought to be dominated by early bedding-in of the device, with anodic current transients higher than values observed during steady-state in Chapter 6. Interestingly these

early current transients did not display a fully developed twin-peak following of the loading profile typically observed for these bearings as outlined in Chapter 6. A slight primary peak may be seen around ‘toe-off’ but was not clearly defined and appeared to be dominated by the secondary peaks.

### 8.1.2 - Inclination (After 333k Cycles)

Before a second series of tests was performed the bearing was articulated for 333,000 cycles under the same standard ISO-14242 profile [166]. This was done in order to begin the bedding-in process of the device and reach an electrochemically stable state whereby the effect of changing the cup inclination could be evaluated without being dominated by high short-term initial currents. After the 333,000 cycles were completed, the lubricant serum was changed and the same test profile performed previously on the ‘new bearing’ was repeated for 30 to 50° cup inclinations. Figure 8.4 shows the OCP over the course of articulation for the second series of tests after 333 kcycles of articulation.

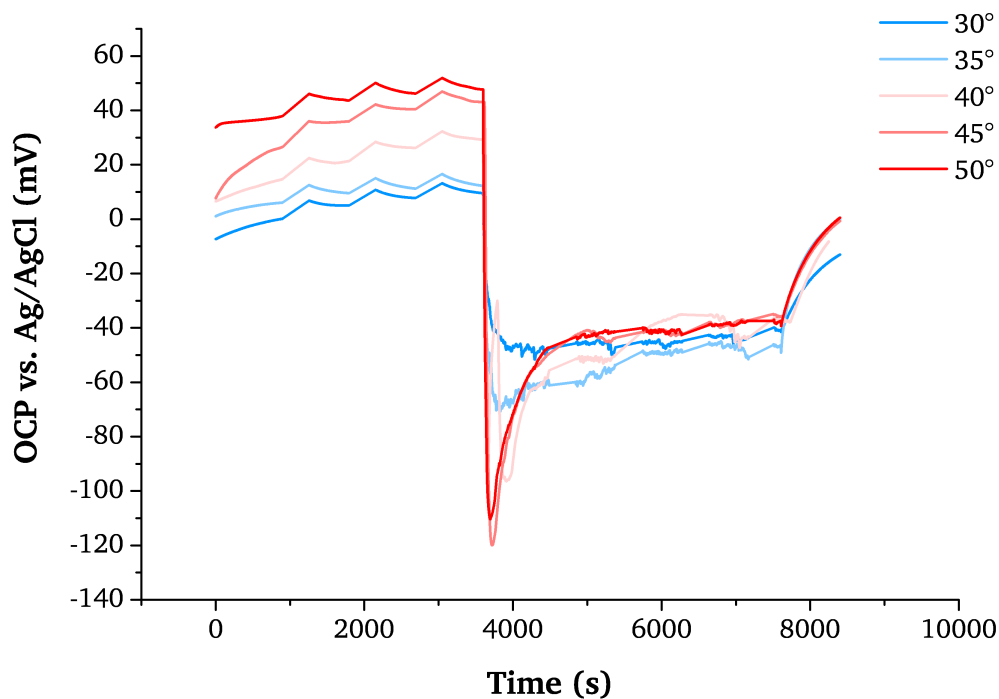


Figure 8.4: Open circuit potential for a 28 mm MoM bearing, after 333 kcycles of sliding, articulating under an ISO 14242-1 profile for 4,000 cycles at varying angles of cup inclination.

Again a static OCP of between 0 and +50 mV was established after 3,600 seconds of stabilisation for all angles of inclination. Upon the initiation of sliding much smaller cathodic shifts in OCP were observed. At 30 and 35° shifts of approximately -50 and -75 mV were noted respectively. The OCP also gradually moved more noble during sliding, remaining at approximately -50 mV until sliding was halted and OCP again shifted noble. This behaviour is similar to trends observed under standard gait and shown in Chapter 6, wherein OCP gradually shifted noble during sliding.

Greater cathodic shifts were again observed at higher angles of inclination than at the low angles; both 45 and 50° shifted cathodically by approximately -150 mV. These initial lower OCP values quickly ennobled over the first 1,000 cycles of sliding however, reaching values similar to those observed at 30°.

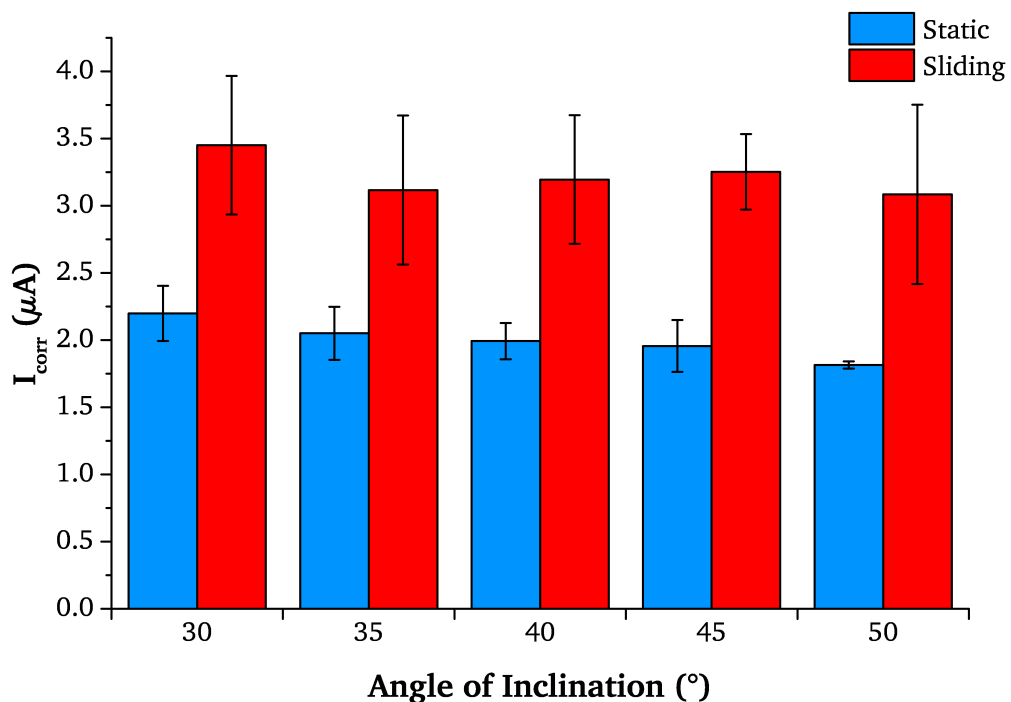


Figure 8.5: Corrosion current ( $I_{corr}$ ) for a 28 mm MoM bearing, after 333 kcycles of sliding, under static and sliding conditions at varying angles of cup inclination. Error bars represent standard deviation,  $n = 3$ .

Static and sliding corrosion currents for the second series of tests can be seen in Figure 8.5. The bearing had appeared to reach a steady-state with  $I_{corr}$  values of approximately 2.0 - 2.25 and 3.0 - 3.5  $\mu A$  under static and sliding respectively. The

sliding values after 333 kcycles for  $I_{corr}$  were more comparable to those observed for MoM bearings under standard gait on the pneumatic simulator in Chapter 6. There was again no observed significant change in corrosion current as a result of increased angle of inclination (ANOVA,  $p < 0.05$ ). The lack of any effect of inclination on measured current was also mirrored in the anodic polarisation current transients, shown in Figure 8.6.

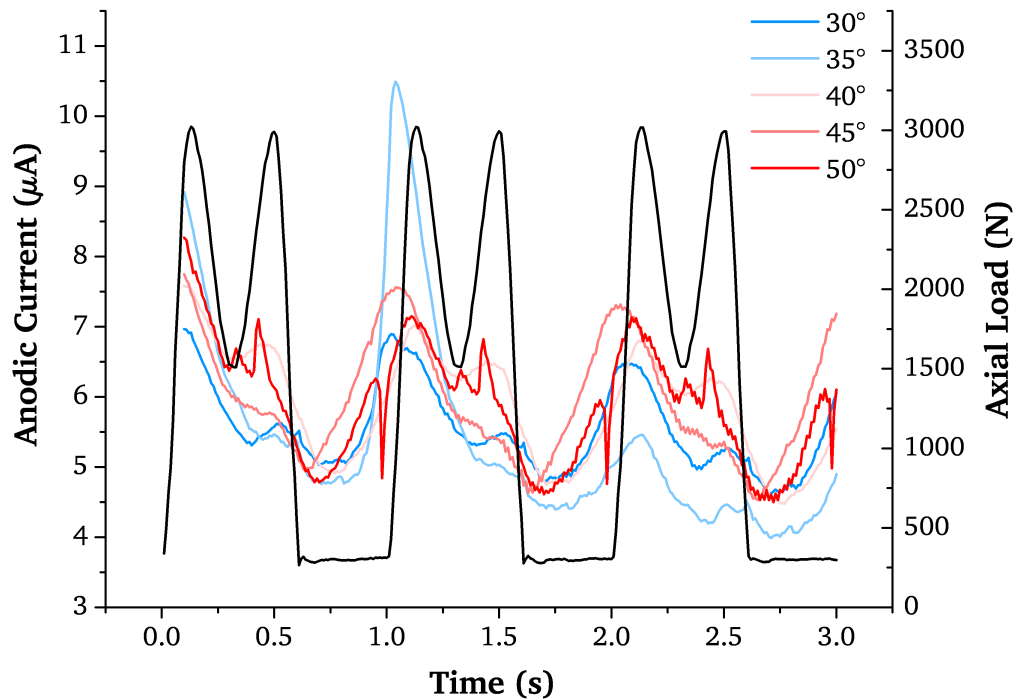


Figure 8.6: Anodic current transients (+50 mV vs. OCP) for a 28 mm MoM bearing, after 333 kcycles of sliding, articulating under an ISO 14242-1 profile at varying angles of cup inclination.

At 30° inclination a base-line current of approximately 5  $\mu\text{A}$  was observed with peaks of approximately 6.5 - 7.0  $\mu\text{A}$ . Moving to 45 and 50° a similar base-line anodic current was established with slightly larger peaks of 7.0 - 7.5  $\mu\text{A}$ . Whilst Figure 8.6 does seem to suggest a trend of increased anodic current with increased cup inclination although no significance was found in the peak values (ANOVA,  $p < 0.05$ ). Having also allowed the bedding-in process for a period of cycles, the anodic current transients shown in Figure 8.6 also established a much clearer twin-peak shape with well defined primary peaks.

The series of tests performed after 333 kcycles again did not reveal clear increased

corrosion currents as a result of higher angles of inclination. These results countered the hypothesis that a more severe rim-contact induced by inclination would increase the tribocorrosive degradation. This also did not appear to agree with the literature which demonstrated higher simulator lubricant ion levels with inclination [202].

In both series of tests, 'new bearing' and after 333 kcycles, larger cathodic shifts in OCP upon sliding for higher inclination did not appear to agree with the LPR and polarisation results. However, as shown in Figure 8.4, the OCP rapidly recovered to low-inclination values before the first LPR sweep was taken. This first LPR sweep may therefore be missing early degradation of the device.

A new hypothesis was formed that under continuous cyclic 1 Hz testing the bearings can quickly reach an 'electrochemical steady-state.' This is not only unrepresentative of *in vivo* articulation during different activities, but also may be limiting the assessment of corrosive degradation which is very much a time dependant process. A new method for assessing the corrosive loss over the first cycles after initiation of sliding was needed to capture this information.

### **8.1.3 - Inclination (Polarisation)**

In order to investigate the corrosive degradation immediately after the initiation of sliding a third series of tests was performed. The bearing was allowed to stabilise for 3,600 seconds, then polarised to +0 mV versus the *Ag/AgCl* reference electrode as opposed to the working electrode OCP. Sliding was then initiated for 600 cycles and the resultant anodic current was sampled at 5 Hz. The experiment was repeated three times in 'parallel' and 'series' configurations shown in Figures 8.7 and 8.8 respectively. Under the 'parallel' configuration three repeats were performed at a given inclination before the angle was increased. Under 'series' the angle was increased after each test then reverted back to 30°.

Under both approaches a clear trend of increased anodic current as a result of

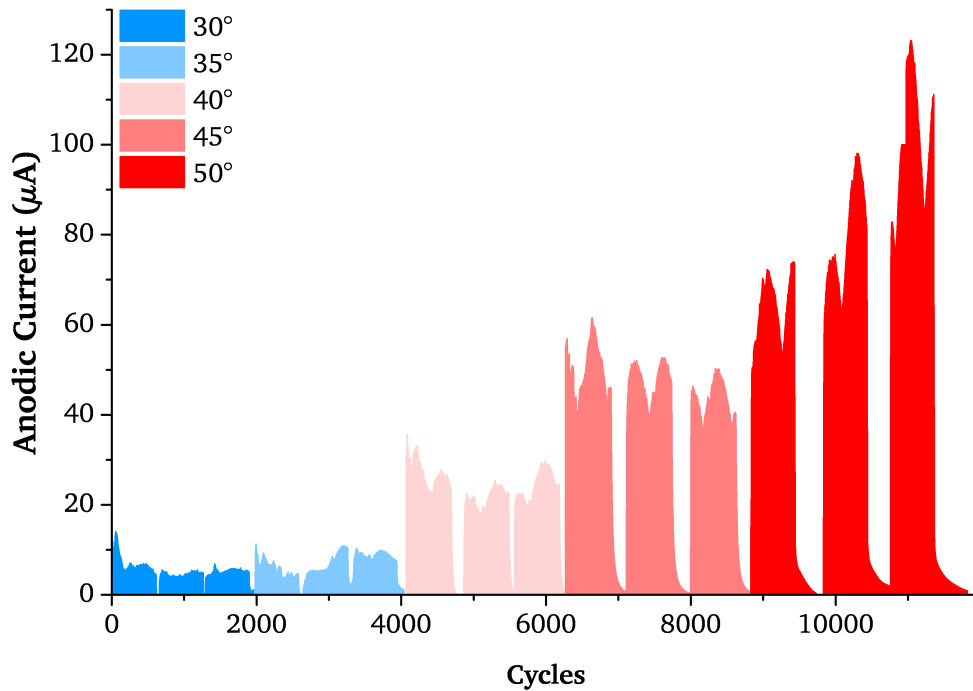


Figure 8.7: Anodic current transients (+0 mV vs. Ref.) over the first 600 cycles for a 28 mm MoM bearing, after 333 kcycles of sliding, articulating under an ISO 14242-1 profile at varying angles of cup inclination increased in ‘parallel.’

inclination was observed. In ‘parallel’ at 30 and 35° anodic currents of approximately 4 - 10  $\mu\text{A}$  were noted which agreed with steady-state values reported both in Chapter 6 and the series of tests after 333 kcycles of articulation. Upon increasing the inclination to 40° the anodic currents immediately increased to 20 - 40  $\mu\text{A}$  and again to 40 - 60  $\mu\text{A}$  at 45°. At the final 50° inclination the anodic current increased to 60 - 70  $\mu\text{A}$  for the first repeat and continued to climb to over 120  $\mu\text{A}$  by the third repeat. This represents over an order of magnitude increase in the observed anodic current as a result of a 20° increase in the inclination of the bearing.

Under the ‘series’ configuration a trend was observed of increased anodic current at lower inclination immediately following a high inclination test. The ‘series’ tests were started immediately after the ‘parallel’ tests and at 30° (following the ‘parallel’ 50°) a higher anodic current of approximately 25  $\mu\text{A}$  was observed. As the inclination was increased the anodic current transient also increased to approximate averages of 50, 60, 90 and 110  $\mu\text{A}$ . Upon reverting back to 30° even higher

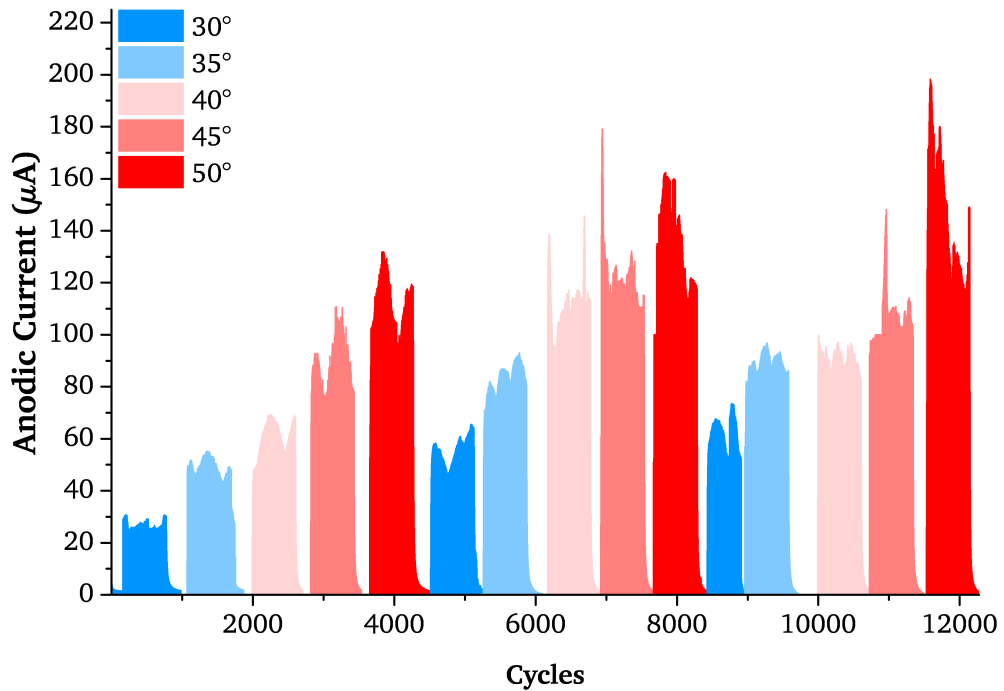


Figure 8.8: Anodic current transients (+0 mV vs. Ref.) over the first 600 cycles for a 28 mm MoM bearing, after 333 kcycles of sliding, articulating under an ISO 14242-1 profile at varying angles of cup inclination increased in ‘series.’

transients of approximately 50  $\mu\text{A}$  were recorded and this pattern occurred again for the third repeats.

#### 8.1.4 - Retroversion

A second malpositioning scenario was also investigated, namely increased retroversion. As discussed in Chapter 3 retroversion of the acetabular cup can also affect the lubrication and performance of a device. The retroversion of the acetabular cup was increased from 0° (coincident with the coronal plane) to 20° again in 5° increments and polarised to 0 mV vs. reference for 600 cycles of sliding. The anodic current transients, sampled at 5 Hz, can be seen in Figure 8.9.

Under increased retroversion a similar trend of raised anodic current was observed. At 0° version an average current of approximately 18  $\mu\text{A}$  was noted. Upon increasing the retroversion to 5° the current immediately increased to an average of approximately 24  $\mu\text{A}$ . This trend continued with average currents of approxi-

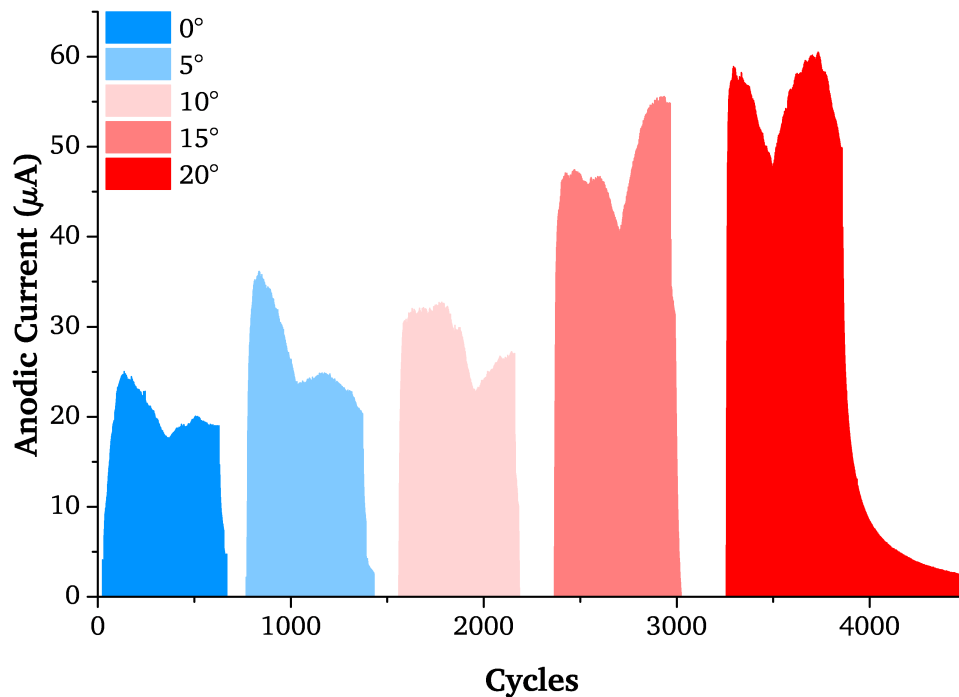


Figure 8.9: Anodic current transients (+0 mV vs. Ref.) over the first 600 cycles for a 28 mm MoM bearing, after 333 kcycles of sliding, articulating under an ISO 14242-1 profile at varying angles of cup retroversion.

mately 28, 45 and 55  $\mu\text{A}$  for 10, 15 and 20° retroversion respectively. Whilst not as large an increase as observed for inclination this still represents a significant growth in corrosive degradation as a result of a different mode of malpositioning.

## 8.2 - Link Between Corrosion and Tribology

The nature of the Full-ISO Electromechanical Simulator enabled a much greater degree of accuracy in the response and following of a given load profile input. As shown in Figure 4.11 the near exact following of the load and rotational axes enables a much greater degree of accuracy when syncing the measured anodic current transients over a cycle. Previous studies by Hesketh *et al.* [15, 150] have attempted to link the anodic current to a ‘severity factor’ calculated from the tribological conditions at a given point in the cycle. Hesketh *et al.* [15] noted that the main features of their ‘severity factor’ were observed in the anodic current, but the two appeared out of phase. Observations made in Chapters 6 and 7 of this thesis agreed with this finding, whereby peaks in the anodic current measured during

articulation also appeared to be out of phase with the axial load.

In order to determine if this phase lag was purely a time delay in the electrochemical cell or a function of the cycle tribology a 28 mm MoM device was placed in the Full-ISO Electromechanical Simulator. The bearing was articulated under a standard ISO 14242-1 loading profile [166] for 333 kcycles. The bearing was then run at different cycle frequencies from 0.4 to 1.4 Hz for 1,800 seconds, the OCP plot for which is shown in Figure 8.10. Finally during sliding the bearing was polarised to +50 mV vs. OCP and the resultant anodic current transient was sampled at 100 Hz. The anodic current for each cycle frequency can be seen alongside axial load in Figure 8.11.

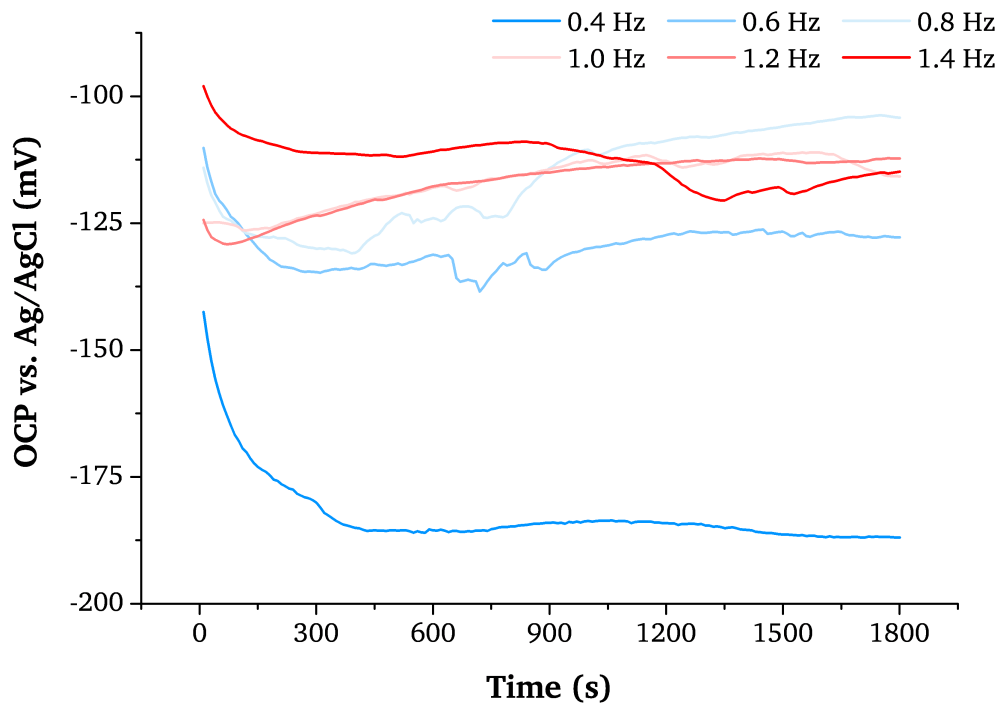


Figure 8.10: Open circuit potential for a 28 mm MoM bearing after 333 kcycles of articulation under an ISO 14242-1 profile at cycle frequencies ranging from 0.4 to 1.4 Hz.

Similar to other tests performed, once sliding was initiated a cathodic shift in OCP was noted at all frequencies, shown in Figure 8.10. At the lower cycle frequencies (< 1.0 Hz) larger and more sustained cathodic shifts were observed. At 0.4 Hz for example the OCP shifted cathodically to approximately -185 mV and remained stable there during sliding. At 0.6 and 0.8 Hz there were also larger cathodic

shifts but, as observed previously, the OCP gradually shifted noble to similar values noted for the standard 1.0 Hz ( $\approx$  -100 to -130 mV). At 1.4 Hz this relationship appeared to change with a slight cathodic shift upon sliding and then continued to shift cathodically over the remainder of the experiment. The larger and more sustained cathodic shifts appeared to result in larger anodic current transients, shown in Figure 8.11.

The transients closely matched typical shapes seen on the pneumatic simulator, although a direct comparison is difficult as the loading profile was different. At all cycle frequencies a twin peak profile was noted with a primary peak appearing during ‘toe-off’ and a typically larger secondary peak at the initiation of ‘heel-strike.’ Figure 8.12 shows the peak anodic currents and initial OCP cathodic shift for each frequency. These values are plotted against the maximum entrainment velocity ( $u$ ) over a cycle, calculated later in this section. As described above, greater initial cathodic shifts were observed when reducing the cycle frequency from 1.0 Hz. This was coupled with an increase in the peak anodic current noted during polarisation after 1,800 seconds. Increasing the frequency from 1.0 Hz also resulted in larger initial cathodic shifts at 1.2 and 1.4 Hz, but the peak anodic current continued to fall, possibly due to changes in the lubrication regime.

The position of the anodic peaks in current remained fairly consistent between frequencies and occurred at similar points in the cycle. A trend of decreasing anodic current magnitude with increasing cycle frequency was also noted. Had the phase difference been purely a time delay inherent in the electrochemical cell, the current peaks would have been expected to occur a fixed time after a peak in load for all frequencies. This did not appear to be the case and in-fact the time delay between peaks in load and current reduced with increasing frequency, as shown in Figure 8.13.

The reduction in time delay occurred at a similar ratio to the increase in cycle frequency. This further suggested that the peaks were occurring at the same point

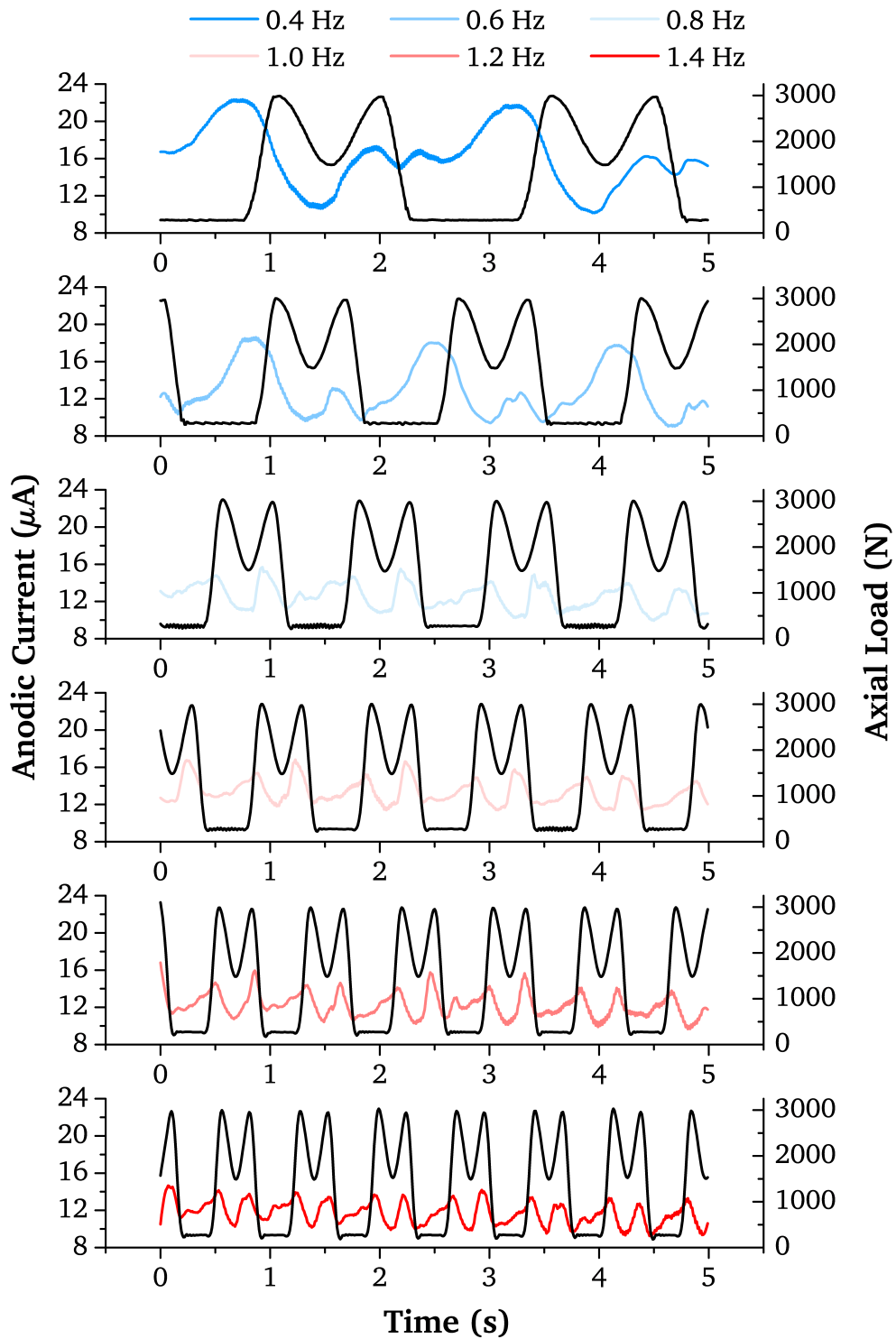


Figure 8.11: Anodic current transient (+50 mV vs. OCP) and axial load for a 28 mm MoM bearing under an ISO 14242-1 profile at cycle frequencies ranging from 0.4 to 1.4 Hz.

in the cycle, rather than being delayed after the loading peak. They were therefore not thought to be simply out of phase with the load, but a response to some other tribological factor at that point in the cycle. The ‘severity factor’ first pro-

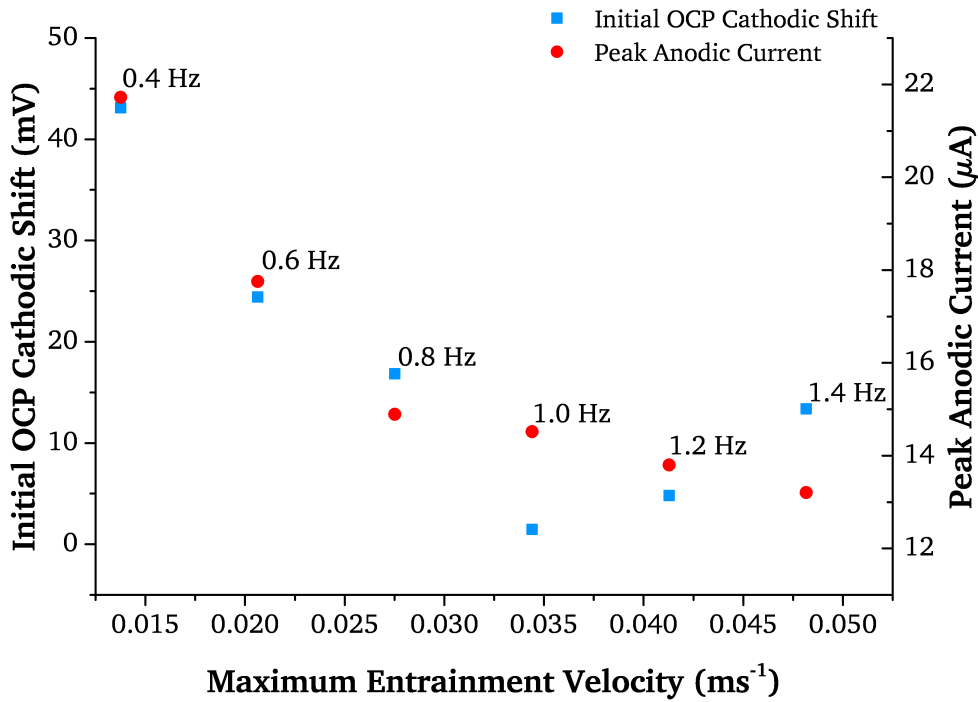


Figure 8.12: Initial OCP cathodic shift and peak anodic current for a 28 mm MoM bearing under an ISO 14242-1 profile at cycle frequencies ranging from 0.4 to 1.4 Hz.

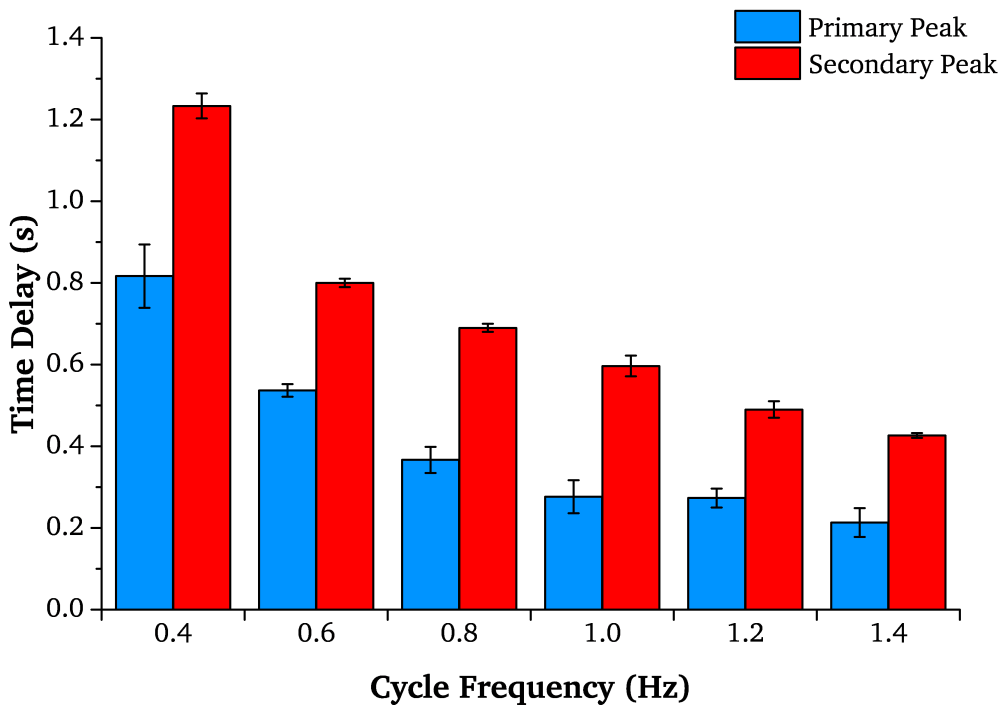


Figure 8.13: Time delay between peaks in axial load and anodic current transient for different cycle frequencies. Error bars represent standard deviation,  $n = 3$ .

posed by Hesketh *et al.* [15] was a first attempt to characterise the tribological condition and link it to the corrosive degradation. However this appeared to be as

inadequate as comparing to the loading curve.

The simplified 2D model shown in Chapter 2 (Figure 2.6) was utilised for this study in an attempt to plot the Theoretical Minimum Film Thickness ( $h_{min}$ ) with the Anodic Current. The Anodic Current was therefore rescaled as a function of cycle percentage, and can be seen Figure 8.14 for each frequency.

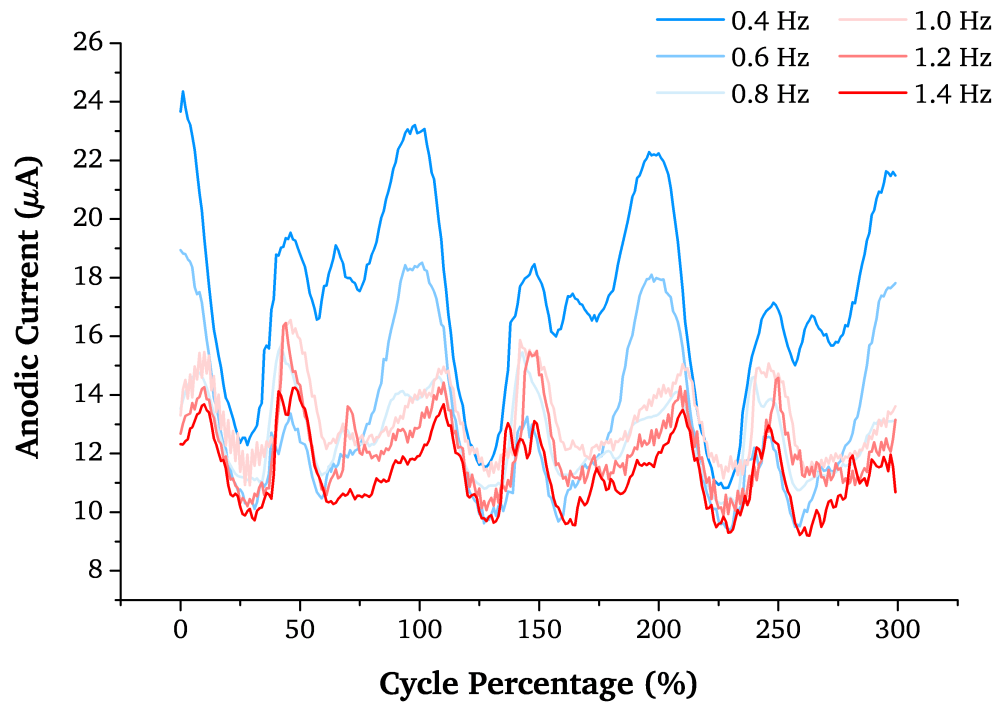


Figure 8.14: Three cycles of anodic current transient (+50 mV vs. OCP) for a 28 mm MoM bearing articulating under an ISO 14242-1 profile at cycle frequencies ranging from 0.4 to 1.4 Hz.

When viewed as a function of the cycle percentage, as in Figure 8.14, the alignment of peaks in Anodic Current to a particular point of a cycle became much clearer. Peaks appeared to occur at approximately 50 % through each cycle and at the end of each cycle for 0.4 and 0.6 Hz, i.e. 100 %. For the faster frequencies the secondary peaks shifted slightly into the next cycle at approximately 15 %. At 0.4 Hz a third peak was also noted in-between the primary and secondary peaks which had not been observed previously in any other tests.

The Hamrock-Dowson equation (Equation 2.10) was used to estimate the minimum film thickness over the three cycles. Standard values of Young's Modulus

and Poisson's Ratio for *CoCrMo* alloy were used ( $E = 230$  MPa,  $\nu = 0.3$ ) and a diametrical clearance of  $100 \mu\text{m}$  was taken. In order to calculate the lubricant entrainment velocity ( $u$ ) at each point in the cycle the change in position for each rotational axis was used to calculate an angular velocity. The angular velocity was converted to a sliding speed for each axis for the 28 mm diameter bearing and then combined to give a resultant vector, as per Equation 8.1.

$$u_{res} = \sqrt{u_{FE}^2 + u_{AA}^2 + u_{IE}^2} \quad (8.1)$$

- Where:
- $u_{res}$  = Resultant entrainment velocity (m/s)
  - $u_{FE}$  = Flexion / Extension entrainment velocity (m/s)
  - $u_{AA}$  = Abduction / Adduction entrainment velocity (m/s)
  - $u_{IE}$  = Internal / External rotation entrainment velocity (m/s)

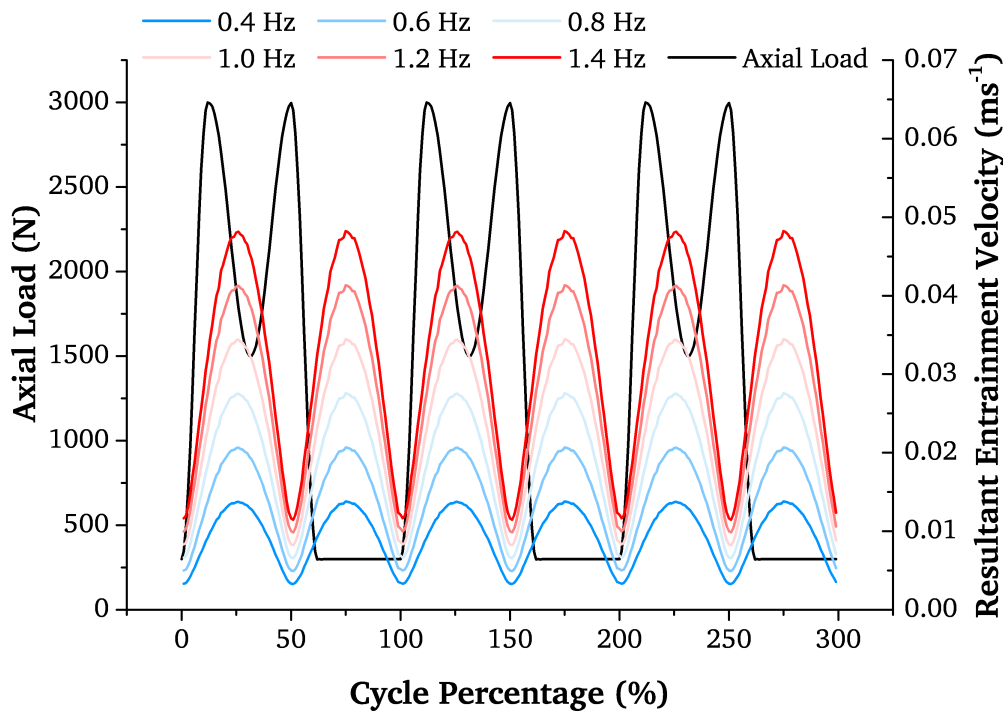


Figure 8.15: Axial Force and Resultant Entrainment Velocity at the contact for a 28 mm MoM bearing articulating under an ISO 14242-1 profile at cycle frequencies ranging from 0.4 to 1.4 Hz.

Figure 8.15 shows the axial force and calculated resultant entrainment velocity over three cycles for each cycle frequency. An assumption of the Hamrock-Dowson equation is that the system is in 'steady-state' and neglects phenomena such as

'squeeze film,' lubricant entrainment occurs at a 1:1 ratio with angular velocity. Thus the shape and locations of peaks in entrainment velocity did not vary but the magnitude of those peaks did change. The maximum entrainment velocity at each frequency varied from approximately 0.014 to 0.048 ms<sup>-1</sup>. This was a much larger than the variance between minimum entrainment velocities, which ranged from 0.012 to 0.003 ms<sup>-1</sup>. The points of minimum entrainment occurred at approximately 50 and 100 % through each cycle, i.e. at 'toe-off' and the initiation of 'heel-strike' for the next cycle. This corresponded to the peaks in anodic current for each frequency noted in Figure 8.14.

The minimum film thickness was then inverted ( $1/h_{min}$ ) in order to give peaks at points in the cycle when the film was thinnest. This would correspond to more asperity-asperity contact during sliding and thus more depassivation of the surface; represented by peaks in current. The inverted minimum film thickness was plotted for each cycle frequency with anodic current and can be seen in Figure 8.16.

The inverted minimum film thickness appeared to give a much better correlation between the anodic current and the tribological conditions at a given point in the cycle than the 'severity factor' previously proposed by Hesketh *et al.* [15, 150]. Figure 8.16 shows for each cycle frequency the peaks in anodic current aligned reasonably well with points of minimum film thickness. This appeared to confirm the hypothesis that at these points in each cycle more asperity-asperity contact occurred, as a result of a thinner lubricating film, which resulted in a more severe depassivation of the protective oxide layer and thus greater corrosive degradation at the sliding interface.

The magnitude of current also appeared to scale with the magnitude of inverted film thickness between the cycle frequencies. Moving from 0.4 to 1.4 Hz the peak anodic current fell from approximately 22 to 13  $\mu\text{A}$ . The maximum inverted film thickness also fell from approximately 0.15 to 0.06 (1/nm). When viewed on the

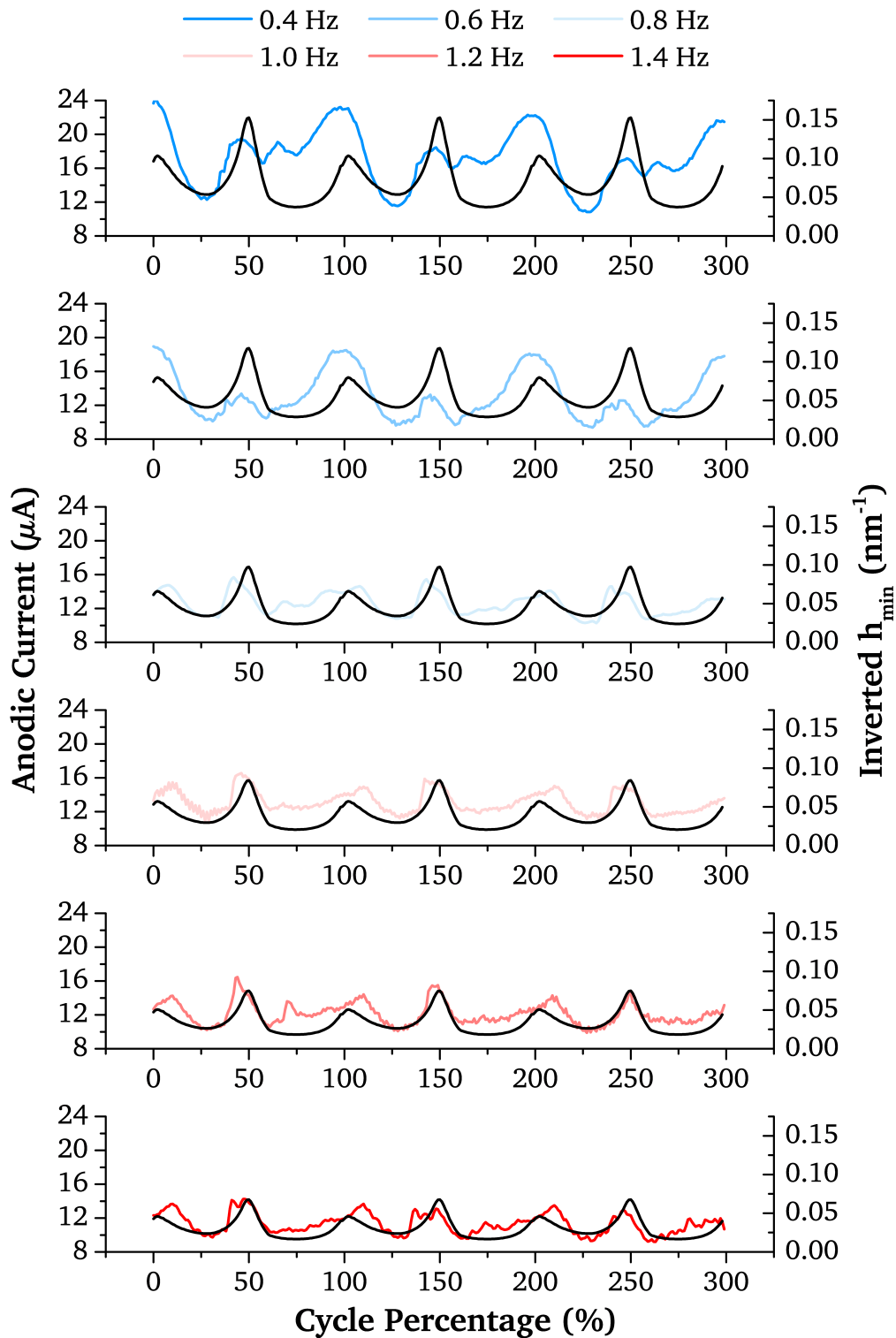


Figure 8.16: Anodic Current Transient (+50 mV vs. OCP) and Inverted Theoretical Minimum Film Thickness for a 28 mm MoM bearing under an ISO 14242-1 profile at cycle frequencies ranging from 0.4 to 1.4 Hz.

same scale, as in Figure 8.16, there appeared to be a good correlation between the overall tribological severity at a given frequency and the resultant anodic current.

The simplified 2D model applied in this study appeared to still have limitations. Whilst being closer to linking the tribology of a cycle to the corrosive degradation some things did not fully correlate. For example according to the model the primary peak in inverted film thickness at ‘toe-off’ (50 %) was always more severe than the secondary peak at the initiation of ‘heel-strike’ (100 %). This was not always mirrored in the anodic current transient however. At the lower frequencies, and in previous experiments reported in Chapters 6 and 7, typically the secondary peaks are larger than the primary peaks as shown at 0.4 and 0.6 Hz. The anodic current at 0.4 Hz also displayed a strange third peak which was completely unexplained by the model. This third peak had not typically been seen previously in any experiment in the present study, although Hesketh *et al.* [15] did demonstrate three-peak transients for 36 mm bearings.

### **8.3 - Daily Living Activities**

Another current focus in the literature on, adverse loading is testing under so called ‘Daily Living Activities.’ A continuous 1 Hz walking profile, as typically performed in simulator studies, is not how THR bearings articulate *in vivo* [173, 175, 176]. Throughout a given day a person may go through a number of different articulation profiles one after another such as: walking, climbing stairs, stumbling etc. All of which subject the device to different loads and also much larger areas of the bearing surface will undergo sliding and rubbing.

As mentioned earlier in this chapter it may be possible for continuous cyclic 1 Hz simulator testing to achieve an electrochemical ‘steady-state.’ It is also possible that this may occur in terms of the tribology and mechanical wear. Hadley *et al.* [121–123] demonstrated that simply introducing dwell periods in between cycles, termed ‘stop-dwell-start’ testing (SDS), resulted in five to fifteen fold increases in the mean gravimetric wear rate of 36 mm MoM bearings. This was hypothesised as resulting from the loss of lubricating films during the dwell period.

The aim of this section was therefore to take an initial look at how some of these Daily Living cycles perform electrochemically in the Full-ISO simulator. Data provided by Bergmann *et al.* [173, 175] was used to generate three Daily Living profiles; a 1 Hz ‘physiological gait,’ a 0.667 Hz ‘stair climb’ and a combined 0.5 Hz ‘chair down - up’ profile intended to mimic sitting in and getting out of a chair. The three profiles can be seen in Figure 4.13.

The 28 mm MoM bearing was subjected to the same test conditions used when varying the cycle frequency. The bearing was articulated under the different daily living profiles for 1,800 seconds then subjected to an anodic polarisation of +50 mV vs. OCP and the resultant anodic current sampled at 100 Hz. Similarly the axial load and positional data for the profiles was fed into the simplified 2D model and Hamrock-Dowson equation in order to calculate the theoretical minimum film thickness ( $h_{min}$ ) over each of the cycles. Whilst not performed in a true daily living scenario, the current transients served as a first look at the corrosive degradation under these profiles.

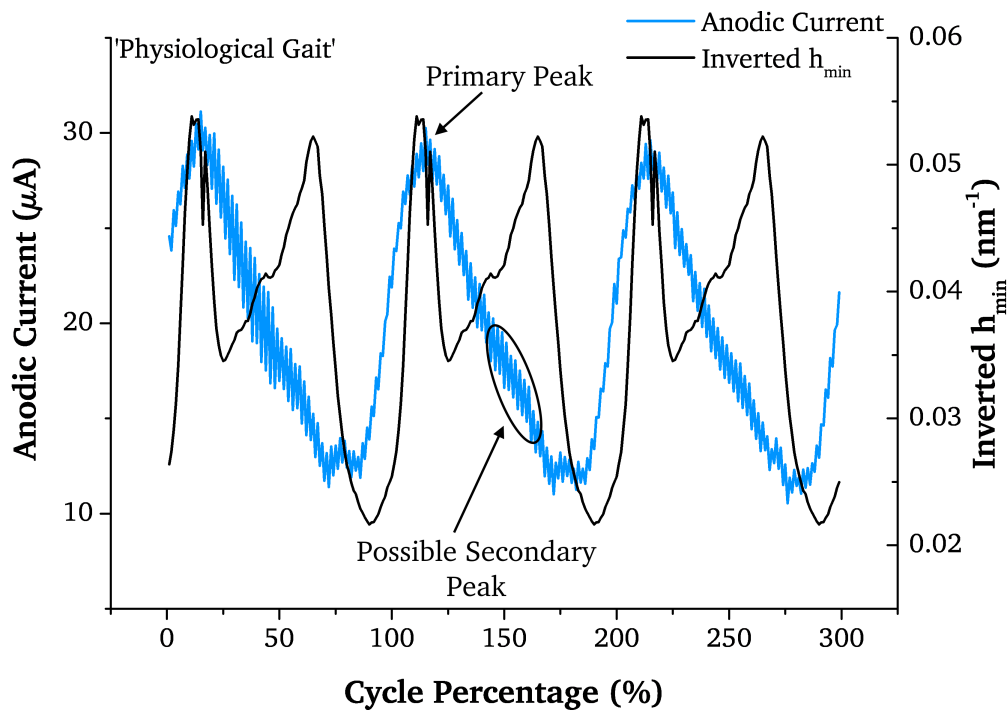


Figure 8.17: Anodic Current Transient (+50 mV vs. OCP) and Inverted Theoretical Minimum Film Thickness for a 28 mm MoM bearing under a ‘Physiological Gait’ cycle derived from data provided by Bergmann *et al.* [173, 175].

Figures 8.17, 8.18 and 8.19 show the anodic current transients and inverted film thickness as a function of cycle percentage for the 'physiological gait,' 'stair climb' and 'chair down - up' profiles respectively. Under 'physiological gait' the shape of the anodic current transient, shown in Figure 8.17, was different to those noted for the ISO 14242-1 profiles. The transient shape appeared to consist only of a single peak of approximately  $30 \mu\text{A}$  which occurred at the initiation of 'heel-strike.' This peak in current aligned with a peak in the inverted film thickness, although the model appeared to break down further in the cycle. A second peak in inverted film thickness was noted approximately at 'toe-off' but was not coupled with a peak in current, which continued to fall until the next 'heel-strike.' There was a slight change to the current curve around this point but was not a clearly well defined peak. Both of the inverted film thickness peaks occurred approximately at points of maximum and minimum Flexion / Extension; where the entrainment velocity was at a minimum. The simplicity of the model may have underestimated the film thickness at the 'toe-off' point of the more complex 'physiological' profile, as observed and discussed by Gao *et al.* [205, 206].

Under the 'stair climb' profile, shown in Figure 8.18, the current transient took on a completely new shape, not seen previously. A large primary peak initiated just after the 'toe-off' point approximately 75 % through each cycle. The magnitude of this peak was also double that of 'physiological gait' at approximately  $59 \mu\text{A}$ . A much smaller secondary peak was observed soon after at approximately 20 % through each cycle. Again the simplified 2D model for inverted film thickness did not appear to align with the current transient and showed completely different shapes and peaks that occurred at different points through each cycle.

The anodic current transient for the 'chair down - up' profile demonstrated multiple peaks throughout each cycle ranging from  $17.5 \mu\text{A}$  to  $28 - 29 \mu\text{A}$ , shown in Figure 8.19. Some of the peaks were also fairly broad and occurred over as much as 50 % of each cycle which would translate to high corrosive material loss. Whilst

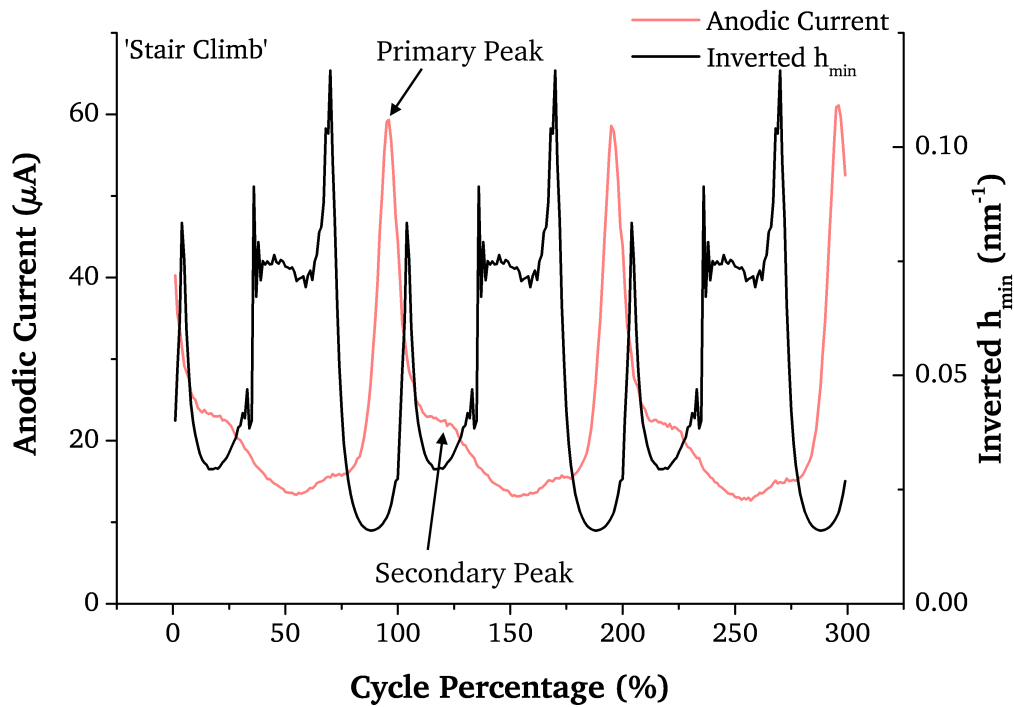


Figure 8.18: Anodic Current Transient (+50 mV vs. OCP) and Inverted Theoretical Minimum Film Thickness for a 28 mm MoM bearing under a 'Stair Climb' cycle derived from data provided by Bergmann *et al.* [173, 175].

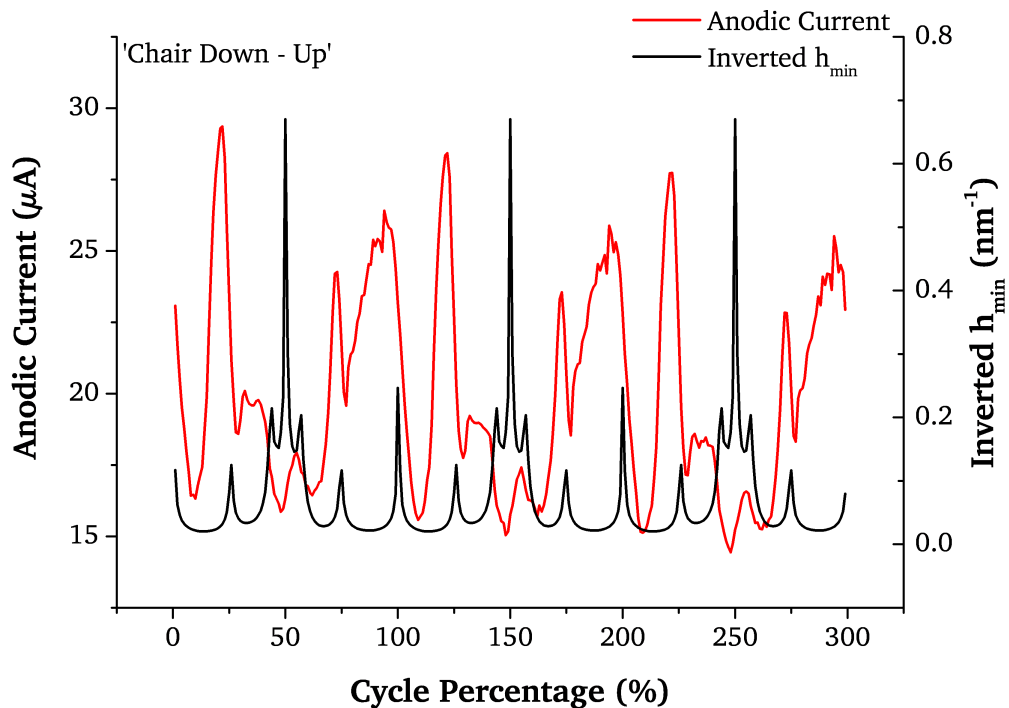


Figure 8.19: Anodic Current Transient (+50 mV vs. OCP) and Inverted Theoretical Minimum Film Thickness for a 28 mm MoM bearing under a 'Chair Down - Up' cycle derived from data provided by Bergmann *et al.* [173, 175].

again there did not appear to be a good alignment between the current and the inverted film thickness, the simplified model did appear to pick up on the complex nature of the profile; resulting in several points of minimum film thickness.

## 8.4 - Summary

- Acetabular malpositioning (inclination and retroversion) resulted in significantly higher anodic current transients over the first 600 cycles of articulation.
- Initial corrosive degradation appeared to be dominated by the ‘bedding-in’ process of the bearing.
- A simplified 2D lubrication model based on an expression of the Hamrock-Dowson equation showed close agreement with the current transients of a 28 mm bearing articulating to an ISO-14242 gait cycle.
- This model did not appear to align with the more complicated motion of ‘daily living’ profiles. These profiles were not run in ‘steady state’ conditions in that the profiles were run for 333 kcycles before testing, which may have been a complicating factor.

The electrochemical degradation of Metal-on-Metal devices under so-called Adverse Loading scenarios was discussed in this chapter. The results of experiments indicated that continuous 1 Hz cyclic simulator testing may not fully capture and explain the degradation of THR implants, or how they are likely to perform *in vivo*. Full joint simulators are currently used as benchmarking tools, to assess one design or material against another. As the poor clinical performance of MoM devices and the subsequent market recalls have demonstrated, more stringent testing is required as part of pre-clinical THR assessment.

Malpositioning can have a large effect on the measured gravimetric wear for devices [127–129, 203, 204] but perhaps more importantly for MoM bearings

change the degradation mechanism and increase the release of metal ions into the joint by an order of magnitude. Periodicity in anodic current transients and a simplified lubrication model has shown a clear link between the tribology over a cycle and the resultant corrosive degradation. More sophisticated models are clearly required to fully assess and map the tribology at the sliding interface, in order to better predict implant performance.

## Chapter 9 - Discussion

The second generation of Metal-on-Metal Total Hip Replacements, both traditional and resurfacing designs, are widely accepted to have been a clinical failure. Following the rapid downturn in their use they have been the subject of various medical device alerts issued in the UK [80–82] and US [83]. These alerts advised restricted implantation of Metal-on-Metal devices in the patient demographics they had been originally targeted at. They also recommended closer follow-up procedures for patients with MoM hips already implanted, such as yearly *Co* and *Cr* blood and urine ion level checks. In 2014 the UK's National Institute for Health and Care Excellence (NICE) recommended stricter guidelines for hip replacement devices; suggesting they should demonstrate less than 5 % failure rates at 10 years [207]. Only two MoM bearings met the new guidelines; one of which, the Birmingham Resurfacing device, was found more recently to have much worse success rates than previously thought for smaller bearing diameters and in women [208, 209].

The recall of these devices from the market has also been significantly costly for the medical device manufacturers. As well as the cost of revision surgeries, they have been the subject of intense litigation and negative press. Stryker (MI, USA) settled a class action lawsuit brought by 1,500 plaintiffs for \$1.4 billion [210]. Johnson & Johnson (NJ, USA), the parent company behind the DePuy ASR device (Depuy Synthes, UK), settled another class action brought by 8,000 patients for \$4 billion [211]. In a separate case five patients were also awarded \$498 million from Johnson & Johnson in March 2016, almost \$360 million of which was punitive damages [212]. The cost in patient suffering as a result of a poor performance must also be considered. One of the primary indicators for revision surgery of MoM devices recorded in the UK was pain [79]. As discussed in Chapter 3 their failure and need for early revision is also often associated with other conditions

such as tissue necrosis, metallosis, ALVAL and pseudotumors.

The full extent of how MoM devices were likely to perform *in vivo*, and thus their mentioned complications, was not captured in pre-clinical testing. The industry gold-standard, Metal-on-Polymer bearings pioneered by Charnley [2, 72], typically achieve success rates of > 95 % at ten years follow-up [213]. Their longer term survival however is often limited by aseptic loosening of the components, caused by osteolysis induced by polymer wear debris. Gravimetric wear rates from components articulated in hip simulators, and wear debris analysis, can therefore be a good measure of how a new MoP design or material is likely to fair in the body. This is largely how the second generation of MoM THRs were benchmarked and compared to MoP bearings; through hip simulation and comparison of gravimetrically assessed wear rates.

Metal-on-Polymer wear rates vary greatly depending on bearing size and the material type and processing. Typical figures used for comparison with Metal-on-Metal bearings were in the magnitude of 30 mm<sup>3</sup> per million cycles of articulation [108, 214–216]. Figure 9.1 shows volumetric wear rates of MoM devices reported across various hip simulator studies since their introduction and values for MoP wear they were assessed against. The initial excitement around second generation MoM THRs was clearly very understandable. The gravimetrically determined wear rates per million cycles in like-for-like hip simulation was often two orders of magnitude lower, or more, under comparable walking cycles [108, 112, 113, 116, 125, 154, 201, 202, 217–220]. This was also coupled with promising clinical studies which demonstrated good early success and lower penetration rates found in retrieved MoM components [96, 221–223]. Isolation of the wear debris also suggested a smaller particle size distribution which was thought to lie outside the ‘bio-active’ range for wear induced osteolysis [52, 76, 224].

The surprising poor clinical performance of MoM THR bearings has therefore been the focus of much research and study within the recent literature. A large part of

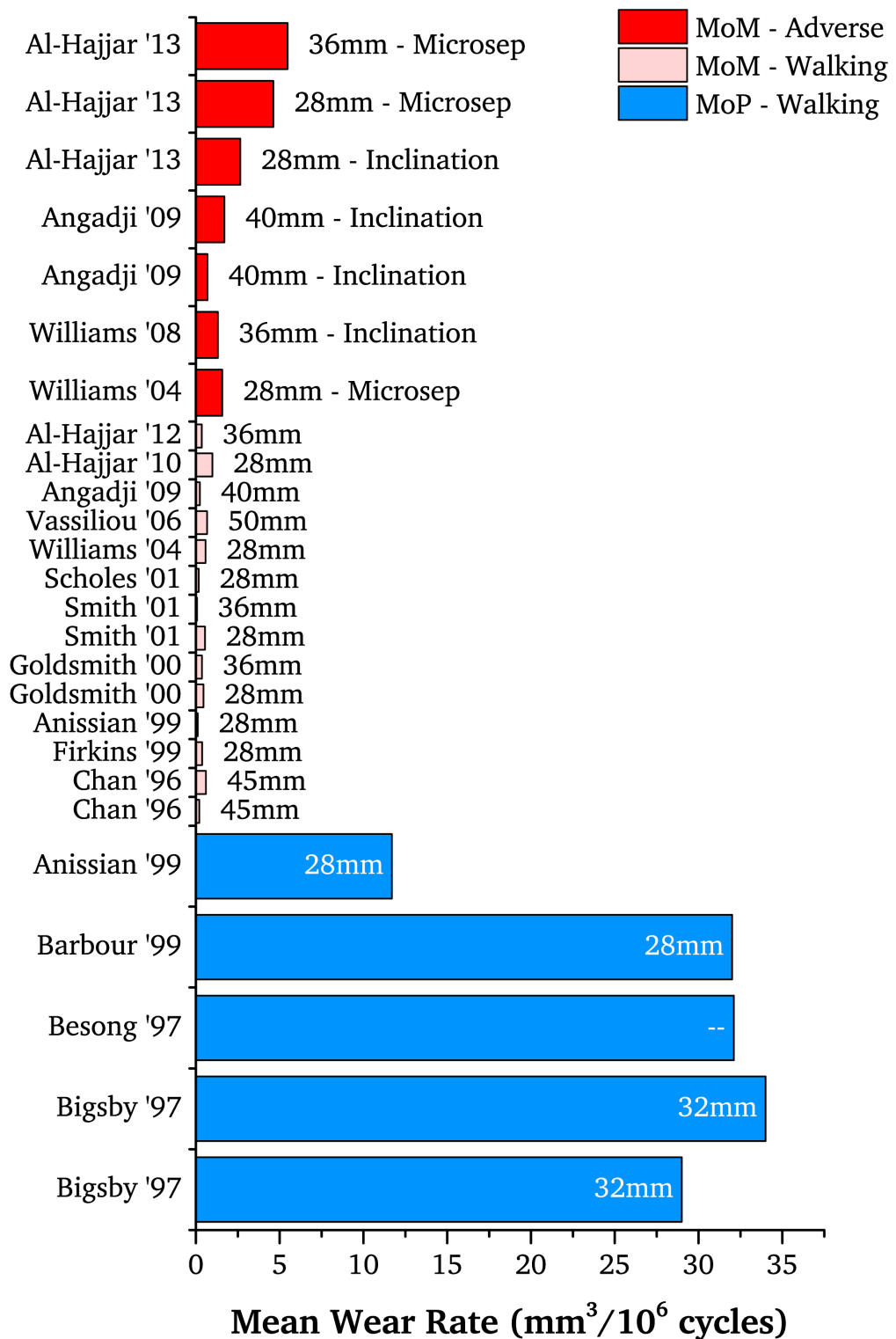


Figure 9.1: Hip simulator reported volumetric wear rate for MoP devices under walking [108, 214–216] and MoM devices under walking [108, 112, 113, 116, 125, 154, 201, 202, 217–220] and adverse loading conditions [124, 126, 201, 220].

that focus at the bearing surface has been on so-called adverse loading conditions affecting higher wear rates. Much of the current debate in the literature also sur-

rounds modular tapers. Whilst the focus of this thesis is on the sliding bearing surface, a growing number of studies cite fretting and corrosion within the modular taper as a primary or compounding cause for their poor clinical performance [225–230]. An ISO 14242 gait cycle began to be recognised as the ‘best-case’ scenario, but *in vivo* the prostheses can be subjected to much more severe loading and articulation. Acetabular malpositioning, such as high inclination, and severe articulating conditions, such as microseparation, have since demonstrated increased MoM simulator wear rates compared to normal walking or ISO standard cycles [124, 126, 201, 220]. Many of the adverse loading studies in the literature suggest these observed higher wear rates may be responsible for the poor MoM clinical performance *in vivo*. There is an ongoing drive to assess components during pre-clinical testing in worst-case conditions and hip simulation is therefore becoming more and more advanced to achieve this.

The adverse loading wear rates shown in Figure 9.1 are still much less than the typical walking MoP wear rates since their introduction. These studies still mostly relied on a gravimetrically determined wear rate to benchmark their performance. As has been demonstrated the degradation of Metal-on-Metal sliding interfaces is a complex mix of mechanical wear, corrosion material loss and synergistic acceleration of material loss. Without a complete understanding of the degradation mechanisms which make up this total volume loss, and the pathways to failure for these devices it is very likely that, had this data been available alongside the initial simulator studies, it would have still been seen as favourable for Metal-on-Metal bearings. Comparing like-for-like wear rates showed a two order of magnitude reduction and now, even under the most severe simulation conditions, a significant wear rate reduction from MoP was still observed. Wear rate, assessed either gravimetrically or through volumetric form profile analysis, does not fully capture the pertinent information relevant to tribocorrosion degradation which is critical to the success of hard bearings *in vivo* with a metallic sliding component.

This chapter aims to summarise and discuss the results presented in this study and consider their implications for pre-clinical testing of medical devices.

## **9.1 - Adverse Loading**

The results of the experiments performed on the simple configuration pin-on-plate tribometer suggested that an increase in contact pressure can result in an increase in corrosion. Tribometer contacts typically operate in boundary lubrication conditions. This increase can be expected to follow a linear relationship with increasing load if following the simplified wear laws. However the conforming contact of Metal-on-Metal bearings may behave very differently from the simplified tribometer system, operating in different lubrication regimes and larger contact areas.

Various types of adverse loading conditions have been used to assess the performance of 28 mm Metal-on-Metal bearings in electrochemically-instrumented hip simulators. Evidence presented has demonstrated that the tribological conditions during articulation can play a critical role in accelerating corrosive material loss and the overall contribution of corrosion to total mass loss.

### **9.1.1 - Microseparation**

As discussed, the industry and research community are becoming increasingly interested in the effects of adverse loading situations and daily living activities on the performance of total hip replacements. A continuous simple twin-peak profile may not be the best method for assessing these devices before they are implanted in patients. The use of a three electrode electrochemical cell has highlighted how the mechanism of material loss from the device may change by applying an adverse loading situation.

Moving from a Standard Gait profile to the application of 0.8 mm of Microseparation leads to differences in the OCP response and a significant increase in the estimated corrosive loss across both bearing couples. Comparing two specific bear-

ings in the Metal-on-Metal series, corrosive volume loss was estimated at 0.029 and 0.24 mm<sup>3</sup> under Standard Gait and Microseparation respectively. This represents a near order of magnitude increase in the volume of material lost directly from the bearing surface. Under the MoC series similar patterns were observed with increases from 0.013 and 0.017 mm<sup>3</sup> to 0.09 mm<sup>3</sup>. The low value of 0.047 mm<sup>3</sup> for the first MoC microseparated bearing was likely due to a problem with the electrode used within the first 333k cycles, and thus the actual corrosive material loss may have been higher. As noted in Chapter 7 if similar values for  $I_{corr}$  were assumed over the first 333 kcycles for this bearing an equivalent value of 0.09 mm<sup>3</sup> would have also been observed. This would have resulted in a contribution from corrosion to total volume loss of 12 % for this bearing.

Previous studies have examined the gravimetric material loss from 28 mm MoM bearings with the application of microseparation. One study demonstrated an insignificant increase in wear over the first million cycles [124]. After the initial bedding-in period the wear rate under microseparation increased, resulting in a 2.6 fold increase in total gravimetric material loss after five million cycles. Another study reported a three-to four fold increase over the first two million cycles, not separating the data for the initial million cycles [125]. These increases have previously been attributed to the breakdown of lubrication caused by the much more severe contact occurring at heel-strike, where the femoral head may also connect with the edge/rim of the acetabular cup [231]. Contact pressures as a result of a smaller 0.25 mm of microseparation have been estimated through modelling to be as high as 927 MPa for a 28 mm MoM bearing [172], as shown in Figure 9.2. At 28 mm this high contact pressure is localised at the rim of the acetabular cup. For the smaller level of microseparation this rapidly falls to approximately 350 MPa and the contact moved towards the centre of the acetabular cup. Mak *et al.* [182] have also modelled contact pressures as high as 672 MPa for Metal-on-Ceramic bearings, as shown in Figure 9.2.

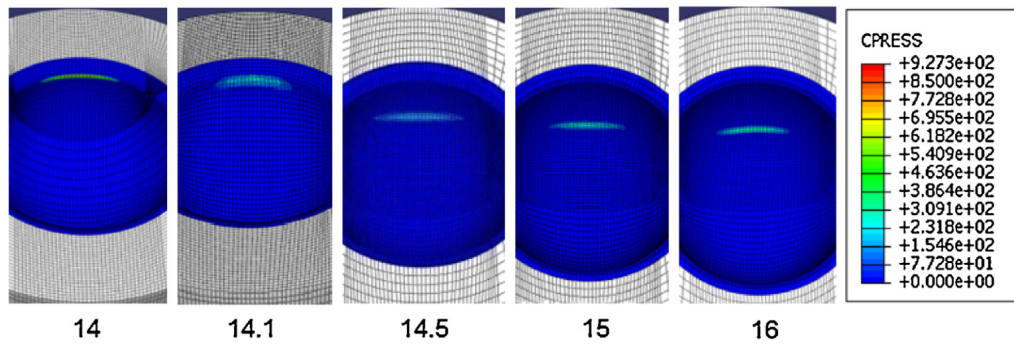


Figure 9.2: Contour plots of the contact pressure (MPa) at the inner surface of acetabular cup with different major radii (mm) under 0.25 mm micro-lateralization [172]. Reproduced with permission (see Appendix 2).

The tribological contact is also likely to be very different, moving from Standard Gait sliding with sub-100 MPa contact pressures to more of a cutting action when meeting the rim under microseparation. This is highlighted with the typical ‘stripe wear’ pattern observed in the CMM analysis. This stripe pattern is typical of edge or rim loading and normally noted in Ceramic-on-Ceramic devices [56, 232]. This action results in a more aggressive depassivation of the surface, resulting in a significantly higher rate of corrosion and therefore a higher rate of release of metallic ions directly at the bearing surface. This is also demonstrated in the anodic current transients directly measured by applying a small overpotential to the bearing. On moving from Standard Gait to Microseparation, there is not only a change in the transient shapes for MoM and MoC, we also see an order of magnitude increase in peak currents.

Interestingly, for the Metal-on-Metal bearings subjected to microseparation, the volume of material lost within the ‘stripe wear’ region of one femoral head was estimated at 0.167 mm<sup>3</sup> via CMM analysis, shown as the black region in Figure 9.3. Comparatively the estimated corrosive material loss from the entire bearing, determined by LPR, was 0.24 mm<sup>3</sup>. Corrosive material loss therefore appeared to be a more significant contributor to total mass loss than the material removed from the stripe region of the femoral head as a result of microseparation / edge contact. This does not include the volume of material removed from the edge of acetabular

cup side of the micro-separating contact. This was not observed for the Metal-on-Ceramic bearings as the volume loss determined by CMM, specifically within the 'stripe,' was 0.188 mm<sup>3</sup>. The estimated corrosive mass loss from the entire femoral head was 0.09 mm<sup>3</sup> which is approximately half that of the total volume within the stripe. This may have been due the metal acetabular cup present in the Metal-on-Metal bearing. The estimated corrosive mass loss in this instance included the entire exposed metallic surface area. The estimated corrosive mass loss from the Metal-on-Ceramic bearing was only from the femoral head.

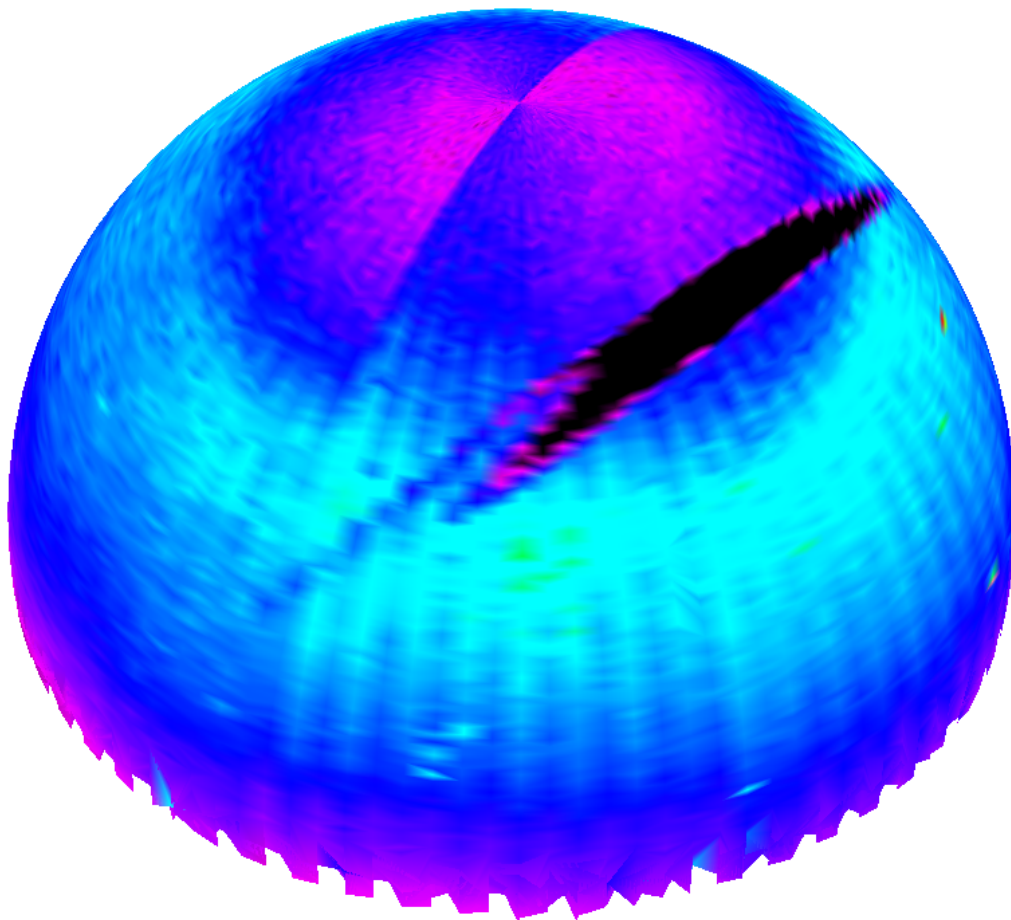


Figure 9.3: Sphere form profile analysis of a 28 mm femoral head after 1 MCycles articulation against a metal acetabular liner under 0.8 mm microseparation. The black region represents the deviation from the nominal sphere over the 'stripe wear' region.

The increase in the corrosive material lost represents a shift in the importance of corrosive degradation taking place at the bearing surface. As a result of moving from Standard Gait to Microseparation the estimated contribution of corrosion to

the total material degradation moved from 4-8 % of the total to as much as 17 % for the MoC series. Within the stripe region mechanical wear may have been more important for the MoC series with the ceramic counterface. Even larger corrosive percentage contribution has been demonstrated under boundary lubricated contacts in simple reciprocating tribometer studies [150]. Changes of the sliding regime to anything representing less than ideal conditions (i.e. adverse loading) could have large implications on the material degradation as a direct result of corrosion.

### 9.1.2 - Acetabular Malpositioning

Acetabular malpositioning, also of interest within the literature as a form of adverse loading, has also been shown to increase the corrosive material loss. Initially, on a new bearing surface, an increase in inclination to 50° was not found to result in any notable increase in corrosion current, as measured by the short term testing profile described in Section 4.2.5. This level of inclination, limited by the 28 mm samples and the geometry of the machine, is relatively low compared to other studies and *in vivo* evidence (> 60°) [125, 126]. As such, it may not have been sufficient to prove the initial hypothesis that an edge-loading contact would result in higher corrosion.

The corrosion currents determined by LPR scans were much larger than had been observed, even at 30°, on the pneumatic simulator or after ‘bedding-in’ on the Full-ISO simulator. The first LPR on the pneumatic simulator was not taken until after 3 hours of sliding, whereas under the short term test all three were performed within 45 minutes. This suggested that the bearing was still ‘bedding-in’ and was therefore run for 333k cycles before repeating the test. Again, no significant difference was noted at 50° inclination, although the corrosion currents determined by LPR better matched values observed during other testing in Chapters 6 and 7. The OCP curves now demonstrated much larger cathodic shifts upon the initiation of sliding at higher angles of inclination, shown in Figure 8.4. As such potentiostatic

anodic polarisation tests were performed over the first 600 cycles in an attempt to capture that early degradation.

As can be seen in Figures 8.7 and 8.8, and 8.9 for retroversion, acetabular malpositioning can result in higher corrosive material loss upon the initiation of sliding. Increased inclination from 30 to 50° resulted in anodic current values as high as 120  $\mu\text{A}$ . The areas highlighted underneath the curve represent the total charge transferred during sliding. These increases were not captured by relatively long LPR scans performed during continuous articulation.

For inclination, this increase was likely to be due to the change in the contact conditions. As shown in Figure 9.4, increasing from an inclination angle of 30 to 50° reduces the size of the conformal contact and thus the ability of the entrained lubricant to support a proportion of the applied load.

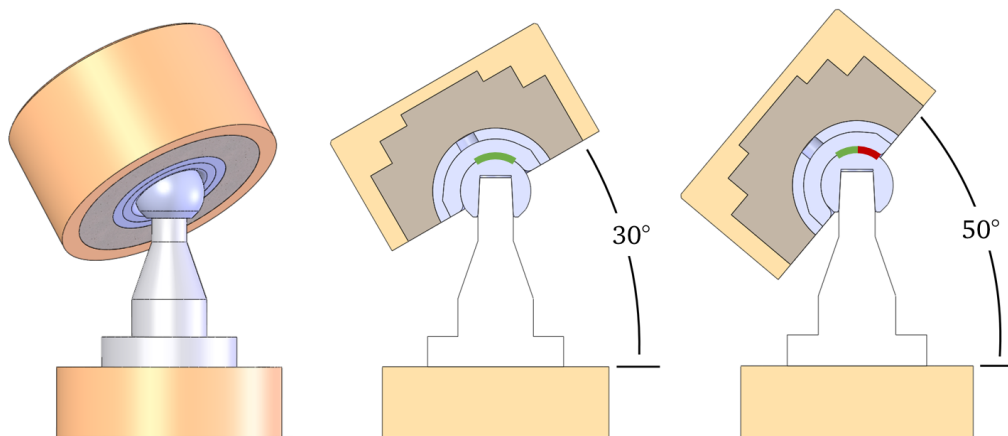


Figure 9.4: Schematic illustration of the hip simulator test cell at different angles of inclination.

It is important to note that under polarisation the system is being driven by the electrochemical cell, in this case to measure an anodic current, and is not fully representative of a system corroding at  $E_{corr}$ . The results presented some interesting trends, for example when conducting the tests in ‘parallel’ or in ‘series’ configurations. When performing tests at the same inclination after each other in ‘parallel,’ the measured anodic current was fairly consistent up until 50° (Figure 8.7). In ‘series’ however, when reverting back to 30° after a high inclination the measured

currents were much higher than seen previously. This may have large implications on the use of continuous profiles for simulation in that isolated 'adverse' events, such as a stumble or single microseparation, can result in higher corrosion in the following normal articulation.

## 9.2 - Metal-on-Metal vs. Metal-on-Ceramic

Metal-on-Ceramic bearings, first conceived by Firkins *et al.* [196], were seen as another possible Hard-on-Hard bearing combination. The devices never achieved clinical popularity [16], however analysis in instrumented hip simulators facilitates study of a single active metallic surface during full hip articulation. This couple configuration is often used as such in tribometer studies, with a ceramic pin sliding against a metallic surface, to analyse the depassivation of the single passive alloy surface [37, 148, 149]. The large titanium acetabular shell is also removed from the electrochemical cell which may be an additional factor influencing electrochemical deterioration.

The Open Circuit Potential response of the Metal-on-Ceramic bearings was different to the Metal-on-Metal series. Compared to the more typical response of an electrochemically instrumented sliding couple, the MoC series displayed an initial low OCP with a small cathodic shift upon the initiation of sliding. The OCP then displayed the same shift towards more noble values as that observed in the MoM bearings, although it was much more rapid. This is not a typical response seen in tribometer studies, which display sustained OCP drops on the initiation of sliding, despite being a similar material combination, which suggests the difference is system related.

Under articulation the Metal-on-Ceramic series followed similar trends to the Metal-on-Metal series with significant increases in estimated corrosive material loss and in peak anodic currents under microseparation. The shape of the anodic currents also changed under microseparation (Figure 7.8) and was different to the

observed microseparation shape under standard gait (Figure 6.8). It was unclear why the transient shapes were so different. The typically observed large single peak for Metal-on-Metal bearings under microseparation may have been a function of the two active sliding surfaces.

Overall, the observed currents were lower for the MoC series. The lower currents may be explained simply by the fact that only one active surface is present in the contact. The values for corrosion current ( $I_{corr}$ ) and the net anodic current transient are the overall currents measured through the electrochemical cell. With only one active surface the area of depassivated metal is less and there may have been similar current densities between the experiments. Differences in the tribological conditions may also have affected the corrosive degradation. Nominally, the contact between the two bearing combinations is similar, with similar values for radial clearance, initial surface roughness and thus lubrication regime. However the OCP trends for the MoM and MoC series, the latter of which did not display a typical cathodic tribocorrosion shift, suggests a difference in the effect of tribological conditions. Further work is needed to elucidate these mechanisms.

Also of importance in the hip simulator cell is the presence of the titanium acetabular shell. Under the Metal-on-Metal contact the sliding interface was electrically connected to the exposed surface of the titanium shell through the cup liner. This connection is not present for the Metal-on-Ceramic series as the ceramic liner insulated the metal femoral head from the shell. The MoM series therefore represents a mixed metal system, whereas the electrochemical analysis of the MoC series is purely concerned with the CoCrMo femoral head. Titanium is a much more noble metal than CoCrMo and connected to the sliding interface may polarise the depassivated wear scar, forming a galvanic cell and increasing corrosion [225, 233]. Bryant *et al.* [234] demonstrated this phenomena by utilising a titanium ring connected to the working electrode and exposed to the lubricant during fretting at the stem/cement interface. Also of importance is the fact that the MoC series came

from a different manufacturer and was a low carbon CoCrMo alloy.

### 9.3 - Assessment of Degradation

The measurement of wear and material loss from components articulated in hip simulators has long been a challenge. Gravimetric assessment of components, although frequently used, still poses difficulties. Water adsorption in polymer materials must be accounted for the the use of soak controls and strict cleaning and preparation for weighing [59, 166]. Metal and ceramic components after 0.3 Mcycles of standard gait can often present mass changes as a result of wear in the order of 0.1 milligrams; which can approach the measurement accuracy of the measurement balance.

Hip simulation and tribometer studies can also result in a wide range of results, even in the same laboratory and simulator. Dowson [235] examined reported Metal-on-Metal wear rates of one hundred studies across eight labs. A large variance of between approximately 0.01 and 1.62 mm<sup>3</sup> in steady state wear rates was found for given bearing properties. ‘Running-in’ wear was also noted to be as high as approxiamtely 16 mm<sup>3</sup>.

More recently Medley [236] examined several MoM pre- and post-clinical studies and found no correlation between wear rate and a  $1/R$  parameter related to bearing radius and clearance, shown in Figure 9.5.

There is evidence emerging in the literature that simple gravimetric assessment of components, following cyclic continuous 1 Hz simulator testing, is not a reliable indicator for real world *in vivo* performance [237–239]. For the industry gold standard MoP bearings the main failure mechanisms are reasonably well understood; i.e. wear debris induced osteolysis and aseptic loosening [52, 73]. As such, a gravimetric wear rate and debris particle size distributions from simulator benchmarking may be useful for MoP bearing combinations. For other materials, devices or bearing combinations with less understood or unknown failure mechanisms, a

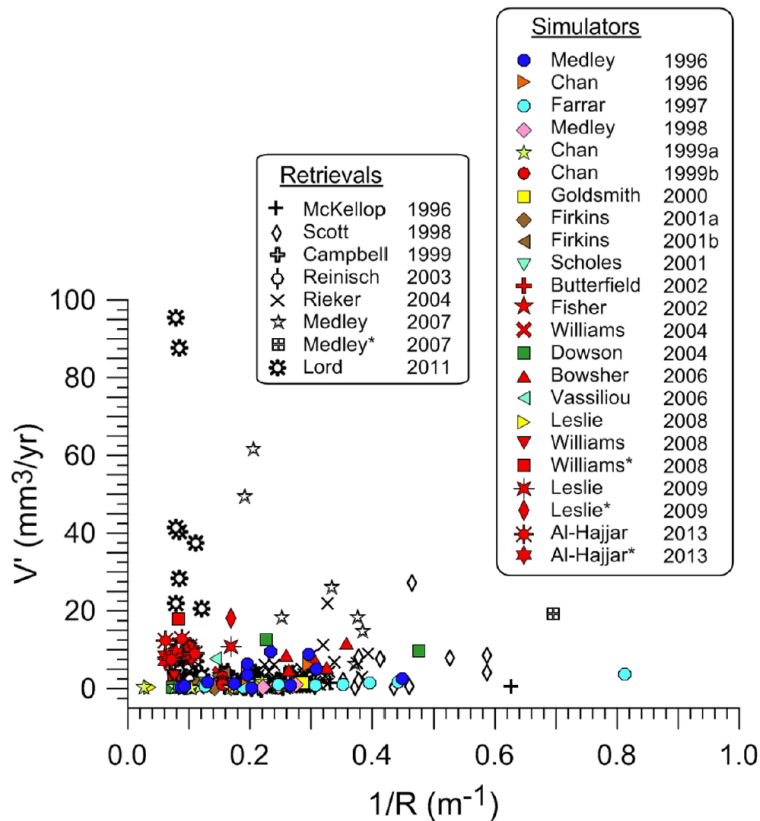


Figure 9.5: Simulator wear rates for Metal-on-Metal bearings reported across several laboratory studies; the points in red are under some adverse loading scenario. Reproduced with permission.

much more thorough and systematic approach to testing is needed. Particularly for sliding interfaces with a metallic surface *in situ* techniques such as electrochemistry are critical [240]. Comparing such devices' gravimetric wear rates to a MoP design, as was done during pre-clinical testing of second-generation MoM [27, 108, 112, 116], is not useful. Wear particles from MoP devices, although can illicit an immune response, do not typically degrade further. Whereas particles from MoM devices may go on to corrode and release more metallic ions in conjunction with the active sliding interfaces.

de Villiers *et al.* [239] examined MoM bearings with *AgCrN* coatings in an orbital hip simulator and found *Co* and *Ag* ions present in the lubricant after testing, despite negligible gravimetric material loss. Saikko *et al.* [237, 238] examined various adverse loading techniques across different devices and bearing combinations. Unless the test condition exceeded a devices' 'endurance limit' gravimetrically de-

terminated wear rates generally displayed low variance between tests. The evidence presented in results of this study have also demonstrated a shift in the contribution of corrosion to total material loss through adverse loading [241, 242]. This suggests a shift in the importance of corrosion and may be a more important indicator of the performance of MoM prostheses which fail due to metallosis, ALVAL, ARMD and pseudotumors [99–103]. Of the methods of assessment for material loss used throughout this study, the electrochemical cell has been the most reliable and repeatable when compared to gravimetric or sphere form analysis.

Simulator design is also improving with next generation simulators capable of more axes of motion and wider operating profiles. This will enable future testing to incorporate adverse loading and daily living cycles to greater effect. When comparing these new simulators to the previous generation however, a more complicated three-axes of motion Full-ISO walking profile only marginally increased the reported gravimetric wear [243], and was used to justify the continued use of the previous generation. With the new simulators a new generation of pre-clinical assessment is needed. *In situ* methods for assessing material loss and more varied testing regimes than continuous 1 Hz articulation need to be explored. Coupled with improved testing techniques, a greater understanding of how tribological systems can affect total material loss needs to be developed. The modelling of interfaces with metallic surfaces has therefore been a focus in the literature [205, 206].

Whilst there has been much success, a tribocorrosive contact is an incredibly complicated interface and difficult to model and predict; as evidenced by the simplified 2D model used in this study. There was some success correlating the model with an ISO walking profile, but it was not capable of describing the more complicated daily living cycles. Existing models in the literature are improving but don't always agree with experimental data. More work is therefore needed to move towards a comprehensive 3D tribology and tribocorrosion model, validated with *in situ* ex-

perimental techniques. This would be an incredibly powerful tool for pre-clinical assessment of devices and assisting patient selection.

## 9.4 - Linking Tribology to Electrochemical Degradation

The anodic current transients for Metal-on-Metal and Metal-on-Ceramic bearings have shown that there is a close link between the electrochemical degradation and the tribological conditions at the bearing surface. The transient curves presented in Chapters 6 and 7 (Figures 6.4, 6.8, 7.4 and 7.8) were typical curves observed over the one million cycles applied to those bearings. In reality the shape and magnitude of the curves varied over the course of each test. Some further example curves for MoM under standard gait are shown in Figure 9.6. Changes in the magnitude or shape may have been related to changes at the contact over the course of the test, such as tribofilm formation or working of the subsurface layer. No clear correlation was found, however, between parameters of the transient curves such as peak or base level current (as described in Figure 6.4) to other values electrochemical measurements; such as the measured OCP or  $I_{corr}$  determined by LPR was found. To further investigate the link between the tribological conditions and anodic current transient a new bearing was taken and studies on the Full-ISO simulator are described in Chapter 8.

The simplified 2D model used to estimate the theoretical minimum film thickness showed close agreement to the anodic current transients captured for the 28 mm diameter bearing articulated under an ISO walking profile. This appeared to confirm that at these points in each cycle more asperity-asperity contact occurred as a result of a thinner lubricating film, which in turn resulted in more severe de-passivation of the surface and thus greater corrosive degradation at the sliding interface. At all but the slowest frequency (0.4 Hz) a clear repeating two-peak shape was noted both in the inverted film thickness and anodic current. The anodic current transients shown in Figure 8.11 closely matched typical shapes seen in previous studies on a pneumatic simulator for 28 mm MoM bearings [241]. The

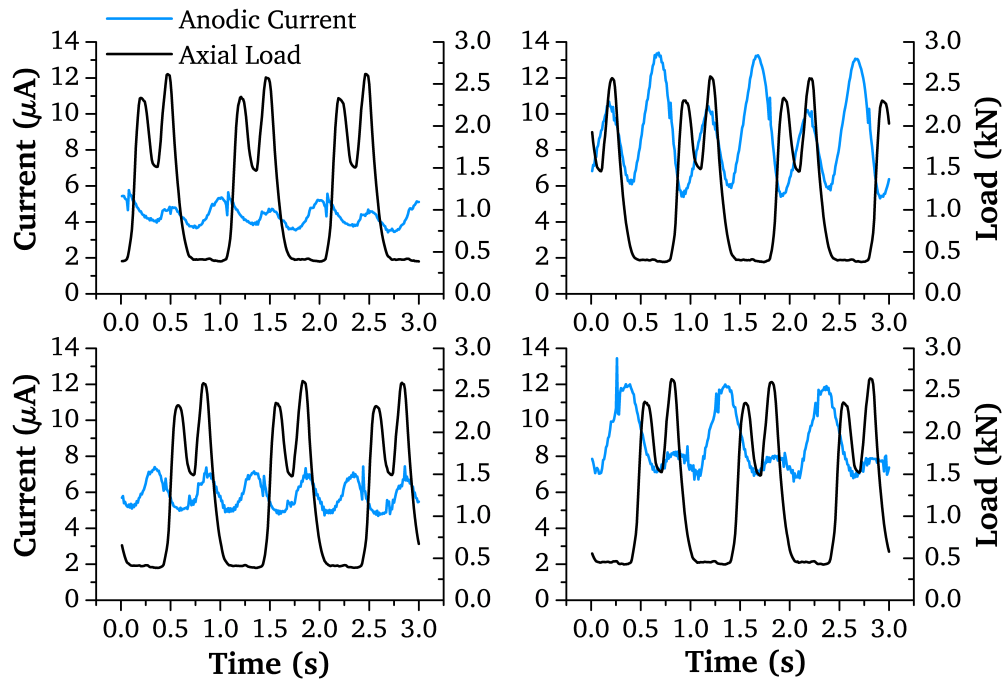


Figure 9.6: Example anodic current transients for 28 mm MoM bearings articulating under an ISO 14242 walking gait cycle.

position of both primary and secondary peaks aligned reasonably well at similar points in the cycle. Also the magnitude of the peaks scaled similarly between the frequencies under ISO walking after bedding-in.

The reduction in time delay observed between peaks in load and the primary and secondary peaks in current further suggests a response to the tribology at that point in the cycle. Figure 9.7 shows how these time delay values between the peaks in axial load and anodic current were determined. Had the phase difference been purely a time delay inherent in the electrochemical cell, the current peaks would have been expected to occur a fixed time after a peak in load for all frequencies.

This did not appear to be the case and in-fact the time delay reduced at a similar ratio to the increase in cycle frequency, as shown in Figure 8.13. This further suggested that the peaks were occurring at the same point in the cycle, rather than being delayed after the loading peak. They were therefore not thought to be simply out of phase with the load, but a response to some other tribological factor

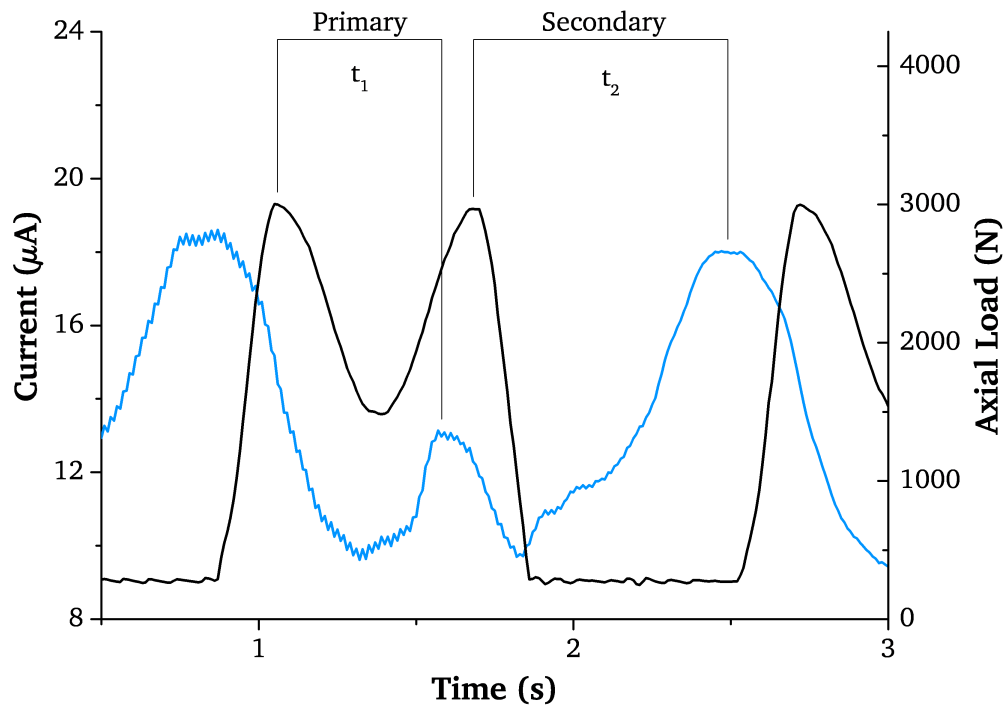


Figure 9.7: Example of how the time delay between the primary and secondary peaks in load and anodic current were determined.

at that point in the cycle.

The ‘severity factor’ first proposed by Hesketh *et al.* [15] was a first attempt to characterise this and link it to the corrosive degradation. The ‘severity factor’ appeared to be similarly inadequate as attempting to synchronise the current to the loading curve. Both axial load and angular velocity, components of the severity factor, are functions of the minimum film thickness. Current peaks also appeared to occur at points of minimum entrainment, rather than maximum load or ‘severity.’ An inverted film thickness parameter therefore appears better suited to describing the tribological conditions at the interface for tribocorrosion.

Determining film thickness is not a trivial task; especially for the 28 mm bearing used in the present study for example which operates typically in a mixed lubrication regime. Whilst the simplified 2D model may have shown good agreement across the different ISO profile frequencies, when applied to the daily living profiles the model broke down. Under ‘physiological gait’ a secondary peak in inverted film thickness was not found in the anodic current transient. The profile shape for

'stair climb' did not match at all. Interestingly the inverted film thickness for 'chair down-up' showed a profile with several sharp peaks over a cycle which was evidenced in the anodic transient although no clear alignment between peaks was noted. The observed current transients were also much larger for the daily living profiles than had been noted for the ISO walking profiles. This may have been a combination of the profiles' severity and also the device had not been bedded-in with these profiles, meaning that the larger ranges of motion exposed new areas of the bearing surface to articulation.

The tribological conditions a MoM bearing articulates under is a large contributing factor to the amount of corrosive material loss caused during sliding. Evidence has been presented that this is the case for microseparation, inclination and retroversion. Periodicity in anodic current transients over a cycle of sliding reinforce that link on a much smaller scale. Being able to correlate the two could be a powerful tool both for pre-clinical assessment as well as identifying potential patient demographics a given device may be unsuitable for.

#### **9.4.1 - Periodicity in Anodic Current Transients**

The 'severity factor' (Equation 3.1) proposed by Hesketh *et al.* [15] was an initial attempt to tie the anodic current trends for Metal-on-Metal bearings, observed in the hip simulator, to their tribological conditions during sliding. As discussed the predicted contact severity did not align with observed peaks in current, initially thought to be pre-peaks. Upon further inspection in Chapters 6 & 7 of this thesis, the anodic current transients were thought to be out of phase with the loading profile, rather than pre-peaks. The relationship proposed by Hesketh *et al.* also resulted in a severity factor which was very sensitive to the loading curve. The minimum film thickness ( $h_{min}$ ) is a function of the entraining velocity ( $u$ ), viscosity / shear rate and to a lesser extent load ( $W$ ) at any given point in the cycle. The angular velocity also converts to an entrainment velocity ( $u$ ) simply as a function of the bearing diameter and is thus interchangeable when discussing proportion-

ality. When resolved, as shown in Equation 9.1, the ‘severity factor’ takes the load input scaled by a power of 1.21 and the entrainment velocity scaled by a power of 0.35.

$$\begin{aligned}
 I &\propto \frac{W\omega}{h_{min}} & (3.1) \\
 &\propto \frac{Wu}{h_{min}} \\
 &\propto \frac{Wu}{2.8R' \left(\frac{\eta u}{E'R'}\right)^{0.65} \left(\frac{W}{E'R'^2}\right)^{-0.21}} \\
 &\propto \frac{Wu}{k_1 (k_2 u)^{0.65} (k_3 W)^{-0.21}} \\
 &\propto \frac{Wu}{W^{-0.21} u^{0.65}} \\
 &\propto W^{1.21} u^{0.35} & (9.1)
 \end{aligned}$$

Where:

$$\begin{aligned}
 k_1 &= \text{Assumed constant } (2.8R') \\
 k_2 &= \text{Assumed constant } \left(\frac{\eta}{E'R'}\right) \\
 k_3 &= \text{Assumed constant } \left(\frac{W}{E'R'^2}\right)
 \end{aligned}$$

This only holds true when parameters such as the viscosity ( $\eta$ ) and effective radius ( $R'$ ) are equated to mean values throughout a cycle which won't necessarily be the case. Synovial fluid and bovine serums have been shown to be non-Newtonian fluids [244], and as shown in Figures 6.9 and 7.10 the bearing surfaces can have changes in local radius. For the 2D Hamrock-Dowson model used in Section 8.2 these parameters were assumed constant. When applied to the ISO 14242 used on the Full-ISO simulator the severity factor essentially became a rescaled loading curve, as shown in Figure 9.8.

Although they are not directly comparable, due to the different loading profile used by Hesketh *et al.* [15, 150], when applied to the ISO 14242 walking cycle the ‘severity factor’ did appear to result in a similar shape. Peaks in severity occur at approximately 15 and 45 % through the course of the cycle, followed by a large portion of low severity during the swing phase. This clearly does not agree

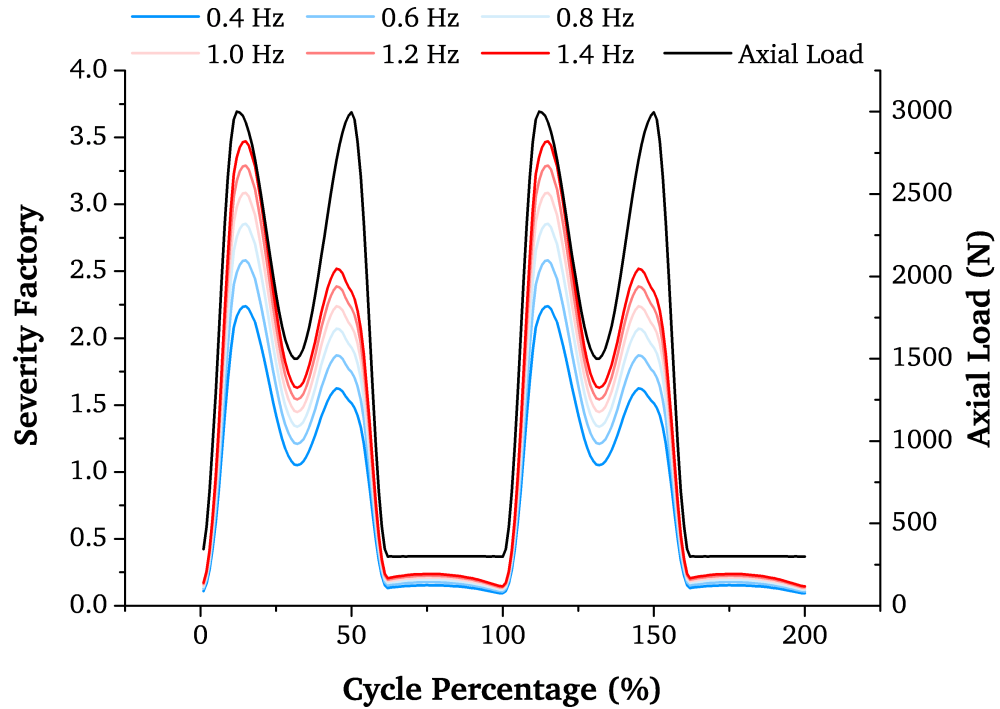


Figure 9.8: Severity Factor proposed by Hesketh *et al.* [15] applied to the parameters used in the Hamrock-Dowson model used in this study.

with the anodic current transients recorded on the Full-ISO simulator for these frequencies, whereby peaks in current were noted under toe-off and over and towards the end of the swing phase.

Interestingly, the severity factor increases with increased cycle frequency. This is due to how angular velocity / entrainment is accounted for. Even though scaled down by a power of 0.35, increasing sliding velocity still increases the severity factor of the contact as the loading curve is the same between frequencies. Only the entrainment velocity changes. The opposite was noted in Chapter 8 for the anodic current transients under the different frequencies on the 28 mm MoM bearing tested. The magnitude of anodic current reduced with increased frequency and thus increased entrainment. This trend was observed by the inverted theoretical minimum film thickness which also scaled reasonably well with the current magnitudes, shown in Figure 8.16.

It is important to note that the minimum film thickness, determined by the expression of the Hamrock-Dowson equation (Equation 2.10), is theoretical. The

expression calculates an average of the minimum thickness around the trailing edge of an elastohydrodynamic contact. It is also limited in that it is a simplified 2D model which assumes steady-state conditions and neglects phenomena such as squeeze-films. Determining a minimum film thickness does not mean that the bearing surfaces will have separated by at least that distance. This is dependent on the lambda ratio, as discussed, and the composite roughness ( $R_a$ ) of both surfaces. Most MoM bearings will in fact almost always be operating under mixed lubrication with some mixed, fluid film and asperity contact conditions. What the expression may be giving is a measure of the entrainment of lubricant and pressurisation; thus some proportion of load supported by fluid pressure.

For given conditions this may reduce the contact pressure transmitted through asperity contacts or reduce the total number of asperity contacts. With more favourable tribological conditions, damage to the surface oxide may be reduced and thus a reduction in depassivation and corrosive material loss due to exposure of the bulk alloy. This appears to be the case for the current transients across both MoM and MoC contacts on both simulators shown in Chapters 6, 7 and 8. Peaks in current appear to occur at points of minimum entrainment during sliding.

#### **9.4.2 - 'Daily Living' Cycles**

When applied to other cycles, derived from data collated by Bergmann *et al.* [173, 175], the model broke down and predicted vastly different shapes than measured under potentiostatic polarisation. Under the 'physiological gait' cycle for example, shown in Figure 8.17, a second peak in the inverted minimum film thickness was not clearly observed in the anodic current transient. It is important to consider that the anodic current transients reported at the different frequencies, were measured from a bearing which had undergone 333k cycles of 'bedding-in' under that profile. When compared to the transient from the previous inclination series on the new bearing surface, shown in Figure 9.9, the shapes are reasonably similar. Both show a primary peak in current which begins over the swing phase and peaks

just before the ‘heel-strike.’ The magnitude of anodic current is also similar, with peaks at approximately 30 - 33  $\mu\text{A}$ , increased from approximately 16  $\mu\text{A}$  under the ISO profile. The ‘bedding-in’ process appeared to reduce the magnitude of anodic current measured, possibly due to polishing or mechanical working of the sub-surface layer. When changing to the physiological gait cycle, the device would have begun articulating over new, previously undamaged areas of the surface.

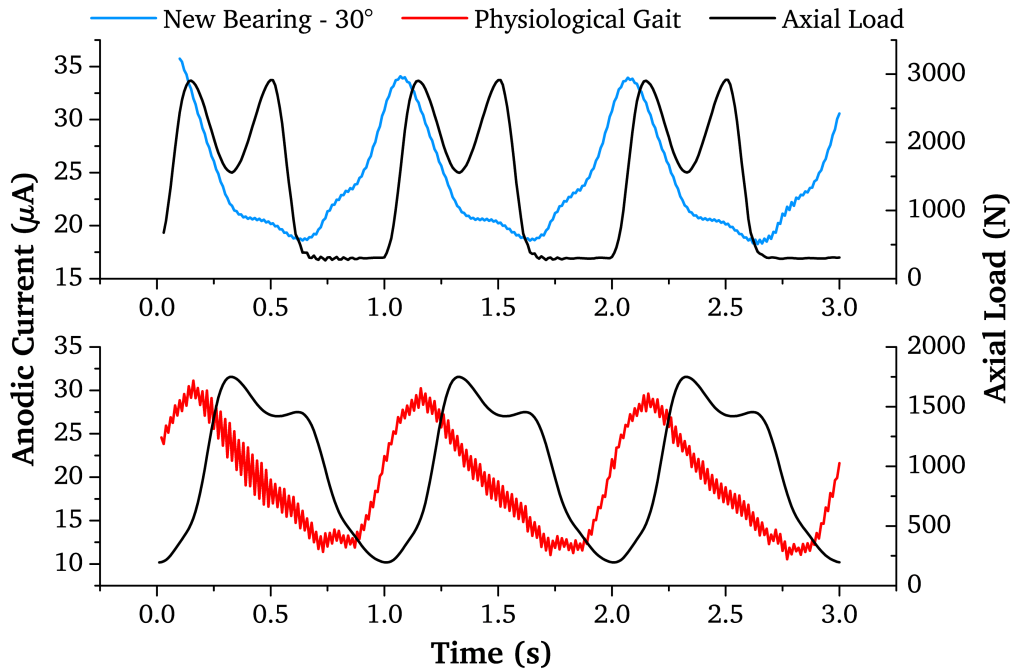


Figure 9.9: Anodic current transients (+50 mV vs. OCP) for a new 28 mm MoM bearing articulating under an ISO 14242-1 profile and upon switching to the physiological gait daily living cycle.

This may have further implications for how daily living cycles are examined in future hip simulation testing. *In vivo*, a patient would be rapidly changing from one type of cycle to another. It is important when performing ‘daily living’ scenarios in a hip simulator to mimic such behaviour. If cycles are articulated at a constant 1 Hz, in large batches of thousands of cycles, the corrosive degradation may be underestimated.

The transients presented in Figure 9.9 also demonstrate the possibility that the current follows after unloading events in the cycle. The anodic current appears to begin increasing after unloading occurs at ‘heel-strike’ and after ‘toe-off’ during

the swing phase. This would be in agreement with studies by Sun *et al.* [186, 191] which suggest that during loading events the surface is depassivated. At that point the asperities are still in contact and not exposed to the electrolyte. Only upon unloading do the surfaces separate and corrosion can take place. Separating this phenomenon from the links to inverted film thickness should be the focus of future work.

### 9.4.3 - Tribocorrosion Modelling

The sliding velocity or stroke frequency is often a function of corrosive material loss ( $V_{chem}$ ,  $C_w$ ) in models which attempt to quantify wear and corrosion for sliding passive metallic interfaces [37, 148]. As velocity increases more asperity contacts would be expected to depassivate over a given time period and thus corrosive current increases. As shown in the previous chapter lubrication phenomena such as EHL can revert this relationship whereby entrained lubricant supports a portion of the load through fluid pressure and lower currents are observed; likely due to reduced asperity damage. An example of such a model is the recently proposed tribocorrosion model by Cao *et al.* [245, 246]. The chemical mass loss component of the Cao model is shown in Equation 9.2.

$$V_{chem} = \frac{k_c Q_p M v_s (F_n / H)^{0.5}}{n F \rho} \quad (9.2)$$

Where:	$k_c$	=	Proportionality factor
	$Q_p$	=	Passivation charge density (mC/cm <sup>2</sup> )
	$M$	=	Atomic Mass (g/mol)
	$v_s$	=	Sliding velocity (mm/s)
	$F_n$	=	Normal force (N)
	$H$	=	Microsurface Hardness (HV)
	$n$	=	Oxidation valence
	$F$	=	Faraday's constant (C/mol)
	$\rho$	=	Density (g/cm <sup>3</sup> )

As shown, the chemical mass loss is partly a function of the sliding velocity ( $v_s$ ). The Cao model did attempt to account for the effects of lubrication by replacing the normal force ( $F_n$ ) with an 'effective force,' shown in Equation 9.3 [245]. The predicted theoretical minimum film thickness, determined by the same Hamrock-Dowson expression (Equation 2.10), therefore reduces the load supported by asperity contacts by a power of 1.49. This effective force was determined by a relationship noted by Dowson [235] between simulator wear rates for MoM devices reported across different laboratory studies and the predicted  $h_{min}$  for given bearing diameters, shown in Figure 9.10.

$$F_{eff} = k_0 \frac{F_n}{(h_{min})^{1.49}} \quad (9.3)$$

Where:	$F_{eff}$	=	Effective normal force (N)
	$k_0$	=	Proportionality factor

Given the electrochemical results observed in Chapters 6, 7 and 8 the use of a gravimetrically assessed total wear rate as a component of modelling tribochemical mass loss appears fundamentally flawed. Corrosive degradation does not necessarily obey a given relationship to the total mass loss, but rather the contact conditions. Including the effects of lubrication, the chemical component of the Cao model resolves as shown in Equation 9.4, where  $k_{chem}$  is a proportionality

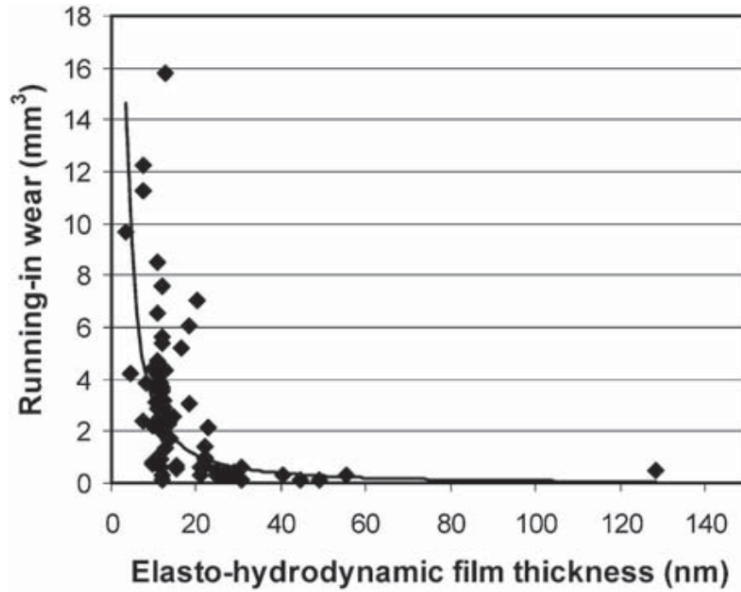


Figure 9.10: Running in wear of Metal-on-Metal bearings versus the predicted film thickness [235].

constant for chemical wear.

$$V_{chem} = k_{chem} \frac{MQ_p(E')^{0.3278}}{nF\rho\eta^{0.4843}} \cdot \frac{(F_n)^{0.6565}(v_s)^{0.5158}}{(R')^{0.5158}H^{0.5}} \quad (9.4)$$

The Cao model therefore includes components of load and sliding velocity. Equation 9.4 applies different weights to them with load scaling by a power of 0.6565 and velocity by a power of 0.5158; meaning they are roughly equal in importance to chemical wear. This results in a prediction of chemical wear over a walking gait cycle, shown in Figure 9.11, which appears fairly similar to the severity factor proposed by Hesketh *et al.* [15, 150]. Two peaks in chemical mass loss are present at approximately 0.15 and 0.4 % through the cycle. This is followed by an additional third peak at approximately 0.55 % and a period of low degradation over the swing phase. Interestingly, under the Cao model, the chemical mass loss tends to zero at the toe-off point of the cycle and at the end of the swing phase. This is due to the sliding velocity tending to zero at those points.

This directly contradicts the anodic current transients observed in the electrochemically instrumented hip simulators, which reach maximum peaks at these points

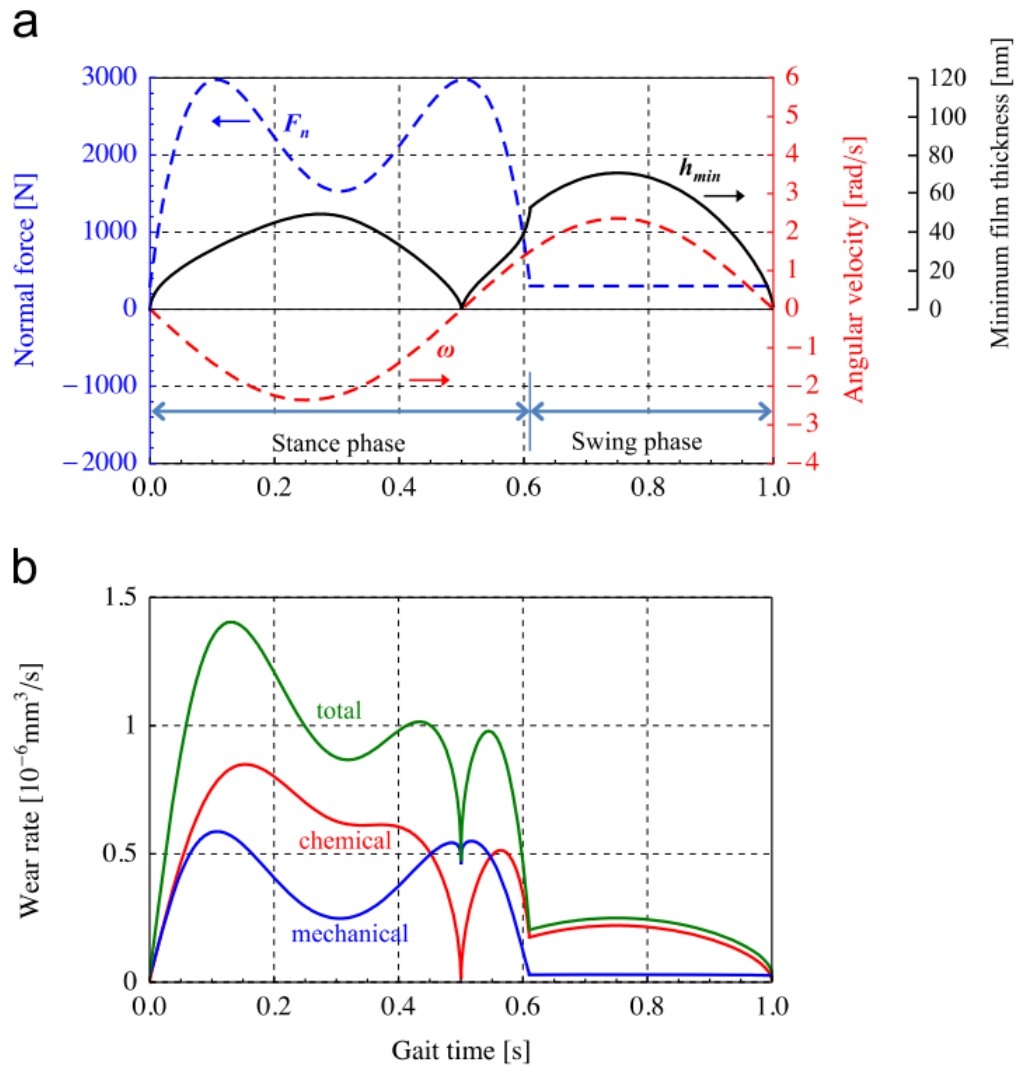


Figure 9.11: Total, mechanical and chemical mass loss as predicted by the Cao *et al.* [245, 246] tribocorrosion model for a given articulation cycle [245]. Reproduced with permission (see Appendix 2).

in the cycle. The Cao model also predicts the degradation of MoM bearings to be electrochemically dominant over the majority of the cycle which has not been found to be the case for 28 or 36 mm bearings in simulators instrumented with a three-electrode electrochemical cell [15, 150, 241, 242].

The depassivation of the bearing surface of Metal-on-Metal bearings during sliding occurs over a relatively large contact area. To fully assess and model the contact many factors must be carefully considered. A full 3D model of the lubrication, contact and surface depassivation would be important for determining the different mechanisms of material loss.

## 9.5 - Summary

The use of *in situ* electrochemistry can often be challenging and difficult to interpret when compared to traditional methods of wear assessment. It provides valuable insight into the mechanisms of material loss for metallic sliding contacts. For Metal-on-Metal Total Hip Replacements this may be much more relevant to indications for failure of the prosthesis. There are also great benefits to having a live measurement during sliding, primary of which is that the electrochemical cell enables a much more detailed examination of the role tribology can play when compared to a 'mm<sup>3</sup>/Mcycle' gravimetric wear rate after 5 million cycles.

This chapter has discussed the complex nature of the tribocorrosive degradation of Metal-on-Metal THRs. Under adverse loading scenarios the method of material loss from the bearing can be very different than under a standard gait articulation. This corrosive loss and release of ions, from the bearing surface or wear debris, may be more relevant to the indications for failure and early revision of Metal-on-Metal devices. The nature of current hip simulation techniques and methods of assessment have also been shown to limit the corrosion of the bearing surface. New materials or prostheses designs must consider and quantify these pathways of degradation in order to predict safely *in vivo* performance.

# Chapter 10 - Conclusions and Further Work

## 10.1 - Conclusions

Following the clinical failure of second generation Metal-on-Metal THR's and the resulting fallout of their recall from the market there has been much focus on the pre-clinical assessment of orthopaedic medical devices. The recent studies in the literature suggest adverse loading plays a critical role and results in increased MoM wear rate and thus failure. As much more advanced simulation techniques are seen to be necessary to go beyond the standard ISO 14242 five million cycle test it becomes essential to assess devices under worst-case scenarios.

The degradation mechanisms of MoM total hip bearings are not fully elucidated through gravimetric determination of mass loss. It is likely tribocorrosive material loss is more relevant to the indications of failure of MoM devices such as metallosis, tissue necrosis, pseudotumor, ALVAL and ARMD. Pre-clinical testing must include more relevant measures of degradation, as well as advanced simulation, for a given device. The conclusions from this thesis are:

### **Simple Configuration Tribometer:**

- Increasing the load and thus contact pressure in a simple configuration metal-on-metal pin-on-plate reciprocating tribometer was seen to increase the measured tribocorrosive material loss during sliding.
- A general trend of increasing surface roughness and estimated wear volume was noted with increasing contact pressure.
- This warranted further investigation into the effects of tribological conditions on corrosive material loss for MoM bearings under hip simulation.

### **Metal-on-Metal Hip Simulation:**

- Under full hip simulation moving from a standard gait articulation to 0.8 mm of microseparation on 28 mm Metal-on-Metal bearings the estimated material loss as a result of corrosion increased by roughly an order of magnitude.
- Anodic current transients displayed periodicity, previously observed in 36 mm bearings, supporting the concept of a link between the tribology of a cycle and corrosive degradation. The transient shape and magnitude was also very different between standard gait and microseparation articulation, further reinforcing this link.
- The formation of carbon-rich proteinaceous tribofilms on the surface was coupled with changing trends noted in the electrochemistry under standard gait; as had been reported previously for 36 mm bearings. The changes occurred over a much longer period for the 28 mm bearings.
- Similar to what had been seen previously a growth in the subsurface nanocrystalline layer was noted underneath the 'stripe-wear' region of a microseparated 28 mm metal-on-metal femoral head.

#### **Metal-on-Ceramic Hip Simulation:**

- Similar trends in corrosive degradation were noted in the simplified Metal-on-Ceramic contact as were observed for the Metal-on-Metal bearings.
- Moving from a standard gait articulation to a microseparation increased the estimated material corrosive mass loss from the femoral from 0.013 and 0.017 mm<sup>3</sup> to 0.094 mm<sup>3</sup>.
- Comparing the gravimetrically determined mass loss to corrosive loss, the percentage contribution of corrosion from the femoral head to total degradation increased from approximately 4-8 % to as much as 17.7 %.
- Peaks in the anodic current transients also increased by nearly an order of

magnitude, similar to the Metal-on-Metal bearings, although a different typical transient shape was noted under microseparation.

- CMM and RedLux sphere profile analysis showed minimal wear under standard gait but clear ‘stripe wear’ and ‘basal stripe’ patterns under microseparation. After only 1 Mcycle however the wear scars did not deviate sufficiently from the nominal sphere to attain accurate volume loss measurements.

#### **Acetabular Malpositioning:**

- Increased acetabular inclination and retroversion resulted in significantly higher anodic current transients over the first 600 cycles of articulation.
- Initial corrosive degradation appeared to be dominated by the ‘bedding-in’ process of the bearing.
- Continuous 1 Hz cyclic simulator articulation may underestimate the corrosive material loss.
- When moving back to a low inclination from a high level of inclination the measured currents were higher, suggesting adverse loading events (e.g. isolated microseparation or stumbling) may have an effect on corrosive degradation during otherwise normal articulation.

#### **Tribocorrosion Modelling:**

- A clear link between the tribology over a gait cycle and electrochemical material loss exists as evidenced by the measured anodic current transients.
- A simplified 2D expression of the Theoretical Minimum Film Thickness ( $h_{min}$ , Hamrock-Dowson model) appeared to align and scale with the measured currents.
- Existing models which rely on sliding velocity as a main constituent of chem-

ical loss may be underestimating the effects of lubrication when considering Metal-on-Metal THR contacts.

- Moving from the ISO 14242 walking cycle just to a physiological gait demonstrated an increase in anodic current transient as fresh areas of the bearing surface was exposed. This was further shown under different daily living cycles.
- Continuous 1 Hz testing of gait cycles may miss large corrosive degradation when switching to different articulations over low cycle numbers.

## 10.2 - Limitations

- **Bearing Diameter** - Only relatively low diameter (28 mm) Metal-on-Metal and Metal-on-Ceramic bearings were studied. One of the original goals of MoM bearings was to take the greatest opportunity to operate, fully or partially, in the fluid film lubrication regime. Lubricant entrainment and fluid pressure would support a proportion of the load during articulation and reduce wear. As such the majority of MoM resurfacing and traditional THR devices were large diameter (46+ mm). As discussed in Chapter 6, approximately 80 % of the MoM bearings still implanted in the UK in 2014 had diameters ranging from 46 to 54+ mm [16]. Much of the adverse loading literature of recent years have typically have focused on < 40mm bearings, possibly due to availability of test samples.
- **Low Repeats** - The majority of work was undertaken on a single station hip simulator and due to the nature of the market the availability MoM test components was low. As such only a small number of repeats were able to be performed in the time frame of this study. Many of the conclusions drawn from the electrochemical data have been from a small number of bearings or observations on trends. Traditional hip simulator studies rely on large 'n' numbers to counteract the variability inherent in simulator testing and

to be able to examine statistical significance. The role of electrochemical degradation, while clearly of great significance, has yet to be fully explored.

- **Electrochemical Cell** - The combined reference / counter electrodes used throughout all tests could be relatively sensitive to spoiling and other failures when submerged for long time periods in proteinaceous media. This compounded the low number of repeats for each test resulting in data that was discarded.
- **Protein Concentration** - The protein concentration of 17 g/L for the lubricant was selected in part to enable comparisons to be made with previous electrochemical work performed by Hesketh *et al.* [14, 15, 150, 162] on 36 mm bearings. The ISO 14242 standard at the time called for a 25 % volume dilution or to a minimum protein concentration of 17 g/L. Since revision the standard now calls for 30 g/L in hip simulation tests [166]. Protein concentration can play a large role in the wear rate and must therefore be considered carefully.

It is not possible to fully follow the standard when using *in situ* electrochemistry. ISO 14242 calls for dilution with deionised water which lacks conductivity and specific anions and cations present in synovial fluid. Some laboratories are still using the 25 % (v/v) dilution in modern studies to compare with old data.

### 10.3 - Future Work

Metal-on-Metal devices were nearly entirely recalled from the market, and very few are still implanted today. Further studies are nevertheless important for those patients with bearings still implanted. It is also important for the development of future devices as the degradation mechanisms must be fully elucidated in order to predict *in vivo* performance.

- **Beyond ISO** - The industry is moving towards more advanced simulation

techniques and profiles, all of which can result in very different tribocorrosive performance when articulating over different surface areas. The nature of cyclic 1 Hz continuous simulator testing may severely underestimate the role of time testing and bedding-in dependent corrosive phenomena. The replication of *in vivo* articulation should be the goal, and the study of electrochemical degradation of MoM bearings is critical, such as;

- True daily living cycles, i.e. moving from a walking cycle, to a stumble, to a stair climb etc. Not just different profiles running for 1000s of cycles at a time.
  - Stop-Dwell-Start (SDS) testing as explored by Hadley *et al.* [121–123].
  - Introduced third-body wear debris.
- **Beyond ‘bedding-in’** - The long-term electrochemical performance of bearings beyond the 1 - 2 Mcycle ‘bedding-in’ period and into steady-state wear needs to be investigated.
  - **Beyond 28 mm** - Investigate the corrosive degradation large diameter resurfacing devices which to the authors knowledge have not been assessed electrochemically, despite their clinical popularity.
  - **Full system** - Local galvanic cells between the active wear scar and passive undamaged surface play a large role in tribocorrosive degradation. The bearing surface is not the only tribological system in a traditional MoM THR. As such synergistic effects may occur between the bearing surface and modular tapers, or the stem-cement interface, if one or more contacts are under tribocorrosion.
  - **Metal-on-Polymer** - The implications this work may have for MoP systems is unknown. How the modular taper degrades under true anatomical orientation and articulation is unclear as current testing is under relatively simple

configurations. There has also been recent interest in harder and composite polymer materials such as PEEKs and Carbon Fibre Reinforced PEEKs [247]. These materials may depassivate the metallic femoral head during sliding and also result in accelerated corrosive loss.

## References

- [1] Gomez, P. F. and Morcuende, J. A. Early Attempts at Hip Arthroplasty - 1700s to 1950s. *Iowa Orthop J.* 2005, **36**, pp. 25–29.
- [2] Charnley, J. The long-term results of low-friction arthroplasty of the hip performed as a primary intervention. *JBJSBr.* 1972, **54**(1), pp. 61–76.
- [3] Liang, M. H., Cullen, K. E., Larson, M. G., Thompson, M. S., Schwartz, J. A., Fossel, A. H., Roberts, W. N. and Sledge, C. B. Cost-effectiveness of total joint arthroplasty in osteoarthritis. *Arthritis & Rheumatism.* 1986, **29**(8), pp. 937–43.
- [4] Crawford, R. W. and Murray, D. W. Total hip replacement: indications for surgery and risk factors for failure. *Annals of the Rheumatic Diseases.* 1997, **56**(8), pp. 455–57.
- [5] Ratner, B. D. A History of Biomaterials. In: Ratner, B. D., ed. *Biomaterials Science: An Introduction to Materials in Medicine.* 2nd ed. London: Elsevier, 2004, pp. 10–19.
- [6] National Joint Registry. *NJR 10th Annual Report for England, Wales and Northern Ireland.* 2013.
- [7] Wimmer, M. A., Sprecher, C., Hauert, R., Täger, G. and Fischer, A. Tribochemical reaction on metal-on-metal hip joint bearings. *Wear.* 2003, **255**(7-12), pp. 1007–14.
- [8] Wimmer, M. A., Fiscer, A., Buscher, R., Pourzal, R., Sprecher, C., Hauert, R. and Jacobs, J. J. Wear mechanisms in metal-on-metal bearings: the importance of tribochemical reaction layers. *J Orthop Res.* 2010, **28**(4), pp. 436–43.
- [9] Liao, Y., Pourzal, R., Wimmer, M. A., Jacobs, J. J., Fischer, A. and Marks, L. D. Graphitic tribological layers in metal-on-metal hip replacements. *Science.* 2011, **334**(6063), pp. 1687–90.

- [10] Pourzal, R., Theissmann, R., Williams, S., Gleising, B., Fisher, J. and Fischer, A. Subsurface changes of a MoM hip implant below different contact zones. *J Mech Behav Biomed Mater.* 2009, **2**(2), pp. 186–91.
- [11] Yan, Y., Neville, A. and Dowson, D. Tribo-corrosion properties of cobalt-based medical implant alloys in simulated biological environments. *Wear.* 2007, **263**(7-12), pp. 1105–11.
- [12] Yan, Y., Neville, A., Dowson, D., Williams, S. and Fisher, J. Tribo-corrosion analysis of wear and metal ion release interactions from metal-on-metal and ceramic-on-metal contacts for the application in artificial hip prostheses. *Proc Inst Mech Eng J.* 2008, **222**(3), pp. 483–92.
- [13] Yan, Y., Neville, A., Dowson, D., Williams, S. and Fisher, J. Electrochemical instrumentation of a hip simulator: a new tool for assessing the role of corrosion in metal-on-metal hip joints. *Proc Inst Mech Eng H.* 2010, **224**(11), pp. 1267–73.
- [14] Hesketh, J., Hu, X., Yan, Y., Dowson, D. and Neville, A. Biotribocorrosion: Some electrochemical observations from an instrumented hip joint simulator. *Tribology International.* 2013, **59**, pp. 332–8.
- [15] Hesketh, J., Meng, Q., Dowson, D. and Neville, A. Biotribocorrosion of metal-on-metal hip replacements: How surface degradation can influence metal ion formation. *Tribology International.* 2013, **65**, pp. 128–37.
- [16] National Joint Registry. *NJR 12th Annual Report: Prostheses used in hip, knee, ankle, elbow and shoulder replacement procedures 2014.* 2015.
- [17] National Joint Registry. *NJR 13th Annual Report: Prostheses used in hip, knee, ankle, elbow and shoulder replacement procedures 2015.* 2016.
- [18] Williams, J. *Engineering Tribology.* Oxford: Oxford University Press, 1994.
- [19] Hertz, H. On the Contact of Elastic Solids. *J Reine Angew Math.* 1881, **92**, pp. 156–71.
- [20] Stachowiak, G. W. and Batchelor, A. W. *Engineering Tribology.* London: Elsevier, 2005.

- [21] UK Tribology. *About UK Tribology*. [Online]. 2016. [Accessed 20th Jan. 2016]. Available from: <http://www.uktribology.net/about>.
- [22] Archard, J. F. Contact and Rubbing of Flat Surfaces. *J Appl Phys*. 1953, **24**(8), pp. 981–8.
- [23] Kato, K. Classification of Wear Mechanisms/Models. In: Stachowiak, G. W., ed. *Wear: Materials, Mechanisms and Practice*. Hoboken: John Wiley & Sons, 2005, pp. 9–20.
- [24] Zum Gar, K. H. *Microstructure and Wear of Materials*. London: Elsevier, 1987.
- [25] Hokkirigawa, K. and Kato, K. Theoretical Estimation of Abrasive Wear Resistance Based on Microscopic Wear Mechanism. *ASME Wear of Materials*. 1989, **1**, pp. 1–8.
- [26] Neville, A. and Morina, A. Wear and Chemistry of Lubricants. In: Stachowiak, G. W., ed. *Wear: Materials, Mechanisms and Practice*. Hoboken: John Wiley & Sons, 2005, pp. 71–94.
- [27] Jin, Z. M., Firkins, P., Farrar, R. and Fisher, J. Analysis and modelling of wear of cobalt-chrome alloys in a pin-on-plate test for a metal-on-metal total hip replacement. *Proc Inst Mech Eng H*. 2000, **214**(6), pp. 559–68.
- [28] Jin, Z. M., Dowson, D. and Fisher, J. Analysis of fluid film lubrication in artificial hip joint replacements with surfaces of high elastic modulus. *Proc Inst Mech Eng H*. 1997, **211**(3), pp. 247–56.
- [29] Fontana, M. G. and Greene, N. D. *Corrosion Engineering*. 2nd ed. Japan: McGraw-Hill, 1993.
- [30] Talbot, D. E. J. and Talbot, J. D. R. *Corrosion science and technology*. 2nd ed. Boca Raton: CRC Press, 2007.
- [31] Tait, W. S. *An Introduction to Electrochemical Corrosion Testing for Practicing Engineers & Scientists*. Pair O Docs Pubns, 1994.
- [32] Herdman, R., Handy, S., Pearson, T., Yamamoto, T., Ishiwata, K., Hara, M. and Nishiyama, T. *Chromium alloy coating with enhanced resistance to*

- corrosion in calcium chloride environments*. US Patent App. 12/409,629. 2010. Available from: <http://www.google.com/patents/US20100243463>.
- [33] Oldfield, J. W. and Sutton, W. H. Crevice Corrosion of Stainless Steels. *Br Corr J*. 1978, **31**(1), pp. 13–22.
- [34] Pistorius, P. C. and Burstein, G. T. Metastable Pitting Corrosion of Stainless Steel and the Transition to Stability. *Phil Trans Phys Sci Eng*. 1992, **341**(1662), pp. 531–59.
- [35] ASTM International. *ASTM G46-94 - Standard Guage for Examination and Evaluation of Pitting Corrosion*. 2013.
- [36] Diomidis, N., Celis, J. P., Ponthiaux, P. and Wenger, F. Tribocorrosion of stainless steel in sulphuric acid: Identification of corrosion-wear components and effect of contact area. *Wear*. 2010, **269**(1-2), pp. 93–103.
- [37] Vieira, A. C., Rocha, L. A., Papageorgiou, N. and Mischler, S. Mechanical and electrochemical deterioration mechanisms in the tribocorrosion of Al alloys in NaCl and in NaNO<sub>3</sub> solutions. *Corrosion Science*. 2012, **54**, pp. 26–35.
- [38] Watson, S. W., Friedersdorf, F. J., Madsen, B. W. and Cramer, S. D. Methods of Measuring Wear-Corrosion Synergism. *Wear*. 1995, **181-183**, pp. 476–84.
- [39] Mathew, M. T., Runa, M. J., Laurent, M., Jacobs, J. J. and Wimmer, M. A. Tribocorrosion behavior of CoCrMo alloy for hip prosthesis as a function of loads: A comparison between two testing systems. *Wear*. 2011, **271**(9-10), pp. 1210–9.
- [40] Mathew, M. T., Jacobs, J. J. and Wimmer, M. A. Wear-Corrosion Synergism in a CoCrMo Hip Bearing Alloy Is Influenced by Proteins. *Clin Ortho Relat Res*. 2012, **470**, pp. 3109–17.
- [41] Williams, D. F. *Definitions in Biomaterials*. Amsterdam: Elsevier, 1987.

- [42] Brunski, J. B. Metals: Basic Principles. In: Ratner, B. D., ed. *Biomaterials Science: An Introduction to Materials in Medicine*. 3rd ed. London: Elsevier, 2013.
- [43] ASTM International. *ASTM F138-13 - Standard Specification for Wrought 18 Chromium - 14 Nickel - 2.5 Molybdenum Stainless Steel Bar and Wire for Surgical Implants*. 2013.
- [44] ASTM International. *ASTM F75-12 - Standard Specification for Cobalt-28 Chromium-6 Molybdenum Alloy Castings and Casting Alloy for Surgical Implants*. 2012.
- [45] ASTM International. *ASTM F1537-00 - Standard Specification for Wrought Cobalt-28-Chromium-6-Molybdenum Alloy for Surgical Implants*. 2000.
- [46] 3T PRD. *Material Specification: Cobalt Chrome Alloy Co28Cr6Mo*. [Online]. 2013. [Accessed 6th Jan. 2015]. Available from: <http://www.3trpd.co.uk>.
- [47] Sumner, D. R. and Galante, J. O. Determinants of Stress Shielding: Design Versus Materials Versus Interface. *Clinical Orthopaedics and Related Research*. 1992, **274**, pp. 202–12.
- [48] Milošev, I. and Strehblow, H. H. The composition of the surface passive film formed on CoCrMo alloy in simulated physiological solution. *Electrochimica Acta*. 2003, **48**(19), pp. 2767–74.
- [49] Brown, S. R., Davies, W. A., DeHeer, D. H. and Swanson, A. B. Long-term survival of McKee-Farrar total hip prostheses. *Clin Orthop Relat Res*. 2002, **402**, pp. 157–63.
- [50] Kim, H., Kim, C. Y., Kim, D. W., Lee, I. S., Lee, G. H., Park, J. C., Lee, S. J. and Lee, K. Y. Wear performance of self-mating contact pairs of TiN and TiAlN coatings on orthopedic grade Ti-6Al-4V. *Biomed Mater*. 2010, **5**(4), p. 044 108.
- [51] Boutin, P. Arthroplastie totale de la hanche par prothese en alumina fritte: etude experimentale et premieres applications cliniques. *Rev Chir Orthop*. 1972, **58**, pp. 229–46.

- [52] Ingham, E. and Fisher, J. Biological reactions to wear debris in total joint replacement. *Proc Inst Mech Eng H*. 2000, **214**(1), pp. 21–37.
- [53] De Aza, A. H., Chevalier, J., Fantozzi, G., Schehl, M. and Torrecillas, R. Crack growth resistance of alumina, zirconia and zirconia toughened alumina ceramics for joint prostheses. *Biomaterials*. 2002, **23**(3), pp. 937–45.
- [54] Piconi, C., Maccauro, G., Muratori, F. and Brach del Prever, E. Alumina and zirconia ceramics in joint replacements. *J App Biomat & Biomech*. 2003, **1**, pp. 19–32.
- [55] Al-Hajjar, M., Leslie, I. J., Tipper, J. L., Williams, S., Fisher, J. and Jennings, L. M. Effect of cup inclination angle during microseparation and rim loading on the wear of BIOLOX® delta ceramic-on-ceramic total hip replacement. *J Biomed Mater Res*. 2010, **95B**(2), pp. 263–8.
- [56] Al-Hajjar, M., Fisher, J., Tipper, J. L., Williams, S. and Jennings, L. M. Wear of 36-mm BIOLOX® delta ceramic-on-ceramic bearing in total hip replacements under edge loading conditions. *Proc Inst Mech Eng H*. 2013, **227**(5), pp. 535–42.
- [57] Clarke, I. C., Pezzotti, G., Lakshminarayanan A. Burgett-Moreno, M. and Donaldson, T. Silicon Nitride Bearings: An Alternative to Oxide Ceramics in Total Hip Arthroplasty. *Orthop Proc*. 2016, **98-B**(SUPP 1), p. 86.
- [58] Amedica. *The Ideal Biomaterial - Silicon nitride plays an active role in promoting faster bone fusion*. [Online]. 2017. [Accessed 29th Jun. 2017]. Available from: <http://www.amedica.com/silicon-nitride>.
- [59] Kurtz, S. M. A Primer on UHMWPE. In: Kurtz, S. M., ed. *UHMWPE Biomaterials Handbook*. 2nd ed. London: Elsevier, 2009, pp. 1–6.
- [60] Cooper, S. L., Visser, S. A., Hergenrother, R. W. and Lamba, N. Polymers - Classes of Materials Used in Medicine. In: Ratner, B. D., ed. *Biomaterials Science: An Introduction to Materials in Medicine*. 2nd ed. London: Elsevier, 2004, pp. 67–79.

- [61] Oral, E. and Muratoglu, O. K. Radiation cross-linking in ultra-high molecular weight polyethylene for orthopaedic applications. *Nucl Instrum Meth Phys Res B*. 2007, **265**(1), pp. 18–22.
- [62] Galvin, A., Kang, L., Tipper, J., Stone, M., Ingham, E., Jin, Z. M. and Fisher, J. Wear of crosslinked polyethylene under different tribological conditions. *J Mater Sci: Mater Med*. 2006, **17**(3), pp. 235–43.
- [63] Global Data. *MediPoint: Total Hip Replacement - Global Analysis and Market Forecasts*. Jul. 2013.
- [64] Orthoworld. *The Orthopaedic Industry Annual Report*. [Online]. 2013. [Accessed 5th Aug. 2013]. Available from: <https://www.orthoworld.com/index.php/main/oiar>.
- [65] McKee, G. K. and Watson-Farrar, J. Replacement of Arthritic Hips by the McKee-Farrar Prosthesis. *JBJSBr*. 1966, **48-B**(2), pp. 245–59.
- [66] Waler, P. S. and Gold, B. L. The tribology (friction, lubrication and wear) of all-metal artificial hip joints. *Wear*. 1971, **17**(4), pp. 285–99.
- [67] Jones, D. A., Lucas, H. K., O'Driscoll, M., Price, C. H. G. and Wibberly, B. Cobalt Toxicity after McKee Hip Arthroplasty. *JBJSBr*. 1975, **57-B**(3), pp. 289–96.
- [68] EURO PHARMAT. *Les Implants articulaires Historique*. [Online]. 2007. [Accessed 7th Oct. 2013]. Available from: <http://www.euro-pharmat.com/>.
- [69] Ring, P. Complete Replacement Arthroplasty of the Hip by the Ring Prosthesis. *JBJSBr*. 1968, **50**(B), pp. 720–31.
- [70] Patterson, M. Ring uncemented hip replacements. The results of revision. *JBJSBr*. 1987, **69**(3), pp. 374–80.
- [71] Harper, G. D., Bull, T., Cobb, A. G. and Bentley, G. Failure of the Ring polyethylene uncemented acetabular cup. *JBJSBr*. 1995, **77**(B), pp. 1129–32.
- [72] Charnley, J. Arthroplasty of the hip. A new operation. *The Lancet*. 1961, **1**(7187), pp. 1129–32.

- [73] Ingham, E. and Fisher, J. The role of macrophages in osteolysis of total joint replacement. *Biomaterials*. 2005, **26**(11), pp. 1271–86.
- [74] Schmalzried, T. O., Szuszczewicz, E. S., Akizuki, K. H., Petersen, T. D. and Amstutz, H. C. Factors correlating with long term survival of McKee-Farrar total hip prostheses. *Clin Orthop Relat Res*. 1996, **329**, S48–59.
- [75] Jacobsson, S. A., Djerf, K. and Wahlstrom, O. Twenty-year results of McKee-Farrar versus Charnley prosthesis. *Clin Orthop Relat Res*. 1996, **329**, S60–68.
- [76] Tipper, J. L., Firkins, P., Besong, A. A., Barbour, P. S. M., Nevelos, J., Stone, M. H., Ingham, E. and Fisher, J. Characterisation of wear debris from UHMWPE on zirconia ceramic, metal-on-metal and alumina ceramic-on-ceramic hip prostheses generated in a physiological anatomical hip joint simulator. *Wear*. 2001, **250**, pp. 120–28.
- [77] Catelas, I., Bobyn, J. D., Medley, J. B., Krygier, J. J., Zukor, D. J. and Huk, O. L. Size, shape, and composition of wear particles from metal–metal hip simulator testing: Effects of alloy and number of loading cycles. *J Biomed Mat Res A*. 2003, **67**(1), pp. 312–27.
- [78] Catelas, I., Campbell, P. A., Bobyn, J. D., Medley, J. B. and Huk, O. L. Wear particles from metal-on-metal total hip replacements: effects of implant design and implantation time. *Proc Inst Mech Eng H*. 2006, **220**(2), pp. 195–208.
- [79] National Joint Registry. *NJR 9th Annual Report for England, Wales and Northern Ireland*. 2012.
- [80] MHRA. *Medical Device Alert: MDA/2012/036*. [Online]. 2012. [Accessed 14th Jul. 2013]. Available from: <http://www.mhra.gov.uk/>.
- [81] MHRA. *Medical Device Alert: MDA/2012/035*. [Online]. 2012. [Accessed 14th Jul. 2013]. Available from: <http://www.mhra.gov.uk/>.
- [82] MHRA. *Medical Device Alert: MDA/2012/016*. [Online]. 2012. [Accessed 14th Jul. 2013]. Available from: <http://www.mhra.gov.uk/>.

- [83] FDA. *FDA Safety Communication: Metal-on-Metal Hip Implants*. [Online]. 2013. [Accessed 17th Aug. 2013]. Available from: <http://www.fda.gov/>.
- [84] Liu, A., Richards, L., Bladen, C. L., Ingham, E., Fisher, J. and Tipper, J. L. The biological response to nanometre-sized polymer particles. *Acta Biomaterialia*. 2015, **23**, pp. 38–51.
- [85] Madl, A. K., Liong, M., Kovoichich, M., Finley, B. L., Paustenbach, D. J. and Oberdörster, G. Toxicology of wear particles of cobalt-chromium alloy metal-on-metal hip implants Part I: Physicochemical properties in patient and simulator studies. *Nanomedicine: Nanotechnology, Biology and Medicine*. 2015, **11**(5), pp. 1201–15.
- [86] Sidaginamale, R. P., Joyce, T. J., Bowsher, J. G., Lord, J. K., Avery, P. J., Natu, S., Nargol, A. V. F. and Langton, D. J. The clinical implications of metal debris release from the taper junctions and bearing surfaces of metal-on-metal hip arthroplasty. *JBJSBr*. 2016, **98**(B), pp. 925–33.
- [87] McCarthy, J. C., Bono, J. V. and O'Donnell, P. J. Custom and Modular Components in Primary Total Hip Replacement. *Clinical Orthopaedics and Related Research*. 1997, **344**, pp. 162–71.
- [88] Toomey, S. D., Hopper, R. H., McAuley, J. P. and Engh, C. A. Modular Component Exchange for Treatment of Recurrent Dislocation of a Total Hip Replacement in Selected Patients. *JBJSAm*. 2001, **83**(10), pp. 1529–33.
- [89] Bryant, M., Ward, M., Farrar, R., Freeman, R., Brummitt, K., Nolan, J. and Neville, A. Characterisation of the surface topography, tomography and chemistry of fretting corrosion product found on retrieved polished femoral stems. *J Mech Behav Biomed Mater*. 2014, **32**, pp. 321–34.
- [90] Goldberg, J. R., Gilbert, J. L., Jacobs, J. J., Bauer, T. W., Paprosky, W. and Leurgans, S. A multicenter retrieval study of the taper interfaces of modular hip prostheses. *Clin Orthop Relat Res*. 2002, (401), pp. 149–61.

- [91] Bryant, M., Farrar, R., Brummitt, K., Freeman, R. and Neville, A. Fretting corrosion of fully cemented polished collarless tapered stems: The influence of PMMA bone cement. *Wear*. 2013, **301**(1-2), pp. 290–99.
- [92] Bryant, M., Farrar, R., Freeman, R., Brummitt, K. and Neville, A. Fretting corrosion characteristics of polished collarless tapered stems in a simulated biological environment. *Tribology International*. 2013, **65**, pp. 105–12.
- [93] Bryant, M., Hu, X., Farrar, R., Brummitt, K., Freeman, R. and Neville, A. Crevice corrosion of biomedical alloys: a novel method of assessing the effects of bone cement and its chemistry. *J Biomed Mater Res B*. 2013, **101**(5), pp. 792–803.
- [94] Bryant, M., Ward, M., Farrar, R., Freeman, R., Brummitt, K., Nolan, J. and Neville, A. Failure analysis of cemented metal-on-metal total hip replacements from a single centre cohort. *Wear*. 2013, **301**(1-2), pp. 226–33.
- [95] Kop, A. M. and Swarts, E. Corrosion of a hip stem with a modular neck taper junction: a retrieval study of 16 cases. *J Arthroplasty*. 2009, **24**(7), pp. 1019–23.
- [96] McMinn, D. J. W., Treacy, R., Lin, K. and Pynsent, P. B. Metal on metal surface replacement of the hip. Experience of the McMinn prosthesis. *Clin Orthop Relat Res*. 1996, (329 Suppl), S89–98.
- [97] Daniel, J., Pynsent, P. B. and McMinn, D. J. W. Metal-on-metal resurfacing of the hip in patients under the age of 55 years with osteoarthritis. *JBJSBr*. 2004, **86-B**(2), pp. 177–84.
- [98] Ball, S. T., Duff, M. J. le and Amstutz, H. C. Early results of conversion of a failed femoral component in hip resurfacing. *J Bone Joint Surg Am*. 2007, **89**(4), pp. 735–41.
- [99] Willert, H. G., Buchhorn, G. H., Fayyazi, A., Flury, R., Windler, M., Köster, G. and Lohmann, C. H. Metal-on-metal bearings and hypersensitivity in

- patients with artificial hip joints. A clinical and histomorphological study. *JBJSAm.* 2005, **87**(1), pp. 28–36.
- [100] Watters, T. S., Cardona, D. M., Menon, K. S., Vinson, E. N., Bolognesi, M. P. and Dodd, L. G. Aseptic lymphocyte-dominated vasculitis-associated lesion: a clinicopathologic review of an underrecognized cause of prosthetic failure. *Am J Clin Pathol.* 2010, **134**(6), pp. 886–93.
- [101] Korovessis, P., Petsinis, G., Repanti, M. and Repantis, T. Metallosis after contemporary metal-on-metal total hip arthroplasty. Five to nine-year follow-up. *JBJSAm.* 2006, **88**(6), pp. 1183–91.
- [102] Campbell, P. A., Ebrahimzadeh, E., Nelson, S., Takamura, K., De Smet, K. A. and Amstutz, H. C. Histological Features of Pseudotumor-like Tissues From Metal-on-Metal Hips. *Clin Orthop Relat Res.* 2010, **468**(9), pp. 2321–27.
- [103] Park, Y. S., Moon, Y. W., Lim, S. J., Yang, J. M., Ahn, G. and Choi, Y. L. Early osteolysis following second-generation metal-on-metal replacement. *JBJSAm.* 2005, **87**(7), pp. 1515–21.
- [104] von Schewelov, T. and Sanzén, L. Catastrophic failure due to aggressive metallosis 4 years after hip resurfacing in a woman in her forties - a case report. *Acta Orthop.* 2010, **81**(3), pp. 402–04.
- [105] O’Kelly, J., Unsworth, A., Dowson, D., Jobbins, B. and Wright, V. Pendulum and simulator for studies of friction in hip joints. *Evaluation of Artificial Joints, The Biological Engineering Society.* 1977, pp. 19–20.
- [106] O’Kelly, J., Unsworth, A., Dowson, D., Hall, D. A. and Wright, V. A study of the role of synovial fluid and its constituents in the friction and lubrication of human hip joints. *ARCHIVE: Engineering in Medicine 1971-1988 (vols 1-17).* 1978, **7**(2), pp. 73–83.
- [107] O’Kelly, J., Unsworth, A., Dowson, D. and Wright, V. An experimental study of friction and lubrication in hip prostheses. *ARCHIVE: Engineering in Medicine 1971-1988 (vols 1-17).* 1979, **8**(3), pp. 153–9.

- [108] Anissian, H. L., Stark, A., Gustafson, A., Good, V. and Clarke, I. C. Metal-on-metal bearing in hip prosthesis generates 100-fold less wear debris than metal-on-polyethylene. *Acta Orthop Scand*. 1999, **70**(6), pp. 578–82.
- [109] Paul, J. P. Forces Transmitted by Joints in the Human Body. *ARCHIVE: Proceedings of the Institution of Mechanical Engineers, Conference Proceedings 1964-1970 (vols 178-184), Various titles labelled Volumes A to S*. 1966, **181**(310), pp. 8–15.
- [110] Anissian, H. L., Stark, A., Good, V., Dahlstrand, H. and Clarke, I. C. The Wear Pattern in Metal-on-metal Hip Prostheses. *J Biomed Mater Res*. 2001, **58**(6), pp. 673–8.
- [111] Dowson, D., McNie, C. M. and Goldsmith, A. A. J. Direct experimental evidence of lubrication in a metal-on-metal total hip replacement tested in a joint simulator. *Proc Inst Mech Eng C*. 2000, **214**(1), pp. 75–86.
- [112] Goldsmith, A. A. J., Dowson, D., Isaac, G. H. and Lancaster, J. G. A comparative joint simulator study of the wear of metal-on-metal and alternative material combinations in hip replacements. *Proc Inst Mech Eng H*. 2000, **214**(1), pp. 39–47.
- [113] Smith, S. L., Dowson, D. and Goldsmith, A. A. J. The effect of femoral head diameter upon lubrication and wear of metal-on-metal total hip replacements. *Proc Inst Mech Eng H*. 2001, **215**(2), pp. 161–70.
- [114] Smith, S. L., Dowson, D. and Goldsmith, A. A. J. The lubrication of metal-on-metal total hip joints: a slide down the Stribeck curve. *Proc Inst Mech Eng J*. 2001, **215**(5), pp. 483–93.
- [115] Firkins, P. J., Tipper, J. L., Ingham, E., Stone, M. H., Farrar, R. and Fisher, J. Influence of simulator kinematics on the wear of metal-on-metal hip prostheses. *Proc Inst Mech Eng H*. 2001, **215**(1), pp. 119–21.
- [116] Scholes, S. C., Green, S. M. and Unsworth, A. The wear of metal-on-metal total hip prostheses measured in a hip simulator. *Proc Inst Mech Eng H*. 2001, **215**(6), pp. 523–30.

- [117] Lewinnek, G. E., Lewis, J. L., Tarr, R., Compere, C. L. and Zimmerman, J. R. Dislocations after total hip-replacement arthroplasties. *JBJSAm.* 1978, **60**(2), pp. 217–20.
- [118] Scheerlinck, T. Cup positioning in total hip arthroplasty. *Acta Orthop Belg.* 2014, **80**, pp. 336–47.
- [119] Elkins, J. M., Callaghan, J. J. and Brown, T. D. The 2014 Frank Stinchfield Award: The ‘landing zone’ for wear and stability in total hip arthroplasty is smaller than we thought: a computational analysis. *Clin Orthop Relat Res.* 2015, **473**(2), pp. 441–52.
- [120] Myant, C., Fowell, M. and Cann, P. The effect of transient motion on Isoviscous-EHL films in compliant, point, contacts. *Tribology International.* 2014, **72**, pp. 98–107.
- [121] Hadley, M., Hadfield, F., Hardaker, C., Isaac, G., Fisher, J., Wye, J. and Barnett, J. Wear of Metal-on-Metal Total Hip Replacements under severe in-vitro test conditions. *Orthopaedic Proceedings.* 2012, **94-B**(SUPP XXXVII), p. 107.
- [122] Hadley, M. *Long Term Functional Simulation of Large Diameter Metal on Metal Hip Implants.* Ph.D. thesis, University of Leeds, 2012.
- [123] Hadley, M., Hardaker, C., Williams, S., Jin, Z., Isaac, G. and Fisher, J. Development of a stop-dwell-start (SDS) protocol for in vitro wear testing of metal-on-metal total hip replacements. In: Kurtz, S. M., Greenwald, A. S., Mihalko, W. H. and Lemons, J. E., ed(s). ASTM Special Technical Publication. PA USA: ASTM International, 2013. vol. 1560 STP, pp. 271–91.
- [124] Williams, S., Leslie, I., Isaac, G., Jin, Z., Ingham, E. and Fisher, J. Tribology and wear of metal-on-metal hip prostheses: influence of cup angle and head position. *JBJSAm.* 2008, **90**(Suppl 3), pp. 111–7.
- [125] Al-Hajjar, M., Williams, S., Fisher, J. and Jennings, L. M. The Influence of Cup Inclination Angle and Head Position on the Wear of Metal-on-Metal

Bearings in Total Hip Replacements. In: *6th World Congress of Biomechanics, 1st–6th Aug. 2010, Singapore.*

- [126] Al-Hajjar, M., Fisher, J., Williams, S., Tipper, J. L. and Jennings, L. M. Effect of femoral head size on the wear of metal on metal bearings in total hip replacements under adverse edge-loading conditions. *J Biomed Mater Res B.* 2013, **101**(2), pp. 213–22.
- [127] De Haan, R., Pattyn, C., Gill, H. S., Murray, D. W., Campbell, P. A. and De Smet, K. Correlation between inclination of the acetabular component and metal ion levels in metal-on-metal hip resurfacing replacement. *JBJSBr.* 2008, **90-B**, pp. 1291–7.
- [128] Hart, A. J., Buddhev, P., Winship, P., Faria, N., Powell, J. J. and Skinner, J. A. Cup inclination angle of greater than 50 degrees increases whole blood concentrations of cobalt and chromium ions after metal-on-metal hip resurfacing. *Hip International.* 2008, **18**(3), pp. 212–9.
- [129] Leslie, I. J., Williams, S., Isaac, G., Ingham, E. and Fisher, J. High cup angle and microseparation increase the wear of hip surface replacements. *Clin Orthop Relat Res.* 2009, **467**(9), pp. 2259–65.
- [130] Hua, X., Li, J., Wang, L., Jin, Z. M., Wilcox, R. and Fisher, J. Contact mechanics of modular metal-on-polyethylene total hip replacement under adverse edge loading conditions. *Journal of Biomechanics.* 2014, **47**(13), pp. 3303–09.
- [131] Dennis, D. A., Komistek, R. D., Northcut, E. J., Ochoa, J. A. and Ritchie, A. "In vivo" determination of hip joint separation and the forces generated due to impact loading conditions. *J Biomech.* 2001, **34**(5), pp. 623–9.
- [132] Komistek, R. D., Dennis, D. A., Ochoa, J. A., Haas, B. D. and Hammill, C. In vivo comparison of hip separation after metal-on-metal or metal-on-polyethylene total hip arthroplasty. *JBJSAm.* 2002, **84-A**(10), pp. 1836–41.

- [133] Williams, S., Butterfield, M., Stewart, T., Ingham, E., Stone, M. and Fisher, J. Wear and deformation of ceramic-on-polyethylene total hip replacements with joint laxity and swing phase microseparation. *Proc Inst Mech Eng H*. 2003, **217**(2), pp. 147–53.
- [134] Mahfouz, M., Baker, C., Komistek, R. D., Dennis, D. A. and DeBrunner, C. A New Method to Measure In Vivo Hip Joint Separation Using Hough Transform. In: *49th ORS Annual Meeting, 2nd–5th Feb. 2003, New Orleans (LA)*.
- [135] Lombardi, A. V., Mallory, T. H., Dennis, D. A., Komistek, R. D., Fada, R. A. and Northcut, E. J. An in vivo determination of total hip arthroplasty pistoning during activity. *J Arthroplasty*. 2000, **15**(6), pp. 702–9.
- [136] Clarke, M. T., Lee, P. T. H., Rayment, A., Villar, R. N. and Rushton, N. Bearing Micro-separation During the Gait Cycle with Metal-on-Metal and Metal-on-Polyethylene Bearings. *JBJSBr*. 2004, **86-B**, pp. 79–80.
- [137] Mohan, S. D., Komistek, R. D., Mahfouz, M., Dennis, D. A. and Anderle, M. R. In Vivo Kinematics for Subjects Implanted with either a Metal-on-Metal or Ceramic-on-Ceramic THA. In: *55th Annual Meeting of Orthopaedic Research Society, 22nd–25th Feb. 2009, Las Vegas (NV)*.
- [138] Mathew, M. T., Uth, T., Hallab, N. J., Pourzal, R., Fischer, A. and Wimmer, M. A. Construction of a tribocorrosion test apparatus for the hip joint: Validation, test methodology and analysis. *Wear*. 2011, **271**(9-10), pp. 2651–59.
- [139] Yan, Y., Neville, A. and Dowson, D. Understanding the role of corrosion in the degradation of metal-on-metal implants. *Proc Inst Mech Eng H*. 2006, **220**(2), pp. 173–80.
- [140] Yan, Y., Neville, A. and Dowson, D. Biotribocorrosion - an appraisal of the time dependence of wear and corrosion interactions: I. The role of corrosion. *Journal of Physics D: Applied Physics*. 2006, **39**(15), pp. 3200–05.

- [141] Yan, Y., Neville, A., Dowson, D. and Williams, S. Tribocorrosion in implants - assessing high carbon and low carbon Co-Cr-Mo alloys by in situ electrochemical measurements. *Tribology International*. 2006, **39**(12), pp. 1509–17.
- [142] Yan, Y., Neville, A. and Dowson, D. Biotribocorrosion of CoCrMo orthopaedic implant materials - Assessing the formation and effect of the biofilm. *Tribology International*. 2007, **40**(10-12), pp. 1492–9.
- [143] Wimmer, M. A., Loos, J., Nassutt, R., Heitkemper, M. and Fischer, A. The acting wear mechanisms on metal-on-metal hip joint bearings: in vitro results. *Wear*. 2001, **250**, pp. 129–39.
- [144] Wimmer, M. A., Nassutt, R., Sprecher, C., Loos, J., Täger, G. and Fischer, A. Investigation on stick phenomena in metal-on-metal hip joints after resting periods. *Proc Inst Mech Eng H*. 2006, **220**(2), pp. 219–27.
- [145] Mischler, S. Wear-Accelerated Corrosion of Passive Metals in Tribocorrosion Systems. *J Electrochem Soc*. 1998, **145**(3), pp. 750–8.
- [146] Mischler, S. Triboelectrochemical techniques and interpretation methods in tribocorrosion: A comparative evaluation. *Tribology International*. 2008, **41**(7), pp. 573–83.
- [147] Mischler, S. and Igual Muñoz, A. Wear of CoCrMo alloys used in metal-on-metal hip joints: A tribocorrosion appraisal. *Wear*. 2013, **297**(1-2), pp. 1081–94.
- [148] Papageorgiou, N. and Mischler, S. Electrochemical Simulation of the Current and Potential Response in Sliding Tribocorrosion. *Tribology Letters*. 2012, **48**(3), pp. 271–83.
- [149] Papageorgiou, N. The relevance of cathode kinetics to the interpretation of triboelectrochemical corrosion. *Tribology International*. 2013, **66**, pp. 60–71.
- [150] Hesketh, J. E. T. *Tribocorrosion of Total Hip Replacements*. Ph.D. thesis, University of Leeds, 2012.

- [151] Yan, Y., Neville, A., Dowson, D., Williams, S. and Fisher, J. The influence of swing phase load on the electrochemical response, friction, and ion release of metal-on-metal hip prostheses in a friction simulator. *Proc Inst Mech Eng J.* 2009, **223**(3), pp. 303–09.
- [152] Bellefontaine, G. *The Corrosion of CoCrMo Alloys for Biomedical Applications*. MRes thesis, University of Birmingham, 2010.
- [153] Yan, Y., Neville, A., Dowson, D., Williams, S. and Fisher, J. Effect of metallic nanoparticles on the biotribocorrosion behaviour of Metal-on-Metal hip prostheses. *Wear.* 2009, **267**(5-8), pp. 683–8.
- [154] Vassiliou, K., D Elfick, A. P., Scholes, S. C. and Unsworth, A. The effect of 'running-in' on the tribology and surface morphology of metal-on-metal Birmingham hip resurfacing device in simulator studies. *Proc Inst Mech Eng H.* 2006, **220**(2), pp. 269–77.
- [155] Liao, Y., Hoffman, E., Wimmer, M., Fischer, A., Jacobs, J. and Marks, L. CoCrMo Metal-on-Metal Hip Replacements. *Phys Chem Chem Phys.* 2013, **15**(3), pp. 746–56.
- [156] Maskiewicz, V. K., Williams, P. A., Prates, S. J., Bowsher, J. G. and Clarke, I. C. Characterization of protein degradation in serum-based lubricants during simulation wear testing of metal-on-metal hip prostheses. *J Biomed Mat Res.* 2010, **94B**(2), pp. 429–40.
- [157] Milošev, I. and Remskar, M. In vivo production of nanosized metal wear debris formed by tribochemical reaction as confirmed by high-resolution TEM and XPS analyses. *J Biomed Mater Res A.* 2009, **91**(4), pp. 1100–10.
- [158] Fink, J., Müller-Heinzerling, T., Pflüger, J., Bubenzer, A., Koidl, P. and Crecelius, G. Structure and bonding of hydrocarbon plasma generated carbon films: An electron energy loss study. *Solid State Communications.* 1983, **47**(9), pp. 687–91.

- [159] Berger, S. D., McKenzie, D. R. and Martin, P. J. EELS analysis of vacuum arc-deposited diamond-like films. *Philosophical Magazine Letters*. 1988, **57**(6), pp. 285–90.
- [160] Derbyshire, F. J., Presland, A. E. B. and Trimm, D. L. Graphite formation by the dissolution-precipitation of carbon in cobalt, nickel and iron. *Carbon*. 1975, **13**, pp. 111–3.
- [161] Nover, G., Stoll, J. B. and von der Gonna, J. Promotion of graphite formation by tectonic stress - a laboratory experiment. *Geophys J Int*. 2005, **160**, pp. 1059–67.
- [162] Hesketh, J., Ward, M., Dowson, D. and Neville, A. The composition of tribofilms produced on metal-on-metal hip bearings. *Biomaterials*. 2014, **35**(7), pp. 2113–9.
- [163] ASTM International. *ASTM F86-09 - Standard Practice for Surface Preparation and Marking of Metallic Surgical Implants*. 2009.
- [164] International Standards Organisation. *ISO 14242-1:2002 - Implants for surgery - Wear of total hip-joint prostheses - Part 1: Loading and displacement parameters for wear-testing machines and corresponding environmental conditions for test*. 2002.
- [165] International Standards Organisation. *ISO 14242-1:2012 - Implants for surgery - Wear of total hip-joint prostheses - Part 1: Loading and displacement parameters for wear-testing machines and corresponding environmental conditions for test*. 2012.
- [166] International Standards Organisation. *ISO 14242-1:2014 - Implants for surgery - Wear of total hip-joint prostheses - Part 1: Loading and displacement parameters for wear-testing machines and corresponding environmental conditions for test*. 2014.
- [167] Brandt, J. M., Brière, L. K., Marr, J., MacDonald, S. J., Bourne, R. B. and Medley, J. B. Biochemical comparisons of osteoarthritic human synovial

- fluid with calf sera used in knee simulator wear testing. *J Biomed Mater Res A*. 2010, **94**(3), pp. 961–71.
- [168] Landolt, D., Mischler, S., Stemp, M. and Barril, S. Third body effects and material fluxes in tribocorrosion systems involving a sliding contact. *Wear*. 2004, **256**(5), pp. 517–24.
- [169] Mischler, S., Rosset, E. A. and Landolt, D. Effect of Corrosion on the Wear Behavior of Passivating Metals in Aqueous Solutions. In: Dowson, D., Taylor, C. M., Childs, T. H. C., Godet, M. and Dalmaz, G., ed(s). *Tribology Series*. Elsevier, 1993. vol. 25, pp. 245–53.
- [170] Mischler, S., Spiegel, A., Stemp, M. and Landolt, D. Influence of passivity on the tribocorrosion of carbon steel in aqueous solutions. *Wear*. 2001, **251**, pp. 1295–307.
- [171] Hesketh, J., Hu, X., Dowson, D. and Neville, A. Tribocorrosion reactions between metal-on-metal and metal-on-polymer surfaces for total hip replacement. *Proc Inst Mech Eng J*. 2012, **226**(6), pp. 564–74.
- [172] Wang, L., Liu, X., Li, D., Liu, F. and Jin, Z. Contact mechanics studies of an ellipsoidal contact bearing surface of metal-on-metal hip prostheses under micro-lateralization. *Med Eng Phys*. 2014, **36**(4), pp. 419–24.
- [173] Bergmann, G., Graichen, F., Rohlmann, A., Bender, A., Heinlein, B., Duda, G. N., Heller, M. O. and Morlock, M. M. Realistic loads for testing hip implants. *Biomed Mater Eng*. 2010, **20**(2), pp. 65–75.
- [174] Paul, J. P. Force Actions Transmitted by Joints in the Human Body. *Proc Royal Soc London B*. 1976, **19**(1107), pp. 163–72.
- [175] Bergmann, G., Deuretzbacher, G., Heller, M., Graichen, F., Rohlmann, A., Strauss, J. and Duda, G. N. Hip contact forces and gait patterns from routine activities. *J Biomech*. 2001, **34**, pp. 859–71.
- [176] Fabry, C., Herrmann, S., Kaehler, M., Klinkenberg, E. D., Woernle, C. and Bader, R. Generation of physiological parameter sets for hip joint motions

- and loads during daily life activities for application in wear simulators of the artificial hip joint. *Med Eng Phys.* 2013, **35**(1), pp. 131–9.
- [177] International Standards Organisation. *ISO 14242-2:2000 - Implants for surgery - Wear of total hip-joint prostheses - Part 2: Methods of measurement.* 2000.
- [178] Windecker, R., Fleischer, M., Korner, K. and Tiziani, H. J. Testing micro devices with fringe projection and white-light interferometry. *Optics and Lasers in Engineering.* 2001, **36**(2), pp. 141–54.
- [179] Hammon, C. *The Basics of Crystallography and Diffraction.* 3rd ed. USA: Oxford University Press, 2009.
- [180] Bryant, M. G. *Fretting-Crevice Corrosion of Cemented Metal on Metal Total Hip Replacements.* Ph.D. thesis, University of Leeds, 2013.
- [181] Mak, M. M., Besong, A. A., Jin, Z. M. and Fisher, J. Effect of microseparation on contact mechanics in ceramic-on-ceramic hip joint replacements. *Proc Inst Mech Eng H.* 2002, **216**(6), pp. 403–8.
- [182] Mak, M., Jin, Z. M., Fisher, J. and Stewart, T. D. Influence of acetabular cup rim design on the contact stress during edge loading in ceramic-on-ceramic hip prostheses. *J Arthroplasty.* 2011, **26**(1), pp. 131–6.
- [183] Sariali, E., Stewart, T., Jin, Z. and Fisher, J. Effect of cup abduction angle and head lateral microseparation on contact stresses in ceramic-on-ceramic total hip arthroplasty. *J Biomech.* 2012, **45**(2), pp. 390–3.
- [184] Wang, L., Williams, S., Udofia, I., Isaac, G., Fisher, J. and Jin, Z. The effect of cup orientation and coverage on contact mechanics and range of motion of metal-on-metal hip resurfacing arthroplasty. *Proc Inst Mech Eng H.* 2012, **226**(11), pp. 877–86.
- [185] Meng, Q., Liu, F., Fisher, J. and Jin, Z. M. Contact mechanics and lubrication analyses of ceramic-on-metal total hip replacements. *Tribology International.* 2013, **63**, pp. 51–60.

- [186] Sun, D., Wharton, J. A. and Wood, R. J. K. Effects of proteins and pH on tribocorrosion performance of cast CoCrMo – a combined electrochemical and tribological study. *Tribology - Materials, Surfaces & Interfaces*. 2008, **2**(3), pp. 150–60.
- [187] Vidal, C. V., Juan, A. O. and Igual Muñoz, A. Adsorption of bovine serum albumin on CoCrMo surface: Effect of temperature and protein concentration. *Colloids and Surfaces B: Biointerfaces*. 2010, **80**, pp. 1–11.
- [188] Hodgson, A. W. E., Kurz, S., Virtanen, S., Fervel, V., Olsson, C. O. A. and Mischler, S. Passive and transpassive behaviour of CoCrMo in simulated biological solutions. *Electrochimica Acta*. 2004, **49**(13), pp. 2167–78.
- [189] Igual Muñoz, A. and Mischler, S. Interactive Effects of Albumin and Phosphate Ions on the Corrosion of CoCrMo Implant Alloy. *Journal of The Electrochemical Society*. 2007, **154**(10), p. C562.
- [190] Yan, Y., Neville, A., Hesketh, J. and Dowson, D. Real-time corrosion measurements to assess biotribocorrosion mechanisms with a hip simulator. *Tribology International*. 2013, **63**, pp. 115–22.
- [191] Sun, D., Wharton, J. A. and Wood, R. J. K. Micro- and Nano-scale Tribocorrosion of Cast CoCrMo. *Tribology Letters*. 2011, **41**, pp. 525–33.
- [192] International Standards Organisation. *BS 7251-4:1990 - Orthopaedic joint prostheses - Part 4. Specification for bearing surfaces of hip joint prostheses*. 1990.
- [193] Stewart, T. D., Tipper, J. L., Insley, G., Streicher, R. M., Ingham, E. and Fisher, J. Long-term wear of ceramic matrix composite materials for hip prostheses under severe swing phase microseparation. *J Biomed Mater Res B*. 2003, **66**(2), pp. 567–573.
- [194] Mathew, M. T., Nagelli, C., Pourzal, R., Fischer, A., Laurent, M. P., Jacobs, J. J. and Wimmer, M. A. Tribolayer formation in a metal-on-metal (MoM) hip joint: an electrochemical investigation. *J Mech Behav Biomed Mater*. 2014, **29**, pp. 199–212.

- [195] Pourzal, R., Martin, E. J., Vajpayee, S., Liao, Y., Wimmer, M. A. and Shull, K. R. Investigation of the role of tribofilms in self-mating CoCrMo systems utilizing a quartz crystal microtribometer. *Tribology International*. 2014, **72**, pp. 161–71.
- [196] Firkins, P. J., Tipper, J. L., Ingham, E., Stone, M. H., Farrar, R. and Fisher, J. A novel low wearing differential hardness, ceramic-on-metal hip joint prosthesis. *J Biomech*. 2001, **34**(10), pp. 1291–98.
- [197] Brown, C., Williams, S., Tipper, J. L., Fisher, J. and Ingham, E. Characterisation of wear particles produced by metal on metal and ceramic on metal hip prostheses under standard and microseparation simulation. *J Mater Sci: Mater Med*. 2007, **18**(5), pp. 819–27.
- [198] Williams, S., Schepers, A., Isaac, G., Hardaker, C., Ingham, E., van der Jagt, D., Breckon, A. and Fisher, J. The 2007 Otto Aufranc Award. Ceramic-on-metal hip arthroplasties: a comparative in vitro and in vivo study. *Clin Orthop Relat Res*. 2007, **465**, pp. 23–32.
- [199] Isaac, G. H., Brockett, C. L., Breckon, A., van der Jagt, D., Williams, S., Hardaker, C., Fisher, J. and Schepers, A. Ceramic-on-metal bearings in total hip replacement. *JBJSBr*. 2009, **91**(9), pp. 1134–41.
- [200] Clarke, I. C., Lazennec, J. Y., Brusson, A., Savisaar, C., Bowsher, J. G., Burgett, M. and Donaldson, T. K. Risk of impingement and third-body abrasion with 28-mm metal-on-metal bearings. *Clin Orthop Relat Res*. 2014, **472**(2), pp. 497–508.
- [201] Williams, S., Stewart, T. D., Ingham, E., Stone, M. H. and Fisher, J. Metal-on-metal bearing wear with different swing phase loads. *J Biomed Mater Res B*. 2004, **70**(2), pp. 233–39.
- [202] Al-Hajjar, M. *Wear of Hard-on-Hard Hip Prostheses: Influence of Head Size, Surgical Position, Material and Function*. Ph.D. thesis, University of Leeds, 2012.

- [203] Langton, D. J., Jameson, S. S., Joyce, T. J., Hallab, N. J., Natsu, S. and Nargol, A. V. F. Early failure of metal-on-metal bearings in hip resurfacing and large-diameter total hip replacement. *Bone & Joint Journal*. 2010, **92-B**(1), pp. 38–46.
- [204] Langton, D. J., Joyce, T. J., Mangat, N., Lord, J., van Orsouw, M., De Smet, K. and Nargol, A. V. F. Reducing metal ion release following hip resurfacing arthroplasty. *The Orthopedic clinics of North America*. 2011, **42**(2), pp. 169–80, viii.
- [205] Gao, L., Dowson, D. and Hewson, R. W. Predictive Wear Modelling of the Articulating Metal-on-Metal Hip Replacements. *J Biomed Mater Res B*. 2015, **In press**, pp. 1–10.
- [206] Gao, L., Dowson, D. and Hewson, R. W. A numerical study of non-Newtonian transient elastohydrodynamic lubrication of metal-on-metal hip prostheses. *Tribology International*. 2016, **93**, pp. 486–94.
- [207] NICE. *Updated NICE guidance on hip replacement and resurfacing recommends more durable artificial joints*. [Online]. 2014. [Accessed 20th Jun. 2016]. Available from: <https://www.nice.org.uk/>.
- [208] Smith & Nephew. *Statement regarding BHR System*. [Online]. 2015. [Accessed 20th Jun. 2016]. Available from: <http://www.smith-nephew.com/news-and-media/media-releases/news/statement-regarding-bhr-system/>.
- [209] MHRA. *Medical Device Alert: MDA/2015/024*. [Online]. 2015. [Accessed 20th Jun. 2016]. Available from: <http://www.mhra.gov.uk/>.
- [210] Drugwatch. *Stryker Hip Replacement Verdicts & Settlements*. [Online]. 29th Jul. 2016. [Accessed 20th Sep. 2016]. Available from: <https://www.drugwatch.com/stryker/hip-verdict-settlement/>.
- [211] Bloomberg. *J&J Said to Reach \$4 Billion Deal to Settle Hip Lawsuits*. [Online]. 13th Nov. 2013. [Accessed 20th Sep. 2016]. Available from: <http://www.bloomberg.com/news/2013-11-13-j-j-said-to-reach-4-billion-deal-to-settle-hip-lawsuits.html>.

//www.bloomberg.com/news/articles/2013-11-12/j-j-said-to-reach-4-billion-deal-to-settle-hip-lawsuits.

- [212] Reuters. *Johnson & Johnson hit with \$500 million verdict in hip implant trial*. [Online]. 17th Mar. 2016. [Accessed 20th Sep. 2016]. Available from: <http://www.reuters.com/article/us-johnson-johnson-lawsuit-verdict-idUSKCN0WJ2I2>.
- [213] National Joint Registry. *NJR 13th Annual Report for England, Wales and Northern Ireland*. 2016.
- [214] Bigsby, R. J. A., Hardaker, C. S. and Fisher, J. Wear of ultra-high molecular weight polyethylene acetabular cups in a physiological hip joint simulator in the anatomical position using bovine serum as a lubricant. *Proc Inst Mech Eng H*. 1997, **211**(3), pp. 265–69.
- [215] Besong, A. A., Bigsby, R. J. A., Barbour, P. S. M. and Fisher, J. Effect of head size and loading regime on the wear of UHMWPE acetabular cups in a hip simulator. In: *World Tribology Congress, 8th–12th Sep. 1997, London, UK*.
- [216] Barbour, P. S., Stone, M. H. and Fisher, J. A hip joint simulator study using simplified loading and motion cycles generating physiological wear paths and rates. *Proc Inst Mech Eng H*. 1999, **213**(6), pp. 455–67.
- [217] Chan, F. W., Bobyn, J. D., Medley, J. B., Krygier, J. J., Yue, S. and Tanzer, M. Engineering issues and wear performance of metal on metal hip implants. *Clin Orthop Relat Res*. 1996, (333), pp. 96–107.
- [218] Chan, F. W., Bobyn, J. D., Medley, J. B., Krygier, J. J. and Tanzer, M. Wear and Lubrication of Metal-on-Metal Hip Implants. *Clin Orthop Relat Res*. 1999, (369), pp. 10–24.
- [219] Firkins, P. J., Tipper, J. L., Ingham, E., Stone, M. H., Farrar, R. and Fisher, J. Quantitative analysis of wear debris from metal on metal hip prostheses tested in a physiological hip joint simulator. In: *45th ORS Annual Meeting, 1st–4th Feb. 1999, California, USA*.

- [220] Angadji, A., Royle, M., Collins, S. N. and Shelton, J. C. Influence of cup orientation on the wear performance of metal-on-metal hip replacements. *Proc Inst Mech Eng H*. 2009, **223**(4), pp. 449–57.
- [221] Müller, M. E. The benefits of metal-on-metal total hip replacements. *Clin Orthop Relat Res*. 1995, (311), pp. 54–9.
- [222] McKellop, H., Park, S.-H., Chiesa, R., Doorn, P., Lu, B., Normand, P., Grigoris, P. and Amstutz, H. In Vivo Wear of 3 Types of Metal on Metal Hip Prostheses During 2 Decades of Use. *Clin Orthop Relat Res*. 1996, **329**(3298), pp. 128–40.
- [223] Semlitsch, M. and Willert, H. G. Clinical wear behaviour of ultra-high molecular weight polyethylene cups paired with metal and ceramic ball heads in comparison to metal-on-metal pairings of hip joint replacements. *Proc Inst Mech Eng H*. 1997, **211**(1), pp. 73–88.
- [224] Doorn, P. F., Campbell, P. A., Worrall, J., Benya, P. D., McKellop, H. A. and Amstutz, H. C. Metal wear particle characterization from metal on metal total hip replacements: transmission electron microscopy study of periprosthetic tissues and isolated particles. *J Biomed Mater Res*. 1998, **42**(1), pp. 103–11.
- [225] Gilbert, J. L., Buckley, C. A. and Jacobs, J. J. In vivo corrosion of modular hip prosthesis components in mixed and similar metal combinations. The effect of crevice, stress, motion, and alloy coupling. *J Biomed Mater Res A*. 1993, **27**(12), pp. 1533–44.
- [226] Goldberg, J. R. and Gilbert, J. L. In vitro corrosion testing of modular hip tapers. *J Biomed Mater Res B*. 2003, **64**(2), pp. 78–93.
- [227] Bishop, N., Witt, F., Pourzal, R., Fischer, A., Rüttschi, M., Michel, M. and Morlock, M. Wear patterns of taper connections in retrieved large diameter metal-on-metal bearings. *J Orthop Res*. 2013, **31**(7), pp. 1116–22.
- [228] Kurtz, S. M., MacDonald, D. W., Gilbert, J. L., Mont, M. A., Klein, G., Chen, A., Kraay, M., Hamlin, B. and Rimnac, C. M. Is taper fretting corrosion

- a threat to the clinical performance of large-diameter hips with highly crosslinked polyethylene bearings? In: Greenwald, A., Kurtz, S., Lemons, J. and Mihalko, W., ed(s). ASTM Special Technical Publication. LA USA: ASTM International, 2015. vol. STP1591, pp. 45–58.
- [229] Gilbert, J. L., Mali, S. A. and Sivan, S. Corrosion of Modular Tapers in Total Joint Replacements: A Critical Assessment of Design, Materials, Surface Structure, Mechanics, Electrochemistry, and Biology. In: Greenwald, A., Kurtz, S., Lemons, J. and Mihalko, W., ed(s). ASTM Special Technical Publication. LA USA: ASTM International, 2015. vol. STP1591, pp. 192–223.
- [230] Agne, M. T., Underwood, R. J., Kocagoz, S. B., MacDonald, D. W., Day, J. S., Parvizi, J., Kraay, M. J., Klein, G. R., Cates, H. E. and Kurtz, S. M. Is there material loss at the backside taper in modular CoCr acetabular liners? *Clin Orthop Relat Res.* 2015, **473**(1), pp. 275–85.
- [231] Fisher, J. Bioengineering reasons for the failure of metal-on-metal hip prostheses: an engineer’s perspective. *JBJSBr.* 2011, **93**(8), pp. 1001–4.
- [232] Walter, W. L., Insley, G. M., Walter, W. K. and Tuke, M. A. Edge loading in third generation alumina ceramic-on-ceramic bearings: Stripe wear. *The Journal of Arthroplasty.* 2004, **19**(4), pp. 402–13.
- [233] Arnholt, C. M., MacDonals, D. W., Tohfafarosh, M., Gilbert, J. L., Rimnac, C. M. and Kurtz, S. M. Mechanically Assisted Taper Corrosion in Modular TKA. *J Arthroplasty.* 2014, **29**(9), pp. 205–8.
- [234] Bryant, M., Farrar, R., Freeman, R., Brummitt, K., Nolan, J. and Neville, A. Galvanically enhanced fretting-crevice corrosion of cemented femoral stems. *J Mech Behav Biomed Mater.* 2014, **40**, pp. 275–286.
- [235] Dowson, D. Tribological principles in metal-on-metal hip joint design. *Proc Inst Mech Eng H.* 2006, **220**(2), pp. 161–71.

- [236] Medley, J. B. Can physical joint simulators be used to anticipate clinical wear problems of new joint replacement implants prior to market release? *Proc Inst Mech Eng H*. 2016, **230**(5), pp. 347–58.
- [237] Saikko, V., Ahlroos, T., Revitzer, H., Ryti, O. and Kuosmanen, P. The effect of acetabular cup position on wear of a large-diameter metal-on-metal prosthesis studied with a hip joint simulator. *Tribology International*. 2013, **60**, pp. 70–6.
- [238] Saikko, V. Effect of increased load on the wear of a large diameter metal-on-metal modular hip prosthesis with a high inclination angle of the acetabular cup. *Tribology International*. 2016, **96**, pp. 149–54.
- [239] de Villiers, D. and Shelton, J. C. Measurement outcomes from hip simulators. *Proc Inst Mech Eng H*. 2016, **230**(5), pp. 398–05.
- [240] Neville, A., Hesketh, J., Beadling, A. R., Bryant, M. G. and Dowson, D. Incorporating corrosion measurement in hip wear simulators: An added complication or a necessity? *Proc Inst Mech Eng H*. 2016, **230**(5), pp. 406–20.
- [241] Beadling, A. R., Bryant, M., Dowson, D. and Neville, A. The Effect of Microseparation on Corrosion Rates of Metal-on-Metal Total Hip Replacements. In: *NACE International, Corrosion 2015, 15th–19th Mar. 2015, Dallas, TX*.
- [242] Beadling, A. R., Bryant, M., Dowson, D. and Neville, A. Tribocorrosion of hard-on-hard total hip replacements with metal and ceramic counterfaces under standard and adverse loading conditions. *Tribology International*. 2016, **103**, pp. 359–67.
- [243] Ali, M., Al-Hajjar, M., Partridge, S., Williams, S., Fisher, J. and Jennings, L. M. Influence of hip joint simulator design and mechanics on the wear and creep of metal-on-polyethylene bearings. *Proc Inst Mech Eng H*. 2016, **230**(5), pp. 389–97.

- [244] Fam, H., Bryant, J. T. and Kontopoulou, M. Rheological properties of synovial fluids. *Biorheology*. 2007, **44**(2), pp. 59–74.
- [245] Cao, S., Guadalupe Maldonado, S. and Mischler, S. Tribocorrosion of passive metals in the mixed lubrication regime: theoretical model and application to metal-on-metal artificial hip joints. *Wear*. 2015, **324-325**, pp. 55–63.
- [246] Cao, S. and Mischler, S. Assessment of a recent tribocorrosion model for wear of metal-on-metal hip joints: Comparison between model predictions and simulator results. *Wear*. 2016, **362-363**, pp. 170–78.
- [247] Brockett, C. L., Carbone, S., Abdelgaied, A., Fisher, J. and Jennings, L. M. Influence of contact pressure, cross-shear and counterface material on the wear of PEEK and CFR-PEEK for orthopaedic applications. *J Mech Behav Biomed Mater*. 2016, **63**, pp. 10–16.

# Appendix A - Oral and Poster Presentations

## A.1 - Oral Presentations

Beadling, A., Hesketh, J., Bryant, M., Dowson, D. and Neville, A. Tribocorrosion of Metal-on-Metal Hip Replacements: Initial observations for different diameter bearings. In: *5th World Tribology Congress, 8th-13th Sep. 2013, Torino (Italy)*.

Beadling, A. R., Bryant, M., Dowson, D. and Neville, A. The Effect of Microseparation on the Degradation of Metal-on-Metal Total Hip Replacements. In: *41st Leeds-Lyon Symposium on Tribology, 2nd-5th Sep. 2014, Leeds (UK)*.

Beadling, A., Bryant, M., Dowson, D. and Neville, A. The Effect of Microseparation on the Contribution of Corrosion to the Total Degradation of Metal-on-Metal Total Hip Replacements. In: *55th Corrosion Science Symposium, 29th-30th Sep. 2014, Manchester (UK)*.

Beadling, A. R., Bryant, M., Dowson, D. and Neville, A. Tribocorrosion of Total Hip Replacements. In: *IMEchE 23rd Mission of Tribology Research, 3rd Dec. 2014, London (UK)*.

Beadling, A. R., Bryant, M., Dowson, D. and Neville, A. The Effect of Microseparation on the Degradation of Metal-on-Metal Total Hip Replacements. In: *NACE Corrosion 2015, 15th-19th Mar. 2015, Dallas (USA)*.

Beadling, A. R., Bryant, M., Dowson, D. and Neville, A. A Link Between the Tribology and Corrosive Degradation of Metal-on-Metal THR. In: *43rd Leeds-Lyon Symposium on Tribology, 6th-9th Sep. 2016, Leeds (UK)*.

Beadling, A. R., Bryant, M., Dowson, D. and Neville, A. Adverse loading effects on tribocorrosive degradation of a 28mm metal-on-metal hip replacement bearing. In: *3rd International Conference on BioTribology, 11th-14th Sep. 2016, London*

(UK).

## **A.2 - Poster Presentations**

Beadling, A., Bryant, M., Dowson, D. and Neville, A. Tribocorrosion - Current concepts in Metal-on-Metal Hip Replacements. In: *NACE Corrosion 2014, 9th-13th Mar. 2014, San Antonio (TX, USA)*.

Beadling, A. R., Bryant, M., Dowson, D. and Neville, A. Tribocorrosion in Hard-on-Hard Total Hip Replacement Bearing Couples. In: *61st ORS Annual Meeting, 28th-31st Mar. 2015, Las Vegas (NV, USA)*.

Beadling, A. R., Bryant, M., Dowson, D. and Neville, A. Tribocorrosion of Hard-on-Hard Total Hip Replacements with Metal and Ceramic Counterfaces. In: *42nd Leeds-Lyon Symposium on Tribology, 7th-9th Sep. 2015, Lyon (France)*.

Beadling, A., Bryant, M., Dowson, D. and Neville, A. Effect of Cup Inclination on the Tribocorrosion of Metal-on-Metal Hip Replacements. In: *UK Tribology Network Launch Event, 21st Oct. 2015, London (UK)*.

## Appendix B - Image Reproduction Permissions

**Figure 3.9:** Wear coefficients for HC and LC CoCrMo alloy and 316L Stainless Steel in different lubricants [141].

**ELSEVIER LICENSE  
TERMS AND CONDITIONS**

Feb 18, 2016

---

This is a License Agreement between Andrew R Beadling ("You") and Elsevier ("Elsevier") provided by Copyright Clearance Center ("CCC"). The license consists of your order details, the terms and conditions provided by Elsevier, and the payment terms and conditions.

**All payments must be made in full to CCC. For payment instructions, please see information listed at the bottom of this form.**

Supplier	Elsevier Limited The Boulevard, Langford Lane Kidlington, Oxford, OX5 1GB, UK
Registered Company Number	1982084
Customer name	Andrew R Beadling
Customer address	School of Mechanical Engineering Leeds, West Yorkshire LS2 9JT
License number	3811991352532
License date	Feb 18, 2016
Licensed content publisher	Elsevier
Licensed content publication	Tribology International
Licensed content title	Tribocorrosion in implants—assessing high carbon and low carbon Co-Cr-Mo alloys by in situ electrochemical measurements
Licensed content author	Yu Yan, Anne Neville, Duncan Dowson, Sophie Williams
Licensed content date	December 2006
Licensed content volume number	39
Licensed content issue number	12
Number of pages	9
Start Page	1509
End Page	1517
Type of Use	reuse in a thesis/dissertation
Portion	figures/tables/illustrations
Number of figures/tables/illustrations	1
Format	both print and electronic
Are you the author of this Elsevier article?	No
Will you be translating?	No
Original figure numbers	Fig 4
Title of your thesis/dissertation	Biotribocorrosion of Hard-on-Hard Bearing Surfaces in Orthopaedic Hip Replacements
Expected completion date	Apr 2016
Estimated size (number of pages)	250

**Figure 3.10:** Anodic current and friction coefficient for silicon nitride articulating against HC CoCrMo alloy [11].

**ELSEVIER LICENSE  
TERMS AND CONDITIONS**

Feb 29, 2016

---

This is a License Agreement between Andrew R Beadling ("You") and Elsevier ("Elsevier") provided by Copyright Clearance Center ("CCC"). The license consists of your order details, the terms and conditions provided by Elsevier, and the payment terms and conditions.

**All payments must be made in full to CCC. For payment instructions, please see information listed at the bottom of this form.**

Supplier	Elsevier Limited The Boulevard, Langford Lane Kidlington, Oxford, OX5 1GB, UK
Registered Company Number	1982084
Customer name	Andrew R Beadling
Customer address	School of Mechanical Engineering Leeds, West Yorkshire LS2 9JT
License number	3818291131100
License date	Feb 29, 2016
Licensed content publisher	Elsevier
Licensed content publication	Wear
Licensed content title	Tribo-corrosion properties of cobalt-based medical implant alloys in simulated biological environments
Licensed content author	Yu Yan, Anne Neville, Duncan Dowson
Licensed content date	10 September 2007
Licensed content volume number	263
Licensed content issue number	7-12
Number of pages	7
Start Page	1105
End Page	1111
Type of Use	reuse in a thesis/dissertation
Portion	figures/tables/illustrations
Number of figures/tables/illustrations	1
Format	both print and electronic
Are you the author of this Elsevier article?	No
Will you be translating?	No
Original figure numbers	Fig 13
Title of your thesis/dissertation	Biotribocorrosion of Hard-on-Hard Bearing Surfaces in Orthopaedic Hip Replacements
Expected completion date	Apr 2016
Estimated size (number of pages)	250

**Figure 3.11:** Schematic of the pendulum friction simulator used by Yan et al. [153].

<b>ELSEVIER LICENSE TERMS AND CONDITIONS</b>	
	Jan 28, 2016
<hr/>	
<p>This is a License Agreement between Andrew R Beadling ("You") and Elsevier ("Elsevier") provided by Copyright Clearance Center ("CCC"). The license consists of your order details, the terms and conditions provided by Elsevier, and the payment terms and conditions.</p>	
<p><b>All payments must be made in full to CCC. For payment instructions, please see information listed at the bottom of this form.</b></p>	
Supplier	Elsevier Limited The Boulevard, Langford Lane Kidlington, Oxford, OX5 1GB, UK
Registered Company Number	1982084
Customer name	Andrew R Beadling
Customer address	School of Mechanical Engineering Leeds, West Yorkshire LS2 9JT
License number	3797690297895
License date	Jan 28, 2016
Licensed content publisher	Elsevier
Licensed content publication	Wear
Licensed content title	Effect of metallic nanoparticles on the biotribocorrosion behaviour of Metal-on-Metal hip prostheses
Licensed content author	Y. Yan, A. Neville, D. Dowson, S. Williams, J. Fisher
Licensed content date	15 June 2009
Licensed content volume number	267
Licensed content issue number	5-8
Number of pages	6
Start Page	683
End Page	688
Type of Use	reuse in a thesis/dissertation
Intended publisher of new work	other
Portion	figures/tables/illustrations
Number of figures/tables/illustrations	1
Format	both print and electronic
Are you the author of this Elsevier article?	No
Will you be translating?	No
Original figure numbers	Fig. 1
Title of your thesis/dissertation	Biotribocorrosion of Hard-on-Hard Bearing Surfaces in Orthopaedic Hip Replacements
Expected completion date	Apr 2016
Estimated size (number of pages)	250

**Figure 3.12:** Cyclic variation in potentiostatic current during articulation of a 36 mm HC CoCr hip bearing [15].

**ELSEVIER LICENSE  
TERMS AND CONDITIONS**

Jan 28, 2016

This is a License Agreement between Andrew R Beadling ("You") and Elsevier ("Elsevier") provided by Copyright Clearance Center ("CCC"). The license consists of your order details, the terms and conditions provided by Elsevier, and the payment terms and conditions.

**All payments must be made in full to CCC. For payment instructions, please see information listed at the bottom of this form.**

Supplier	Elsevier Limited The Boulevard, Langford Lane Kidlington, Oxford, OX5 1GB, UK
Registered Company Number	1982084
Customer name	Andrew R Beadling
Customer address	School of Mechanical Engineering Leeds, West Yorkshire LS2 9JT
License number	3797671373979
License date	Jan 28, 2016
Licensed content publisher	Elsevier
Licensed content publication	Tribology International
Licensed content title	Biotribocorrosion of metal-on-metal hip replacements: How surface degradation can influence metal ion formation
Licensed content author	James Hesketh, Qingen Meng, Duncan Dowson, Anne Neville
Licensed content date	September 2013
Licensed content volume number	65
Licensed content issue number	n/a
Number of pages	10
Start Page	128
End Page	137
Type of Use	reuse in a thesis/dissertation
Portion	figures/tables/illustrations
Number of figures/tables/illustrations	1
Format	both print and electronic
Are you the author of this Elsevier article?	No
Will you be translating?	No
Original figure numbers	Fig. 6
Title of your thesis/dissertation	Biotribocorrosion of Hard-on-Hard Bearing Surfaces in Orthopaedic Hip Replacements
Expected completion date	Apr 2016
Estimated size (number of pages)	250

**Figure 3.13:** The Acetabular Liner (left) and Femoral Head (right) from an explanted McKee-Farrar prosthesis displaying a visible tribofilm formation on both surfaces [7].

**ELSEVIER LICENSE  
TERMS AND CONDITIONS**

Jan 28, 2016

---

This is a License Agreement between Andrew R Beadling ("You") and Elsevier ("Elsevier") provided by Copyright Clearance Center ("CCC"). The license consists of your order details, the terms and conditions provided by Elsevier, and the payment terms and conditions.

**All payments must be made in full to CCC. For payment instructions, please see information listed at the bottom of this form.**

Supplier	Elsevier Limited The Boulevard, Langford Lane Kidlington, Oxford, OX5 1GB, UK
Registered Company Number	1982084
Customer name	Andrew R Beadling
Customer address	School of Mechanical Engineering Leeds, West Yorkshire LS2 9JT
License number	3797611091477
License date	Jan 28, 2016
Licensed content publisher	Elsevier
Licensed content publication	Wear
Licensed content title	Tribochemical reaction on metal-on-metal hip joint bearings A comparison between in-vitro and in-vivo results
Licensed content author	M.A. Wimmer, C. Sprecher, R. Hauert, G. Täger, A. Fischer
Licensed content date	August–September 2003
Licensed content volume number	255
Licensed content issue number	7-12
Number of pages	8
Start Page	1007
End Page	1014
Type of Use	reuse in a thesis/dissertation
Portion	figures/tables/illustrations
Number of figures/tables/illustrations	2
Format	both print and electronic
Are you the author of this Elsevier article?	No
Will you be translating?	No
Original figure numbers	Fig 1. a) + b)
Title of your thesis/dissertation	Biotribocorrosion of Hard-on-Hard Bearing Surfaces in Orthopaedic Hip Replacements
Expected completion date	Apr 2016
Estimated size (number of pages)	250

**Figure 3.14:** EELS spectra of dried bovine serum, the tribological layer and graphite [9].

**THE AMERICAN ASSOCIATION FOR THE ADVANCEMENT OF SCIENCE LICENSE  
TERMS AND CONDITIONS**

Jan 28, 2016

---

This is a License Agreement between Andrew R Beadling ("You") and The American Association for the Advancement of Science ("The American Association for the Advancement of Science") provided by Copyright Clearance Center ("CCC"). The license consists of your order details, the terms and conditions provided by The American Association for the Advancement of Science, and the payment terms and conditions.

**All payments must be made in full to CCC. For payment instructions, please see information listed at the bottom of this form.**

License Number	3797681404908
License date	Jan 28, 2016
Licensed content publisher	The American Association for the Advancement of Science
Licensed content publication	Science
Licensed content title	Graphitic Tribological Layers in Metal-on-Metal Hip Replacements
Licensed content author	Y. Liao,R. Pourzal,M. A. Wimmer,J. J. Jacobs,A. Fischer,L. D. Marks
Licensed content date	Dec 23, 2011
Volume number	334
Issue number	6063
Type of Use	Thesis / Dissertation
Requestor type	Scientist/individual at a research institution
Format	Print and electronic
Portion	Figure
Number of figures/tables	1
Order reference number	None
Title of your thesis / dissertation	Biotribocorrosion of Hard-on-Hard Bearing Surfaces in Orthopaedic Hip Replacements
Expected completion date	Apr 2016
Estimated size(pages)	250

**Figure 4.16:** Schematic of White-Light Interferometry set-up [178].

**ELSEVIER LICENSE  
TERMS AND CONDITIONS**

Jan 28, 2016

This is a License Agreement between Andrew R Beadling ("You") and Elsevier ("Elsevier") provided by Copyright Clearance Center ("CCC"). The license consists of your order details, the terms and conditions provided by Elsevier, and the payment terms and conditions.

**All payments must be made in full to CCC. For payment instructions, please see information listed at the bottom of this form.**

Supplier	Elsevier Limited The Boulevard, Langford Lane Kidlington, Oxford, OX5 1GB, UK
Registered Company Number	1982084
Customer name	Andrew R Beadling
Customer address	School of Mechanical Engineering Leeds, West Yorkshire LS2 9JT
License number	3797691430936
License date	Jan 28, 2016
Licensed content publisher	Elsevier
Licensed content publication	Optics and Lasers in Engineering
Licensed content title	Testing micro devices with fringe projection and white-light interferometry
Licensed content author	Robert Windecker, Matthias Fleischer, Klaus Körner, Hans J. Tiziani
Licensed content date	August 2001
Licensed content volume number	36
Licensed content issue number	2
Number of pages	14
Start Page	141
End Page	154
Type of Use	reuse in a thesis/dissertation
Intended publisher of new work	other
Portion	figures/tables/illustrations
Number of figures/tables/illustrations	1
Format	both print and electronic
Are you the author of this Elsevier article?	No
Will you be translating?	No
Original figure numbers	Fig. 7
Title of your thesis/dissertation	Biotribocorrosion of Hard-on-Hard Bearing Surfaces in Orthopaedic Hip Replacements
Expected completion date	Apr 2016
Estimated size (number of pages)	250

**Figure 9.2:** Contour plots of the contact pressure (MPa) at the inner surface of acetabular cup with different major radii (mm) under 0.25 mm micro-lateralization [172].

**ELSEVIER LICENSE  
TERMS AND CONDITIONS**

Oct 26, 2016

---

This Agreement between Andrew R Beadling ("You") and Elsevier ("Elsevier") consists of your license details and the terms and conditions provided by Elsevier and Copyright Clearance Center.

License Number	3976420560450
License date	Oct 26, 2016
Licensed Content Publisher	Elsevier
Licensed Content Publication	Medical Engineering & Physics
Licensed Content Title	Contact mechanics studies of an ellipsoidal contact bearing surface of metal-on-metal hip prostheses under micro-lateralization
Licensed Content Author	Ling Wang,Xiaohua Liu,Dichen Li,Feng Liu,Zhongmin Jin
Licensed Content Date	April 2014
Licensed Content Volume Number	36
Licensed Content Issue Number	4
Licensed Content Pages	6
Start Page	419
End Page	424
Type of Use	reuse in a thesis/dissertation
Portion	figures/tables/illustrations
Number of figures/tables/illustrations	1
Format	both print and electronic
Are you the author of this Elsevier article?	No
Will you be translating?	No
Order reference number	
Original figure numbers	2
Title of your thesis/dissertation	Biotribocorrosion of Hard-on-Hard Bearing Surfaces in Orthopaedic Hip Replacements
Expected completion date	Apr 2016
Estimated size (number of pages)	250

**Figure 9.11:** Total, mechanical and chemical mass loss as predicted by the Cao *et al.* [245, 246] tribocorrosion model for a given articulation cycle [245].

**ELSEVIER LICENSE  
TERMS AND CONDITIONS**

Oct 15, 2016

This Agreement between Andrew R Beadling ("You") and Elsevier ("Elsevier") consists of your license details and the terms and conditions provided by Elsevier and Copyright Clearance Center.

License Number	3970150375343
License date	Oct 15, 2016
Licensed Content Publisher	Elsevier
Licensed Content Publication	Wear
Licensed Content Title	Tribocorrosion of passive metals in the mixed lubrication regime: theoretical model and application to metal-on-metal artificial hip joints
Licensed Content Author	Shoufan Cao,Sandra Guadalupe Maldonado,Stefano Mischler
Licensed Content Date	15 February 2015
Licensed Content Volume Number	324
Licensed Content Issue Number	n/a
Licensed Content Pages	9
Start Page	55
End Page	63
Type of Use	reuse in a thesis/dissertation
Portion	figures/tables/illustrations
Number of figures/tables/illustrations	1
Format	both print and electronic
Are you the author of this Elsevier article?	No
Will you be translating?	No
Order reference number	
Original figure numbers	Figure 5
Title of your thesis/dissertation	Biotribocorrosion of Hard-on-Hard Bearing Surfaces in Orthopaedic Hip Replacements
Expected completion date	Apr 2016
Estimated size (number of pages)	250
Elsevier VAT number	GB 494 6272 12
Requestor Location	Andrew R Beadling School of Mechanical Engineering Woodhouse Lane University of Leeds Leeds, West Yorkshire LS2 9JT United Kingdom Attn: Andrew R Beadling
Customer VAT ID	GB613451470
Total	0.00 GBP